Synthesis of Multicomponent Metal-Organic Frameworks and Investigations of Their Physical Properties

A thesis presented in partial fulfilment of the requirements of the degree of

Doctor of Philosophy

in

Chemistry

at Massey University, Manawatu, New Zealand

Adil Alkaş

2019

To nomadic peoples everywhere

Abstract

Multicomponent metal-organic frameworks (MOFs) are built up from multiple ligands that are geometrically distinct. These ligands occupy specific positions in the MOF lattice. Installing different functionalities at precise locations in the framework is an important step in making MOFs for specific applications. This can be achieved by designing functionalized ligands for multicomponent MOFs. This study was, firstly, focused on design and synthesis of new linkers. The study then covered preparation of a number of quaternary MOFs. Furthermore, the study was focused on the physical and chemical properties of these MOFs, such as their catalytic activity, gas adsorption and fluorescence behaviours.

Contributions

All the work in this thesis was completed by Adil Alkaş

Except:

- Joel Cornelio assisted with the fluorescence measurements and analyses presented in Chapter 2.
- Seok J. Lee modelled the single crystal structures of MUF-77-cat-1, MUF-77-pipcdc-NH and MUF-77-azecdc-NH in Chapters 3 and 4.
- David Perl helped with modelling the single crystal structure of MUF-tat-benzyl.
- Omid T. Qazvini calculated the void fractions of several MOFs.
- HPLC conditions for the catalysis study were established by Dr. Tian-You Zhou.
- The syntheses and some of the analyses presented in Chapter 6 were conducted by Laurine Friche and Shikeale Harris under the supervision of Adil Alkaş.
- All ES-MS analyses were conducted by David Lun.

Acknowledgements

I would like to take the opportunity to thank the large number of people who have contributed to my PhD research and thesis. First, I would like to thank my supervisor Professor Shane Telfer for providing me this wonderful PhD opportunity and scholarship to carry out research in MOF chemistry. Thank you for your expert guidance on all matters throughout this PhD, from the big picture all the way to technical details. Thank you for providing funding for me to attend conferences and symposiums.

I would also like to thank my co-supervisor, Catherine Whitby, for her guidance and support. I also thank, Dr. Tian-You Zhou for much-valued advice and assistance in organic chemistry, David Lun for his technical assistance and providing ES-MS data. I also thank Dr. Pat Edwards for assisting NMR experiments. I also thank Seok June Lee, Joel Cornelio, David Perl, Omid Taheri, Heather Jameson, Laurine Friche, Shikeale Harris, Maulik Mungalpara, Bernhard Auer, Simon Guery, Thibaud Noiret, Dr. Ben Yin, Dr. John Clements, Nisansala Bandara, Tim Craig, Nicholas Symon and all other past Telfer group members for scientific discussions and technical assistance.

I would like to acknowledge the financial support from RSNZ Marsden Fund for a Doctoral scholarship, School of Fundamental Sciences for my fourth-year student fee funding. I also thank the SFS postgraduate travel fund for supporting me to attend conferences in California and Delft. I greatly thank the MacDiarmid Institute for organizing and supporting annual student and postdoc symposiums and AMN-8 conference in Queenstown.

I also thank IFS administration and technical staff for their great assistance during my PhD research and thesis writing.

I must thank Aziz Guzel and Yasemin Acar for their support and encouragement over the last few years.

Finally, I would like to thank Johanna Gassner for her love and support.

Abbreviations

ANG	adsorbed natural gas
BET	Brunauer-Emmett-Teller
Boc	*tert*-butoxycarbonyl
CNG	compressed natural gas
COF	covalent organic framework
DBF	*N*,*N*-dibutylformamide
DEF	*N*,*N*-diethylformamide
DMF	*N*,*N*-dimethylformamide
DMSO	dimethyl sulfoxide
HKUST	Hong Kong University of Science and Technology
IRMOF	isoreticular metal-organic framework
IUPAC	International Union of Pure and Applied Chemistry
LNG	liquefied natural gas
MAF	metal azolate framework
MC	multicomponent
MC-MOF	multicomponent metal-organic framework
MCP	microporous coordination polymer
MIL	Matérial Institut Lavoisier
MMPF	metal-metalloporphyrin framework
MOF	metal-organic framework
MTV	multivariate
MTV-MOF	multivariate metal-organic framework
MUF	Massey University framework
NJU	Nanjing University
NMR	nuclear magnetic resonance
PCN	porous coordination network

PCP	porous coordination polymer
PSM	postsynthetic modification
PXRD	powder x-ray diffraction
SBU	secondary building unit
SCXRD	single crystal x-ray diffraction
SEM	scanning electron microscopy
STP	standard temperature and pressure
TGA	Thermogravimetric analysis
TFA	Trifluoroacetic acid
UiO	University of Oslo
UMCM	University of Michigan crystalline material
XRD	X-ray diffraction
ZIF	zeolitic imidazolate framework

Publications and thesis structure

Publications relevant to this thesis

1. **A. Alkaş**, J. Cornelio, S. G. Telfer, Tritopic Triazatruxene Ligands for Multicomponent Metal-Organic Frameworks, *Chem. Asian J*. **2018**, 14, 1167-1174.
   I carried out the experimental and computational work, put together the electronic supporting information, and wrote the first draft of this paper.

Additional publications

2. J. Cornelio, T-Y. Zhou, **A. Alkaş,** S. G. Telfer, Systematic Tuning of the Luminescence Output of Multicomponent Metal-Organic Framework, *J. Am. Chem. Soc.* **2018**, 140, 45, 15470-1547.
3. T. Boonprab, P. Harding, K. S. Murray, W. Phonsri, S. G. Telfer, **A. Alkaş**, R. Ketkew, Y. Tantirubgrotechai, G. N. L. Jameson, D. J. Harding, Solvatomorphism and Anion Effects in Predominantly Low Spin Iron(III) Schiff Base Complexes, *Dalton Trans*. **2018**, 47, 12449-12458.
4. D. Sertphon, K. S. Murray, W. Phonsri, J. Jover, E. Ruiz, S. G. Telfer, **A. Alkaş**, P. Harding and D. J. Harding, Slow Relaxation of Magnetization in Bis-mer-tridentate Octahedral Co(II) Complex, *Dalton Trans*. **2018**, 47, 859.
5. D. Sertphon, D. J. Harding, P. Harding, K. S. Murray, B. Moubaraki, H. Adams, **A. Alkaş** and S. G. Telfer, Substituent-Influenced Spin Crossover in Fe^{III} Quinolylsalicylaldiminates, *Eur. J. Inorg. Chem*, **2016**, 432-438.
6. P. Insiti, P. Jitthiang, P. Harding, K. Chainok, R. Chotima, J. Sirirak, S. Blackwood, **A. Alkaş**, S. G. Telfer and D. J. Harding, Substituent modulated packing in octahedral Ni(II) complexes, *Polyhedron*, **2016**, 242-248.

Table of Contents

Chapter 1 Introduction

1.1 Metal Organic-Frameworks (MOFs)

1.1.1 Definition and terminology

MOFs are a class of porous crystalline materials in which inorganic units (metal ions and clusters) are bridged via multidentate organic ligands to form multi-dimensional networks (Figure 1.1). The term "metal-organic framework" was first introduced by Yaghi in 1995. However, the difference between this term, coordination polymers (CPs) and coordination networks (CNs) was not very clear until the beginning of 2010s. In 2013, the International Union of Pure and Applied Chemistry (IUPAC) published its recommendations to introduce some clarity to the definitions and terminologies used in the field of MOFs.[1] According to IUPAC recommendations, *a MOF is a coordination network with organic ligands containing potential voids.* And a coordination network refers to *a coordination compound extending through repeating coordination entities in two or three dimensions.* The publication also defines a coordination polymer as *a coordination compound with repeating coordination entities extending in one, two or three dimensions*. In essence, coordination networks are a subclass of coordination polymers, and MOFs a further subclass of coordination networks. Nevertheless, the term MOF is still not the only term used in the field. Some research groups prefer to use different terms such as porous coordination polymers (PCPs),[2] microporous coordination polymers (MCPs),[3] and porous coordination networks (PCNs).[4]

In this thesis, the term MOF will be used according to the IUPAC recommendations and all materials initially reported with alternative terms will be referred to as MOFs.

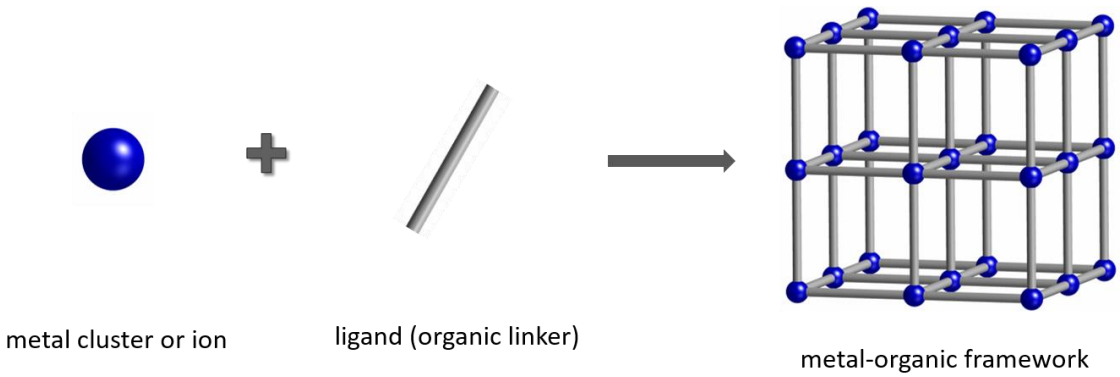

Figure 1. 1 A schematic illustration of MOF formation and network structure. Multidentate ligands bind metal clusters through multiple points of extension to form three dimensional networks.

There are no guidelines on nomenclature of MOFs. Generally, a nickname (e.g. MOF-5)[5] or abbreviated formula, such as $[Zn_4O(FMA)_3]$,[6] are used. IUPAC agrees that researchers can name new compounds based on their place of origin followed by a number such as NU-100[7] (Northwestern University) and MUF-32[8] (Massey University Frameworks).

1.1.2 A brief history of MOFs

MOFs are a subclass of coordination networks. Therefore, the historical development of MOFs is closely associated to that of coordination networks. Perhaps the earliest coordination network is Prussian blue, $Fe_4[Fe(CN)_6]_3 \cdot XH_2O$. It was first synthesized in 1706 as a pigment and its crystal structure was not known until 1977.[9] Its polymeric structure has a cubic network topology in which six-coordinated Fe(II) and Fe(III) ions are connected by linear divergent CN^- ligands.

In 1989, Robson proposed that three dimensional polymeric frameworks can be obtained by linking together tetrahedral or octahedral metal nodes and rod-like organic linkers.[10] Later in 1990, he also predicted the properties of these new materials to be as follows: a) High porosity and low density with thermal, chemical and mechanical stability; b) Pores that allow facile diffusion and separation of molecular or ionic guest molecules; c) Structures that are suitable for introduction of one or more catalytic sites via chemical functionalization of organic linkers.[11]

In 1995, the structure of $[Cu_2(4,4\text{-bipy})_3](NO_3)_2]$ and $Co(btc)(pyridine)_2$ (btc = 1,3,5-benzenetricarboxylate) were reported and the term metal-organic frameworks was used for the first time.[12-13] In 1997, researchers reported some coordination networks which could adsorb small gas molecules, such as N_2, O_2 and CH_4, at high pressure.[14] Later, in 1998, the porosity of $[Zn_2(bdc)_4(H_2O)_2]$ was demonstrated by N_2 adsorption isotherms at low pressure and temperature.[15] However, none of these materials exhibited the desired porosity and stability. A major turning point in chemistry of MOFs occurred in 1999 when MOF-5[5] and HKUST-1[16] were reported.

The synthesis of MOF-5 created great excitement due to its exceptional properties. It maintained its porosity after removal of guest molecules and demonstrated high thermal stability. It exhibited the highest porosity and surface area recorded at the time. Its Langmuir surface area was first calculated to be 2900 m^2/g. This value was later found to be 4400 m^2/g by using optimal synthetic conditions and careful handling. Its BET (Brunauer-Emmett-

Teller[17]) surface area and pore volume were found to be 3800 m^2/g and 1.04 cm^3/g respectively.[18] As shown in Figure 1.2, MOF-5 is constructed from $Zn_4O(CO_2)_6$ cluster and 1,4-benzendicarboxylic acid (H_2bdc) and has an cubic network structure. Each $Zn_4O(CO_2)_6$ cluster contains four ZnO_4 tetrahedra with a common vertex and six carboxylate C atoms that define an octahedral geometry.

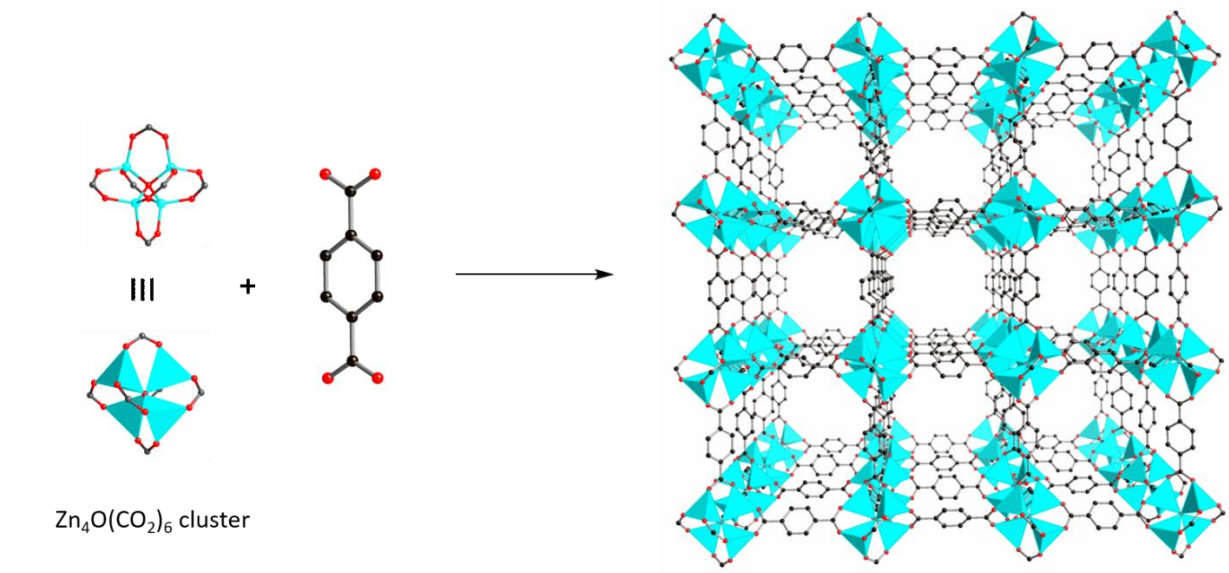

Figure 1. 2 A scheme illustrating the conceptual route to MOF-5 by linking tetranuclear zinc(II) clusters and bdc ligands. On the right is the single crystal structure of MOF-5. Hydrogen atoms are omitted for clarity. Atom colors: carbon: black, oxygen: red, zinc: cyan.

After the synthesis of MOF-5, another significant advance in the chemistry of MOFs was the development of a powerful strategy for pore functionalization and expansion which was described by Yaghi and coworkers in 2002. This strategy allows preparation of MOFs with the same overall network structures by using functionalized or elongated ligands.[19] It is based on "isoreticular synthesis" which is described as *the process of assembling judiciously designed rigid molecular building blocks into predetermined ordered structures, which are held together by strong bonding*.[20] As shown in Figure 1.3, all of these ligands can form MOFs with the same network topology under the same or similar reaction conditions. A family of frameworks assembled in this way is classified as isoreticular MOFs (IRMOFs). The isoreticular synthesis approach can also be applied to MOFs containing tritopic linkers, as will be later discussed in section 1.2.3.

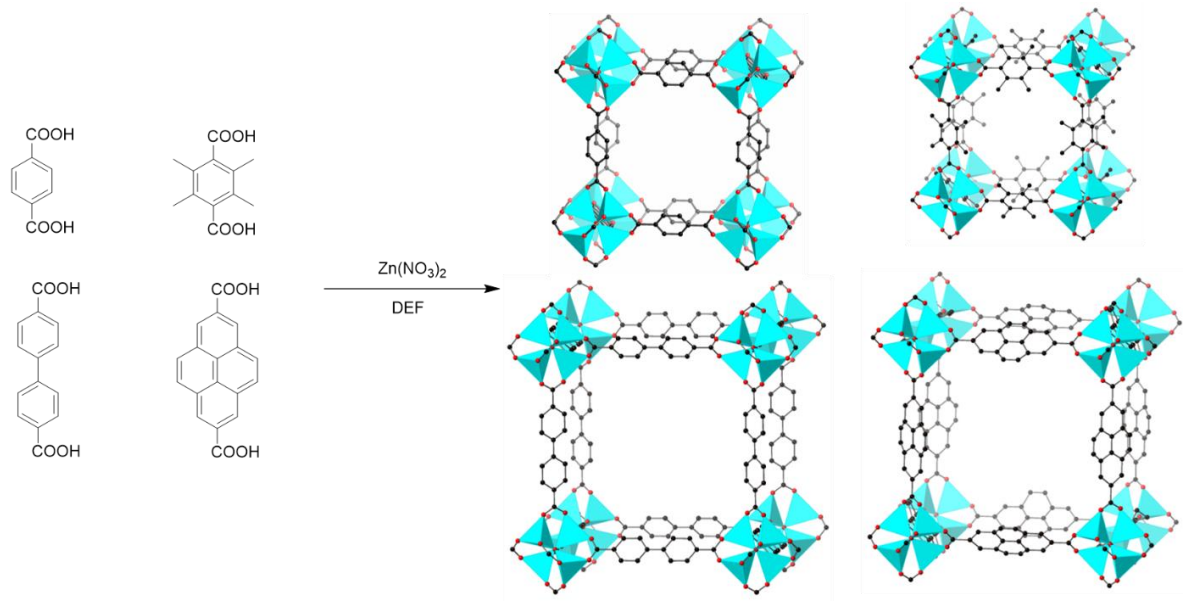

Figure 1. 3 A scheme illustrating the synthesis of isoreticular MOFs by using ligands with different lengths or distinct functional groups.

Other milestones in MOF chemistry are the syntheses of two groups of highly stable materials. The first group is the MOFs which are constructed from high valent metals and carboxylates. The second one is zeolitic imidazolate frameworks (ZIF) which are built up from metal ions and imidazolates. The stability of these materials is related to the strong coordination bond between metal ions and ligands. This will be further discussed in section 1.1.4.

MIL-100 was reported in 2005 and it is the prototype of MOFs which show resistance to degradation by hydrolysis.[21] It was firstly synthesized by combining H_2bdc and chromium(III) nitrate under hydrothermal conditions in the presence of hydrofluoric acid. Six bdc linkers are coordinated to four six-connected $Cr_3O(H_2O)_2F(CO_2)_6$ to form a tetrahedral cage. Each tetrahedral cage is further linked with four other cages through sharing their vertices. MIL-100 describes a **mnt** network. It has two types of mesopores with diameters of 29 Å and 34 Å. These large pores have been demonstrated to accommodate guest particles up to 13.1 Å in diameter. The coordinated water molecules on the $Cr_3O(H_2O)_2F(CO_2)_6$ cluster can be removed to create open metal sites and these sites can be functionalized further for selective gas sorption and catalysis.[22-24] Some isostructural frameworks have been reported by replacing chromium by other trivalent cations such as Fe(III), V(III) and Al(III).[24-26] A number of MIL-101 analogues have also been prepared by using either elongated or functionalized ditopic carboxylates.[25, 27]

As mentioned above, MIL-100 has a **mnt** network. The type of network is usually symbolized with three lower cases letter in bold. The geometry and binding sites of organic ligands along with the connectivity of metal clusters define the topology of MOFs.

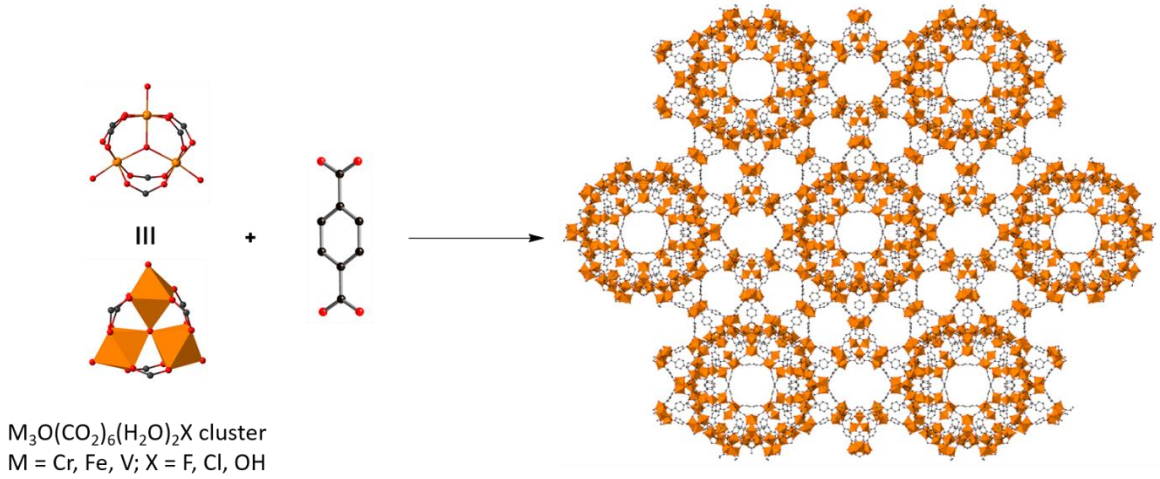

Figure 1. 4 A scheme illustrating the conceptual route to MIL-101 by linking trinuclear chromium(III) clusters and bdc ligands. On the right is the single crystal structure of MIL-101. Hydrogen atoms are omitted for clarity. Atom colors: carbon: black, oxygen: red, chromium: orange.

1.1.3 Synthesis of MOF

Over the last two decades a variety of methods have been developed for preparation of MOFs. Solvothermal synthesis is the most commonly used method.[28] Typically, it is carried out by combining a metal salt and an organic linker in a high boiling point solvent (e.g. DMF or DEF) in a screw-cap vial. The mixture is then heated in an oven or on a hot plate for an appropriate amount of time. Reaction temperature, time, reagent concentration and pH are important parameters that can affect the topology, phase purity and crystal size of the resulting material.[29] The feed ratio of organic ligands is very important in the case of the synthesis of multicomponent MOFs (see section 1.3.2.).

Early synthetic methods for MOFs involved the use of bases, such as triethylamine, to deprotonate carboxyl groups. Later, it was found that decomposition of formamide solvents, such as DMF or DEF, in the presence of water can generate the corresponding amine to deprotonate carboxylate groups. The amount of water used in the reaction mixture plays a key role in the synthesis of MOFs. Since water is also able to coordinate the metal ions, an excess

of water can prevent the formation of the desired MOF. A deficit of water, on the other hand, reduces the rate of hydrolysis of formamide solvent, which can limit MOF crystallization.

In the syntheses of MOFs containing trivalent or tetravalent metals, framework formation is so rapid that the resulting product either has low crystallinity or is amorphous.[30] To prevent this from happening and to obtain a material with a better crystallinity, modulators are often used. Modulators are monotopic ligands which can slow down the MOF formation by competing with the linkers for metal coordination sites. Benzoic acid, acetic acid and hydrochloric acid are commonly used modulators.

After synthesis, MOFs pass through an "activation" stage. MOF activation generally refers to the removal of occluded solvent molecules. In some cases, excess linkers are also trapped in the pores of framework. The first step in activation process is exchanging of the solvent with a lower boiling-point solvent. This solvent is then removed by heating the material under vacuum.[31-32] In some cases, when the framework is sensitive to solvent exchange, the material is washed with supercritical carbon dioxide to remove the solvent.[33]

1.1.4 Stability of MOFs

The stability of MOFs generally refers to their robustness towards water or moisture.[34-35] Water can cause degradation of the framework structure by breaking metal-ligand bonds via a hydrolysis process.[36] Water stability is important because synthesis, storage and application conditions usually involve a certain amount of water (including atmospheric water vapour).

The metal-ligand bond strength is an important parameter in the chemistry of MOFs and identifies their thermodynamic stability. Strong coordination bonds are usually observed based on the hard/soft acid/base (HSAB) principle.[37-38] According to this principle, high-valent metal ions (Fe^{3+}, Cr^{3+}, Zr^{4+}, etc.) can form stable MOFs with hard bases such as carboxylate-based ligands. Ferey and coworkers reported early examples of Fe(III) and Cr(III)-based stable MOFs.[21, 39] The first Zr(IV)-based MOF, known as UiO-66[40], was reported by Lillerud's group in 2008. It is synthesized from H_2bdc and zirconium(IV) chloride in DMF. In the structure of UiO-66, $Zr_6O_4(OH)_4(CO_2)_{12}$ clusters are linked by ditopic bdc linkers to form a **fcu** network. UiO-66 is extremely stable in water, aqueous acid and base.[41] This is due to the high thermodynamic stability of the $Zr_6O_4(OH)_4(CO_2)_{12}$ cluster. The amount of energy required for the hydrolysis of the first carboxylate site is 38.2 kcal/mol.[42]

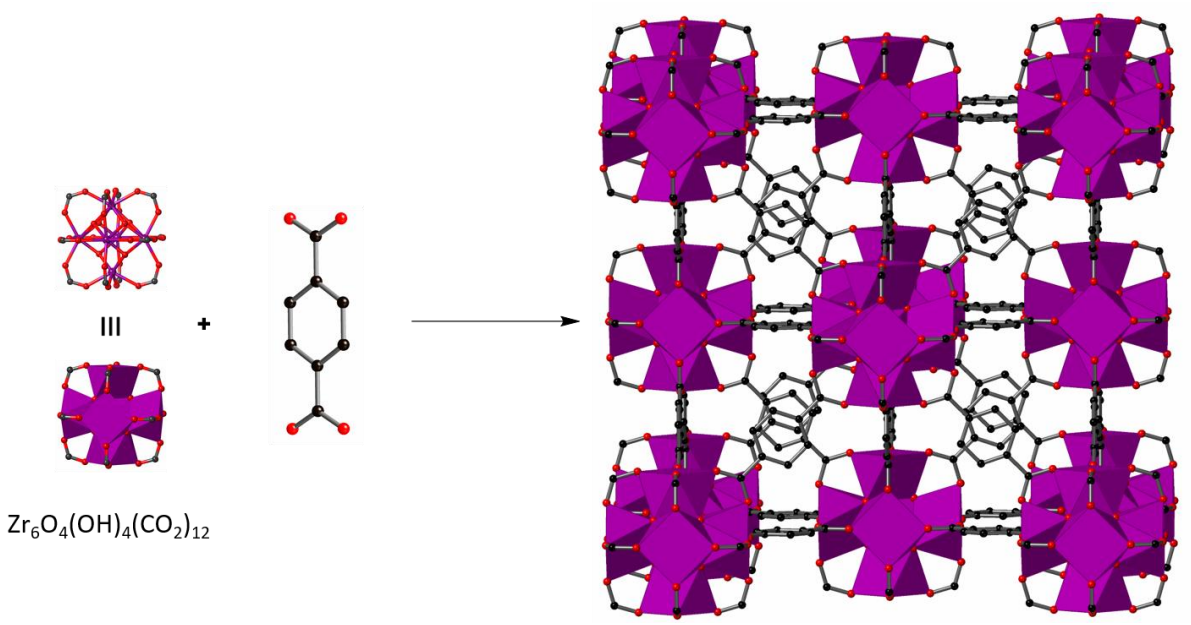

Figure 1. 5 A scheme illustrating the conceptual route to UiO-66 by linking hexanuclear zirconium(IV) clusters and bdc ligands. On the right is the single crystal structure of UiO-66. Hydrogen atoms are omitted for clarity. Atom colors: carbon: black, oxygen: red, zirconium: dark magenta.

Based on the HSAB principle, stable MOFs can be formed by soft azolate ligands (imidazolates, triazolates and tetrazolates) and soft divalent metal ions such as Zn^{2+}, Co^{2+}, etc. Zeolitic imidazolate frameworks (ZIF) are well-known examples of this group.[43] ZIF-8 was reported independently by Chen's and Yaghi's groups in 2006.[43-44] It is synthesized by combining zinc nitrate and 2-methylimidazole under solvothermal conditions. It shows an exceptional resistance to hydrolysis under neutral and basic aqueous conditions even in boiling 8 M aqueous NaOH for 24 hours. However, it is not stable under acidic conditions. It has large pores with 11.6 Å in diameter and these pores are connected through small windows with 3.3 Å in size. Its BET surface area and pore volume were found to be 1630 m^2/g and 0.64 cm^3/g respectively.[43]

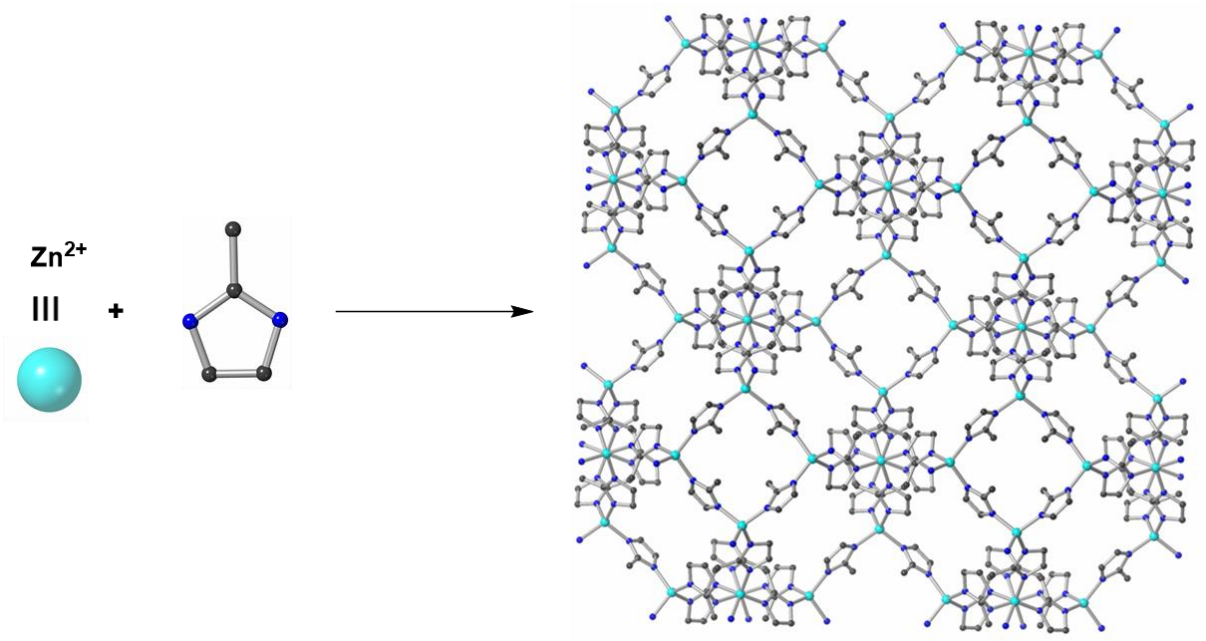

Figure 1. 6 A scheme illustrating the conceptual route to ZIF-8 by linking zinc(II) ions and 2-methylimidazole ligands. On the right is the single crystal structure of ZIF-8. Hydrogen atoms are omitted for clarity. Atom colors: carbon: black, nitrogen: blue, zinc: cyan.

Kinetic factors also have important effects on the stability of MOFs. Using rigid ligands can improve the kinetic stability of MOFs. For instance, UiO-66, UiO-67 and UiO-68 are isostructural MOFs containing the same Zr-based cluster. However, having the shorter and rigid ligand, UiO-66 is more stable than UiO-67 and UiO-68. Similarly, Rosseinsky and coworkers have showed that rigid H_4ptba (4,4',4",4"-(pyrene-1,3,6,8-tetrayltetrakis-(ethyne-2,1-diyl))tetrabenzoic acid) ligand can form more stable MOFs than flexible H_4btba (4,4',4",4"-([1,1-1'-biphenyl]3,3',5,5'-tetrayltetrakis-(ethyne-2,1-diyl))tetrabenzoic acid) with the same metal cluster.[45] In addition, MOF stability can also be enhanced by introducing hydrophilic groups onto ligands. Omary and co-workers reported hydrophobic fluorinated MOFs showing remarkable water stability.[46-47] The Telfer group recently showed that nonpolar alkyl groups in MUF-77 (Massey University Frameworks) play a key role in the stability of this framework. MUF-77 has exceptional stability compared to similar zinc-carboxylate based MOFs.[48]

1.2 Building units for MOFs

1.2.1 Diversity of inorganic clusters

Most MOFs are built up from metal clusters (one notable exception are ZIFs, which are constructed from individual metal ions). Figure 1.7 illustrates some common clusters used in

construction of metal carboxylate MOFs. These units are formed *in situ* under specific synthetic conditions. Metal clusters are thermally stable due to the high binding energy between organic ligands and cluster compared to that of metal ions and monodentate ligands.[49] One of the most common clusters formed by metal ions and carboxylate ligands is four-connected $M_2(CO_2)_4$ (M = Cu, Zn, Co and other divalent metals) and it has a square paddle-wheel geometry. Six-connected $Zn_4O(CO_2)_6$ cluster has the same structure as basic zinc acetate cluster with an octahedral geometry.[50] Co(II) and Be(II) can also form this cluster.[51-52] Six-connected trigonal prismatic $M_3O(CO_2)_6(H_2O)_2X$ is common among trivalent metals. More information about the diversity of metal clusters can be found in the literature.[49, 53-55]

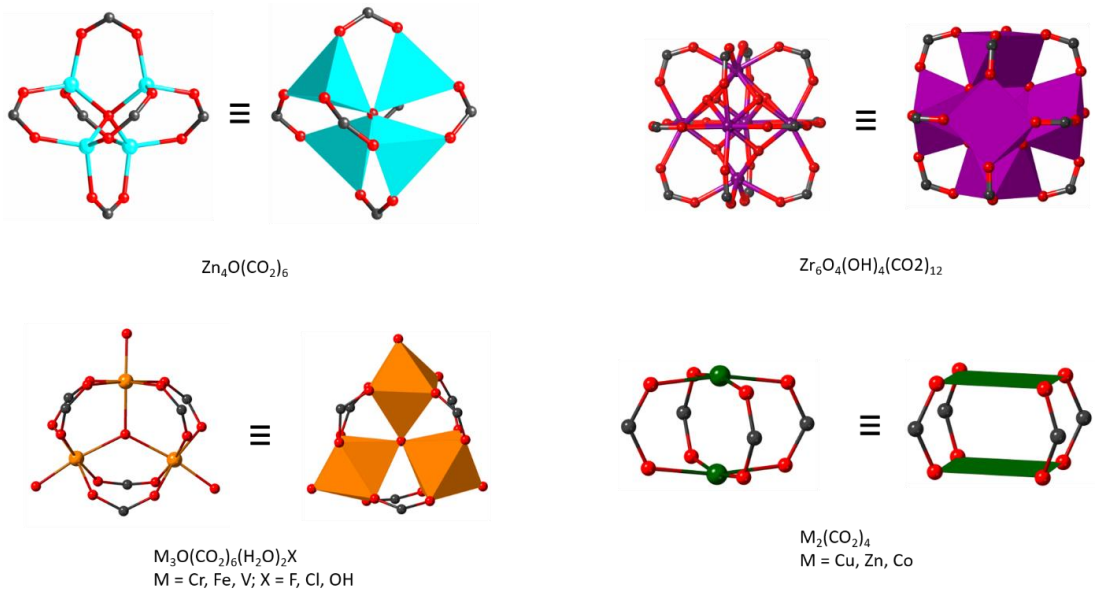

Figure 1. 7 Some common clusters observed in metal carboxylate MOFs. Atom colors: carbon: dark grey, oxygen: red, zinc: cyan, zirconium: dark magenta, chromium: orange, copper: green.

1.2.2 Diversity of organic linkers

Typical organic linkers used in MOF chemistry are: linear ditopic, triangular tritopic, square planar tetratopic, tetrahedral tetratopic and planar hexatopic linkers (Figure 1.8).[56-58] These ligands can be functionalized with appropriate substituents to tune chemical and physical characteristics of the MOF pores. Although commercially available linkers provide a pathway to rapid and inexpensive MOF preparation, some research groups design and synthesize their own ligands using conventional organic synthesis. In conventional synthesis the organic linkers

are prepared step-by-step from organic precursors and the resulting compounds are then used in the self-assembly of MOFs.

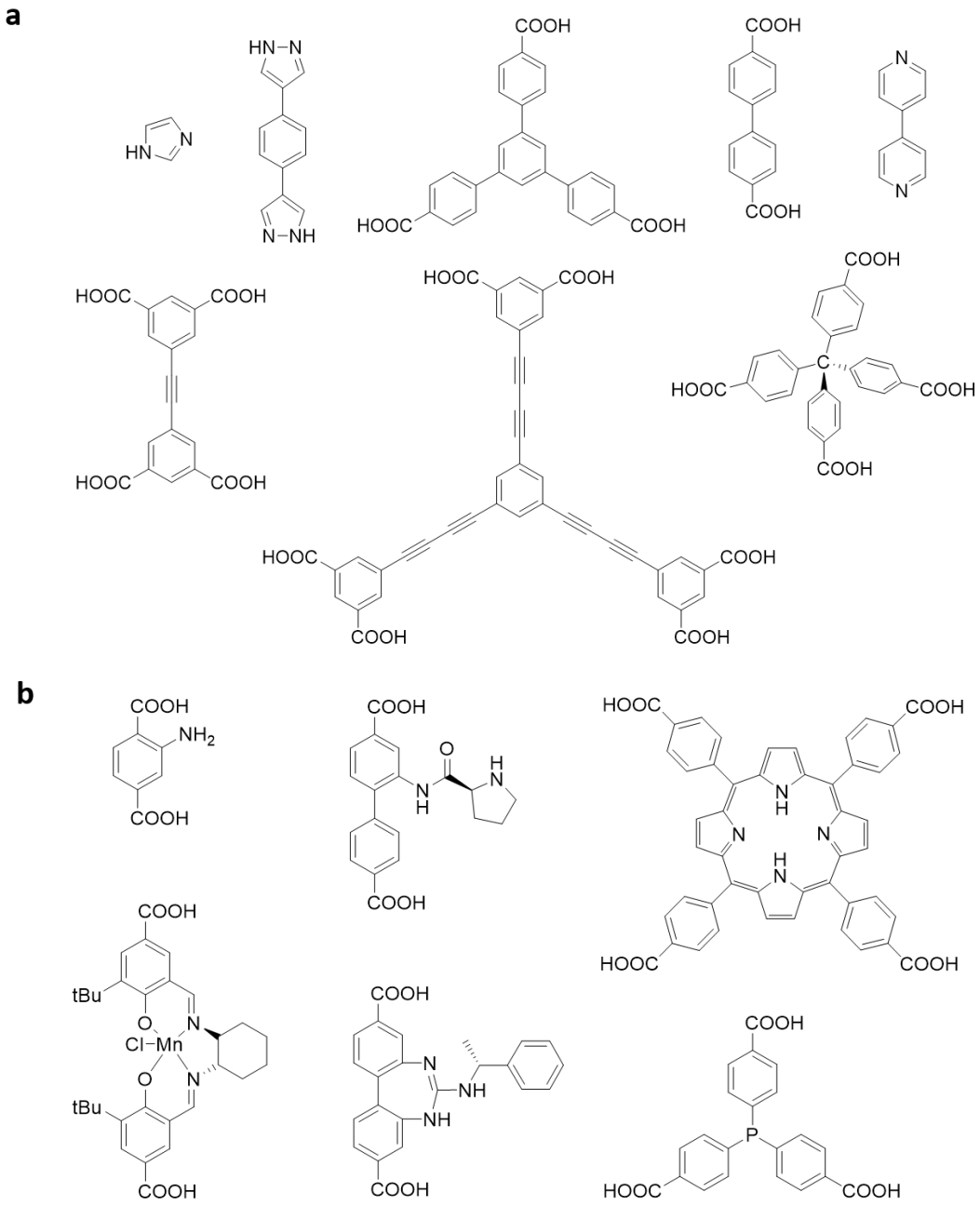

Figure 1. 8 Examples of a) some di-, tri-, tetra- and hexatopic linkers, b) ligands with different functional groups that can bring useful properties to MOFs.

1.2.3 Tritopic linkers

The prototypical tritopic carboxylate linker is 1,3,5-benzentricarboxylic acid (H_3btc). It forms HKUST-1[16] with dicopper paddle-wheel clusters. In the framework each btc linker is connected to three paddle-wheel SBUs to form a T_d octahedron. Four linkers occupy triangular

faces of the octahedron while six clusters are located at the vertices. Further connections with other units form a cubic framework with **tbo** topology as shown in Figure 1.9.

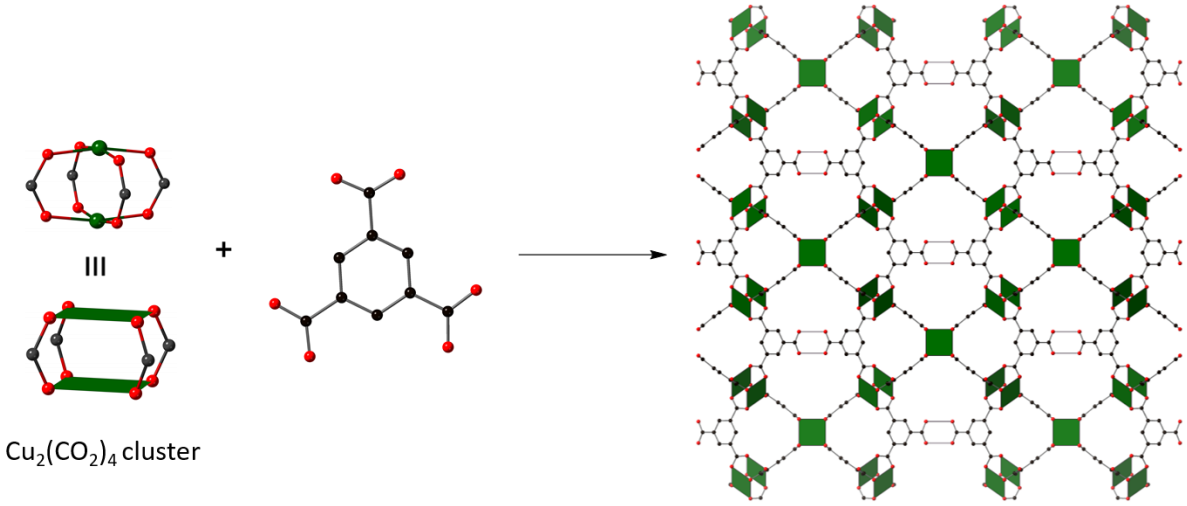

Figure 1. 9 A scheme illustrating the conceptual route to HKUST-1 by linking dinuclear copper(II) clusters and btc ligands. On the right is the single crystal structure of HKUST-1. Hydrogen atoms are omitted for clarity. Atom colors: carbon: black, oxygen: red, copper: green.

Other tritopic linkers that can form a **tbo** topology with copper paddle-wheel clusters are tatab (4,4',4''-s-triazine-1,3,5-triyltri-p-aminobenzoate), htb (4,4',4''-(1,3,4,6,7,9,9-heptaazaphenalene-2,5,8-triyl)tribenzoate), tatb (4,4',4''-s-triazine-2,4,6-triyl-tri-tribenzoate) and bbc (4,4',4''-(benzene-1,3,5-triyl-tris)(benzene-4-1-diyl))tribenzoate). They form meso-MOF-1,[59] PCN-htb,[60] PCN-6,[60] and MOF-399,[60] respectively. Among these MOFs, MOF-399 has the highest void fraction (94%) and the lowest density (0.126 g/cm^3).

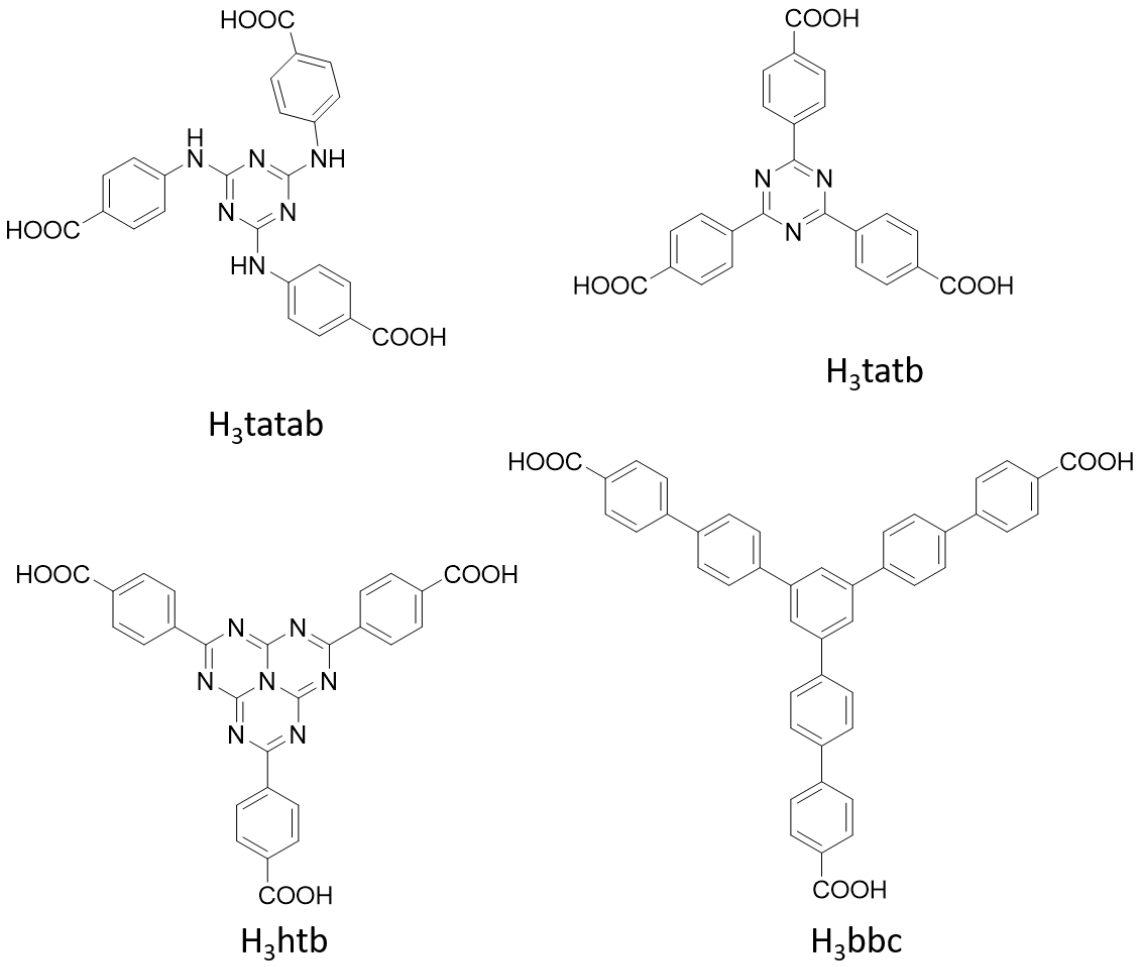

Figure 1. 10 Extended tritopic linkers: H_3tatab, H_3tatb, H_3htb and H_3bbc.

The btc linker can be extended to btb (1,3,5-benzentribenzoate) by addition of three phenylene rings (Figure 1.11). Btb produces MOF-177[61] with 6-connected octahedral $Zn_4O(CO_2)_6$ clusters. This MOF features a **qom** topology. Btb can be further extended to bte (4,4',4"-(benzene-1,3,5-tryl-tris(ethyne-2,1diyl))tribenzoate) and bbc. Using bte and bbc ligands, Yaghi and co-workers prepared MOF-180[62] and MOF-200[62] respectively, which have the same topology as MOF-177 (Figure 1.12).

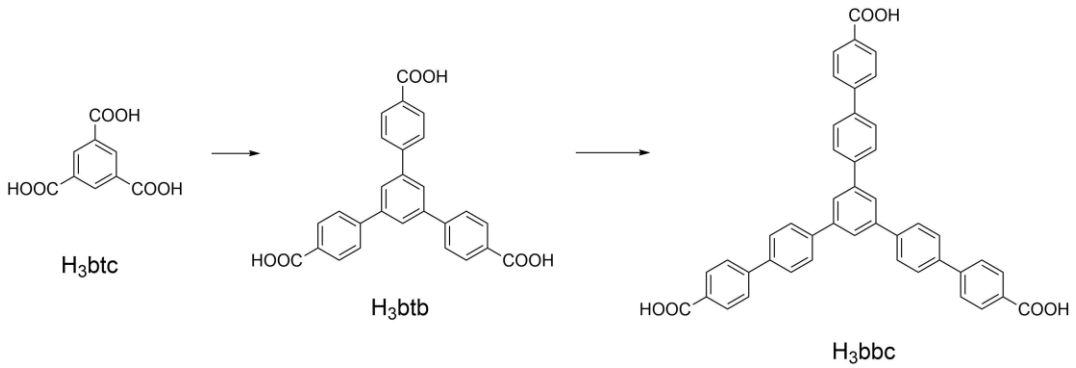

Figure 1. 11 Schematic illustration of extension of H3btc and H3btb by addition of phenylene rings.

Maintaining the same topology and obtaining larger pores by linker expansion is not always easy as expanded ligands often form fragile frameworks. Also, large void spaces within the crystal framework often encourages interpenetration, where two lattices grown within each other and reduce the overall porosity.[63] Unlike the IRMOF series, the expanded structures of MOF-177 are non-interpenetrated due to the unique **qom** topology. This topology is a (6,3)-connected net with the centre of the octahedral $Zn_4O(CO_2)_6$ cluster as the site of 6-connection and the centre of the btc linker as the site of 3-connection. The overall structure of this net plays a key role in preventing interpenetration.

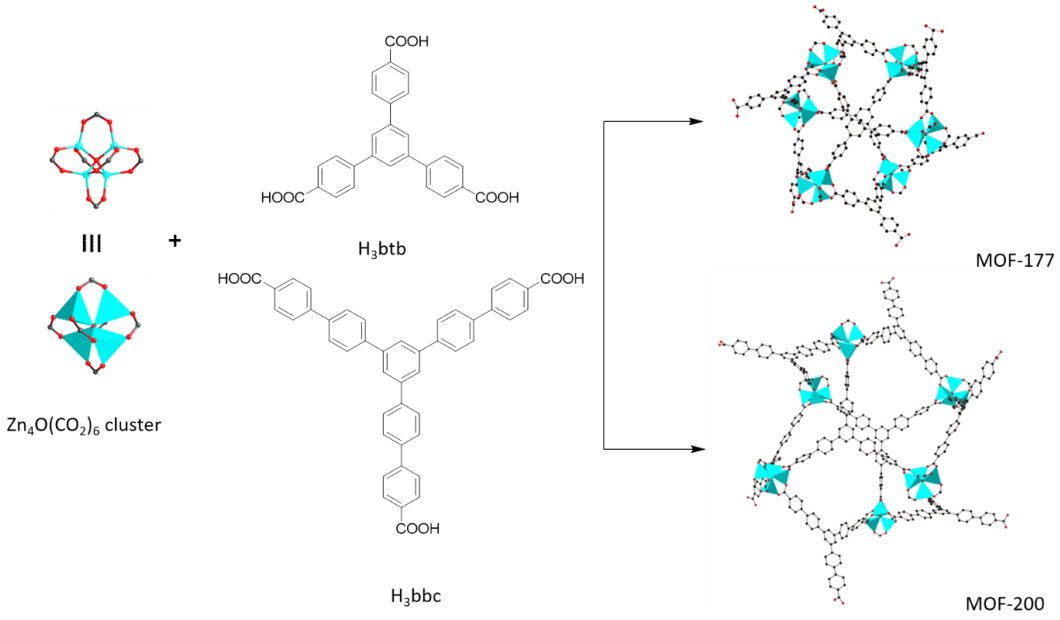

Figure 1. 12 A scheme illustrating the conceptual route to MOF-177 and MOF-200 by linking tetranuclear zinc(II) clusters and tritopic linkers btb and bbc ligands respectively. On the right are the single crystal structures of MOF-177 and -200. Hydrogen atoms are omitted for clarity. Atom colors: carbon: black, oxygen: red, zinc: cyan.

Some tritopic linkers with lower symmetry have also been reported. For example, H_3bhtc (biphenyl-3,4′,5-tricarboxylic acid) forms UMCM-150.[64] Because the three carboxylate groups are not symmetrically identical, they form two different clusters with copper(II) ions. The carboxylates at the 3- and 5-positions form dicopper paddle-wheel clusters while the carboxylate at 4'-position produces a $Cu_3(CO_2)_6$ cluster with six points of extension (Figure 1.13). This results in an unusual (3,4,6)-connected network. Researchers later reported an isostructural MOF, termed NJU-Bai3[65] (NJU-Bai = Nanjing University Bai group), which was built up by using a longer linker, H_3caia (5-(4-carboxybenzoylamino)-isophthalic acid) instead of H_3bhtc.

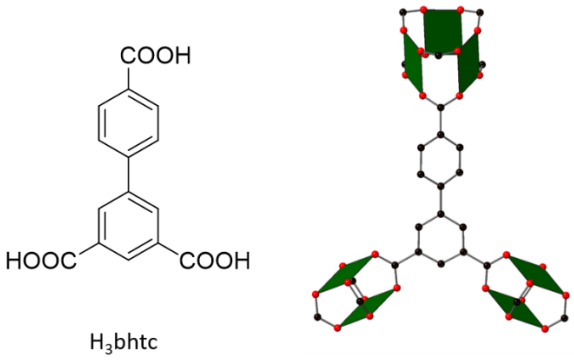

Figure 1. 13 The molecular structure of tritopic linker H_3bhtc and illustration of bhtc in UMCM-150 connected to dicopper paddle-wheel and trinuclear copper clusters.

Beside the carboxylate based tritopic linkers, a number of azolate containing tritopic linkers also have been studied due to their strong coordination ability with divalent metal ions. The Long group reported four pyrazolate-bridged MOFs named $M_3(btp)_2$ (M = Ni, Cu, Zn and Co; H_3btp = 1,3,5-tris(1H-pyrazol-4-yl)benzene).[66] Amonst these MOFs, $Ni_3(btp)_2$ is thermally stable up to 430 °C and chemically stable in boiling aqueous solutions at different pH values. This group also reported triazolate containing Co-bttri (H_3bttri = 1,3,5-tri(1H-1,2,3-triazole-5-yl)benzene).[67] The coordinated solvent in the structure of Co-bttri can be removed under vacuum at 150 °C to create open metal sites. Gas adsorption measurements show that open metal sites in the framework interact much more strongly with O_2 than with N_2. Although they have a low basicity compared to other azolates, tetrazolate-based linkers have been used in construction of many MOFs.[68-70] Btt (1,3,5-benzenetristetrazolate) has been studied in M-btt (M = Mn, Fe, Cu) type MOFs.[71] Mn-btt is a 3,8-connected anionic porous frameworks and shows permanent porosity. It has a high H_2 uptake (6.9 wt%) at 77 K and 90 bar.

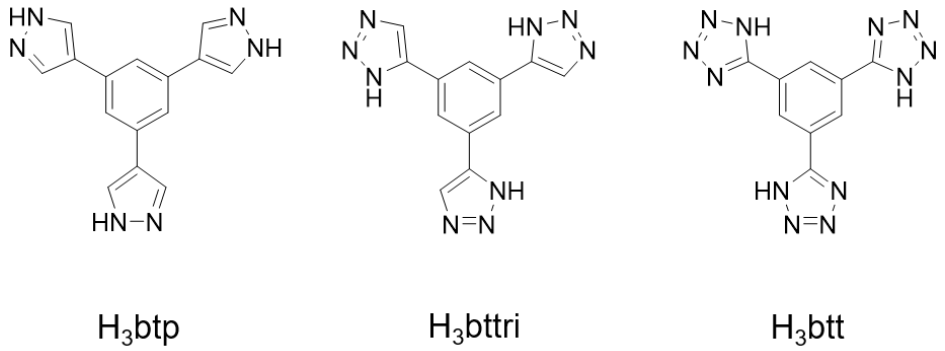

Figure 1. 14 Pyr-, tri- and tetrazole containing tritopic linkers.

1.3 Multicomponent MOFs

Multicomponent MOFs are materials with a higher degree of structural complexity compared to simple MOFs formed by only one type of organic linker and one type of metal cluster. In terms of the type of different organic linkers that they contain, multicomponent MOFs can be divided into two groups. First group, also known as multivariate MOFs (MTV-MOFs), are formed from linkers that have the same length, geometry and connectivity but bear different functionalities. The second group, on the other hand, are built from two or more geometrically distinct linkers. Multicomponent MOFs can also be prepared by using different types of clusters, rather than different ligands. Multicomponent MOFs have attracted much attention recently because they offer a unique approach to MOF functionalization to tune and control the internal environment and related properties of MOFs for use in a variety of applications.

1.3.1 Multivariate MOFs (MTV-MOFs)

An early series of MTV-MOFs was reported by Yaghi and co-workers in 2010, referred to as MTV-MOF-5.[72] Here, each member contained two or more terephthalic acid derivatives. The most complex MTV-MOF-5 contains eight different ligands (H_2bdc and its derivatives). These ligands are indiscriminately distributed throughout the framework. Because the ligands are not located in specific locations, it is hard to determine the structure of this MOFs with X-ray diffraction techniques. To better understand the structure of MTV-MOFs advanced solid-state NMR in combination with molecular modelling techniques are needed.[73] Nonetheless, the MTV-MOF strategy can provide frameworks with different properties compared to the

corresponding single component MOFs. In MTV-MOF-5 case, for instance, addition of different functionalities results in a significant enhancement in selectivity for carbon dioxide over carbon monoxide.

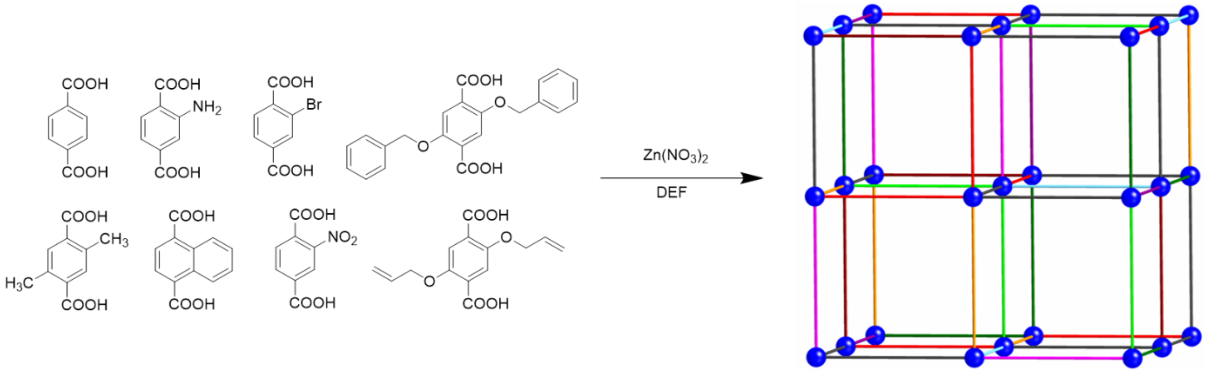

Figure 1. 15 A scheme that illustrates the formation of complex MTV-MOF-5 by reacting eight different ligands and zinc nitrate in DEF results in the frameworks with random distribution of ligands.[72]

The MTV-MOF strategy was later used by Cui *et al.* to construct MOFs containing two or three chiral metallosalen[74] based linkers.[75] Their ligands bear different combinations of metals (Fe, Cr, V, Co, Mn and Cu) as catalytically active units. They showed that these MOFs can cooperatively catalyze asymmetric sequential alkene epoxidation and ring opening reactions.

1.3.2 MOFs containing more than one type of ligand

As mentioned in section 1.3, multicomponent MOFs are built from geometrically distinct linkers. The advantage of using distinct ligands in making multicomponent MOFs is that they can be differentiated during crystallization of the MOF and occupy specific positions in the resulting lattice. Therefore, if the ligands are functionalized, the functional groups will also be located in precise locations in the framework. This provides an opportunity to tune and control the physical and chemical properties of the pores for specific applications.

The first multicomponent MOF constructed from two distinct linkers and one metal cluster was reported in 2003.[76] But, ternary MOFs received much deserved attention after Matzger and co-workers reported UMCM-1[77] (UMCM = University of Michigan Crystalline Material). This material, with a formula of $Zn_4O(bdc)(btb)_{4/3}$, consists of Zn_4O nodes linked together by two bdc and four btb linkers arranged in an octahedral geometry. The ligands are located in distinct lattice sites. The framework has a well-ordered, periodic and non-interpenetrated structure with

a high surface area (4160 m^2/g). It retains its crystallinity even after heating at 300 ˚C for three hours.

A common practical challenge in the synthesis of multicomponent MOFs is obtaining the desired MOF in phase-pure form. Multicomponent MOF formation is very sensitive to the feed ratio of ligands, because each ligand can independently form a MOF. For instance, UMCM-1 usually crystallizes at ratios between 3:2 and 1:1 of H_3btb:H_2bdc. An excess amount of H_2bdc produces either MOF-5 loaded with H_3btb occupying defect sites or a mixture of UMCM-1 and MOF-5. Similarly, an excess amount of H_3btb leads to MOF-177 [$Zn_4O(btb)_2$] or a mixture of UMCM-1 and MOF-177.

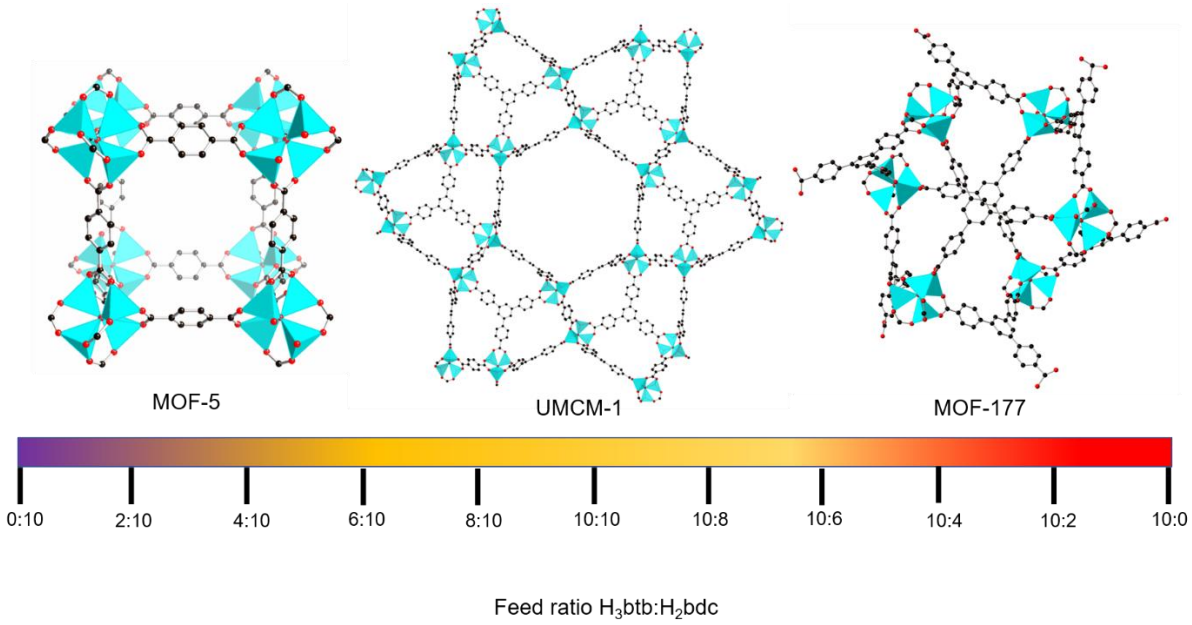

Figure 1. 16 Phase diagram for synthesis of UMCM-1.

The Matzger group later reported a series of UMCM type ternary MOFs including UMCM-2[78] and UMCM-3[79]. Additionally, researchers reported ternary MOFs containing two ditopic linkers such as SUMOF-4[80] (SU = Stockholm University). Yang *et al*. recently reported a cadmium based homochiral ternary MOF containing 4,4′-((naphthalene1,4-dicarbonyl)bis(azanediyl))dibenzoic acid and 4,4′-bipyridine (4,4′-bipy).[81]

In 2013, the Telfer group reported the first quaternary MOF, known as MUF-7.[82] This material was obtained by reacting H_3btb, H_2bpdc and H_2bdc with $Zn(NO_3)_2$ in DEF at 85 °C. MUF-7 crystallizes in *I*-43*d* space group and has **ith-d** topology. As shown in Figure 1.17, the three ligands are located in precise positions to form a well-ordered structure. After

characterization of MUF-7, the group proposed an approach, called programable pores, for preparation of isoreticular quaternary MOFs. According to this approach, functional groups could be appended to one, two or three of the ligands to make new quaternary MOF variants. Importantly, these variants will retain the topology of the parent framework having functional groups in precise lattice sites without any defect or disorder. In their study on MUF-7, the Telfer group prepared an isoreticular family of MOFs using functionalized analogues of the three ligands. The group found that by introducing functionalities in the framework, the MOF pores can be designed to tune its adsorption behaviours.

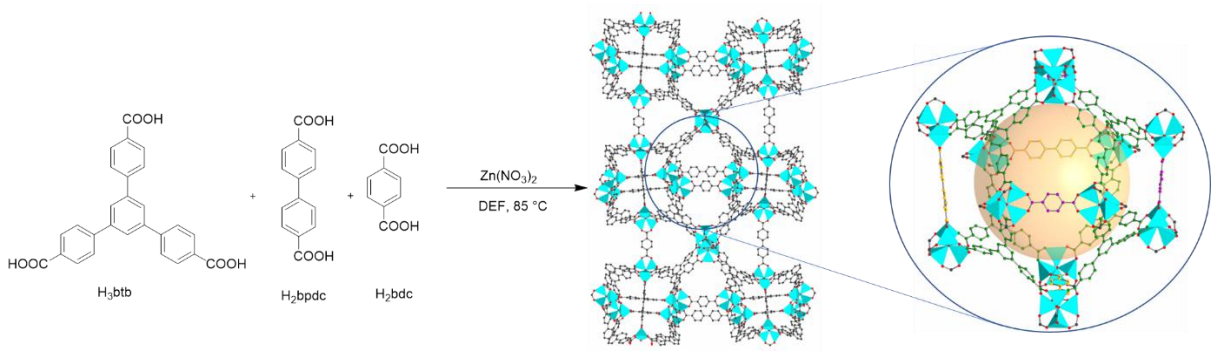

Figure 1. 17 A scheme illustrating the synthetic route to MUF-7 by combining zinc(II) nitrate, tritopic btb, ditopic bpdc and bdc linkers in DEF. In the middle is a view of the single crystal structure of MUF-7. Hydrogen atoms are omitted for clarity. Atom colors: carbon: black, oxygen: red, zinc: cyan. The position of three ligands in tetrahedral cavity is shown on the right. Ligand colors: btb: green, bpdc: yellow, bdc: magenta.

The Telfer group later reported a second family of quaternary MOFs termed as MUF-77.[48] Compared to MUF-7, in MUF-77 the H_3btb ligand is replaced with a truxene based tricarboxylate linker. MUF-77 also has **ith-d** topology but crystallizes in the *P*m-3 space group. MUF-77 has a greater water stability compared to MUF-7 due to hydrophobic alkyl chains on truxene based ligand. The group also synthesized a series of MUF-77 derivatives in which one of ditopic linkers bears a chiral, enantio-pure catalytically active proline[83] group while the other two ligands had different functional groups.[84] The group showed that MOF pores can be designed to modulate the asymmetric aldol reaction between acetone and 4-nitrobenzaldehyde. More examples of quaternary MOFs can be found in literature.[8, 85-86] In Chapter 2, I will present a new family of quaternary MOFs which is isostructural to MUF-77.

Zhou and co-workers recently reported a quinary MOF based on 8-connected Zr_6 clusters.[87] Unlike the bottom-up self-assembly of the ternary and quaternary MOFs that mentioned above, this MOF was constructed via post-synthetic modification method. In their study, using a

carbazole based tetracarboxylate linker they first built up a precursor MOF termed PCN-9, which has coordinatively unsaturated Zr sites. They subsequently installed three ditopic linkers of different lengths to obtain a quinary MOF.

1.4 Applications of MOFs

MOFs are promising materials for a number of applications. Clean energy related applications such as hydrogen and methane storage, and CO_2 capture are perhaps the most significant applications of MOFs.[88-89] Some other uses include catalysis,[90] drug delivery,[91] chemical sensing,[92-94] photovoltaics,[95] biomedical imaging,[96] and semiconductors.[97] In the next sections hydrogen and methane storage, CO_2 capture, and catalysis will be briefly discussed.

1.4.1 Hydrogen and methane storage

Hydrogen is considered as a good alternative energy source to fossil fuels due to its high gravimetric combustion heat and environmentally-friendly post combustion products.[98] However, the low boiling point and critical temperature of hydrogen causes problems for its storage and transportation.[99] Early methods for hydrogen storage required a large amount of energy for liquefying it and keeping the tanks cool. High-pressure techniques, on the other hand, involve the usage of very heavy equipment which reduces the real gravimetric capacity of the tanks.[99] Due to their highly porous nature and structural tunability MOFs are promising materials that can be used as adsorbents for hydrogen storage. Hydrogen can be stored in tanks filled with MOF at 77 K and relatively low pressure. This technique requires much less energy compared to cryogenic liquid hydrogen tanks due to the interactions between the MOF surface and hydrogen guest molecules. [89] Open metal sites in a MOF structure have high hydrogen binding affinities. Therefore, MOFs containing high open metal site density such as MOF-74-M (M = Co, Ni, Mg and Zn) series have been widely studied.[100-103] The size and shape of internal pores have an important effect on the interactions between MOFs surface and hydrogen. Usually MOFs with large pores are not desirable for hydrogen storage. Many MOFs containing suitable pore size and shape for hydrogen adsorption have been reported.[104-106] In addition, some interpenetrated MOFs structures were found to have much higher hydrogen uptake compared to their non-interpenetrated parent frameworks. For example, PCN-6 is a twofold interpenetrated MOF which is constructed by Cu(II) and tatb (4,4',4''-s-triazine-2,4,6-triyltribenzoate). At 77 K and 1.2 bar, the hydrogen uptake of PCN-6 is 1.9 wt% which is 70% higher than that of its non-interpenetrated version.[60, 107]

Another alternative energy source is methane which constitutes a large portion of natural gas. It has the highest energy density and lowest CO_2 emission per unit of energy production compared to fossil fuels. Due to its low boiling point (112 K), it is in the gaseous state at ambient temperature and pressure. Therefore, it has a low volumetric energy density (0.04 MJ/L).[108-109] Currently the most commonly used technologies for natural gas storage are: liquefied natural gas (LNG) and compressed natural gas (CNG) systems. LNG can be stored with cryogenic cooling systems, while CNG requires multi-stage compressors and heavy high-pressure tanks. Alternatively, it is possible to store natural gas at ambient temperature and moderate pressures by using adsorbents. Because MOFs are a class of porous materials, they have also been investigated for adsorbed natural gas (ANG) systems.[110-111]

The electrostatic interaction between MOFs and CH_4 is an important factor for methane capacity of MOFs which usually occurs at open metal sites. MOF-74 series has also notable CH_4 uptake capacity as its hydrogen affinity mentioned above. In this series, Ni-MOF-74 has the highest total volumetric CH_4 capacity which is a result of strong polarizing ability of Ni^{2+} ions causing the strongest electrostatic interaction with methane. It has a capacity of 230 cm^3/cm^3 at 298 K and 35 bar.[108] Another type of interactions between MOFs and CH_4 is van der Waals interactions. In 2016, Chen and co-workers reported MAF-38 which has no open metal sites. It is constructed from Zn^{2+} ions, HPypz (4-(1*H*-pyrazol-4-yl)pyridine) and H_3btb. Its methane uptake reaches 263 cm^3/cm^3 at 298 K and 65 bar. Since it does not have any open metal sites, van der Waals interaction is responsible for its methane uptake.[112]

[Co(bdp)][113] (H_2bdp = 1,4-benzenedi(4'-pyrazole)), reported in 2015, has the highest working capacity for CH_4 adsorption. Its adsorption isotherm shows a small uptake at about 5 bar at room temperature. After that point, the uptake dramatically increases which means that at the desorption stage most of absorbed CH_4 can be released when the pressure drops to 5 bar. It was found that its flexible structure is responsible for this behaviour.

1.4.2 CO_2 separation

CO_2 is one of the main gases responsible for global warming which is released into the atmosphere from various anthropogenic activities such as fossil fuel burning. Therefore, it is crucial to develop technologies to prevent CO_2 emission. A practical and effective solution for reducing CO_2 release is capturing it from the post-combustion flue gas. Flue gas is a mixture that consists of nitrogen (70%), CO_2 (10-15%), water vapor (10-12%) and other gases. Current technology for selective CO_2 capture involves using aqueous organic amine solutions. Due to

the large heat capacity of water, it requires a high regeneration energy. Alternatively, porous adsorbents including MOFs have been investigated for separation of CO_2 from flue gas.[114-115] A flow diagram for the capture of CO_2 is given in Figure 1.18. The first step is the removal of water and other minor gases. Then, CO_2 is captured by an adsorbent. After a desorption stage purified CO_2 is isolated by compression.

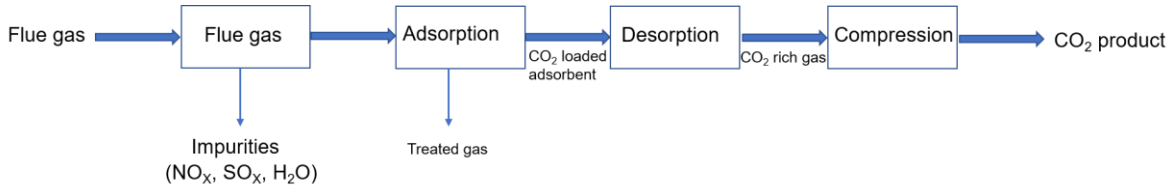

Figure 1. 18 A flow chart illustrating the separation of CO_2 from flue gas via sorption process.[115]

A good adsorbent for CO_2 separation is expected to have following properties: i) The adsorbent should be highly selective for CO_2 over other gases, especially N_2. ii) It should possess a high working capacity. iii) It needs to be stable under typical operating conditions. iv) The energy required for regeneration should be as low as possible.[115]

Several strategies have been developed by researchers to improve the adsorption selectivity of CO_2 over other adsorbates.[89] One of these strategies is the preparation of MOFs containing high open metal site densities. Mg-MOF-74, for example, has a high CO_2 uptake at low pressure under dry conditions.[116] Open metal sites have strong interactions with CO_2. However, in the presence of moisture, water is more likely to occupy these sites and thus decrease the adsorption capacity. Another method is introducing amino groups into MOFs. Long and co-workers reported a series of MOFs in which open metal sites are functionalized with amino groups. mmen-Mg_2(dobpdc) for example has good CO_2 selectivity even in the presence of water vapor. Its CO_2 uptake is 3.5 mmol/g at 40 °C and 0.15 bar.[117] Its CO_2 adsorption isotherm shows very little uptake at the low-pressure region, but this is followed by a steep step over a very small pressure range. This unique step is caused by a phase-change in the framework due to cooperative CO_2 sorption. This behaviour results in an exceptionally high working capacity. Moreover, only a small temperature increase is needed to desorb the CO_2, which indicates that the energy required to regenerate the system is low. MOFs can also be functionalized with other polar groups to enhance their affinity towards CO_2. For instance, the hydroxide in $[Co^{II}Co^{III}(OH)Cl_2(bbta)]$ (H_2bbta = 1H,5H-benzo(1,2-d:4,5-d′)bistriazole) was demonstrated to have strong yet reversible interaction with CO_2.[118] Another way to improve the selectivity

of CO_2 is designing MOFs with pores sizes that will allow CO_2 (kinetic diameter = 3.3 Å) to pass through but not N_2 (kinetic diameter = 3.64 Å). SIFSIX-3-M, for example, has suitable pore sizes to afford good selectivity for CO_2, although the interaction between CO_2 and this material are physical interactions.[119]

1.4.3 Catalysis

Zeolites and mesoporous silicates are porous materials commonly used in heterogeneous catalysis. Although the structure of zeolites are open to some certain modifications for size and shape selective catalysis,[120] their small pores and chemical constituents,[121] are not suitable for further functionalization. On the other hand, the structure of ordered mesoporous silicates can be tuned through hydroxyl moieties, but their surfaces are poorly defined and locally inhomogeneous.[122-123] Alternatively, the use of MOFs in heterogeneous catalysis has attracted attention due to their well-ordered permanent porosity, high surface area and structural tuneability. Catalytically-active MOFs can be specifically prepared in at least three different ways: by functionalizing organic linkers, creating open metal sites and encapsulating the catalytically-active units in their pores.[58, 124-126] MOF catalysts can be designed for synergistic catalysis and tandem reactions by introducing multiple functionalities into their structures.[127] Moreover, they can be used as biomimetic platforms.[128]

Due to their structural similarity with the active sites in certain enzymes, linkers containing a metalloporphyrin units have been expected to show good catalytic activity.[129] Ma and coworkers reported a porphyrin-based MOF, MMPF-3,[130] which was used as catalyst for the epoxidation reaction of trans-stilbene. MMPF-3 was obtained by assembling 5,15-bis(3,5-dicarboxyphenyl)-10,20-bis(2,6-dibromophenyl)-porphyrin (H_4dcdbp) and bimetallic Co cluster, $Co_2(\mu_2\text{-}H_2O)(H_2O)_4(COO)_4$. In the cluster two different Co^{2+} ions are bridged by a μ_2-H_2O and two carboxylates of dcdbp. Three aqua ligands are connected to one Co while two carboxylates from another two dcdbp and one H_2O are coordinated to the second Co. MMPF-3 features a **fcu** topology possessing three distinct polyhedral cages. Each cage has 12 Co^{2+} ion centres aligned towards the interior core. This high concentration of Co centres provides a good catalytic activity with a conversion value of 95.7% at 60 °C for 24 hours for the epoxidation reaction of trans-stilbene and MMPF-3 maintains this ability even at its 8th catalytic cycle. Other research groups have also studied porphyrin-based MOFs using different active metal centres such as Fe, Zn, Mn.[131-134]

A good example of the effect of pore environment on catalytic activity of MOFs was shown by the Long group in 2016. They investigated the effect of hydrophobic functionalities on both product selectivity and catalyst stability in a series of iron-based MOFs.[135] The group prepared four MOFs: Fe_2(dotpdc) (H_4dotpdc = 4,4″-dihydroxy-[1,1':4',1"-terphenyl]-3,3"-dicarboxylic acid) and three modified terphenyl derivatives in which the central phenyl ring is functionalized with fluoro, methyl and tert-butyl groups and used them as catalysts for oxidation of cyclohexane to cyclohexanol and cyclohexanone. Fe_2(dotpdc) has one-dimensional hexagonal pores with size of 27 Å and the cluster possesses coordinatively unsaturated Fe(II) sites. The catalysis results show that altering pore sizes and introducing nonpolar groups close to the iron site increases both the alcohol/ketone ratio and turnover number significantly (Figure 1.19).

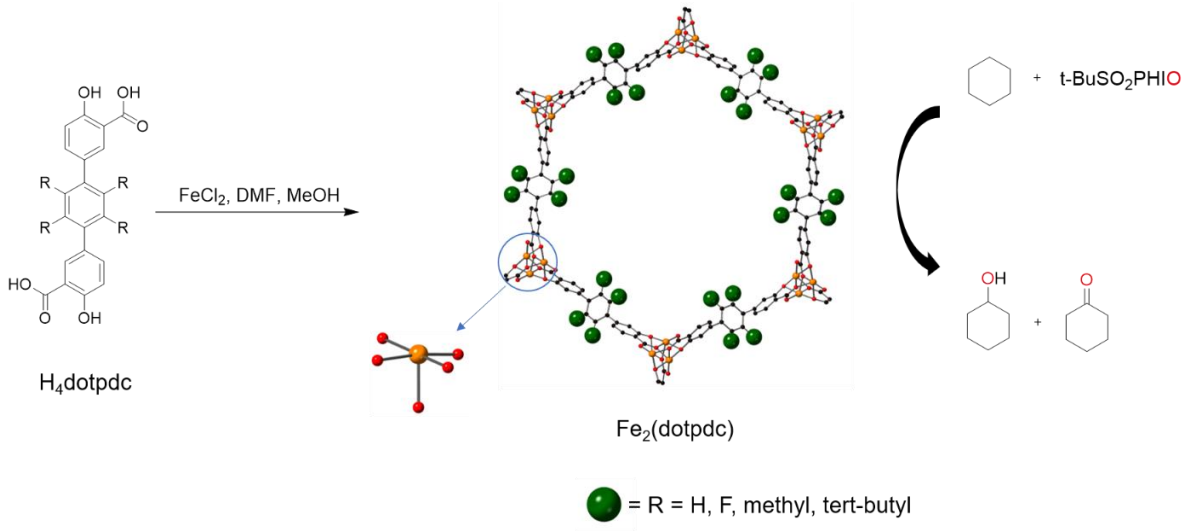

Figure 1. 19 A scheme illustrating the synthetic route to Fe_2(dotpdc) by combining iron(II) chloride and a ditopic dotpdc linker. In the middle is a view of one-dimensional hexagonal pores in the framework and coordination environment of unsaturated Fe(II) site. Atom colors: carbon: black, oxygen: red, iron: orange. The oxidation of cyclohexane to cyclohexanol and cyclohexanone is shown on the right.

Mirkin *et al.* reported zirconium-based UiO-67-bpdc-squar using H_2bpdc and H_2bpdc-squar ligands (Figure 1.20). The squaramide functionality in H_2bpdc-squar is a pseudo-Lewis-acid group which can activate electrophilic moieties toward nucleophilic addition by cooperative hydrogen bonding.[136] However, this hydrogen bonding ability of H_2bpdc-squar can reduce or completely quench its catalytic activity due to self-association. Mirkin and co-workers showed that the catalytic activity of this compound can be increased by incorporating it into a MOF structure. The ester form of this ligand and UiO-67-bpdc-squar was tested to catalyse the Friedel-Crafts reaction of indole and *β*-nitrostyrene. UiO-67-bpdc-squar afforded

95% yield at 50 °C for 24 hours while the ester form of the ligand produced only 7% yield in the same conditions.[137]

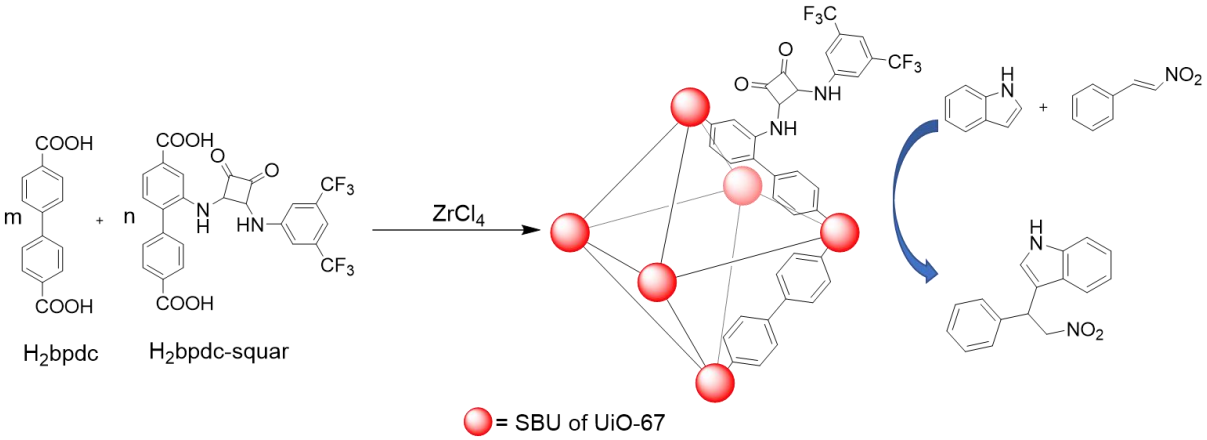

Figure 1. 20 A scheme illustrating the synthetic route to UiO-67-bpdc-squar. The Friedel-Crafts reaction of indole and β-nitrostyrene is shown on the right.

The use of MOFs as adsorbent in CO_2 capture was discussed in the previous section. Additionally, MOFs can be used as catalyst to convert CO_2 into useful chemicals. The insertion of CO_2 into epoxides forms cyclic carbonates which can be used as alkylating agents, electrolytes and aprotic solvents.[124] This reaction can be catalysed by both basic and acidic sites.[138-139] A variety of MOFs have been prepared to catalyse the cycloaddition reaction of CO_2 to different epoxides.[140] Amino functionalized NH_2-UiO-66 shows a good activity in the reaction of CO_2 with styrene oxide. A high conversion (96%) can be obtained in just 4 hours.[141] Recently, Ma and co-workers reported a Zn-based MOF which exhibits high activity for the addition of CO_2 to epichlorohydrin. 99% yield can be reached in only two hours.[142]

In addition to the reactions mentioned above, MOFs have been used in a variety of catalytic transformations such as, cyanosilylation of aldehydes,[143-144] hydrogenation of aromatic ketones,[145] catalytic oxidative desulfurization,[146] oxidation of alcohols to ketones,[147] C-C coupling reactions,[148] Knoevenagel condensation reactions[149-150] and CO to CO_2 oxidation.[151-152]

Chapter 2 Triazatruxene Ligands for Multicomponent MOFs

2.1 Introduction

The geometry and number of binding sites of organic ligands have an important role in the architecture of metal-organic frameworks (MOFs).[57] Typical organic linkers used in MOF chemistry are: linear ditopic, triangular tritopic, square tetratopic and tetrahedral tetratopic linkers.[56-57] These ligands can be functionalized with appropriate substituents to tune chemical and physical characteristics of the MOF pores for further applications, such as gas storage, [153]separation[154] and heterogenous catalysis.[124, 155]

Isoreticular synthesis is a powerful method to tune and control the internal environment and related properties of MOFs with the same framework topologies. This is generally accomplished by either functionalization or extension of organic linkers. Ligand extension can be achieved by addition of an ethynyl bridge or a phenylene ring to the small linker. The prototype for tritopic linkers is 1,3,5-benzenetricarboxylic acid (H_3btc). As mentioned in the previous chapter, by the addition of phenylene spacers it can be extended to 1,3,5-benzenetribenzoate (H_3btb), which forms MOF-177 with octahedral Zn_4O nodes.[61] H_3btb can be extended further to obtain 4,4',4''-(benzene-1,3,5-tryl-tris(ethyne-2,1diyl))tribenzoate (H_3bte), and 4,4',4''-(benzene-1,3,5-tryl-tris(benzene-4,1-diyl))tribenzoate (H_3bbc). Using H_3bte and H_3bbc ligands, Yaghi and co-workers prepared MOF-180 and MOF-200 which have the same topology as MOF-177.[62] A drawback of this type of elongation by phenylene rings is a lack of planarity due to the repulsion of the ortho-hydrogen atoms on adjacent phenyl subunits.[156] On the other hand, in tritopic linkers based on truxene[157] the phenyl subunits are connected by a methylene bridge to rigidify the structure and keep the four phenyl rings coplanar (Figure 2.1a). Furthermore, these ligands can be derivatized with various functionalities at the methylene moieties.[48, 158]

10,15-Dihydro-5*H*-diindolo[3,2-a:3',2'-c]-carbazole (triazatruxene) is a C_3-symmetric, planar π-conjugated cyclotrimer of indole and has three potential sites for functionalization at the 5-, 10- and 15-positions (Figure 2.1c).[159] Because of its openness to modifications, strong electron donating ability and emissive characteristics, its derivatives have attracted much attention in supramolecular chemistry, particularly in organic electronics.[160-162] Its amino and formyl functionalized derivatives (Figure 2.1e-d) have been used as building blocks for construction of covalent organic frameworks (COFs)[163] and molecular polyhedra.[164] However, to date, triazatruxene based ligands have rarely been studied in MOF chemistry. To the best of

our knowledge, only one carboxylic acid functionalized triazatruxene ligand used in MOF synthesis has been reported to date in which carboxylic acid groups are at the 3-, 8- and 13-positions (Figure 2.1f).[165] Having carboxylic acid groups at these position changes both the symmetry and the length of ligand's arms compared to H_3btb. This prevents it from forming MOFs with the same topology as H_3btb and H_3hmtt (Figure 2.1b).

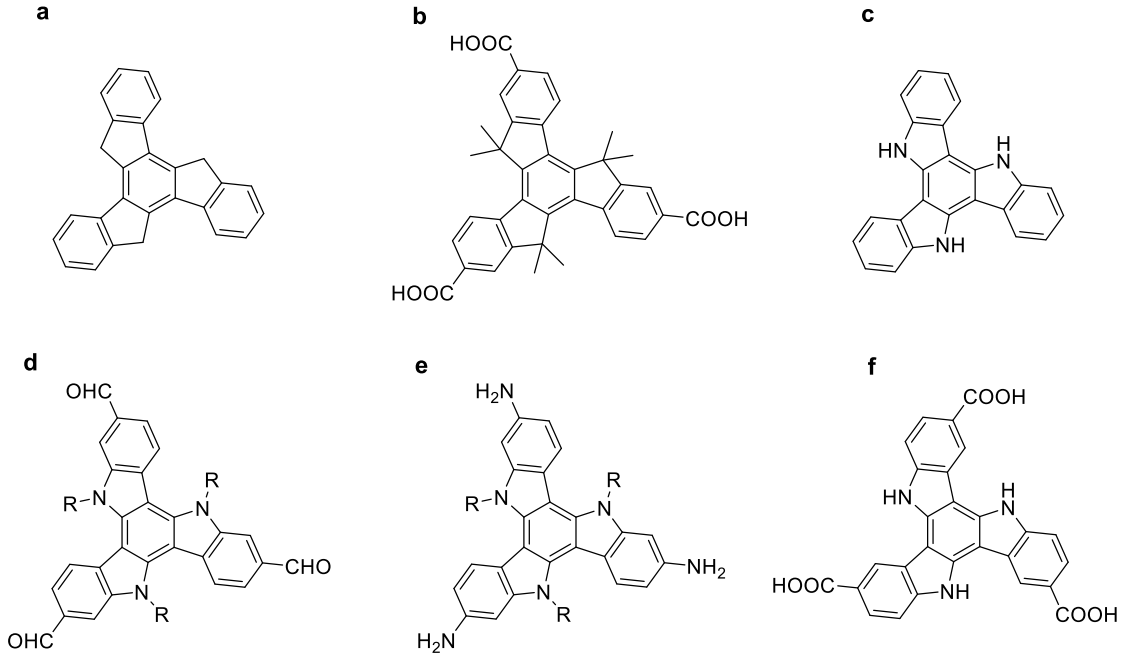

Figure 2. 1 The structures of a) truxene, b) H_3hmtt, c) triazatruxene and its d) formyl, e) amino and f) carboxylic acid derivatives.

In this chapter, I report the synthesis of novel triazatruxene based ligands in which carboxylic acid groups are at the 2-, 7- and 12-positions. Their structural similarity to truxene-based ligands provides an opportunity to use them to diversify multicomponent frameworks. This study will focus on MOFs built up using three topologically distinct carboxylate ligands and Zn_4O clusters. Previously, the Telfer group reported examples of such quaternary MOFs, including MUF-7 and MUF-77, that are based on btb and hmtt.[48, 84] Other groups have also reported quaternary frameworks prepared by similar bottom-up methods.[85, 166] One advantage of these multicomponent MOFs is that the ligands occupy specific positions in the MOF structure without defects and disorder. Programming pore environments by installing different functionalities in precise locations in the framework by appending them to the linkers thus becomes possible. Using triazatruxene based ligands, I prepared a new family of quaternary MOFs, which is termed MUF-777. One useful aspect of the triazatruxene core is that it can be

symmetrically-substituted with various functionalities to systematically create MOFs having different pore sizes with accompanying tuning of framework properties.

2.2 Results and discussion

2.2.1 Synthesis and characterization of ligands

The initial step of this study was to develop a convenient method for trimerization of 1*H*-indole-6-carboxylic acid ethyl ester (Scheme 2.1). Trimerization of some substituted indoles have previously been reported.[167] After modifying the reported conditions, Et_3tat was successfully synthesized, by the reaction of 1*H*-indole-6-carboxylic acid ethyl ester with Br_2 in presence of excess formic acid. The product was obtained directly by precipitation from the reaction mixture in acceptable purity, as shown by ^1H NMR spectroscopy. This compound was then hydrolyzed to obtain the target triazatruxene ligand H_3tat.

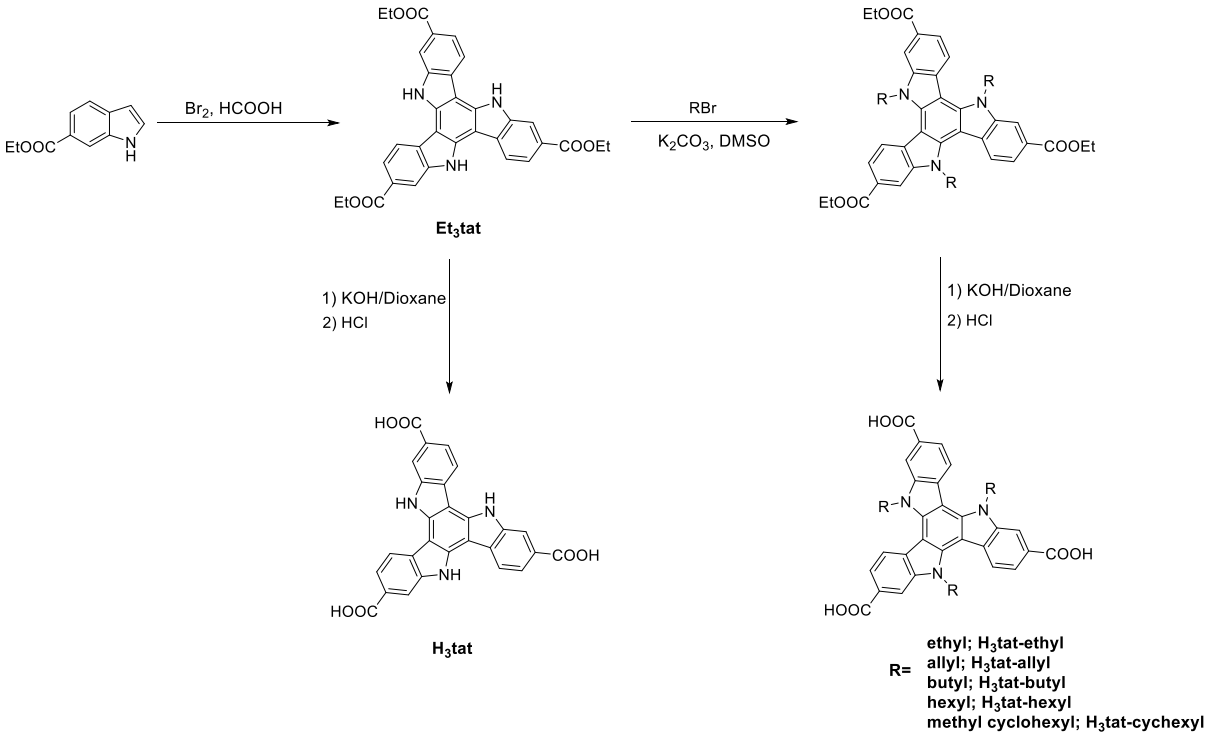

Scheme 2. 1 Synthetic route developed to produce the tat-based ligands.

Five functional group were chosen as additional substituents on Et_3tat: ethyl, allyl, butyl, hexyl and methyl cyclohexyl groups. As outlined in Scheme 2.1, Et_3tat-ethyl, Et_3tat-allyl, Et_3tat-butyl, Et_3tat-hexyl and Et_3tat-cychexyl were prepared by alkylation of Et_3tat. These

compounds were then hydrolyzed to obtain H_3tat-ethyl, H_3tat-allyl, H_3tat-butyl, H_3tat-hexyl and H_3tat-cychexyl (Scheme 2.1). All substituted esters and carboxylic acids were obtained in good yield (65-98%) after purification, where needed, by either recrystallization or column chromatography. Detailed synthetic procedures and characterization of these compounds are available in the experimental section and Electronic Appendix A.

2.2.2 Synthesis and characterization of MUF-777-ethyl

A solvothermal reaction of H_3tat-ethyl, H_2bpdc, and H_2bdc with $Zn(NO_3)_2$ in N,N-diethylformamide (DEF) at 85 ˚C afforded yellow crystals of MUF-777-ethyl (Figure 2.2). This is a quaternary metal-organic framework with the formula $[Zn_4O(\text{tat-ethyl})_{4/3}(bpdc)_{1/2}(bdc)_{1/2}]$. The structure of MUF-777-ethyl was determined by single crystal X-ray diffraction. Single crystal XRD study was carried on a desolvated MUF-777-ethyl crystal at 133 K. A good X-ray diffraction pattern was obtained to a resolution beyond 1.1 Å. The data revealed that MUF-777-ethyl crystallizes in the cubic space group *Pm*-3 and has **ith-d** topology which is identical to the MUF-77-ethyl framework, $[Zn_4O(hett)_{4/3}(bpdc)_{1/2}(bdc)_{1/2}]$.

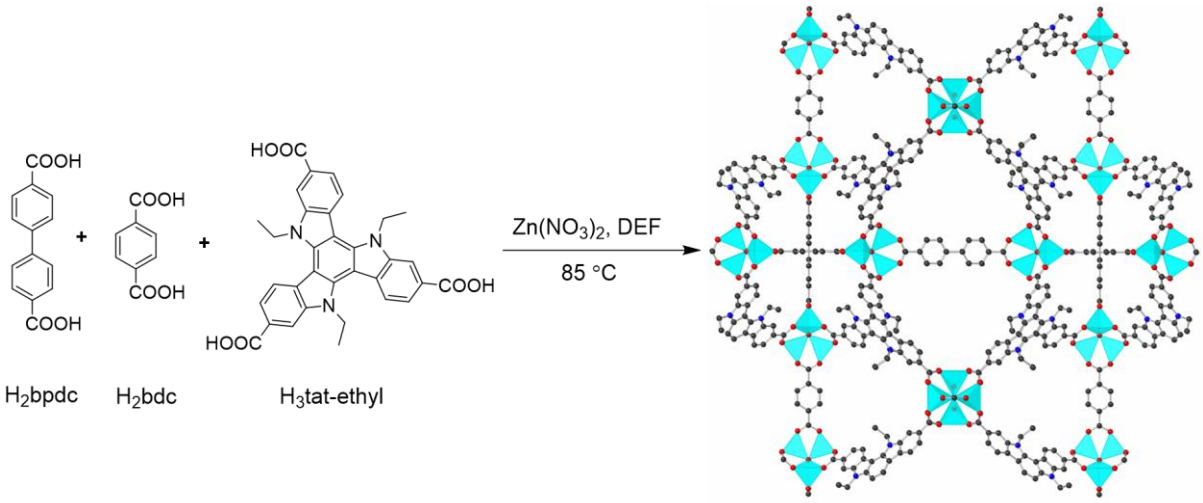

Figure 2. 2 Synthetic route to MUF-777-ethyl and a view of its single crystal structure showing the presence of all three ligands. Atom colors: carbon: black, oxygen: red, nitrogen: blue, zinc: cyan. Hydrogen atoms are omitted for clarity.

As mentioned in Chapter 1, formation of other phases along with the desired phase is not surprising during synthesis of multicomponent MOFs. Because individual ligands and different ligand combinations can independently form a MOF. For instance, for a set of three organic

linkers and only one type of metal node, seven different phases could possibly form.[48] This means that in the synthesis of MUF-777-ethyl there are six other phases competing with the quaternary multicomponent phase.

By optimizing synthetic conditions, MUF-777-ethyl was obtained in a perfect phase purity. Its phase purity was confirmed by ^{1}H NMR spectroscopy of a digested sample (Figure 2.3). It should be noted that NMR spectroscopy is a sensitive diagnostic tool for identifying the purity of multicomponent MOFs since the ratio between the ligands integrals is governed by the framework stoichiometry. This technique can clearly indicate the presence of any side products that do not share the stoichiometry of the framework.

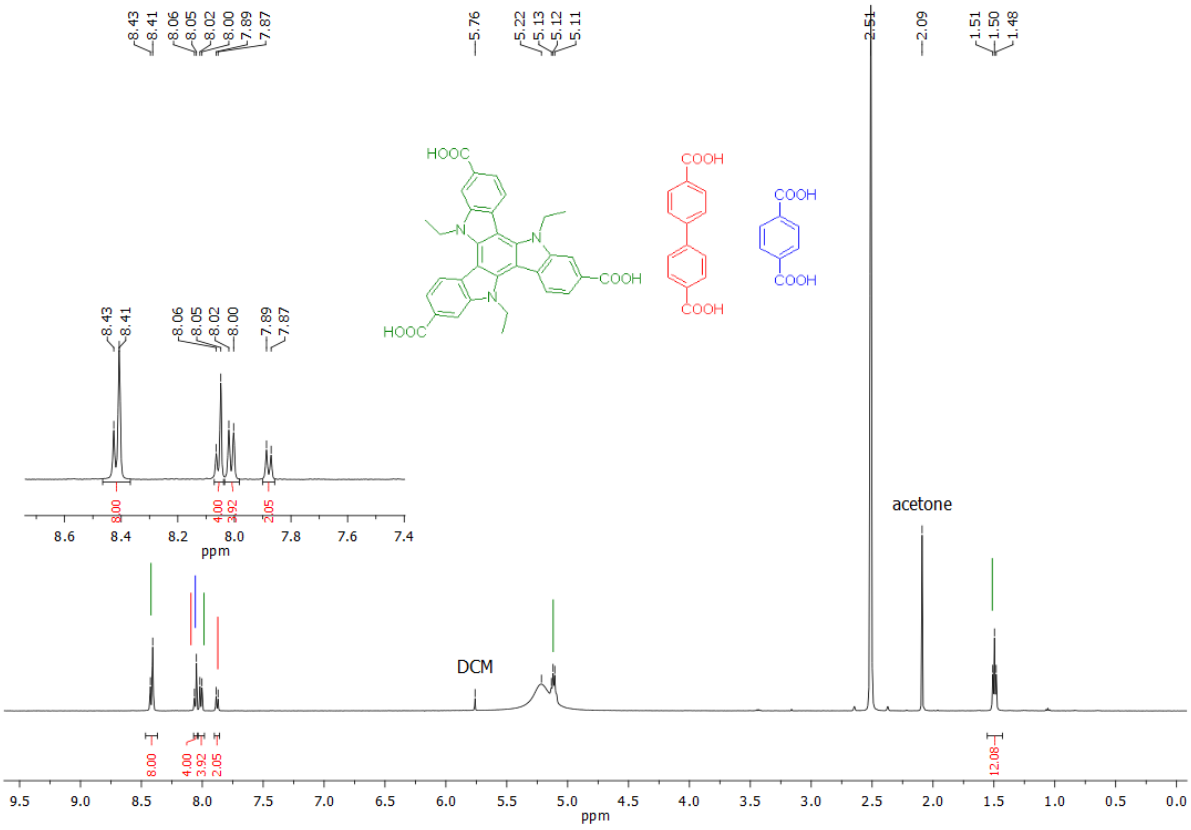

Figure 2. 3 ^{1}H NMR spectrum of MUF-777-ethyl digested in DMSO-d_6/DCl showing the integrals that match with the formula $[Zn_4O(tat\text{-}ethyl)_{4/3}(bpdc)_{1/2}(bdc)_{1/2}]$.

In the structure of MUF-777-ethyl the ligands are linked by six-connected Zn_4O nods. At each SBU four tritopic ligands occupy the equatorial positions, and one bpdc and one bdc ligand fill the axial sites (Figure 2.2). The framework has a low crystallographic density (0.46

g/cm^3) and high calculated[168] porosity (void fraction of 82%). Three types of cavity in MUF-777-ethyl are highlighted in Figure 2.4 The large dodecahedral cavity is defined by 12 Zn_4O clusters, eight tat-ethyl ligands and three pairs of bpdc ligands. The widest distance in this cavity is between two Zn_4O clusters that are facing each other and is nearly 34.5 Å. The cavity can accommodate a sphere with a diameter of around 18.5 Å. In the smaller dodecahedral cavity bdc ligands replace the bpdc ligands. The small tetrahedral cavity, on the other hand, is surrounded by four Zn_4O clusters, two pairs of tat-ethyl ligands, a bpdc ligand and a bdc ligand. Taking advantage of their uniform and complex chemical environments, our group previously showed that these cavities can be designed to modulate asymmetric organocatalysis.[84] A Similar study on catalytically-active MUF-777 variants will be presented in Chapter 3.

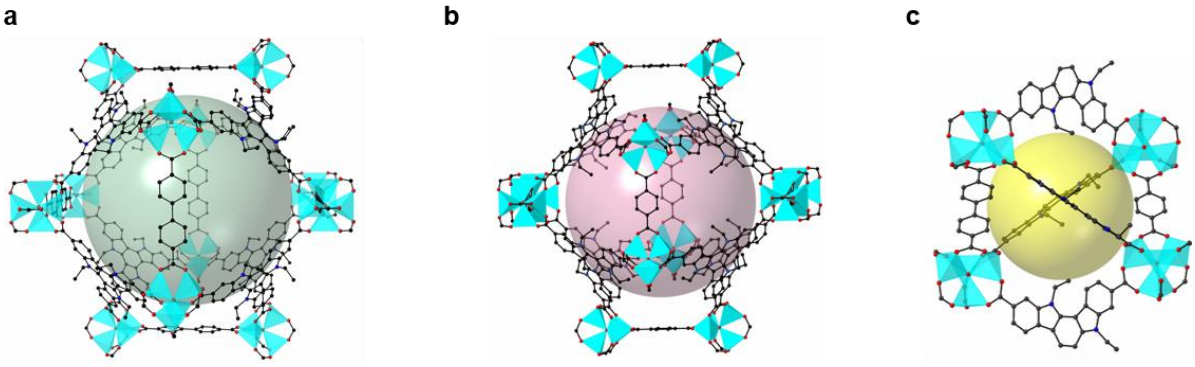

Figure 2. 4 Views of the X-ray crystal structure of MUF-777-ethyl highlighting a) the large dodecahedral cavity, b) the smaller dodecahedral cavity, and c) the tetrahedral cavity. Hydrogen atoms are omitted for clarity.

The bulk identity and thermal stability of MUF-777-ethyl were investigated by PXRD measurements and thermogravimetric analysis (TGA). The TGA curve shows that, after removal of guest solvent molecules from the pores, the framework is thermally stable up to 350 ˚C (Figure 2.5a). To obtain the fully desolvated framework, the as-synthesized MUF-777-ethyl sample was first washed with anhydrous N,N-dimethylformamide (DMF) and then with anhydrous acetone. The sample then was evacuated under high vacuum at 80 ˚C for 20 hours. PXRD experiments showed that the simulated pattern from the SCXRD model matches both the experimental patterns of as-synthesized and desolvated samples (Figure 2.5b). This result demonstrates that the single crystal is representative of the pure bulk sample, and the framework retains its crystallinity after removal of guest molecules.

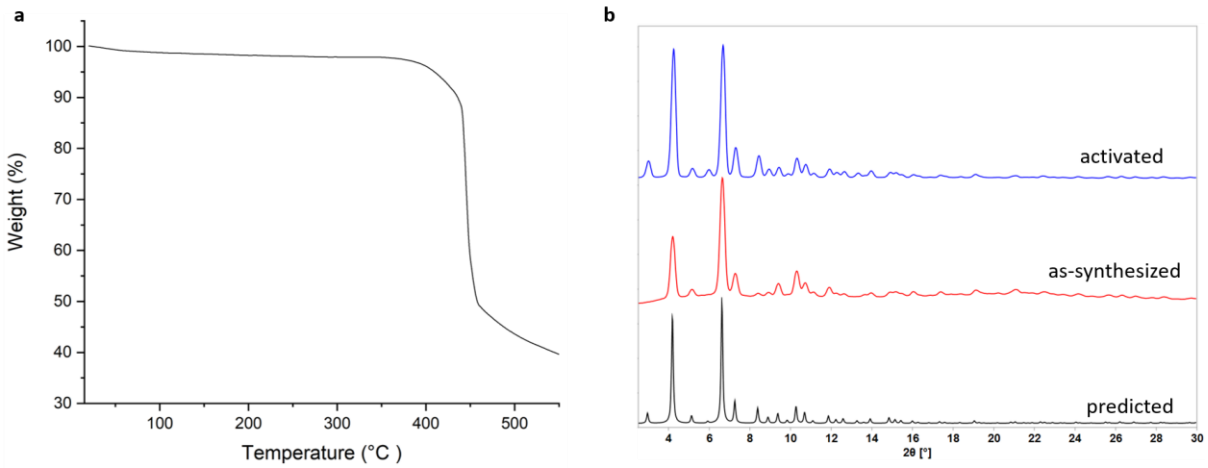

Figure 2. 5 a) TGA curve of MUF-777-ethyl, b) PXRD patterns of as-synthesized and activated samples of MUF-777-ethyl, and the pattern calculated from its SCXRD data.

The porous nature of MUF-777-ethyl was examined by performing low-pressure N_2 adsorption measurements at 77 K (Figure 2.6). The isotherm shows a two-step steep rise in gas uptake below $P/P_o = 0.1$ which is characteristic of materials that have both micropores (pore diameter < 2 nm) and mesopores (2 ≤ pore diameter ≤ 50 nm).[169] Its capacity for taking up N_2 at 77 K is 1160 cm^3/g. This value is higher than that of MUF-77-ethyl which was found to be 1004 cm^3/g.[48] The difference between MUF-777-ethyl and MUF-77-ethyl is their tritopic linkers. The tat-ethyl ligand in MUF-777-ethyl has three ethyl groups while the truxene ligand in MUF-77-ethyl has six ethyl groups. Because the pore volume occupied by these groups in MUF-77-ethyl is higher than that of in MUF-777-ethyl, MUF-77-ethyl has a lower N_2 uptake. On the basis of the N_2 adsorption isotherm, the Brunauer-Emmett-Teller (BET) surface area and pore volume of MUF-777-ethyl were calculated to be 3640 m^2/g and 1.80 cm^3/g, respectively. CO_2, CH_4, C_2H_6 and C_2H_4 isotherms were measured at both 273 K and 298 K (Figures 2.7-2.8). MUF-777-ethyl displays near-linear adsorption behaviour with no appreciable hysteresis for these gases, as expected on the basis of its wide pore windows. The adsorption amounts of MUF-777-ethyl reach up to 49.8 and 23.1 cm^3/g for CO_2 at 273 and 298 K, respectively. MUF-777-ethyl can take up a large amount of C_2H_6 (56.4 cm^3/g) and C_2H_4 (40.7 cm^3/g), and, as expected, a smaller amount of CH_4 (6.9 cm^3/g) at 298 K. It exhibits an adsorption capacity of 128.3, 84.8 and 16.1 cm^3/g for C_2H_6 and C_2H_4 and CH_4 at 298 K, respectively. The high C_2H_6 and C_2H_4 adsorption capacity of MUF-777-ethyl as compared to CH_4 is in line with the larger size and polarizability of C_2H_6 and C_2H_4 relative to CH_4.[170-172]

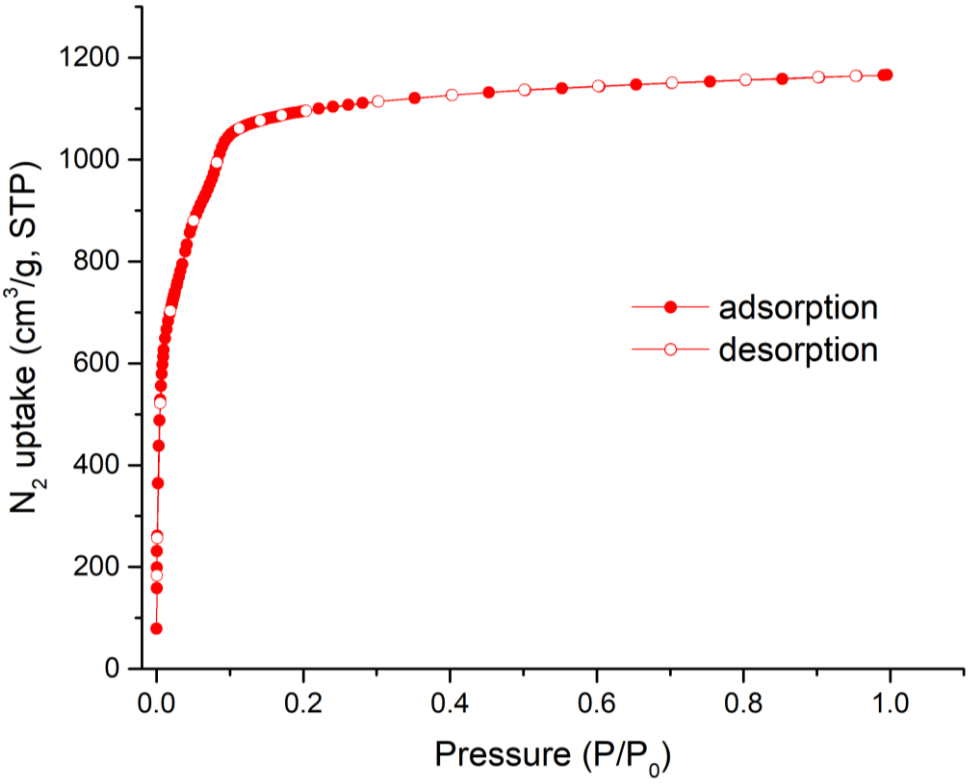

Figure 2. 6 Nitrogen adsorption (filled circles) and desorption (open circles) isotherms of MUF-777-ethyl measured at 77 K.

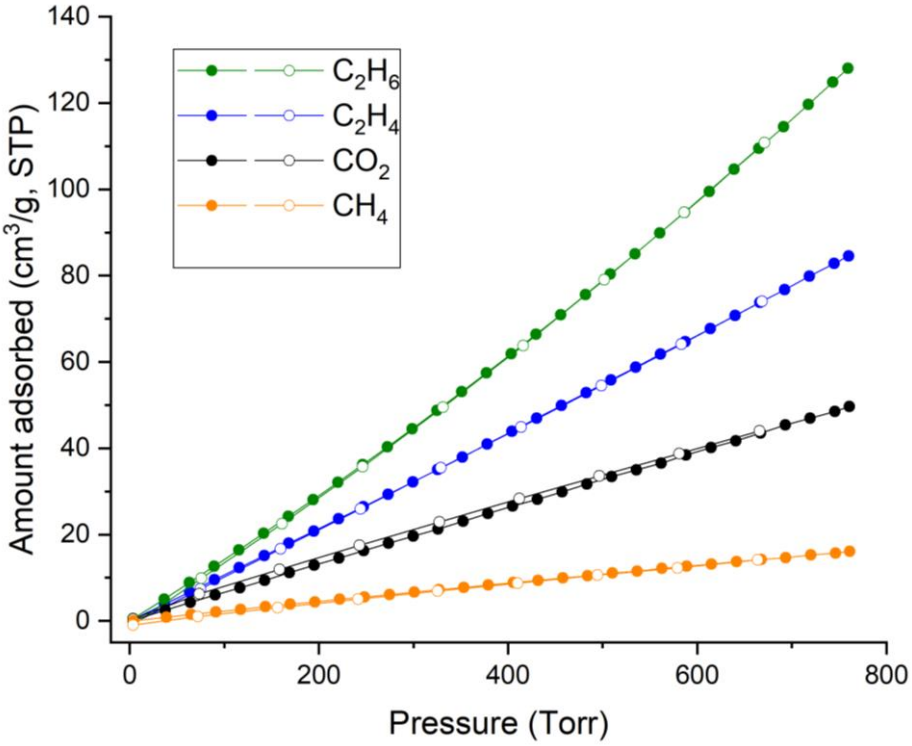

Figure 2. 7 C_2H_6, C_2H_4, CO_2 and CH_4 adsorption (filled circles) and desorption (open circles) of MUF-777-ethyl measured at 273 K.

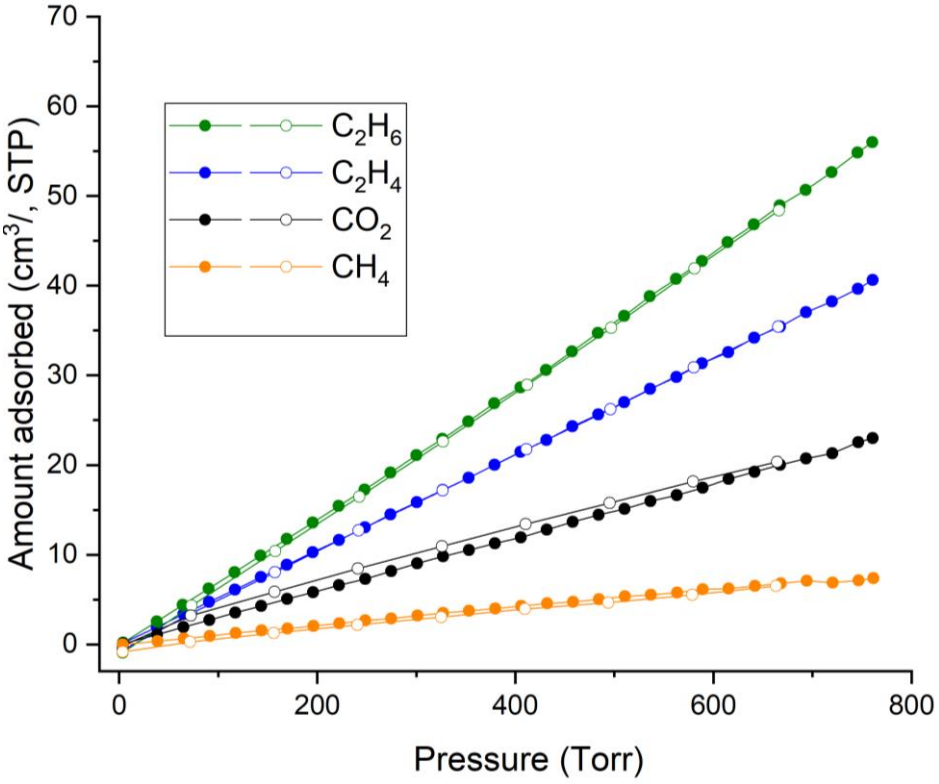

Figure 2. 8 C_2H_6, C_2H_5, CO_2 and CH_4 adsorption (filled circles) and desorption (open circles) of MUF-777-ethyl measured at 293 K.

Next, the stability of MUF-777-ethyl towards atmospheric vapor was studied. A freshly-activated sample was exposed to ambient air over a period of seven days, and PXRD patterns were measured for the first, the third and the seventh days. As shown in Figure 2.9, after the first day a broad peak starts to appear at low angle region. Although, after day seven the peaks belonging to the framework exist, their intensities decrease. This indicates that the framework starts to partially collapse after the first day. This is a lower stability compared to the stability of the parent framework, MUF-77-ethyl. This is possible due to higher rigidity of the truxene ligand in MUF-77-ethyl compared to the tat-ethyl ligand in MUF-777-ethyl.

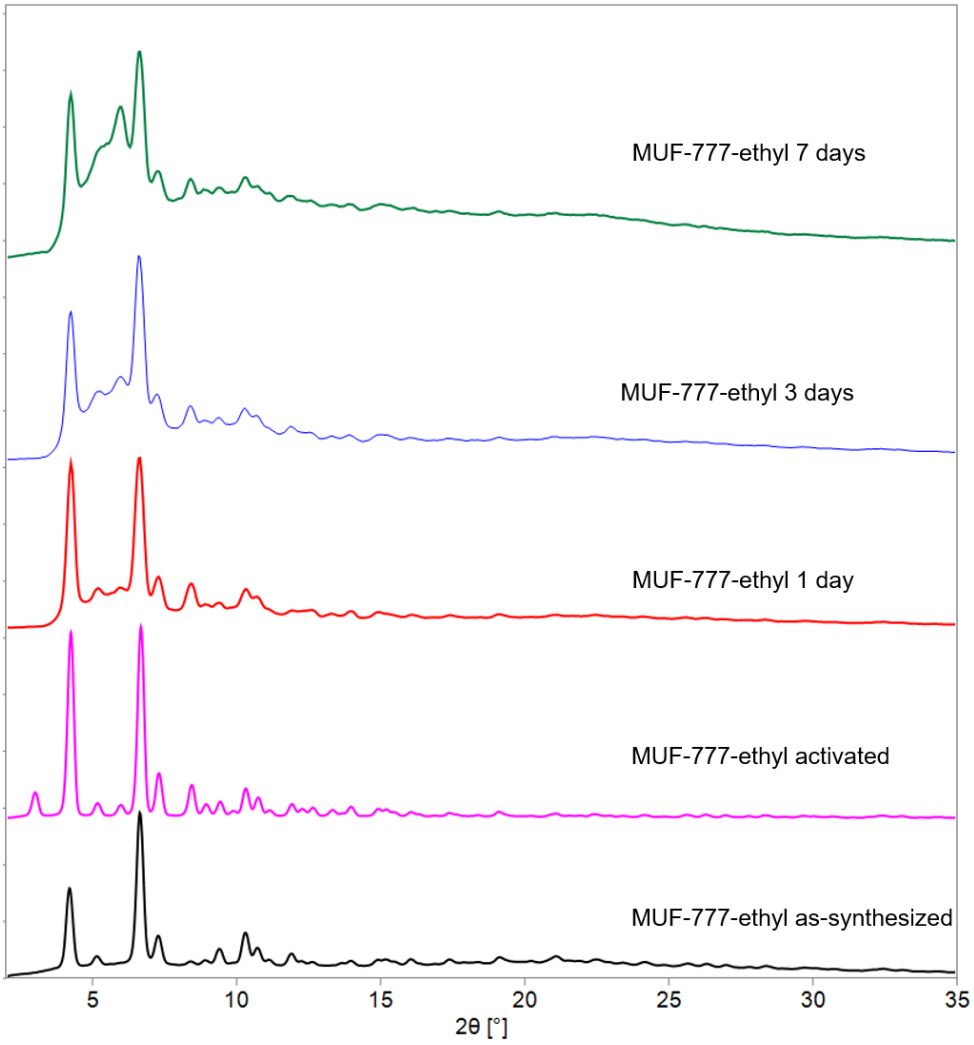

Figure 2. 9 PXRD patterns of MUF-777-ethyl; as-synthesized, activated and samples exposed to air for the stated period.

2.2.3 Synthesis and characterization of MUF-777 and MUF-777-allyl

After the characterization of MUF-777-ethyl, I planned to prepare an isoreticular family of MOFs using the ligands H_3tat, H_3tat-allyl, H_3tat-butyl and H_3tat-hexyl and H_3tat-cychexyl in place of H_3tat-ethyl. On the basis of the isoreticular principle it is expected that these ligands could form quaternary MOFs which are isostructural to MUF-777-ethyl, since their overall geometry is the same as the H_3tat-ethyl ligand. Under similar solvothermal conditions, we found that H_3tat and H_3tat-allyl formed phase-pure MUF-777 and MUF-777-allyl, respectively (Figure 2.10). We observed that the feed ratio of the ligands was critical for obtaining these materials phase-pure. In addition, benzoic acid (BA) was used for the synthesis of these MOFs to grow big crystals.

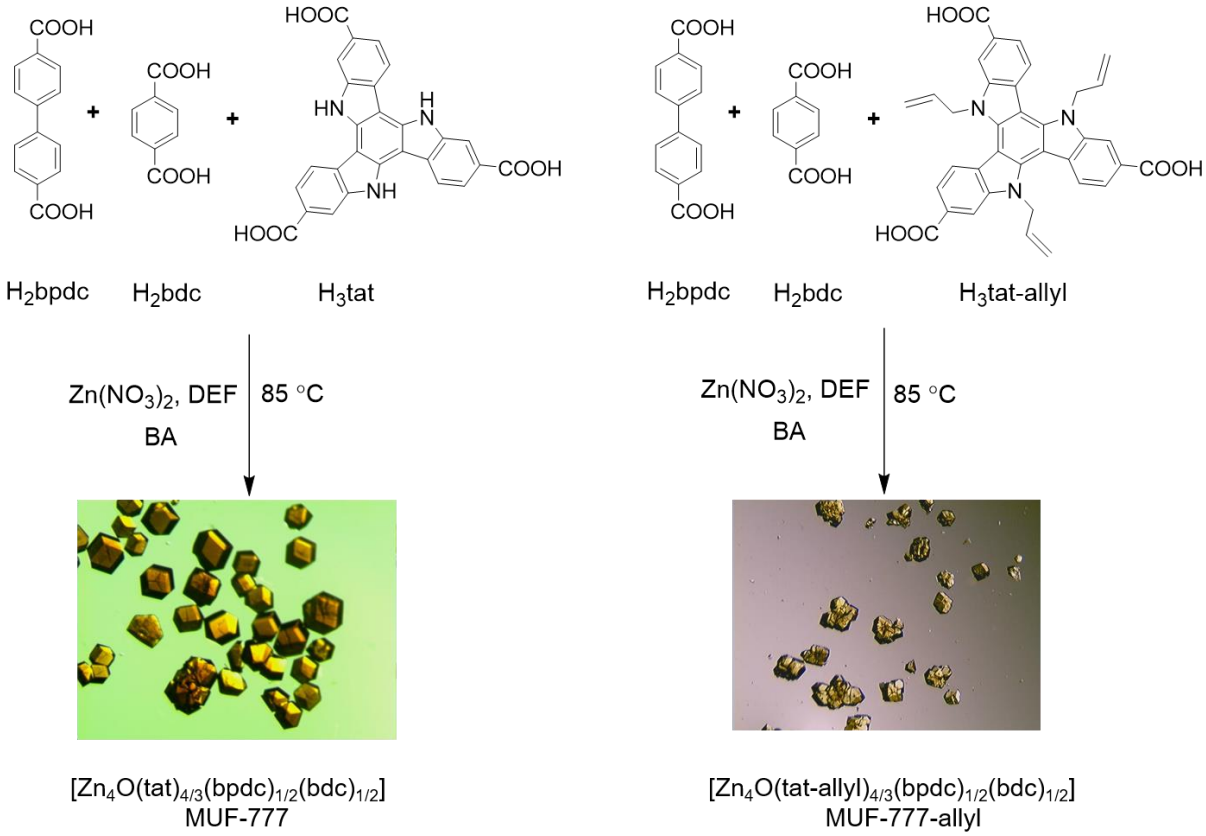

Figure 2. 10 Synthetic routes to MUF-777 and MUF-777-allyl and their optical microscopy images.

The structures of MUF-777 and MUF-777-allyl were confirmed by SCXRD analysis (Table 2.1). These materials are isostructural and share the same overall **ith-d** topology with MUF-777-ethyl. The X-ray diffraction patterns calculated from their SCXRD data match well with their patterns measured on freshly-synthesized samples. This confirms the bulk phase purity of these materials (Figure 2.11). Moreover, PXRD patterns of desolvated samples are in agreement with the patterns of as-synthesized samples implying that these frameworks are stable upon removal of guest molecules.

The TGA plots MUF-777 and MUF-777-allyl show a thermal stability up to 350 ˚C. A significant decrease in the TGA trace of MUF-777-allyl between 350 ˚C and 450 ˚C has a value of 12.5 wt%, which corresponds the expulsion of a C_3H_4 fragment (Figure 2.12). This is presumably the allyl groups that depart as allene gas to leave behind MUF-777 with the tat ligand. The thermolytic expulsion of small ligand fragments can also be observed from other frameworks.[83, 173-175]

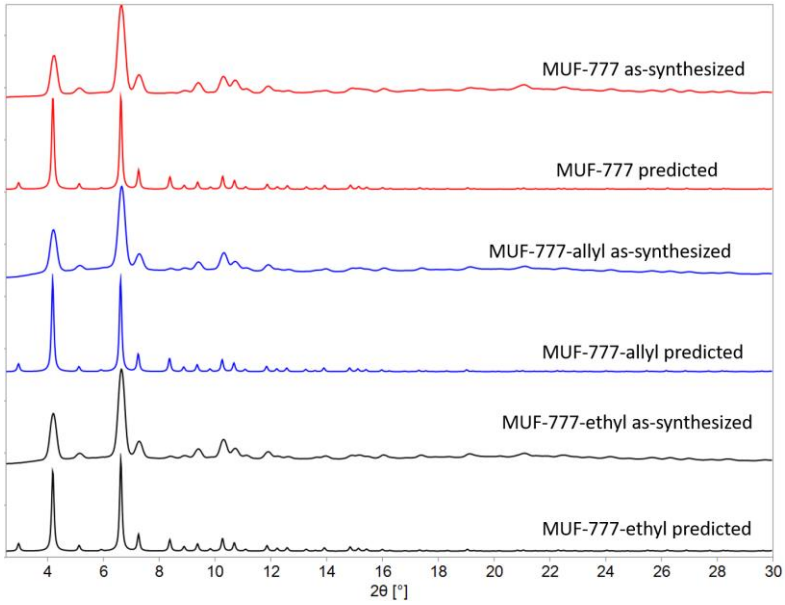

Figure 2. 11 PXRD patterns of MUF-777, MUF-777-allyl and MUF-777-ethyl.

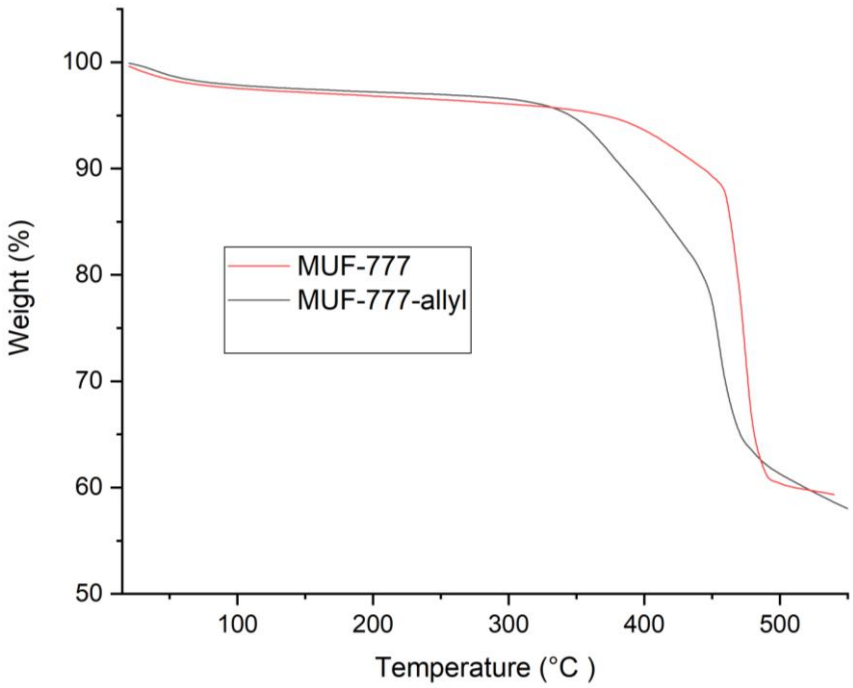

Figure 2. 12 TGA curves of MUF-777 and MUF-777-allyl.

Next, the porosities of these materials were investigated. They were activated with a similar activation procedure that was used for MUF-777-ethyl. The solvent of freshly-synthesized samples were first exchanged with dry DMF then dry acetone. After acetone was decanted, the crystals were activated at 80 °C under vacuum for 20 hours. The capacity of MUF-777 and

MUF-777-allyl for taking up N_2 at 77 K was found to be 1170 cm^3/g and 1030 cm^3/g, respectively. Based on their N_2 uptake capacities, their BET surface areas were calculated to be 3440 and 3170, respectively (Figures 2.24 and 2.25).

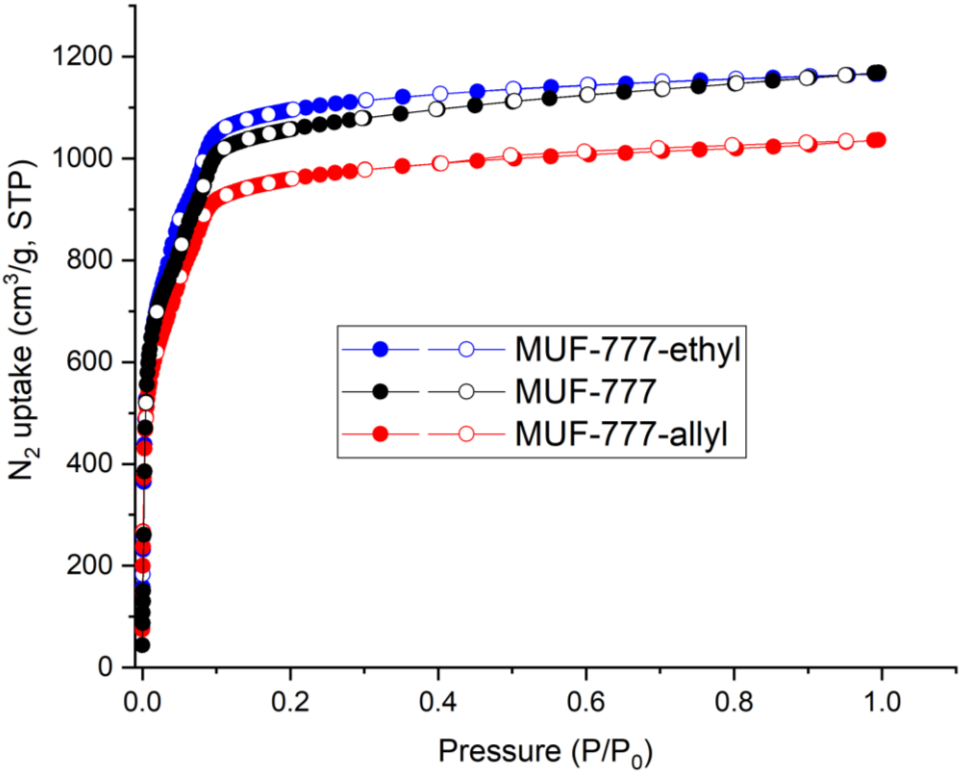

Figure 2. 13 Nitrogen adsorption (filled circles) and desorption (open circles) isotherms of MUF-777, MUF-777-allyl and MUF-777-ethyl measured at 77 K.

^{1}H NMR spectroscopic analysis of a digested sample of MUF-777-allyl showed that the integrals of the peaks match well with the stoichiometry of the framework (Figure 2.14). However, ^{1}H NMR spectroscopic analysis of a digested sample of MUF-777 showed that the integrals of the peaks corresponding to the H_3tat linker was lower than the expected value by about 15%. Some additional peaks were also observed in the spectrum, especially in the chemical shift range of the NH proton. These results indicate that some undesired reactions occur at the NH site under the solvothermal MOF synthesis conditions. To prevent this and obtain a clean ^{1}H NMR spectrum indicative of phase purity of the framework, we developed another procedure for the synthesis of MUF-777. This will be discussed in the next section.

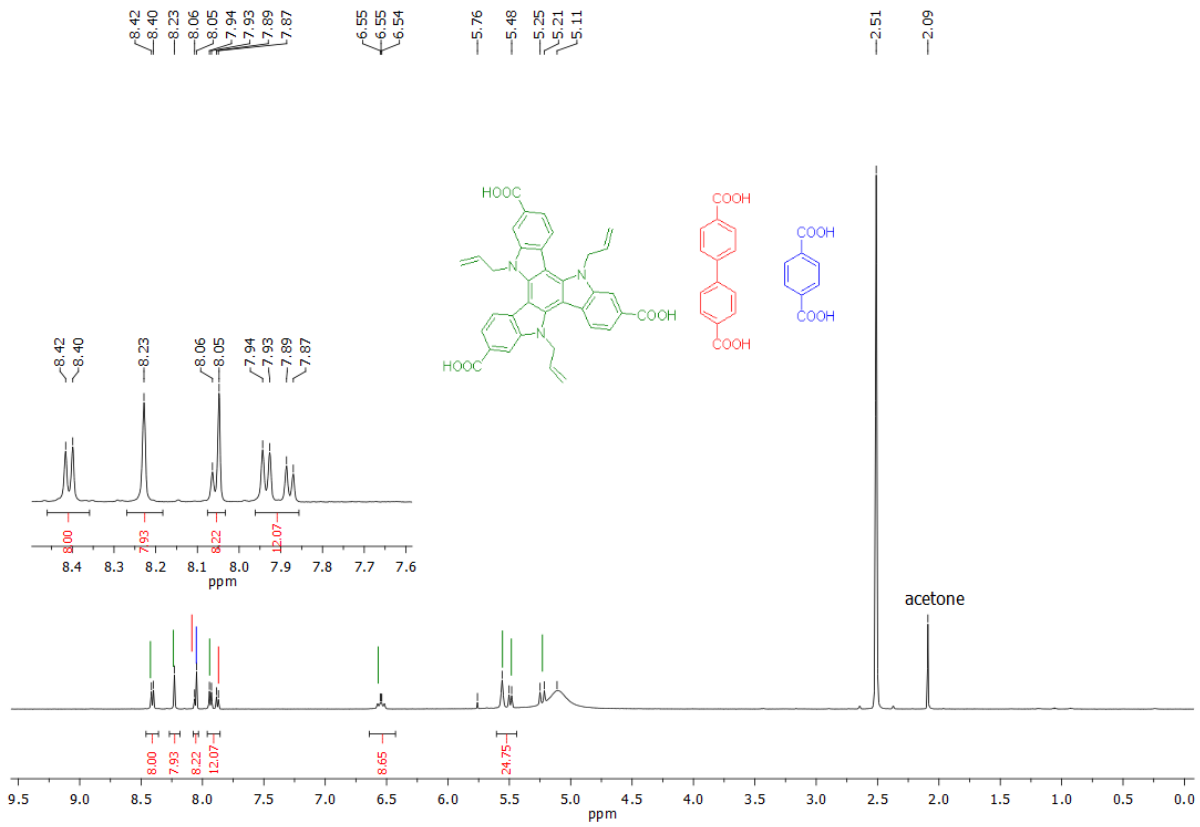

Figure 2. 14 ^{1}H NMR spectrum of MUF-777-allyl digested in DMSO-d_6/DCl showing the integrals that match with the formula $[Zn_4O(tat\text{-}allyl)_{4/3}(bpdc)_{1/2}(bdc)_{1/2}]$.

2.2.4 Room temperature synthesis of MUF-777, MUF-777-butyl, MUF-777-hexyl and MUF-777-cychexyl

In this procedure, the synthesis of MUF-777 was achieved by adding zinc acetate to a solution of H_3tat, H_2bpdc and H_2bdc in DMF at room temperature. After optimization of the feed ratio of the three ligands, phase pure MUF-777 was obtained as nanocrystals.

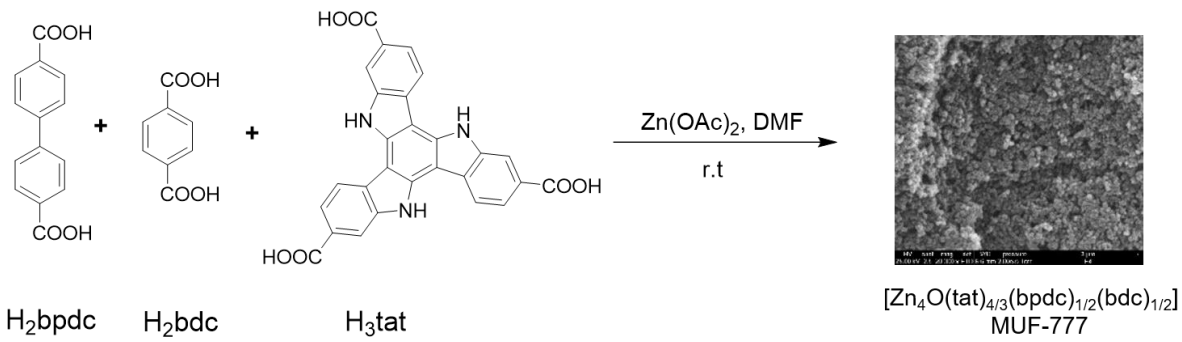

Figure 2. 15 Schematic illustration of room temperature synthesis of MUF-777.

Scanning electron microscopy (SEM) showed that the particle sizes were ranging from 100 to 200 nm (Figure 2.15). PXRD patterns of this material match well with the patterns of the material prepared under solvothermal conditions (2.16). This indicates that the architecture of nanocrystalline MUF-777 is identical to that seen in the large crystals and the lattice adopts an **ith-d** topology with a stoichiometry of $[Zn_4O(tat)_{4/3}(bpdc)_{1/2}(bdc)_{1/2}]$.

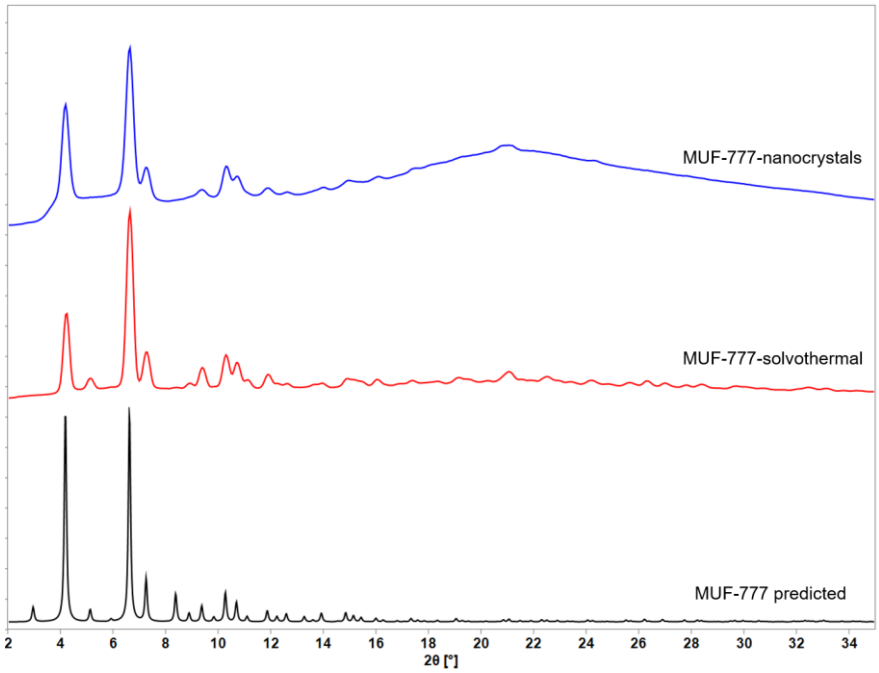

Figure 2. 16 PXRD patterns of MUF-777 samples prepared under solvothermal and room temperature conditions compared to its calculated patterns.

As mentioned in the previous section, ^{1}H NMR spectrum of a digested sample of MUF-777 prepared under solvothermal conditions did not match the framework stoichiometry. As shown in Figure 2.17, in ^{1}H NMR spectrum of a digested sample of MUF-777 nanocrystals the integrals of the peaks match well with the expected framework stoichiometry.

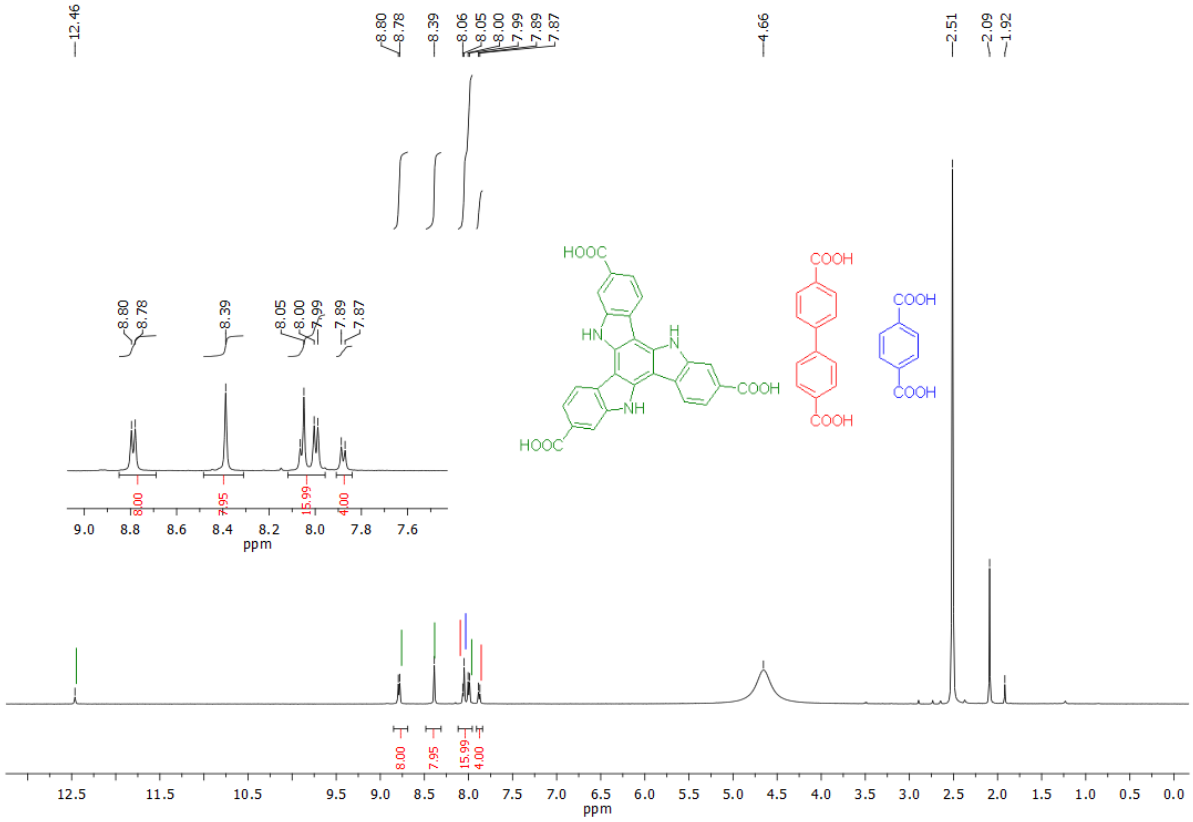

Figure 2. 17 ^{1}H NMR spectrum of MUF-777 nanocrystals digested in DMSO-d_6/DCl showing the integrals that match with the formula $[Zn_4O(tat)_{4/3}(bpdc)_{1/2}(bdc)_{1/2}]$.

Unlike the three ligands discussed so far, H_3tat-butyl, H_3tat-hexyl and H_3tat-cychexyl ligands produced a second phase along with the desired multicomponent product under solvothermal conditions. A series of adjustments in conditions including using modulators, different solvents and changing the feed ratio of the ligands could not prevent the formation of this second phase. However, with the same procedure that formed phase-pure MUF-777 nanocrystals, MUF-777-butyl, MUF-777-hexyl and MUF-777-cychexyl were prepared as nanocrystals (Figure 2.18). It was found that the second phase that formed during the synthesis of these MOFs belonged to a zinc-based MOF containing only triazatruxene ligand. Synthesis and characterization of these binary MOFs will be presented in Chapter 5.

The phase purity of MUF-777-butyl, MUF-777-hexyl and MUF-777-cychexyl nanocrystals was determined by PXRD analysis (Figure 2.19). Their PXRD patterns also indicates that they are isostructural to MUF-777-ethyl. ^{1}H NMR spectroscopic analysis of digested samples of these MOFs demonstrated that the ratio of the ligand integrals matches the ratio expected for $[Zn_4O(tat\text{-}X)_{4/3}(bpdc)_{1/2}(bdc)_{1/2}]$ (X = butyl, hexyl and cyclohexyl)

frameworks. This demonstrates the purity of the nanocrystalline frameworks. Detailed synthetic procedure and ^{1}H NMR spectra of these materials are available in the experimental section and Electronic Appendix A.

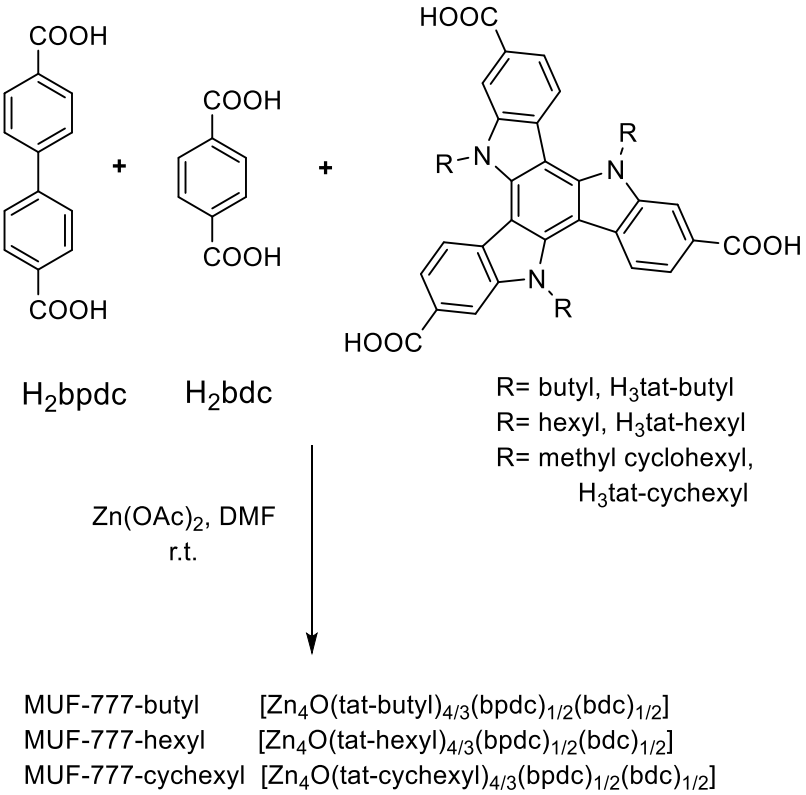

Figure 2. 18 Synthetic route MUF-777-butyl, MUF-777-hexyl and MUF-777-cychexyl.

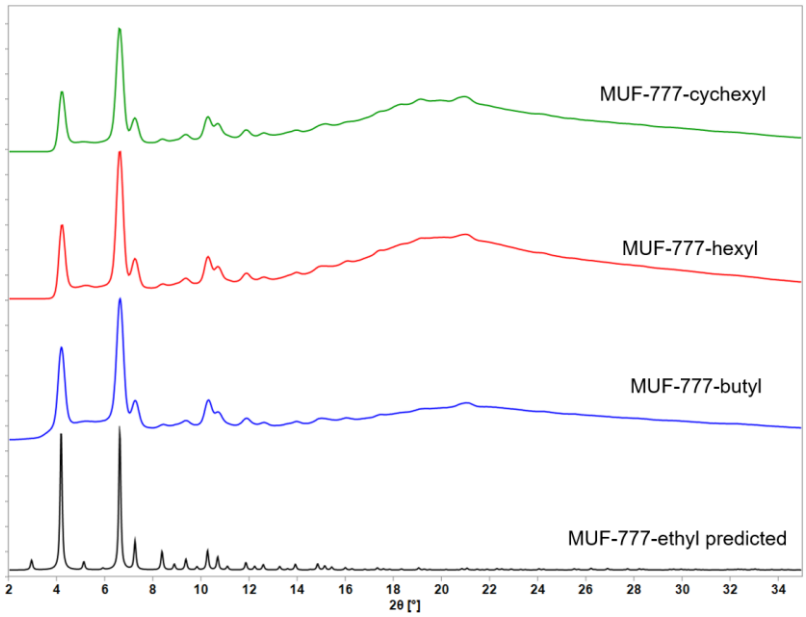

Figure 2. 19 PXRD patterns of MUF-777-butyl, MUF-777-hexyl and MUF-777-butyl MUF-777-cychexyl nanocrystals compared to the calculated patterns of MUF-777-ethyl.

2.2.4 Fluorescence studies

The electron rich nature of triazatruxene derivatives endows them with interesting fluorescence properties which have potential uses in chemical sensing and photon harvesting and conversion. A luminescent COF based on a triazatruxene derivative has recently been reported which shows sensitive fluorescence turn-on behavior towards electron rich arenes.[163] Related light emission was also observed in a triazatruxene containing conjugated microporous polymer.[176] Moreover, researchers have reported triazatruxene-containing molecules and their use in the detection of vapors of nitroaromatic explosives.[177] Compared to these COF and polymer materials above, the high BET surface area of MUF-777 and its available free NH sites may be useful for detection of guests that can act as H-bonding acceptors.

Upon recording emission spectra with an excitation wavelength of 390 nm, we noted that all of the triazatruxene ligands displayed a unique blue luminescence. H_3tat showed a relatively strong emission band at 475 nm. The emission maxima for other ligands were observed in a range between 425 and 475 nm (Figure 2.20a). H_2bpdc and H_2bdc are non-emissive linkers upon 390 nm excitation prior to incorporation in MOFs. The Zn_4O cluster is also non-emissive and the diamagnetic nature of Zn(II) generally does not have a decisive impact on the emission behavior of the linkers.[178] The emission spectra of the $[Zn_4O(tat\text{-}X)_{4/3}(bpdc)_{1/2}(bdc)_{1/2}]$ MOFs were observed between 430 and 490 nm, which correlated closely with the spectral output of the triazatruxene ligands (Figure 2.20b). This information together with the emission spectra of MOFs indicate that the emission profile largely originates from triazatruxene based ligands.

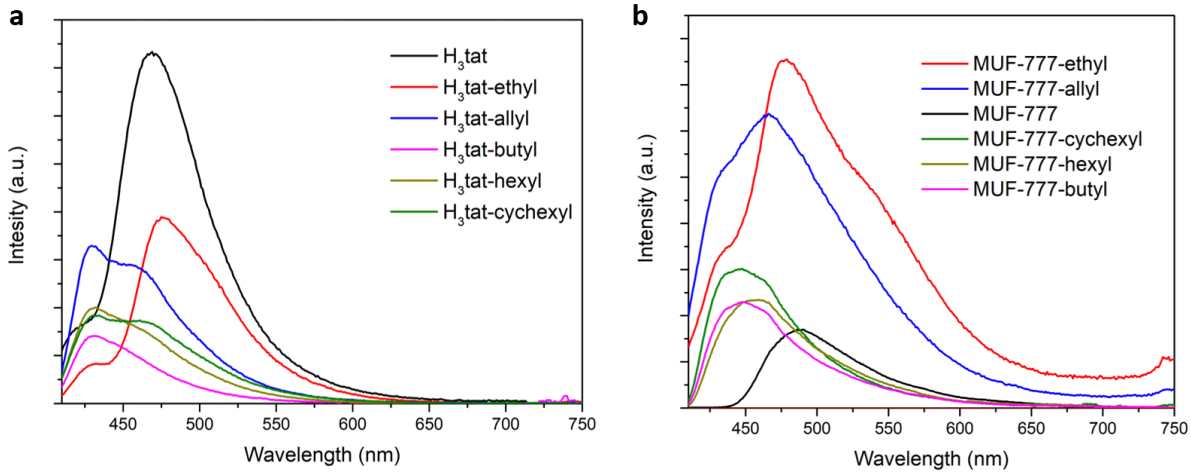

Figure 2. 20 Emission spectra of triazatruxene ligands (dissolved in DMF) their corresponding MOFs (suspended in DMF) when excited at 390 nm.

To explore the sensing ability of MOFs towards H-bonding acceptor guests, titrations were carried out with the gradual addition of the guest to MUF-777 dispersed in dichloromethane while monitoring the spectral output. Upon the addition of benzaldehyde (PhCHO), the fluorescence intensity of MUF-777 decreased significantly until the point where approximately one equivalent guest molecule per NH site was reached (Figure 2.21)**.** Beyond this point the fluorescence intensity continued to drop with a much more limited quenching effect. This result indicates that the quenching effect occurs by hydrogen bonding between the NH groups of the tat linker and the benzaldehyde guest molecules. This hypothesis was tested by the addition of nitrobenzene ($PhNO_2$) and benzonitrile (PhCN). These guests caused a weaker decline in the emission (Figures Figure 2.22). This is consistent with benzaldehyde's quenching effect being largely due to H-bonding because nitro and nitrile groups are much poorer H-bond acceptors than formyl groups.[179-180] The small amount of fluorescence quenching that is observed in the latter cases may be due to π-π interactions of these electron-deficient guests with the electron-rich tat linker. To further confirm that the fluorescence quenching is caused by hydrogen bonding at the NH sites in MUF-777 the titrations of the three guests were carried out on MUF-777-hexyl. Here, the hydrogen bonding sites of the triazatruxene linker are blocked by the hexyl group. As expected, only small changes in the fluorescence intensity of MUF-777-hexyl were observed with the titration of benzaldehyde and nitrobenzene while there was no change with addition of benzonitrile (Figures 2.23). In this light, MUF-777 frameworks join their MUF-77 counterparts in a class of multicomponent materials with rich photophysical properties.[181]

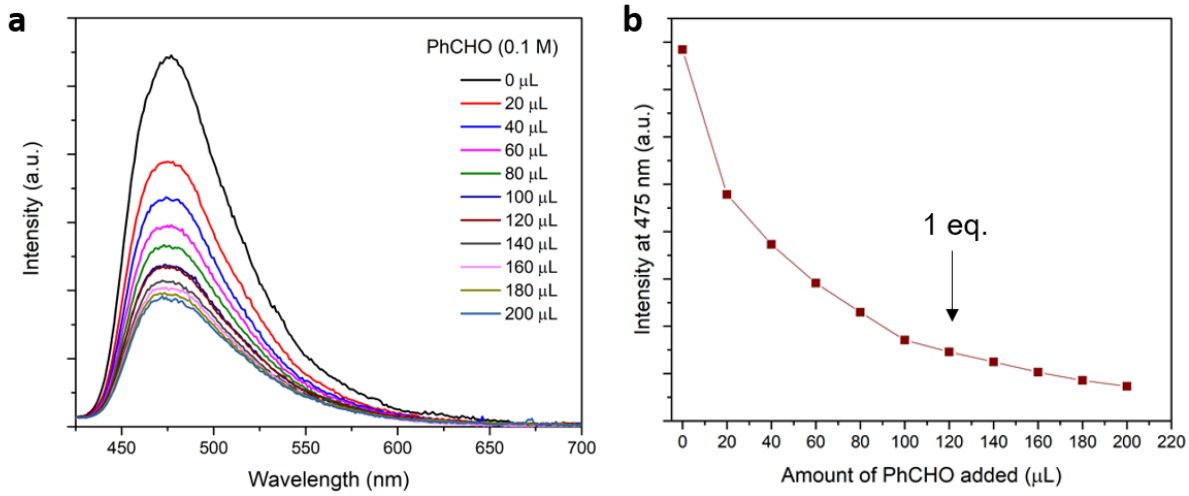

Figure 2. 21 a) Emission spectra of MUF-777 with addition of benzaldehye, and b) corresponding curve showing the reduction in emission intensity with added benzaldehye. The point at which approximately one equivalent of guest per NH site on the MOF has been added is highlighted.

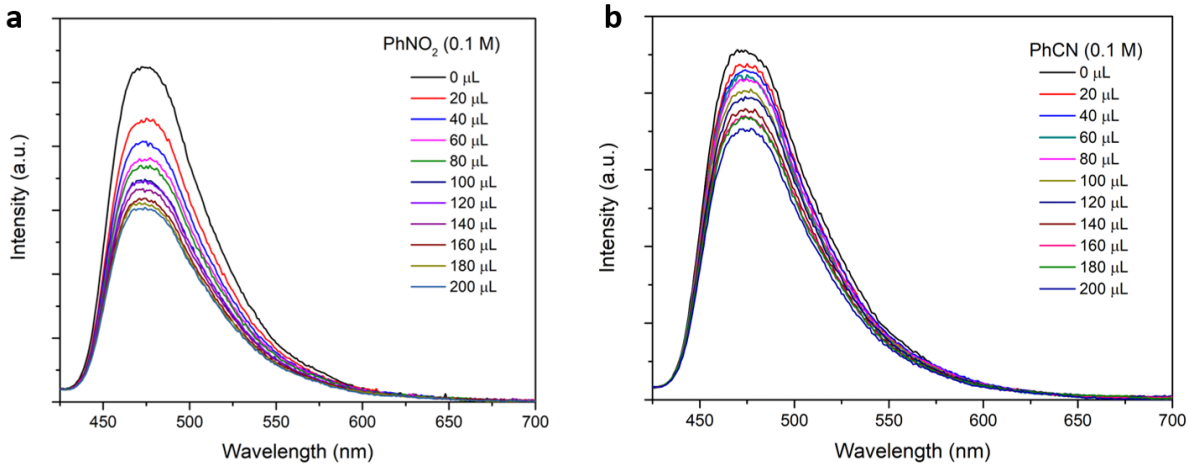

Figure 2. 22 Emission spectra of MUF-777 with addition of a) nitrobenzene and b) benzonitrile.

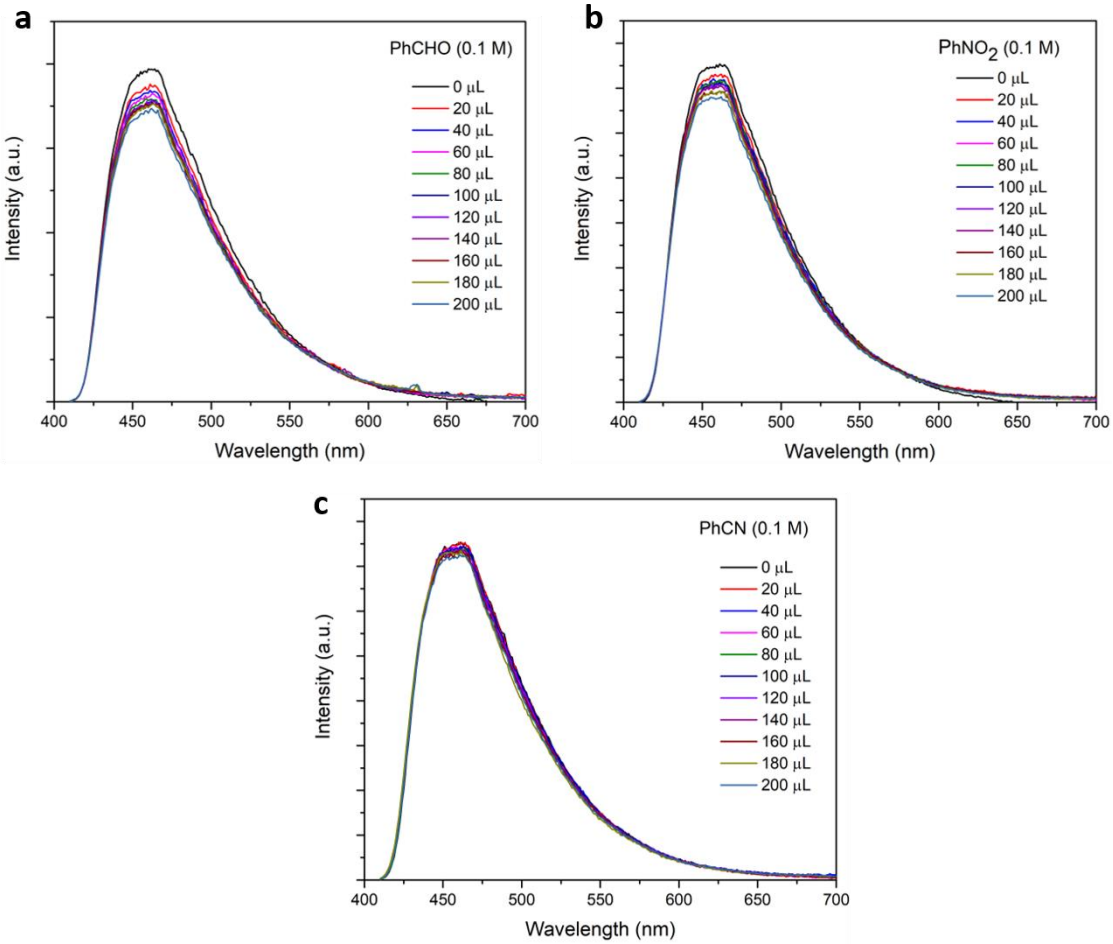

Figure 2. 23 Emission spectra of MUF-777-hexyl with addition of a) benzaldehyde, b) nitrobenzene and c) benzonitrile.

2.3 Conclusion

Syntheses of six new tritopic ligands based on a rigid electron-rich C_3-symmetric triazatruxene core was successfully achieved. Using these triazatruxene ligands along with bpdc and bdc a series of multicomponent MOFs was synthesized. MUF-777, MUF-777-ethyl and MUF-777-allyl were obtained under solvothermal conditions and their structures determined by SCXRD analysis. These materials are well ordered with each of their three linkers positioned in precise locations in the lattice without disorder or defects. TGA and gas adsorption measurements showed that these materials are stable and porous after removal of guest molecules. Additionally, MUF-777-butyl, MUF-777-hexyl and MUF-777-cychexyl were synthesized at room temperature by using zinc acetate instead of zinc nitrate to form nanocrystalline materials. PXRD and ^{1}H NMR spectroscopic analyses revealed that these MUF-777 MOFs define an isoreticular series which differ by the functional group introduced on the N atom sites of the triazatruxene linker. The parent MUF-777 material can form

hydrogen bonds with guest molecules through its NH sites. This may be useful for the detection of proton acceptors by luminescence quenching. Benefitting from the straightforward derivatization of H_3tat, new ligands containing further substituents with different electronic and steric properties can be prepared to tune MOF features such as catalytic activity, gas adsorption and fluorescence output in a programmable way.[82]

2.4 Experimental section

2.4.1 General procedures

All starting materials and solvents were used as received from commercial sources without further purification unless otherwise noted. Column chromatography was carried out on silica gel (grade 60, mesh size 230-400, Scharlau). NMR spectra were recorded at room temperature (unless otherwise noted) on Bruker-400 and Bruker-500 Avance instruments, with the use of the solvent proton as an internal standard.

2.4.2 Ligand synthesis and characterization

Syntheses and characterizations of Et_3tat and H_3tat will be described below. Syntheses and characterizations of all other compounds are available in the Electronic Appendix A.

Et_3tat

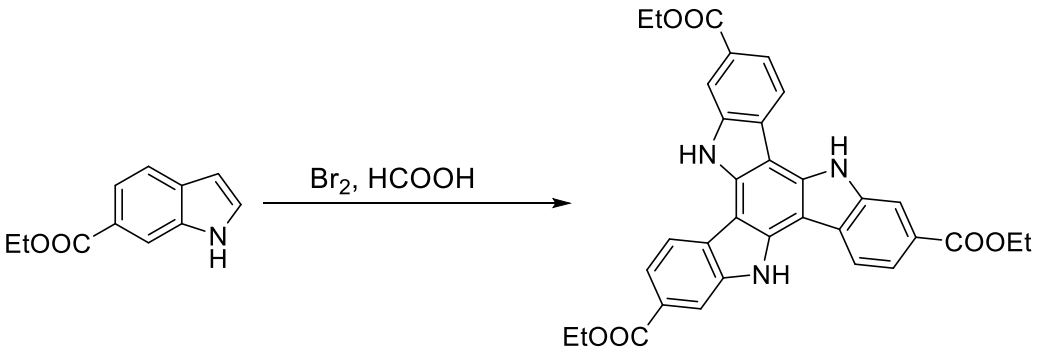

1*H*-Indole-6-carboxylic acid (1.28 g, 6.79 mmol) was dissolved in formic acid (130 mL). To this solution, Br_2 (1.24 g, 7.77 mmol) in formic acid (70 mL) was added slowly over 3 minutes. The mixture was stirred at room temperature overnight. The green solid formed was filtered, washed with formic acid, water and dried under vacuum. Although a minor impurity was detected by ^{1}H NMR spectroscopy, this mixture was used for the next step without further purification. Yield: 575 mg (45%). ^{1}H NMR: (500 MHz, DMSO-*d*6): δ 12.44 (s, 3H), 8.75 (d,

J = 8.2 Hz, 3H), 8.40 (s, 3H), 8.02 (d, *J* = 8.2 Hz, 3H), 4.42 (q, *J* = 7.1 Hz, 6H), 1.44 (t, *J* = 7.1 Hz, 9H). ^{13}C NMR: (125 MHz, DMSO-*d*6): 167.02, 138.40, 136.98, 126.11, 124.35, 121.02, 119.86, 113.00, 101.13, 60.97, 14.82.

H_3tat

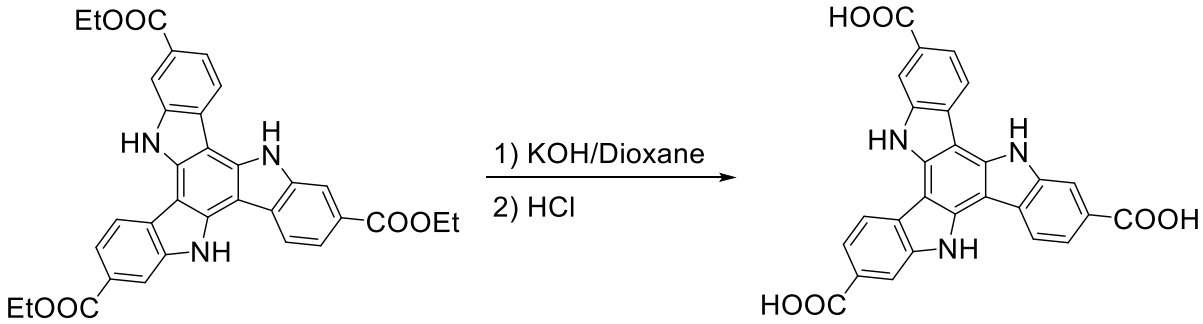

Et_3tat (561 mg, 1 mmol) was dissolved in 30 mL 1:1 (V/V) dioxane/KOH (aq., 1M) and the solution was refluxed for two days. Dioxane was removed under reduced pressure and the reaction mixture then was acidified with 1 M aqueous HCl while it was kept on an ice bath. pH was adjusted to around 1, and the mixture was stirred for 3 hours. The yellow solid formed was filtered, washed with water and dried under vacuum. Yield: 470 mg (98%). ^{1}H NMR: (500 MHz, DMSO-*d*6): δ 12.77 (br, 3H), 12.38 (s, 3H), 8.75 (d, *J* = 8.8 Hz, 6H), 8.38 (s, 3H), 8.01 (d, *J* = 8.2 Hz, 6H) ppm. ^{13}C NMR: (125 MHz, DMSO-*d*6): δ 168.66, 138.43, 136.83, 125.95, 125.26, 121.31, 119.80, 113.16, 101.16 ppm. ESI (negative mode, CH_3OH): m/z = 476.0892 ($[C_{27}H_{14}N_3O_6]^-$, calcd. 476.0877).

2.4.3 MOF synthesis and characterization

MUF-777-ethyl, $[Zn_4O(tat\text{-}ethyl)_{4/3}(bpdc)_{1/2}(bdc)_{1/2}]$

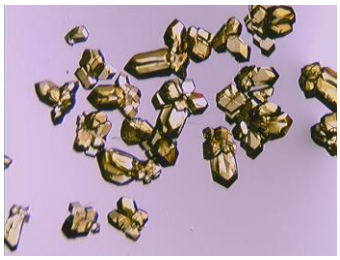

H_3tat-ethyl (4.2 mg, 7.5 µmol), biphenyl-4,4'-dicarboxylic acid (2.3 mg, 9.6 µmol), terephthalic acid (1.2 mg, 7.0 µmol) and $Zn(NO_3)_2{\cdot}4H_2O$ (13.8 mg, 52.8 µmol) were dissolved in anhydrous DEF (1 mL) and water (35 µL) in a 4 mL vial. The reaction mixture was sonicated for 1 minute, then heated in an 85 °C isothermal oven for 17 hours to obtain yellow crystals. For the yield calculation, TGA and NMR analysis, the mother liquor was decanted and replaced with anhydrous DMF. The solvent was then replaced with fresh anhydrous DMF (2 times) and anhydrous acetone (5 times). After acetone was decanted, the crystals were dried under vacuum. The synthesis can

be scaled up by combining H_3tat-ethyl (21.8 mg, 38.9 µmol), biphenyl-4,4'-dicarboxylic acid (12.3 mg, 51.5 µmol), terephthalic acid (7.2 mg, 42.0 µmol), $Zn(NO_3)_2{\cdot}4H_2O$ (70 mg, 267.8 µmol), DEF (5 mL) and water (175 µL) in a 20 mL scintillation vial at 85 °C. Yield: 23 mg.

MUF-777, $[Zn_4O(tat)_{4/3}(bpdc)_{1/2}(bdc)_{1/2}]$

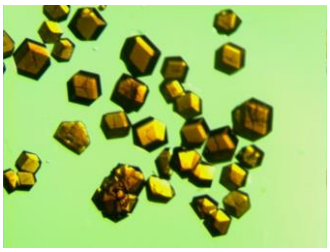

H_3tat (2.7 mg, 5.6 µmol), biphenyl-4,4'-dicarboxylic acid (2.1 mg, 8.8 µmol), terephthalic acid (1.2 mg, 7.0 µmol), benzoic acid (8.5 mg, 70.8 µmol) and $Zn(NO_3)_2{\cdot}4H_2O$ (13.8 mg, 52.8 µmol) were dissolved in anhydrous DEF (1 mL) and water (35 µL) in a 4 mL vial. The reaction mixture was sonicated for 1 minute, then heated in an 85 °C isothermal oven for 20 hours to obtain orange crystals. For yield calculation, TGA and NMR analysis, the mother liquor was decanted and replaced with anhydrous DMF. The solvent was then replaced with fresh anhydrous DMF (2 times) and anhydrous acetone (5 times). After acetone was decanted, the crystals were dried under vacuum. The synthesis was scaled up by combining H_3tat (13 mg, 26.9 µmol), biphenyl-4,4'-dicarboxylic acid (12.0 mg, 50.3 µmol), terephthalic acid (7.0 mg, 40.8 µmol), benzoic acid (43 mg, 385.1 µmol), $Zn(NO_3)_2{\cdot}4H_2O$ (73 mg, 279.3 µmol), DEF (5 mL) and water (170 µL). The reaction was carried out in 20 mL scintillation vials at 85 °C. Yield: 14 mg.

MUF-777-allyl, $[Zn_4O(tat\text{-}allyl)_{4/3}(bpdc)_{1/2}(bdc)_{1/2}]$

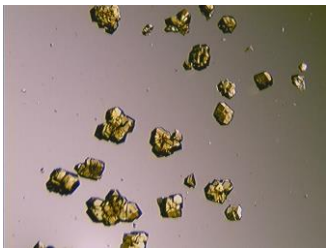

H_3tat-allyl (4.6 mg, 7.8 µmol), biphenyl-4,4'-dicarboxylic acid (2.2 mg, 9.2 µmol), terephthalic acid (1.5 mg, 8.8 µmol), benzoic acid (9.6 mg, 79.9 µmol) and $Zn(NO_3)_2{\cdot}4H_2O$ (13.8 mg, 52.8 µmol) were dissolved in anhydrous DEF (1 mL) and water (35 µL) in a 4 mL vial. The reaction mixture was sonicated for 1 minute, then heated in an 85 °C isothermal oven for 20 hours to obtain dark orange crystals. For yield calculation, TGA and NMR analysis, the mother liquor was decanted and replaced with anhydrous DMF. The solvent was then replaced with fresh anhydrous DMF (2 times) and anhydrous acetone (5 times). After acetone was decanted, the crystals were dried under vacuum. The synthesis was scaled up by combining H_3tat-allyl (23.0 mg, 39.0 µmol), biphenyl-4,4'-dicarboxylic acid (13.2 mg, 55.2 µmol), terephthalic acid (7.6 mg, 44.6 µmol), benzoic acid (55 mg, 454.8 µmol), $Zn(NO_3)_2{\cdot}4H_2O$ (70 mg, 267.8 µmol), DEF (5 mL) and water (200 µL). The reaction was carried out in 20 mL scintillation vials at 85 °C. Yield: 25 mg.

2.4.4 ^{1}H NMR analysis of digested MOF samples

The following protocol was used for digestion of the MOFs for ^{1}H NMR spectroscopy: The sample was washed with dry acetone then soaked in dry acetone then desolvated *in vacuo*. 0.60 mL of DCl/DMSO-d_6 (150 µL/0.45 mL) solution was used to digest around 3 mg MOF. The NMR spectrum was acquired with the clear solution of the digested framework. ^{1}H NMR spectra of MUF-777-butyl, MUF-777-hexyl, MUF-777-cyclohexyl are available in Electronic Appendix A.

2.4.5 Powder X-ray diffraction patterns

All powder X-ray diffraction measurements were carried out on a Rigaku Spider X-ray diffractometer with Cu K_α radiation (Rigaku MM007 microfocus rotating-anode generator), monochromated and focused with high-flux Osmic multilayer mirror optics, and a curved image plate detector. Unless otherwise noted, samples were kept damp with solvent prior to and during measurements. The two-dimensional images of the Debye rings were integrated with 2DP to give 2θ vs I diffractograms. Predicted powder patterns were generated from single crystal structures using Mercury.

2.4.6 Single crystal X-ray diffraction

Crystals of MUF-777-ethyl were desolvated by washing with dry acetone followed by heating at an elevated temperature in vacuo (approx. 80℃, > 1h). For MUF-777 and MUF-777-allyl, the crystals in fresh DMF were used. Individual crystals were selected under a microscope then mounted on a polymer mount with a minimum amount of Fomblin® Y oil. A Rigaku Spider diffractometer equipped with a MicroMax MM007 rotating anode generator (Cu_α radiation, 1.54178 Å), high-flux Osmic multilayer mirror optics, and a curved image-plate detector was used to collect the data. The data were integrated and scaled and averaged with FS Process.[182] Using Olex2[183], the structure was solved with the SHELXT[184] structure solution program using intrinsic phasing and refined with the ShelXL[185] refinement package using least squares minimisation.

Crystallographic data details are summarized in Table 2.1. The data for MUF-777-ethyl was collected at 133 K using a desolvated crystal, while data collection for MUF-777-allyl and MUF-777 were performed on solvated crystals at 293 K. All zinc, oxygen and carbon atoms were found in the electron density difference maps and refined anisotropically except for ethyl

groups on MUF-777-ethyl and allyl groups on MUF-777-allyl. Unrestrained atomic displacement parameters sometimes produced high U_{eq} values during the refinement thus RIGU, SADI, ISOR, DELU and SIMU commands were introduced as appropriate with careful adjustments of the standard deviations. Hydrogen atoms were calculated and refined as a riding model. Disordered carbon atoms of ethyl and allyl groups were located in calculated positions and refined isotropically. Their positions were calculated using Discovery Studio. During the refinement of MUF-777 twinning was found and the use of the appropriate twin law significantly improved the refinement statistics. The oxygen atom of water molecule in MUF-777 was refined with an occupancy of 1/3.

Table 2. 1 Crystallographic data summary.

Compound	**MUF-777**	**MUF-777-ethyl**	**MUF-777-allyl**
Formula	$C_{47}H_{24.67}N_4O_{14.33}Zn_4$	$C_{55}H_{38}NO_{13}Zn_4$	$C_{59}H_{38}N_4O_{13}Zn_4$
Formula weight	1136.19	1224.37	1272.41
Crystal size (mm)	0.25 × 0.22 × 0.20	0.29 × 0.28 × 0.23	0.25 × 0.24 × 0.24
Temperature (K)	293	133	293
Wavelength (Å)	1.54178	1.54178	1.54178
Crystal system	cubic	cubic	cubic
Space group	*Pm*-3	*Pm*-3	*Pm*-3
Unit cell length (Å)	29.8226(10)	29.8095(10)	29.855(2)
Unit cell volume ($Å^3$)	26524(3)	26489(3)	26610(6)
Z	6	6	6
D_{calc} (g cm^{-3})	0.427	0.461	0.476
μ (mm^{-1})	0.779	0.788	0.792
F(000)	3416.0	3720.0	3764.0
Reflns coll./unique, R_{int}	13613 / 3652, 0.047	11509/ 3510, 0.031	9911/ 2815, 0.072
Data range	8 Å > d > 1.1 Å	8 Å > d > 1.1 Å	8 Å > d > 1.2 Å
Completeness	97%	93%	97%
T_{min}, T_{max}	0.38, 1.00	0.58, 1.00	0.29, 1.00
R indices for data with I>2σ(I)	R_1 = 0.0950	R_1 = 0.0929	R_1 = 0.1465
	wR_2 = 0.2791	wR_2 = 0.2810	wR_2 = 0.4303
R indices for all data	R_1 = 0.0992	R_1 = 0.0996	R_1 = 0.1831
	wR_2 = 0.2871	wR_2 = 0.2873	wR_2 = 0.4606
Largest difference peak and hole (e $Å^{-3}$)	0.62/ −0.37	0.67 / −1.16	0.93/ −0.95

2.4.7 Fluorescence measurements

Fluorescence spectra were recorded with Horiba Scientific Fluoromax-4 Spectrofluorimeter. Spectra were corrected for detector and grating efficiencies using FluorEssence, the inhouse software of fluorimeter. The fluorescence measurements of ligands were done with a DMF solution of ligands with an excitation wavelength of 390 nm. The fluorescence of MOFs was measured with a DMF suspension of MOF nanocrystals with an excitation wavelength of 390 nm. For the titration experiment, 200 μL of 0.1 M solution of guest was added to a suspension of 3 mg MOF nanocrystals in 3 mL of dichloromethane in 20 μL portions.

2.4.8 Gas adsorption isotherms

Low pressure gas adsorption isotherms were measured by a volumetric method using a Quantachrome Autosorb iQ2 instrument. All adsorption measurements used ultra-high purity gases. Freshly prepared MOF samples were washed four times with acetone and soaked in dry acetone for two hours. The samples were then transferred to a pre-dried and weighed analysis tube. Excess acetone was removed under vacuum and the tube back filled with argon before being heated at 1 °C per minute to 80 °C under vacuum. The sample was then held under a dynamic vacuum at 10^{-6} Torr for 20 hours. Accurate sample masses were calculated using activated samples after backfilling with nitrogen.

BET surface areas were calculated from N_2 adsorption isotherms at 77 K according to the following procedures[186]**:**

1) The isotherm region where $\boldsymbol{v(1 - P/P_0)}$ increases versus $\boldsymbol{P/P_0}$, where $\boldsymbol{v}$ is the amount of N_2 adsorbed, was identified.

2) Within this isotherm region, sequential data points that led to a positive intercept in the plot of $\frac{\boldsymbol{P/P_0}}{\boldsymbol{v(1-P/P_0)}}$ against $\boldsymbol{P/P_0}$, were found. This plot yields a slope $\boldsymbol{a}$, and a positive intercept $\boldsymbol{b}$.

3) The BET equation was used to calculate the apparent surface area.

$$\frac{1}{v[(p_0/p) - 1]} = \frac{c - 1}{v_m c}\left(\frac{p}{p_0}\right) + \frac{1}{v_m c}$$

where

$$v_m = \frac{1}{a + b} \quad \text{and} \quad c = 1 + \frac{a}{b}$$

The BET surface area is

$$S_{BET} = \frac{v_m \cdot N \cdot s}{V \cdot m}$$

Where N is Avogadro's number, s the adsorption cross section of the adsorbing species (0.162 nm^2 for N_2), V the molar volume of the adsorbate gas, and m the mass of the solid sample.

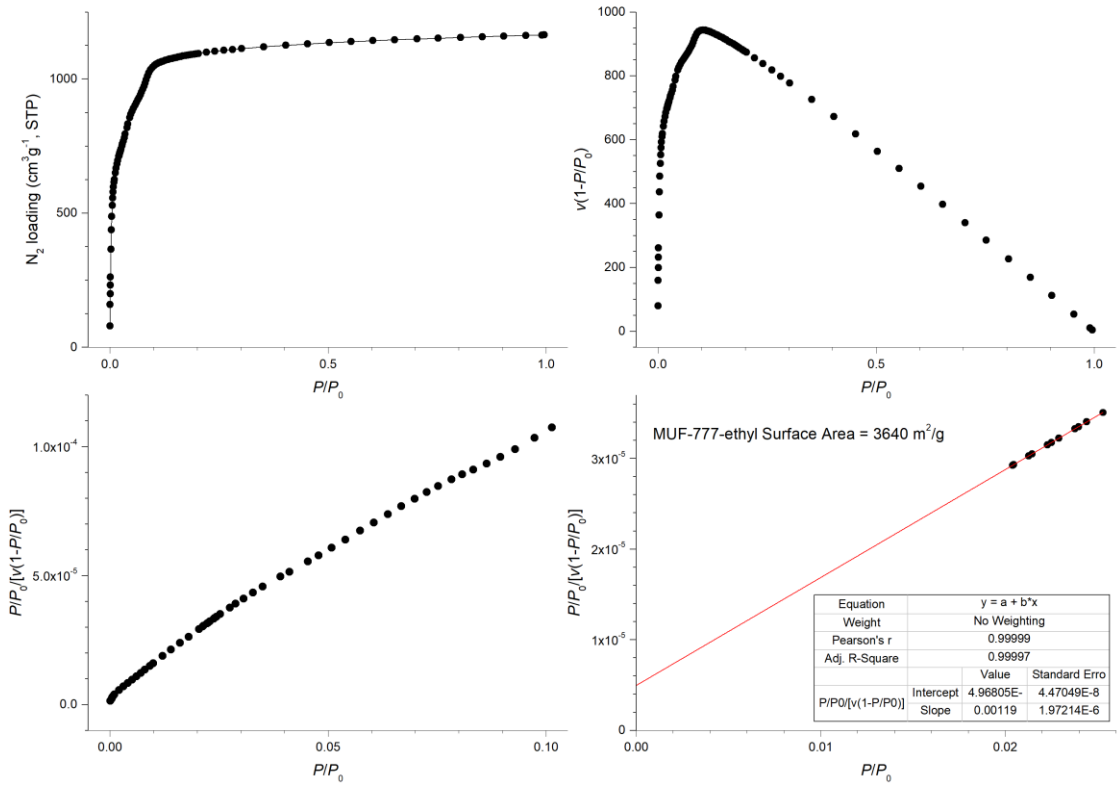

Figure 2. 24 Nitrogen adsorption isotherm at 77 K and BET surface area plots for MUF-777-ethyl.

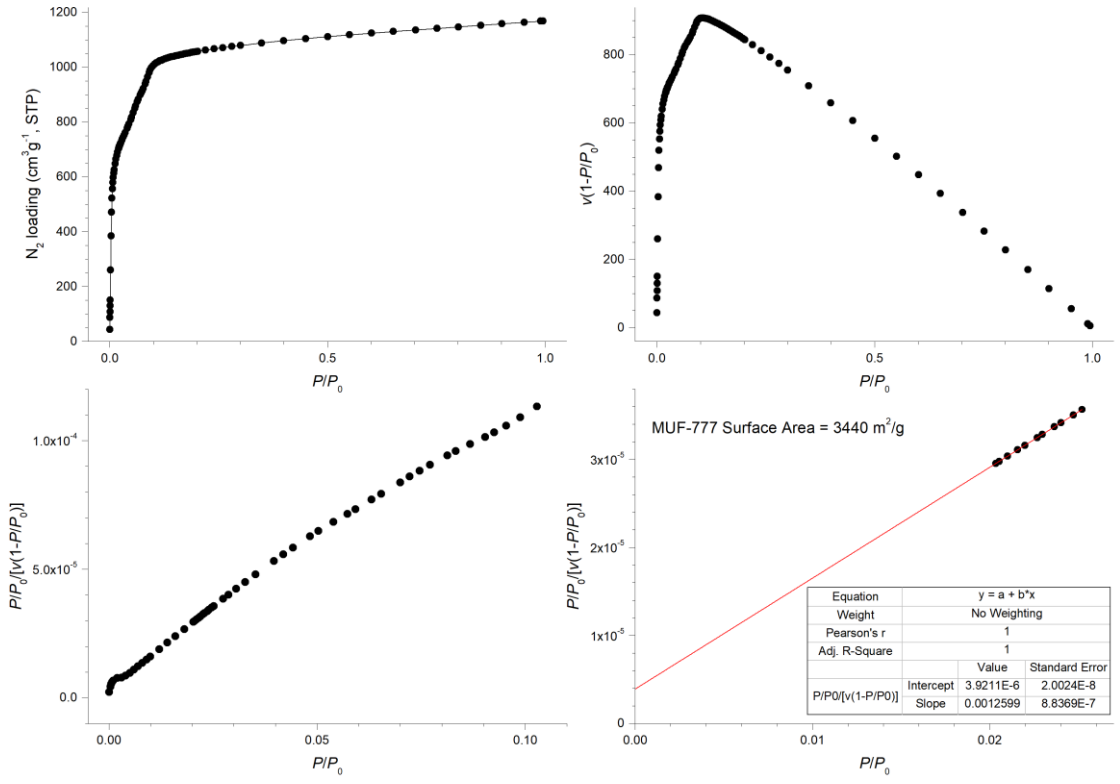

Figure 2. 25 Nitrogen adsorption isotherm at 77 K and BET surface area plots for MUF-777.

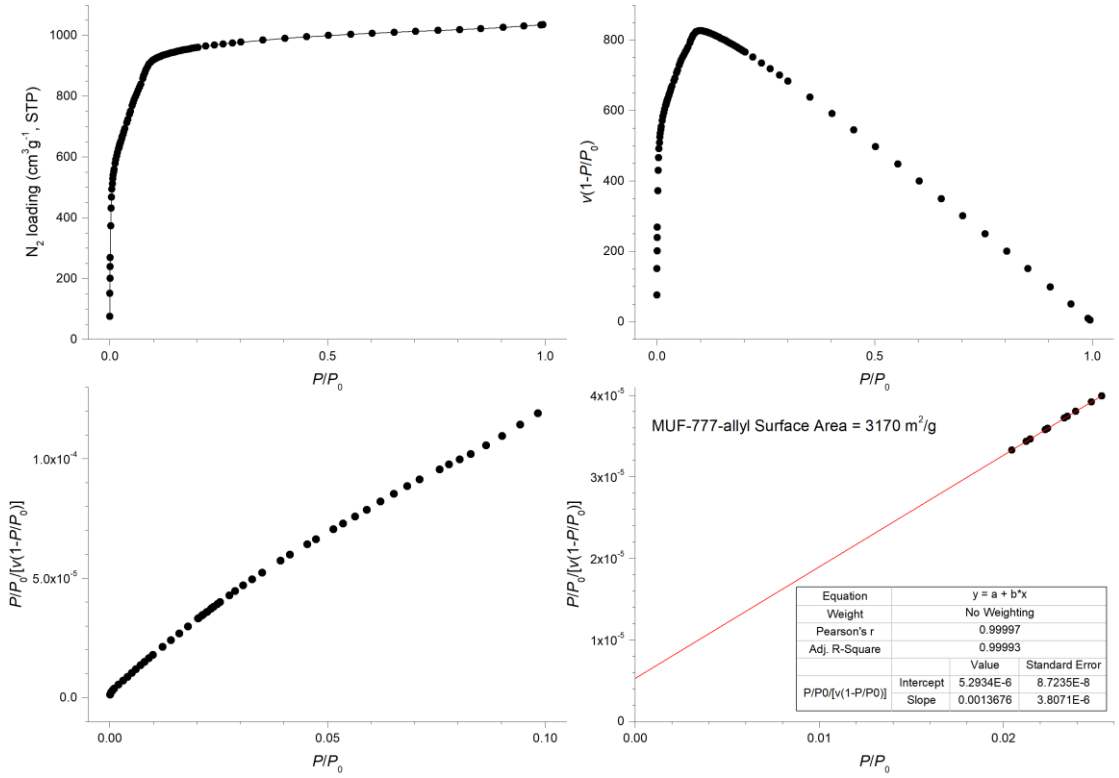

Figure 2. 26 Nitrogen adsorption isotherm at 77 K and BET surface area plots forMUF-777-allyl.

2.4.9 Thermogravimetric analysis (TGA)

Thermogravimetric analyses were performed on a TA Instruments Q50 instrument. Freshly prepared MOF samples were first washed with DMF and then with acetone. After acetone was decanted, the samples were dried under vacuum. Samples were then transferred to an aluminium sample pan and then measurements were performed under an N_2 flow with a heating rate of 5 °C/min.

Chapter 3 Catalysis in MUF-777 and MUF-77 Systems

3.1 Introduction

Catalysis was one of the earliest demonstrated applications in the field of metal-organic frameworks.[187] The high surface areas, tuneable pore sizes, and periodic structures of MOFs offer many advantages to their use in catalysis. Their pores can be engineered to prepare a variety of structures for different catalytic transformations.[188-190] The periodic structure of MOFs allow a uniform dispersion of active site throughout the framework. Moreover, their well-defined structures are important for understanding the mechanism and relationship between structure and catalytic performance.[191]

The advantage of multicomponent MOFs over other materials is that their complex yet well-ordered structures provide an opportunity to create pockets with a precise three-dimensional array of different functional groups, as the Telfer group previously reported with MUF-7, MUF-77 and MUF-777 families of frameworks.[48, 82, 192] To prepare catalytically-active analogues of these materials, the pockets can be designed to contain both an *activator site*, which activates and pre-organizes substrates by covalent or H-bonding to initiate a reaction, and *modulator sites* that can influence the reaction rate and product selectivity through noncovalent interactions.[193-194] By systematic variation of multiple linkers it is possible to prepare a series of catalysts to optimize turnover frequencies and stereoselectivities for a number of reactions. The design and preparation of ligands with activator and modulator sites can be guided by small-molecule catalyst and supramolecular catalyst and enzymes.[194-199] Importantly, the stereoselectivity of the catalyst could be generated not only by a chiral activator but also by a chiral modulator. In addition, MOFs with multiple activator sites could be prepared for synergistic and sequential catalysis.[75, 127]

In 2017, the Telfer group reported a series of MUF-77 analogues which were used as a catalyst system for the asymmetric aldol reaction between acetone and 4-nitrobenzaldehyde. In their MOF system one of the two ditopic linkers bears a proline unit as the activator site while the other two ligands are functionalized with different groups as modulators as shown in Figure 1. An important feature of a MUF-77 catalyst is that all activator sites (proline units) are located in an identical microenvironment as a result of the well-ordered structure of the framework. Thus, this series of MOF can be considered as single-site[200-201] catalysts. Another important feature is that the catalytic pore is suitable for further modifications through modulator linkers. The group observed that modulator groups have a significant influence on both the reaction

rate and the stereoselectivity. For instance, the enantiomeric excess (ee) of the product is enhanced by replacing the parent linker, bpdc, with the dppdc linker. It was also observed that, when bdc-Pro is used as an activator site and truxene linkers with short alkyl chains as modulators, the *S* enantiomer of the product is produced in excess. However, the *R* enantiomer is produced in excess when truxene linkers with longer alkyl chains are used. These results demonstrate that after introducing functional groups to ligands, the framework still has enough pore volume for accommodation and diffusion of catalysis substrates and products. Moreover, it suggests that the activator and modulator sites in the catalytic pocket are positioned in such way that the interaction between the modulator and reaction participants can be received by the catalytic unit.[84, 202]

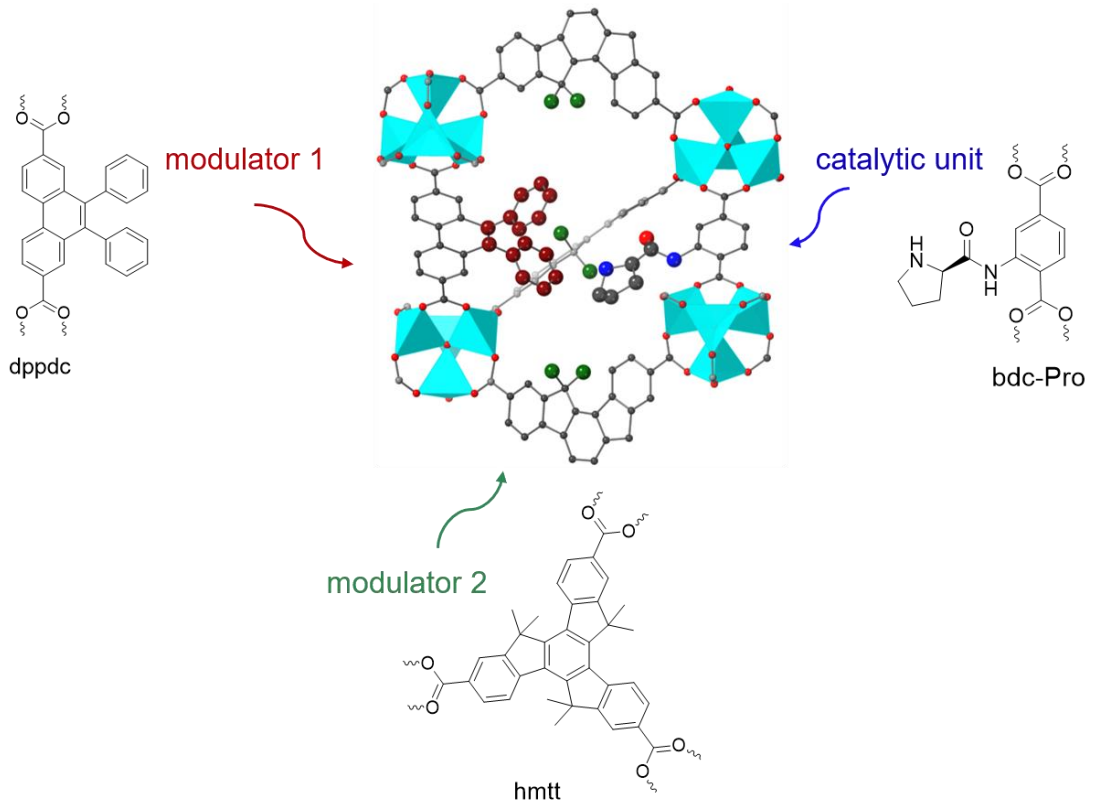

Figure 3. 1 An illustration of ligands with a catalytic unit and modulators and their positions in catalytic pocket of MUF-77.

S-Proline is a naturally available organocatalyst which can accelerate a variety of asymmetric organic reactions, such as Mannich, Michael, Diels-Alder, and aldol reactions, under homogeneous conditions.[203-205] Its derivatives have been incorporated into MOF structures to create heterogeneous catalysts, via coordination on open metal sites,[206] post-synthetic click reaction,[207] and post-synthetic amide coupling.[208] In addition, Telfer group

demonstrated the incorporation of a proline unit through chiral functionalization of linkers prior to MOF synthesis followed by thermal deprotection.[83]

In Chapter 2, I described the synthesis of MUF-777 series from tritopic triazatruxene and ditopic bpdc and bdc ligands. In this chapter, I present two analogues of MUF-777: $[Zn_4O(tat\text{-}ethyl)_{4/3}(bpdc\text{-}Pro)_{1/2}(bdc)_{1/2}]$ and $[Zn_4O(tat\text{-}ethyl)_{4/3}(bpdc)_{1/2}(bdc\text{-}Pro)_{1/2}]$, which contain catalytically-active bpdc-Pro and bdc-Pro ligands respectively. Then, I show how three carbazole based dicarboxylic acid ligands can be used in place of bpdc in making analogues of MUF-77, in which bdc-Pro is used as catalytically-active group. Further, I use these MOFs as catalysts for the asymmetric aldol reaction of acetone and 4-nitrobenzaldehyde.

3.2 Results and discussion

3.2.1 Synthesis and characterization of ligands

Dimethyl 9H-carbazole-2,7-dicarboxylate[209] (Me_2cdc) was prepared according to a literature procedure. Three functional groups were chosen as additional substituents on the nitrogen atom of the carbazole linker. The reaction of Me_2cdc with appropriate alkyl bromide compound in DMSO at 70 °C afforded quantitative yields of Me_2ecdc, $Me_2cychcdc$ and Me_2mcdc, respectively (Scheme 3.1).

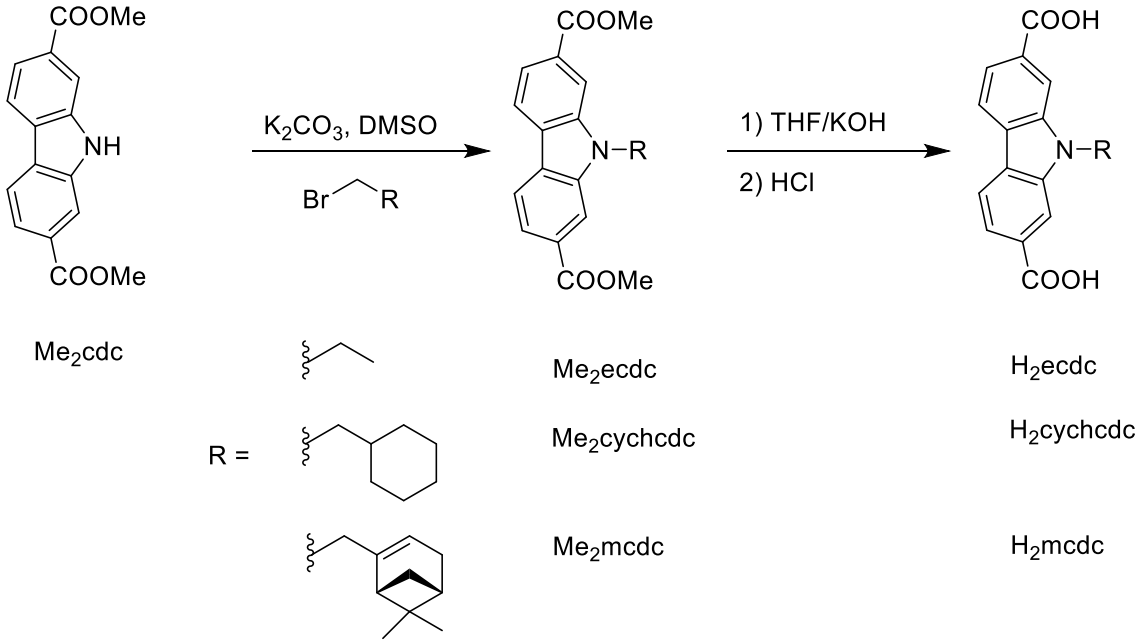

Scheme 3. 1 Synthetic route to the carbazole-based ligands.

These compounds were then hydrolysed to obtain the carboxylic acids H_2ecdc, H_2cychcdc and H_2mcdc. Me_2cychcdc and Me_2mcdc were purified by column chromatography. Me_2ecdc and the corresponding carboxylic acids were obtained in acceptable purity, as shown by NMR spectroscopy and mass spectrometry. Detailed synthetic procedures and characterization of all ester and carboxylic acid compounds are available in the experimental section and Electronic Appendix B.

3.2.2 Synthesis and characterization MUF-777 catalysts

Our first target was to synthesize MUF-777 analogues in which a chiral, enantiopure, catalytically-active proline unit was appended to bpdc or bdc ligands. This was achieved by using a thermolabile protecting group strategy. This strategy has previously been developed by our group.[83, 173-174] The first step is preparation of a precursor framework which contains a *tert*-butoxycarbonyl (Boc) protected proline group (Figure 3.2). This prevents the prolinyl group from taking part in undesired reactions during MOF synthesis. The Boc group then can be removed by a post-synthetic deprotection process which is simply done by heating the framework at <200 °C under vacuum. During this process, the Boc group decomposes to CO_2 and isobutylene gases which escape from the framework to generate a free proline group.

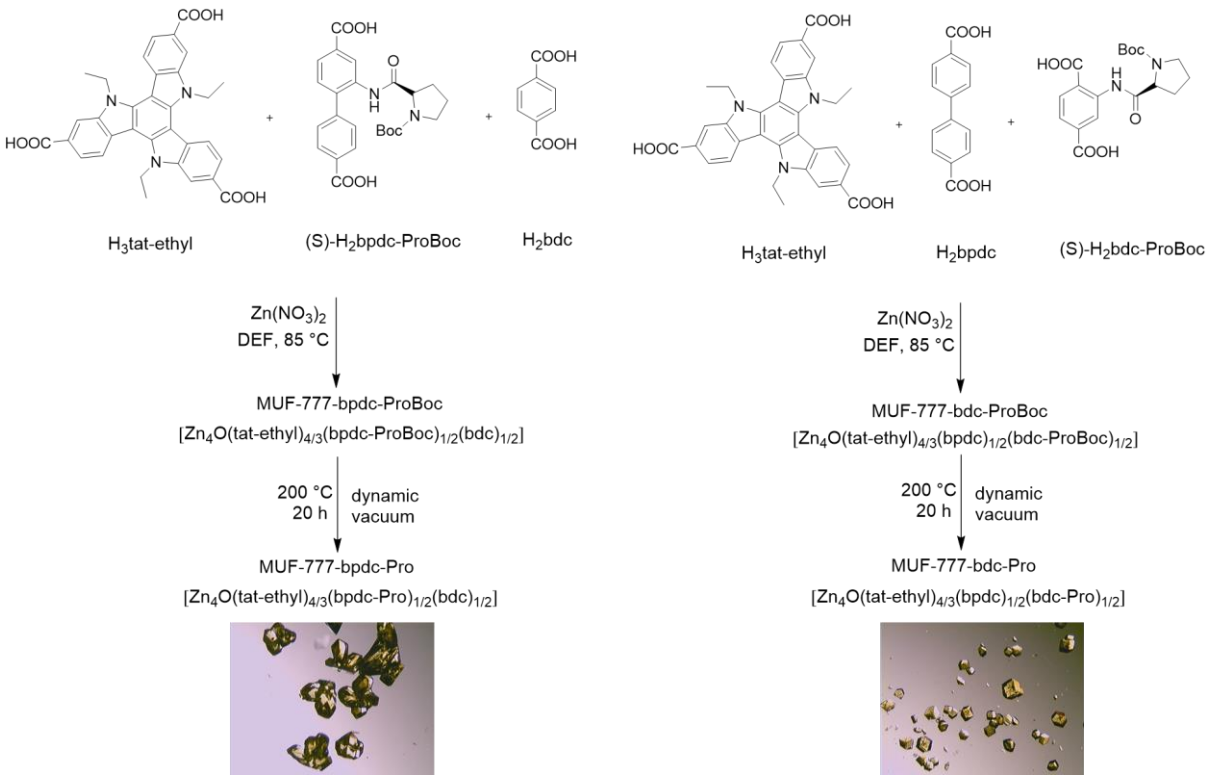

Figure 3. 2 Synthetic route to MUF-777-bpdc-Pro and MUF-777-bdc-Pro and their optical microscopy images.

A solvothermal reaction of H_3tat-ethyl, (*S*)-H_2bpdc-ProBoc, H_2bdc and zinc nitrate in DEF produced yellow crystals. Similar to other members of the MUF-777 series, the crystals fully extinguish at all rotational positions under crossed polarizers on an optical microscope, indicating that they belong to a cubic crystal system. The powder X-ray diffraction patterns of these crystals is almost identical to that of MUF-777-ethyl indicating that this MOF is isostructural to MUF-777 (Figure 3.3). ^{1}H NMR spectrum of a digested sample shows a ratio of 8:3:3 of the three ligands which suggests that the framework has a formula of $[Zn_4O(\text{tat-ethyl})_{4/3}(\text{bpdc-ProBoc})_{1/2}(\text{bdc})_{1/2}]$ (Figure 3.4). This material was termed MUF-777-bpdc-ProBoc.

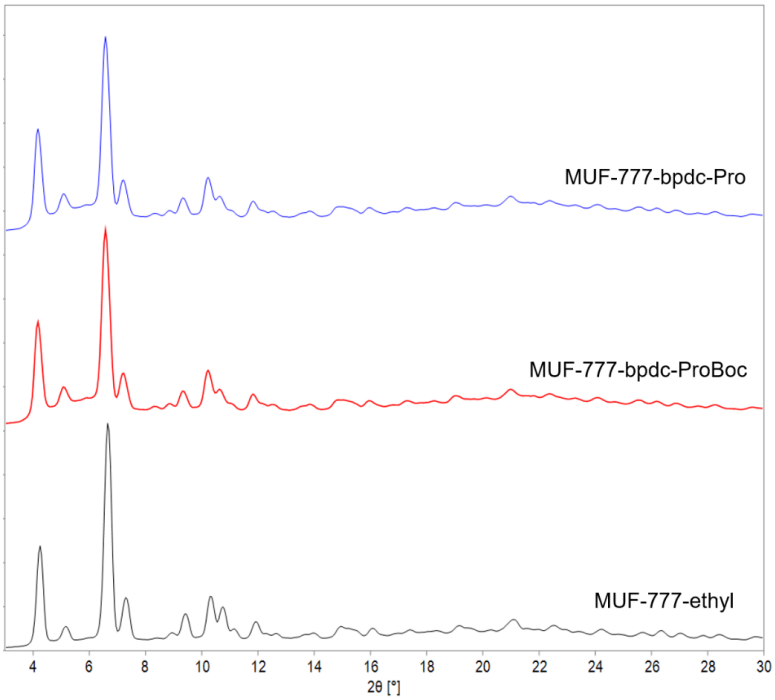

Figure 3. 3 PXRD patterns of MUF-777-ethyl, MUF-777-bpdc-ProBoc and MUF-777-bpdc-Pro.

To obtain the framework containing catalytically-active proline sites, MUF-777-bpdc-ProBoc was thermolyzed at 200 °C for 20 hours under a dynamic vacuum. This process does not change the optical transparency of the sample. ^{1}H NMR spectroscopic analysis of a digested sample of thermolyzed MOF following thermolysis demonstrates that the Boc protecting group is completely removed. Clear evidence for this is the disappearance of the two peaks at 1.34 and 1.36 ppm in the ^{1}H NMR spectrum, which belong to the *tert*-butyl groups of the two conformers of (S)-H_2bpdc-ProBoc in solution (Figure 3.4). The PXRD patterns of MUF-777-

bpdc-Pro is nearly identical to that of MUF-777-bpdc-ProBoc, which suggest that the framework retains its crystallinity and phase-purity (Figure 3.3).

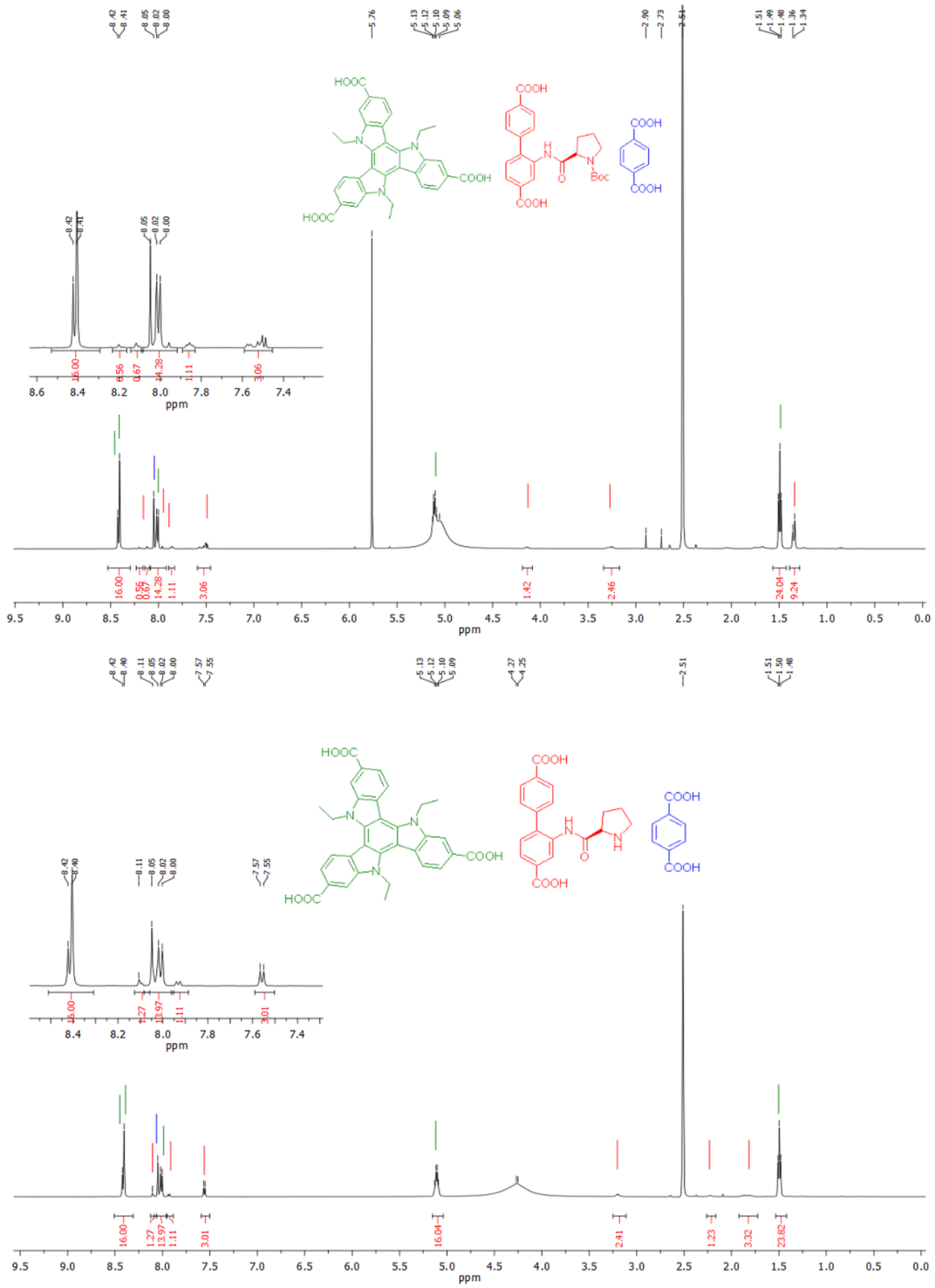

Figure 3. 4 Upper: The ^{1}H NMR spectrum of digested MUF-777-bpdc-ProBoc showing the integrals that match with the formula $[Zn_4O(tat\text{-}ethyl)_{4/3}(bpdc\text{-}ProBoc)_{1/2}(bdc)_{1/2}]$. Note that H_2bpdc-ProBoc shows two sets of proton peaks due its two conformers in solutions and these peaks disappear after thermolysis. Lower: The ^{1}H NMR spectrum of digested MUF-777-bpdc-Pro showing the integrals that match with the formula $[Zn_4O(tat\text{-}ethyl)_{4/3}(bpdc\text{-}Pro)_{1/2}(bdc)_{1/2}]$.

The framework MUF-777-bdc-ProBoc was prepared using similar procedure to that of MUF-777-bpdc-ProBoc (Figure 3.2). This framework then was thermolyzed to obtain catalytically-active MUF-777-bdc-Pro. The identity and phase purity of this material was confirmed by PXRD analysis (Figure 3.5). ^{1}H NMR spectra of digested samples of MUF-777-bdc-ProBoc and MUF-777-bdc-Pro demonstrate that the ratio of the ligand integrals matches the expected framework stoichiometry (Figure 3.6). This material also maintains its optical transparency after the thermolysis process.

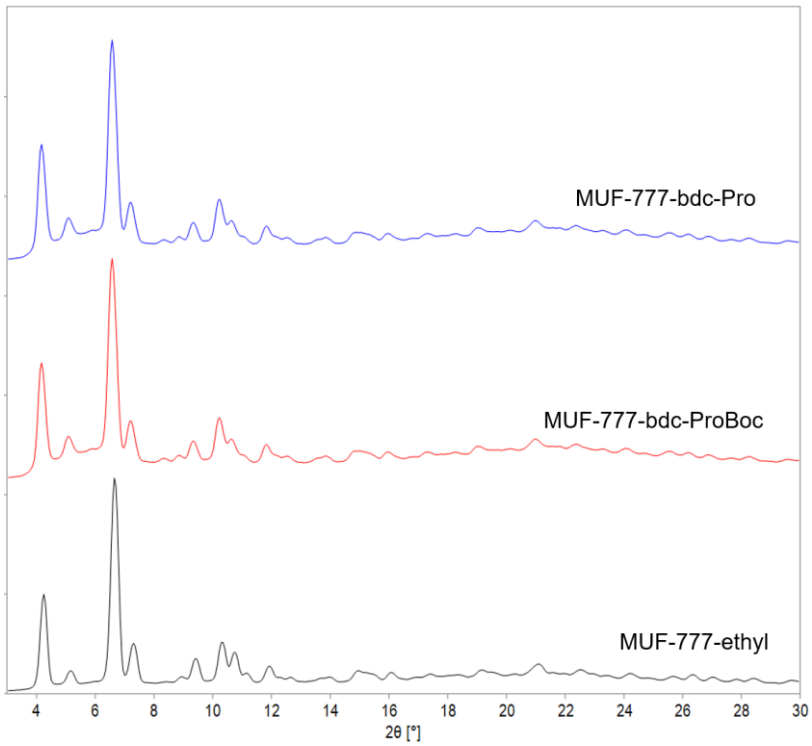

Figure 3. 5 PXRD patterns of MUF-777-ethyl, MUF-777-bdc-ProBoc and MUF-777-bdc-Pro.

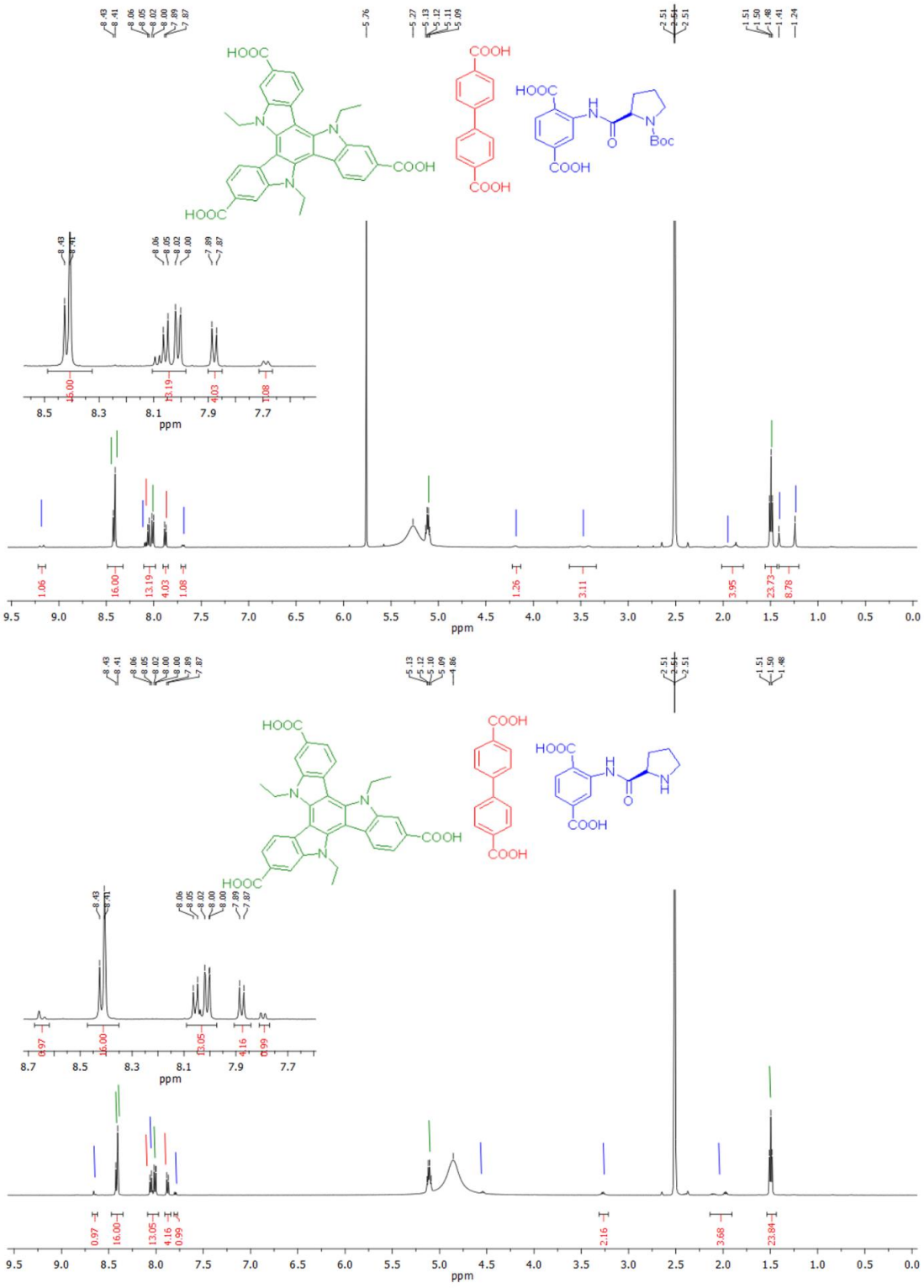

Figure 3. 6 Upper: The ^{1}H NMR spectrum of digested MUF-777-bdc-ProBoc showing the integrals that match with the formula $[Zn_4O(tat\text{-}ethyl)_{4/3}(bpdc)_{1/2}(bdc\text{-}ProBoc)_{1/2}]$. Note that H_2bdc-ProBoc shows two sets of proton peaks due its two conformers in solutions and these peaks disappear after thermolysis. Lower: The ^{1}H NMR spectrum of digested MUF-777-bdc-Pro showing the integrals that match with the formula $[Zn_4O(tat\text{-}ethyl)_{4/3}(bpdc)_{1/2}(bdc\text{-}Pro)_{1/2}]$.

3.2.3 Synthesis and characterization MUF-77 catalysts

As shown in Figure 3.7, three MUF-77 variants, termed MUF-77-cat-1**,** MUF-77-cat-2 and MUF-77-cat-3, were also synthesized. To obtain MUF-77-cat-1, first, the precursor framework was synthesized by a solvothermal reaction of H_3hmtt, H_2ecdc, (S)-H_2bdc-ProBoc and zinc nitrate in DEF. The formula of this framework was determined to be $[Zn_4O(hmtt)_{4/3}(ecdc)_{1/2}(bdc\text{-}ProBoc)_{1/2}]$ by ^{1}H NMR spectroscopy of a digested MOF sample (Figure 6). The framework was then heated at 200 °C for 20 hours under dynamic vacuum to completely remove the Boc protecting group, to obtain MUF-77-cat-1 with a formula of $[Zn_4O(hmtt)_{4/3}(ecdc)_{1/2}(bdc\text{-}Pro)_{1/2}]$ as confirmed by ^{1}H NMR spectroscopy (Figure 3.8). PXRD patterns of these two frameworks are almost identical to that of parent framework, MUF-77-methyl, (Figure 3.9). This indicates that they share the same overall framework topology. It also reveals that the thermolysis process does not change the phase identity and purity of the framework.

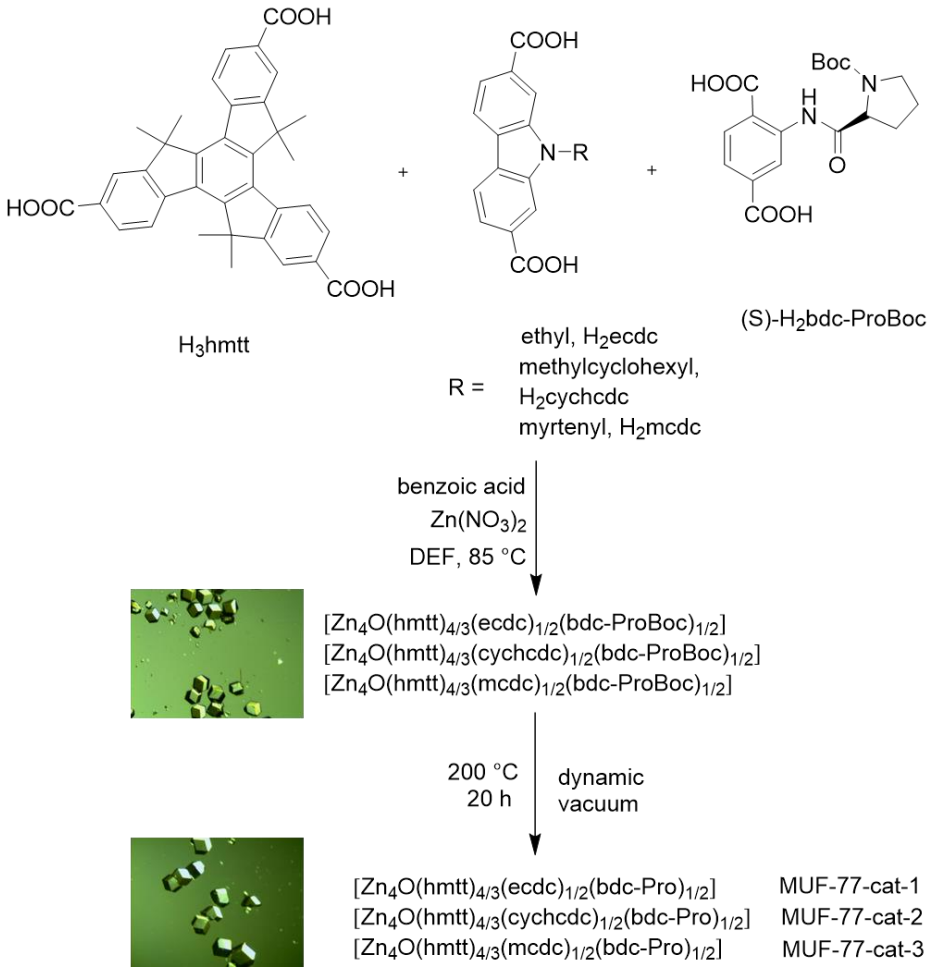

Figure 3. 7 Synthetic route to MUF-77 catalysts and optical microscopy images of MUF-77-cat-1.

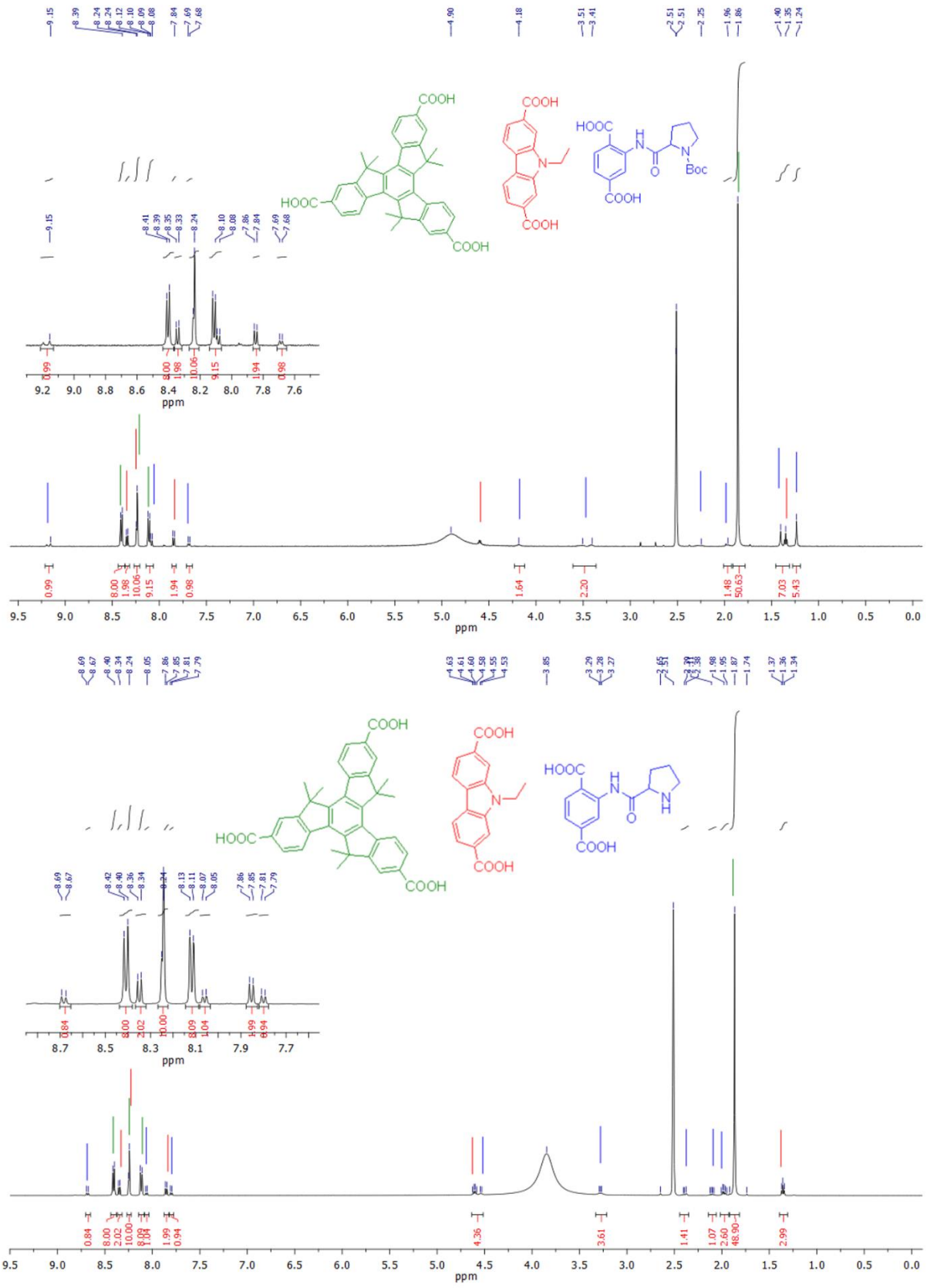

Figure 3. 8 ^{1}H NMR spectra of digested $[Zn_4O(hmtt)_{4/3}(ecdc)_{1/2}(S\text{-}bdc\text{-}ProBoc)_{1/2}]$ (upper) and MUF-77-cat-1 (lower). The measured integrals correspond to the framework stoichiometry. Disappearance of the two proton peaks of the Boc group at 1.24 and 1.41 indicate that thermolysis is completed.

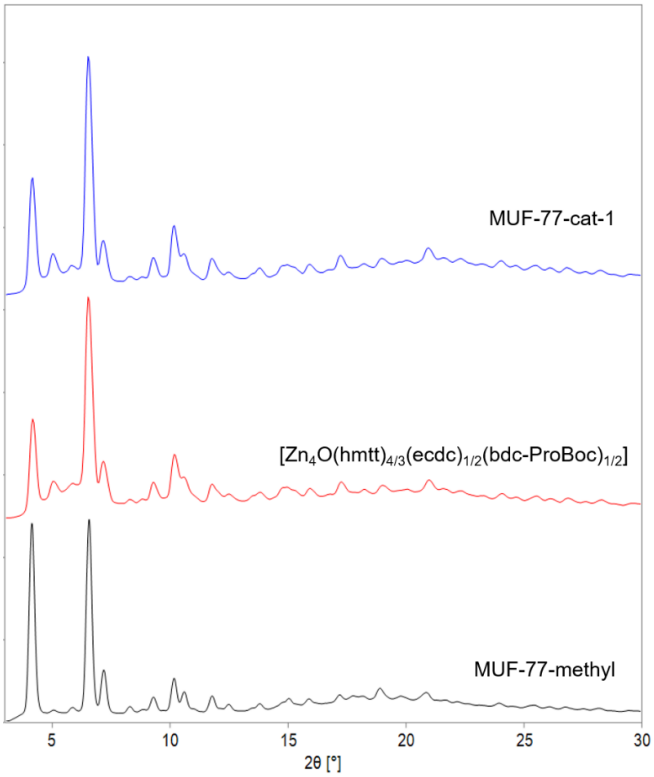

Figure 3. 9 PXRD patterns of MUF-77-methyl, $[Zn_4O(hmtt)_{4/3}(ecdc)_{1/2}(bdc\text{-}ProBoc)_{1/2}]$ and MUF-77-cat-1.

Optical microscopy images show that MUF-77-cat-1 retains its transparency after thermolysis which implies that the thermolysis of $[Zn_4O(hmtt)_{4/3}(ecdc)_{1/2}(bdc\text{-}ProBoc)_{1/2}]$ is a single-crystal-to-single-crystal transformation (Figure 3.7). The SCXRD data of MUF-77-cat-1 was collected at 133 K. The crystal displayed a very good X-ray diffraction pattern which produced good refinement statistics (Table 3.5). Due to the presence of the chiral proline unit, the crystal structure of MUF-77-cat-1 is expected to have a chiral space group. In fact, the chiral space group *P*23 was a possible choice. However, superior statistics, such as the $|E^2 - 1|$ and CFOM, were given by the centrosymmetric *P*m-3 space group, which is the same group as the parent framework, MUF-77-methyl. Therefore, the refinement was carried out in *P*m-3. The bad poor statistical values in *P*23 might be a result of the positional and rotational disorder of the proline unit which means that its chirality does not impact significantly on the diffraction intensities.

As shown in Figure 3.10, the proline unit is situated inside a tetrahedral cavity which is defined by four hmtt ligands, one carbazole ligand and one bdc ligand. The ethyl group on the carbazole ligand is facing the proline unit, while a pair of methyl groups on each hmtt ligand are also located in the same cavity. All proline units occupy the same well-defined local

environment throughout the framework due to well-ordered structure of MUF-77-cat-1. Therefore, proline unit could be considered as a single site catalyst.[201] This is an important feature of MUF-77-cat-1 having influence on producing a uniform catalytic outcome.

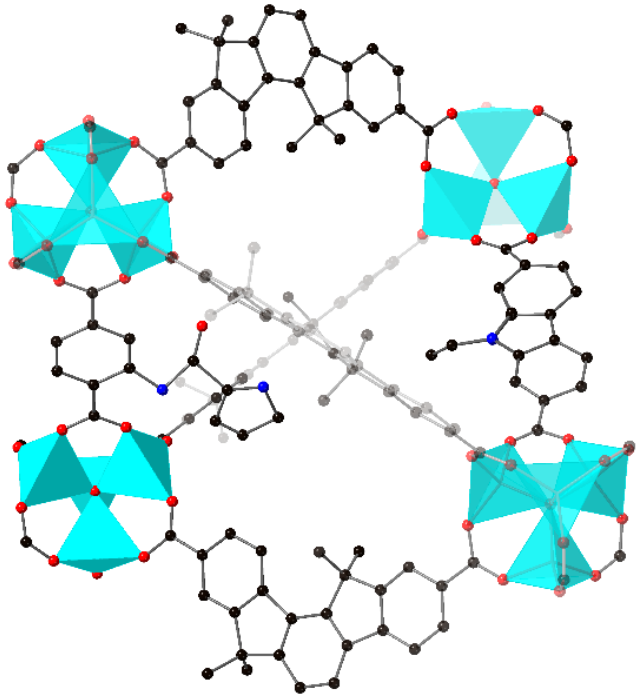

Figure 3. 10 A view illustrating the tetrahedral cavity and positions of activator, and modulator groups in the crystal structure MUF-77-cat-1. Atom colors: carbon: black, oxygen: red, nitrogen: blue, zinc: cyan. Hydrogen atoms are omitted for clarity.

Similarly, $[Zn_4O(hmtt)_{4/3}(cychcdc)_{1/2}(bdc\text{-}ProBoc)_{1/2}]$ and MUF-77-cat-2 were characterized. Their detailed syntheses, ^1H NMR spectra and PXRD patterns are available in Electronic Appendix B. Both materials are isostructural and share the same overall framework topology with MUF-77-cat-1 as confirmed by PXRD analysis. The framework stoichiometry of this material was confirmed by ^1H NMR spectroscopic analysis of digested samples.

Next, $[Zn_4O(hmtt)_{4/3}(mcdc)_{1/2}(bdc\text{-}ProBoc)_{1/2}]$ was synthesized and characterized. The thermolysis conditions mentioned above were used to obtain MUF-77-cat-3. The structure of the thermolyzed MOF matches its precursor framework, as determined by PXRD. However, the ^1H NMR spectroscopic analysis of digested sample of thermolyzed MOF demonstrated that the ratio of ligands integrals does not match the $[Zn_4O(hmtt)_{4/3}(mcdc)_{1/2}(bdc\text{-}ProBoc)_{1/2}]$ stoichiometry. The peaks of H_2mcdc in the aliphatic area are present, as expected for the myrtenyl group, but they have lower integral values than expected. There are also some extra peaks in the aromatic area alongside the peaks of H_2mcdc (Figure 3.11a). This result indicates

that the myrtenyl group on the carbazole ligand is either partially isomerized or expelled under the thermolysis conditions employed for deprotection of the H_2bdc-ProBoc ligand. A potential isomerization process is illustrated in Figure 3.11b. This MOF could be used as a catalyst since there is no problem with the catalytically active ligand. However, the change in the structure of a portion of the mcdc ligand will bring uncertainties to the modulating effect of this ligand on the catalysis. After thermolysis, the framework will contain both the mcdc ligand and new carbazole species by the decomposition of myrtenyl group which will also have some effect on catalysis. Due to this potential source of confusion this material was not explored further.

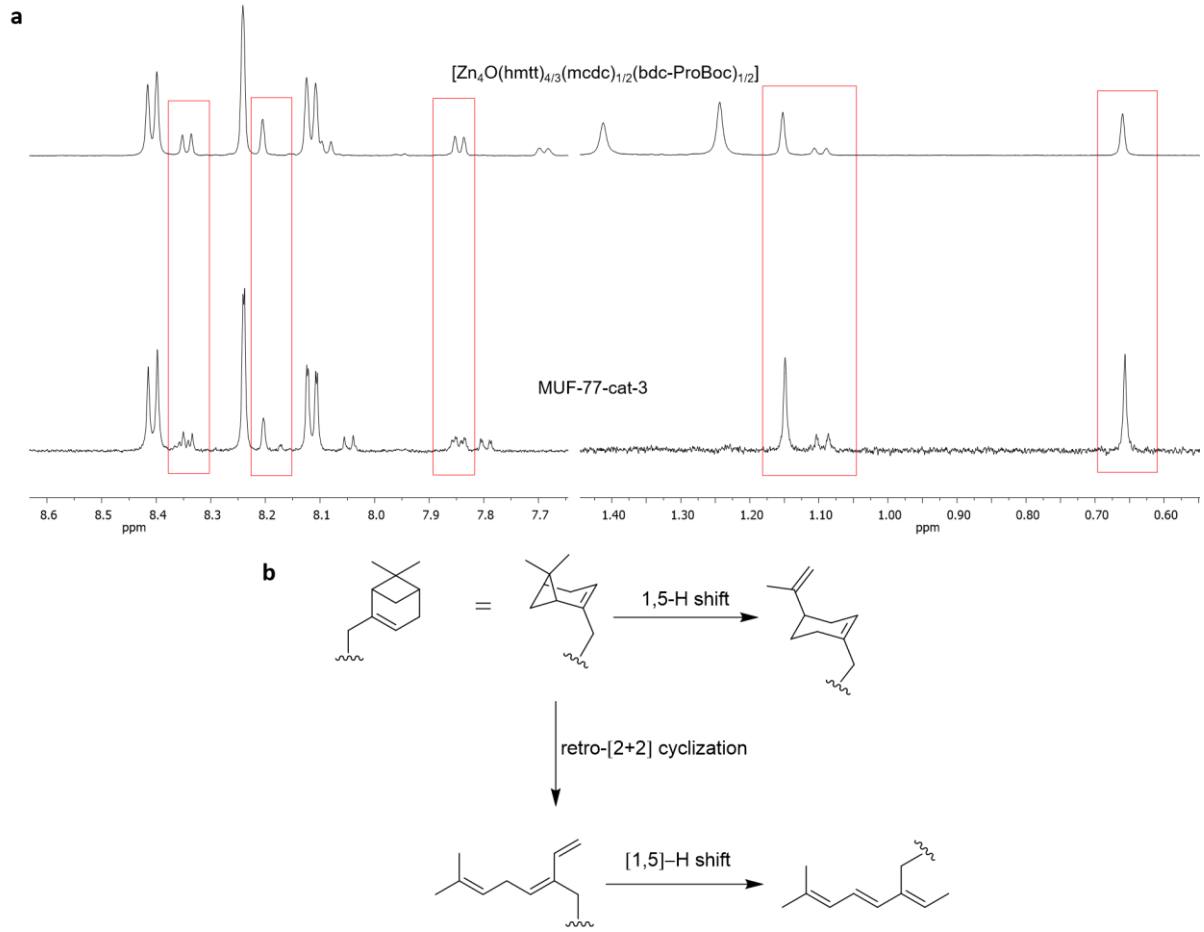

Figure 3. 11 a) Aromatic and aliphatic region of the spectra of digested $[Zn_4O(hmtt)_{4/3}(mcdc)_{1/2}(bdc\text{-}ProBoc)_{1/2}]$ and MUF-77-cat-3. The peaks of the H_2mcdc ligands are shown in red rectangles. b) Schematic illustration for thermal isomerization of the myrtenyl group.[210]

3.2.4 Catalysis studies

The aldol reaction shown in Scheme 3.2 was used to study the catalytic ability of newly synthesized MUF-777 and MUF-77 catalysts. A stock solution of the reagents was prepared by dissolving 4-nitrobenzaldehyde in acetone with 20% water, while the other one was

prepared without water (details are in the experimental section). The condition with 20% of water is the same condition used previously for MUF-77 catalysis.[84] Here, the same condition was used so that catalysis results of MUF-777 system can directly be compared with previously reported results of MUF-77 system. For the catalysis study of new MUF-77 variants, on the other hand, no water was added to the stock solution. Previous MUF-77 derivatives containing bdc-Pro as catalytically active group showed acceptable activities without water, although it was found that the reaction rates increase with addition of water.[84] Nitrobenzene was used as an internal standard for HPLC analysis. No uncatalyzed background reaction was observed over a period of two weeks for the stock solutions. For catalysis reactions, a known amount of MOF crystals was immersed in a known amount of stock solution and the mixture was stood at 20 °C for 24 hours. The supernatant then was analysed by HPLC using a chiral column.

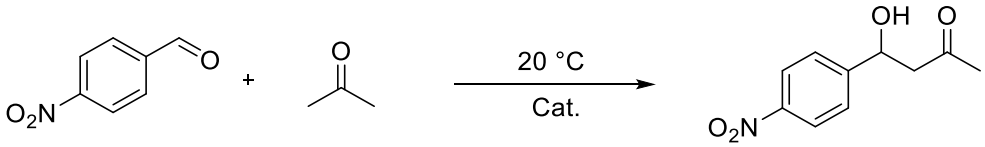

Scheme 3. 2 The asymmetric aldol reaction catalyzed by MUF-777-bpdc-Pro.

3.2.5 Catalysis in MUF-777 system

The catalysis study on MUF-777-bpdc-Pro was conducted using 10% catalyst (moles of proline group with respect to 4-nitrobenzaldehyde) and 1 mL of stock solution containing 20% water. The effect of catalyst loading on catalysis has previously been studied by our group for MUF-77 analogues. In this study, it was found that catalyst loading reaches saturation with around 30 mol % of proline units (with respect to the amount of aldehyde), beyond which the reaction rate does not change with additional catalyst. In the same study, it was also observed that with 10 mol % catalyst loading reasonable conversion could be obtained for the aldol reaction over a period of 24 hours. Therefore, 10 mol % was chosen as a standard catalyst quantity, which is in the typical range for organocatalysts.[84]

We found that MUF-777-bpdc-Pro catalyses the asymmetric aldol reaction of 4-nitrobenzaldehyde and acetone and leads to a 38% conversion of the aldehyde to the aldol product over a period of 24 hours (Table 3.1, Entry 1). This result is reproduceable as confirmed by the values in Entry 2. As a control experiment, firstly, we tried the same reaction using MUF-777-bpdc-ProBoc as catalyst and found that this material is catalytically inactive. These observations imply that the deprotected proline unit is the only catalytically-active site in the

framework and no dissolved or leached material from MUF-777-ProBoc is catalytically active. Next, we filtered the catalyst from the reaction mixture and observed that this halts the reaction, which indicates that no catalytically active species (which may have leached from the framework) are present in the reaction solution. This control experiment confirms that the catalysis is heterogeneous. In addition, the catalytic performance of (S)-Me_2bpdc-Pro (an analogue of the (*S*)-H_2bpdc-Pro linker) was tested. Due to the solubility of (S)-Me_2bpdc-Pro under the catalytic reaction conditions, this catalysis test is homogeneous. This provides an opportunity to compare the performance of an activator in heterogeneous and homogeneous conditions. The results revealed that the catalytic ability of molecular catalyst (S)-Me_2bpdc-Pro in homogeneous conditions is almost the same as that of MUF-777-bpdc-Pro in heterogeneous condition (Table 3.1, Entries 1 and 4). This indicates that heterogenization of the catalytic unit in the MOF does not introduce kinetic barriers such as slow diffusion of the substrates or products.

Table 3. 1 Aldol reaction catalysed by MUF-777-bpdc-Pro, MUF-777-bpdc-ProBoc and (S)-Me_2bpdc-Pro.

Entry	Catalyst	H_2O	Cat. loading	Conversion	Rate constant	e.e.
1	MUF-777-bpdc-Pro	20	10	38.8	0.43	9.1
2	MUF-777-bpdc-Pro	20	10	38.3	0.41	9.0
3	MUF-777-bpdc-ProBoc	20	10	-	-	-
4	(S)-Me_2bpdc-Pro	20	10	39.5	0.49	30.0

Reaction conditions: 10 mol % catalyst (proline unit relative to amount of aldehyde), 0.04 M 4-nitrobenzaldehyde with 20 vol % H_2O at 20 °C. Rate constant unit: L mol^{-1} day^{-1}, based on consumption of 4-nitrobenzaldehyde. The result in Entry 4 has been previously reported.[84]

Next, the recyclability of MUF-777-bpdc-Pro was studied. As shown in Figure 3.12, the activity of the catalyst (its calculated rate constant) drops almost by half after the first cycle and shows slight changes over the next four cycles. PXRD measurement of MUF-777-bpdc-Pro after catalysis shows that it is still crystalline. However, this does not necessarily mean that the entire sample is crystalline since any collapsed portion of the structure will not be detectable by PXRD analysis. The decrease in the activity of the catalyst might be a result of partial collapse in the structure which may slow down the diffusion of reactants. ^{1}H NMR

spectroscopic analysis is a powerful technique to determine the type and ratio of organic linkers in the framework. ^{1}H NMR spectrum of a digested MUF-77-bpdc-Pro after catalysis show that the peak integrals belong to bpdc-Pro ligand are lower than expected values by about 20%. Some additional peaks were also observed in the area where the peaks of bpdc-Pro ligand appear. These peaks might be due to the presence of some side products formed.

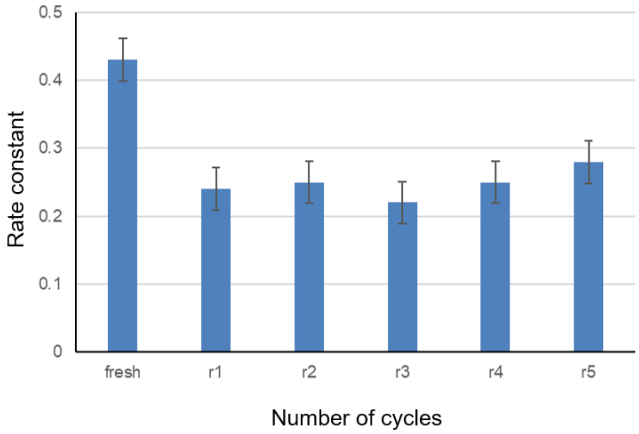

Figure 3. 12 A graph showing the recyclability of catalyst MUF-bpdc-Pro as indicated by the reaction rate constant (L mol^{-1} day^{-1}) under conditions in Entry 1 of Table 1.

The catalytic activity of MUF-777-bdc-Pro was also studied (Table 3.2). One important result is that this catalyst reverses the enantioselectivity compared to both MUF-777-bpdc-Pro and molecular catalyst (S)-Me$_2$bdc-Pro. The reaction rate of homogeneous (S)-Me$_2$bdc-Pro is almost 40 times greater than MUF-777-bdc-Pro. The acceleration of the homogenous reaction might be related to the contribution of carboxymethyl group to noncovalent interactions between the catalytic unit and reactants. Carboxymethyl group is closer to the catalytic unit in the structure of bdc-Pro compared to its position in the structure of bpdc-Pro.

Table 3. 2 Aldol reaction catalysed by MUF-777-bdc-Pro, MUF-777-bdc-ProBoc and (S)-Me_2bdc-Pro.

Entry	Catalyst	H_2O	Cat. loading	Conversion	Rate constant	e.e.
1	MUF-777-bdc-Pro	20	10	12.9	0.11	-26.7
2	MUF-777-bdc-Pro	20	10	9.8	0.10	-29.3
3	MUF-777-bdc-ProBoc	20	10	-	-	-
4	(S)-Me_2bdc-Pro	20	10	98.3	3.98	8.9

Reaction conditions: 10 mol % catalyst (proline unit relative to amount of aldehyde), 0.04 M 4-nitrobenzaldehyde with 20 vol % H_2O at 20 °C. Rate constant unit: L mol^{-1} day^{-1}, based on consumption of 4-nitrobenzaldehyde. The result in Entry 4 has been previously reported.[84]

In Table 3.3, the catalysis results from MUF-777-bpdc-Pro and MUF-777-bdc-Pro are compared with two catalysts that belong to MUF-77 family. The difference between MUF-777-bpdc-Pro and MUF-77-bpdc-Pro is their tritopic linkers (tat-ethyl and hett). From the catalysis results, it is clear that this difference has a significant effect on both reaction rate and enantioselectivity. MUF-777-bpdc-Pro accelerates the reaction greater than MUF-77-bpdc-Pro. On the other hand, the conversion for MUF-777-bdc-Pro is much lower than the conversion for MUF-77-bdc-Pro. For both catalyst families the change of the position of the catalytic proline site from bpdc to bdc ligand reverse the enantioselectivity. However, this relocation decreases the conversion for MUF-777, while it increases the conversion for MUF-77.

The structural analyses for MUF-77 and MUF-777 catalysts showed that these frameworks are well-ordered and retain the topology of their parent framework. This means that the activator sites (prolinyl groups) on the linkers are located in precise positions and have identical microenvironment in the framework. Therefore, these materials can be considered as single-site catalysts. This is important for understanding the structure-activity of these materials. Previously, researchers reported MOF catalysts in which the activity of catalytic pockets could be tuned by modifying pore environments.[211-212] However, due to disorder and defects in these structures it is not easy to correlate the reaction outcome with framework structures. In MUF-77 and MUF-777 systems, on the other hand, catalytic pores can be programmed while retaining the parent framework topology without defect and disorder. Similar pore design strategy has rarely been reported. Long *at al.* reported a series of well-ordered Fe-MOF-74 analogues in which alkyl and fluoro groups located adjacent to the catalytic metal sites.[135] They

demonstrated that the functional groups have significant effect on the catalytic cyclohexane oxidation reaction.

Table 3. 3 Aldol reaction catalyzed by MUF-777-bpdc-Pro, MUF-777-bdc-Pro, MUF-77-bpdc-Pro and MUF-77-bdc-Pro.

Catalyst	Catalyst linker set	Cat. loading	Conversion	e.e.
MUF-777-bpdc-Pro	tat-ethyl/bpdc-Pro/bdc	10	38.8	9.1
MUF-777-bdc-Pro	tat-ethyl/bpdc/bdc-Pro	10	12.9	-26.7
MUF-77-bpdc-Pro	hett/bpdc-Pro/bdc	10	34.0	17.0
MUF-77-bdc-Pro	hett/bpdc/bdc-Pro	10	55.3	-3.7

The catalysis study on MUF-777 revealed that the prolinyl group remains catalytically active upon being attached to the framework. The study also showed that modulator groups have significant effect on the outcome of the asymmetric aldol reaction. Moreover, it demonstrated that stereochemical reversal in enantioselectivity can be achieved by altering the position of the activator in the framework. Inversion of enantioselectivity is a demanding challenge in asymmetric catalysis,[213] because it provides an opportunity to obtain both enantiomers of a reaction product by using only one enantiomer of the catalyst. Achieving a reversal in enantioselectivity by heterogenization of a homogeneous catalyst in a MOF has rarely been observed.[214-215] The advantage of using a multicomponent MOF is that it offers multiple possible sites for installing catalytic units and modulators. This make the framework suitable for installing different functional groups as well as altering the position of each functionality. As demonstrated by MUF-77 and MUF-777 catalysts, by tuning the position of the activator in the framework, the innate enantioselectivity of the catalyst can be reversed. This is also possible by achiral modulator groups as it will be discussed in the next section.

3.2.6 Catalysis in MUF-77 system

For this section, we were interested in the effect of different modulator sites appended to carbazole ligands on the outcome of the aldol reaction. As shown by the single crystal structure of MUF-77-cat-1 earlier, in the catalytic pocket, the ethyl group on the carbazole ligand points

towards the interior of the tetrahedral cavity and faces the activator (proline unit) on the bdc linker. Such a pore environment may be suitable for simultaneous noncovalent interactions between the activator and modulator sites with the reaction participants. Here, the effect of two groups (ethyl and methylcyclohexyl) were studied. Because these groups are hydrophobic and they differ by their sizes, their catalytic outcome could provide information about the effect of hydrophobicity and size of the modulator on catalysis. Moreover, we thought the result for MUF-77-cat-3 would be interesting since the modulator for this catalyst is a chiral group (myrtenyl) on the carbazole ligand. A chiral modulator could potentially either enhance or suppress the enantioselectivity of the chiral activator. However, unfortunately this group partially decomposed during thermolysis conditions, thus the catalysis result for MUF-77-cat-3 is not presented in this section.

The catalysis study involving MUF-77-cat-1 and MUF-77-cat-2 was performed using 10% catalyst (moles of proline group with respect to 4-nitrobenzaldehyde) and 1 mL of stock solution. No water was added to the stock solution. As shown in Table 3.4, these two catalysts can catalyze the aldol reaction. MUF-77-cat-2 accelerates the reaction to a greater extent than MUF-77-cat-1. In addition to the difference in the reaction rate, interestingly, the enantioselectivity is reversed when methyl cyclohexyl is appended to the carbazole ligand in place of ethyl group. Inversion of enantioselectivity was observed in MUF-777 catalysts (in previous section) and in some other MUF-77 variants when the position of activator site changed from the bpdc linker to the bdc linker. In previous MUF-77 variants, it was observed that long alkyl chains, such as hexyl and octyl, on the truxene linker also can both increase the reaction rate and induce enantioselectivity reversal. Based on these observations, it can be said that the size of modulators, which essentially defines the size of the catalytic pocket along with the activator, is important for creating beneficial interactions with the reaction participants.

Table 3. 4 Catalysis results of the Aldol reaction for catalyst MUF-77-cat-1 and MUF-77-cat-2.

Catalyst	Catalyst linker set	Cat. loading	Conversion	Rate constant	e.e.
MUF-77-cat-1	hmtt/ecdc/bdc-Pro	10	23.2	0.33	5.1
MUF-77-cat-2	hmtt/cychcdc/bdc-Pro	10	29.8	0.35	-4.0

Reaction conditions: 10 mol % catalyst (proline unit relative to amount of aldehyde), 0.04 M 4-nitrobenzaldehyde at 20 °C. Rate constant unit: L mol^{-1} day^{-1}, based on consumption of 4-nitrobenzaldehyde.

3.3 Conclusion

Synthesis of new MUF-777 and MUF-77 variants containing homochiral *activation sites*, (S)-proline derivatives, were successfully achieved by ligand functionalization followed by post-synthetic thermal deprotection. The resulting catalytic pores in these materials can be further tuned by *modulator sites*, on the tat linker (in MUF-777) and the carbazole linker (in MUF-77) ligands. In the MUF-777 system, the relocation of the active site from the bpdc ligand to the bdc ligand has a significant effect on the catalysis outcome. It results in a reversed enantioselectivity and a decreased reaction rate. Reversal in enantioselectivity as a result of relocation of the catalytic unit has previously been observed in MUF-77 catalyst systems. This implies the importance of the position of activator units in the pores of framework. The catalysis results of the MUF-77 system reveal that the functional group on the carbazole ligand also has a decisive impact on both the reaction rate and enantioselectivity. Replacing ethyl group on the carbazole with a larger group (methyl cyclohexyl) not only increased the reaction rate but also reversed the enantioselectivity. This result demonstrates the size and position of the modulator are also critical for the outcome of catalysis. Here, only one type of catalytic unit and nonpolar modulators were studied. MUF-77 and MUF-777 catalyst systems could be diversified by functionalizing triazatruxene and carbazole ligands with chiral and hydrophilic modulators or new catalytically-active units.

3.4 Experimental section

3.4.1 General procedure

All starting materials and solvents were used as received from commercial sources without further purification unless otherwise noted. (-)-Myrtenyl bromide,[216] Me_2cdc,[209] (*S*)-H_2bpdc-ProBoc[83] and (*S*)-H_2bdc-ProBoc[84] were prepared via literature procedures. Column chromatography was carried out on silica gel (grade 60, mesh size 230-400, Scharlau). NMR spectra were recorded at room temperature (unless otherwise noted) on Bruker-400 and Bruker-500 Avance instruments, with the use of the solvent proton as an internal standard. High performance liquid chromatography (HPLC) was carried out using a Thermo Fisher Dionex Ultimate 3000 system equipped with a UV detector.

3.4.2 Ligand Synthesis

All carbazole based ligands were synthesized starting from Me_2cdc according to Scheme 3.1. Syntheses of Me_2ecdc and H_2ecdc are described below. Detailed procedures and spectroscopic data on other ligands and their intermediates are available in Electronic Appendix B.

Me_2ecdc

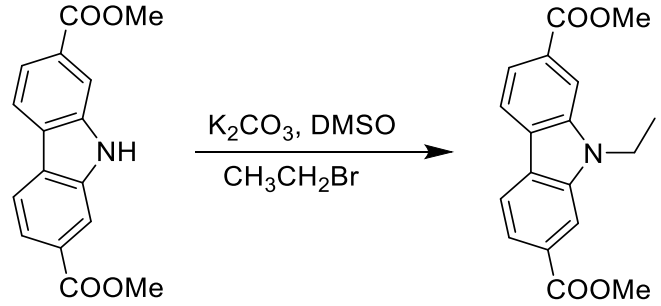

9H-carbazole-2,7-dicarboxylate (283 mg, 1 mmol) and K_2CO_3 (1.4 g) were combined in DMSO (6 mL) and stirred at RT for 15 minutes. Then, ethyl bromide (746 µL, 10 mmol) was added and the reaction mixture stirred at RT overnight. The mixture was poured into cold water and stirred for half an hour. The yellow solid was filtered, washed with water and dried under vacuum. Yield: 290 mg, 0.93 mmol, 93%. ^{1}H NMR (500 MHz, $CDCl_3$): δ 8.23-8.14 (m, 4H), 7.98 (d, *J* = 8.2 Hz, 2H), 4.52 (q, *J* = 7.2 Hz, 2H) 4.03 (s, 6H), 1.51 (t, *J* = 7.2 Hz, 3H) ppm. ^{13}C NMR (125 MHz, $CDCl_3$): δ 167.65, 140.62, 128.32, 125.77, 120.89, 120.38, 110.71, 52.29, 37.90, 14.08 ppm.

H_2ecdc

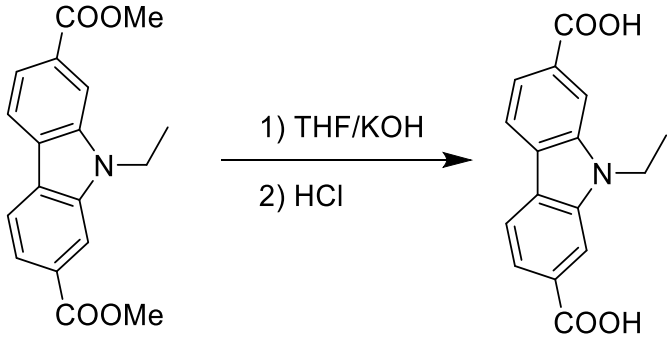

Me_2ecdc (295 mg, 0.95 mmol) was dissolved in 20 mL 1:1 (V/V) THF/KOH (aq., 1M) and the solution was refluxed overnight. THF was removed under reduced pressure and the reaction mixture then was acidified with 1 M aqueous HCl while it was kept on an ice bath. pH was adjusted to around 1, and the mixture was stirred for 1 hour. The yellow solid was filtered, washed with water and dried under vacuum. Yield: 260 mg, 0.92 mmol, 97%. ^{1}H NMR (500

MHz, DMSO-*d*6): δ 13.03 (br, 2H), 8.34 (d, *J* = 8.2 Hz, 2H), 8.25 (s, 2H), 7.86 (d, *J* = 8.1 Hz, 2H), 4.61 (q, *J* = 7.0 Hz, 2H), 1.36 (t, *J* = 7.1, 3H) ppm. ^{13}C NMR (125 MHz, DMSO-*d*6): 168.29, 140.66, 129.50, 125.32, 121.56, 120.52, 111.33, 37.71, 14.30 ppm. ESI (negative mode, CH_3OH): m/z = 282.0768 ($[C_{16}H_{12}NO_4]^-$, calcd. 282.0761).

3.4.3 MOF Synthesis

[Zn_4O(tat-ethyl)$_{4/3}$(bpdc-Pro)$_{1/2}$(bdc)$_{1/2}$]

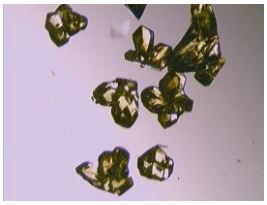

H_3tat-ethyl (21.2 mg, 37.8 μmol), (*S*)-H_2bpdc-ProBoc (17.4 mg, 38.3 μmol), terephthalic acid (6.5 mg, 39.1 μmol) and $Zn(NO_3)_2{\cdot}4H_2O$ (74.0 mg, 283.2 μmol) were dissolved in a mixed solvent of dry DEF (5 mL) and water (175 μL). The reaction was carried out in an 85 °C isothermal oven for 21 hours to obtain yellow crystals. The mother liquor was replaced with anhydrous DMF and this process was repeated five times. The DMF was then replaced with fresh anhydrous acetone and the solvent replenished five times within an hour. The acetone-occluded crystals were thermolyzed to produce [Zn_4O(tat-ethyl)(bpdc-Pro)$_{1/2}$(bdc)$_{1/2}$] by heating the crystals at a rate of 20 °C / min and holding the temperature at 200 °C for 20 hours under a dynamic vacuum. Yield: 24.3 mg.

[Zn_4O(tat-ethyl)$_{4/3}$(bpdc-Pro)$_{1/2}$(bdc)$_{1/2}$]

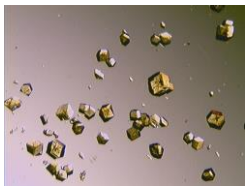

H_3tat-ethyl (21.2 mg, 37.8 μmol), (*S*)-H_2bdc-ProBoc (14.3 mg, 37.8 μmol), H_2bpdc (9.1 mg, 37.6 μmol) and $Zn(NO_3)_2{\cdot}4H_2O$ (74.0 mg, 283 μmol) were dissolved in a mixed solvent of dry DEF (5 mL) and water (100 μL). The reaction was carried out in an 85 °C isothermal oven for 20 hours to obtain yellow crystals. The mother liquor was replaced with anhydrous DMF and this process was repeated five times. The DMF was then replaced with fresh anhydrous acetone and the solvent replenished five times within an hour. The acetone-occluded crystals were thermolyzed to produce [Zn_4O(tat-ethyl)(bpdc)$_{1/2}$(bdc-Pro)$_{1/2}$] by heating the crystals at a rate of 20 °C / min and holding the temperature at 200 °C for 20 hours under a dynamic vacuum. Yield: 23.6 mg.

Detailed synthetic procedure for other MOFs are available in Electronic Appendix B.

3.4.4 ^{1}H NMR spectroscopic analysis of digested MOF samples

The following protocol was used for digestion of the MOFs for ^{1}H NMR spectroscopy: The sample was washed with dry acetone then soaked in dry acetone then desolvated *in vacuo*. A DCl/DMSO-d_6 (0.6 mL, 150 µL/0.45 mL) solution was used to digest around 3 mg MOF. The NMR spectrum was acquired with the clear solution of the digested framework.

3.4.5 Powder X-ray diffraction patterns

All powder X-ray diffraction measurements were carried out on a Rigaku Spider X-ray diffractometer with Cu K_α radiation (Rigaku MM007 microfocus rotating-anode generator), monochromated and focused with high-flux Osmic multilayer mirror optics, and a curved image plate detector. Samples were kept damp with solvent prior to and during measurements. The two-dimensional images of the Debye rings were integrated with 2DP to give 2θ vs I diffractograms. Predicted powder patterns were generated from single crystal structures using Mercury.

3.4.6 Single crystal X-ray diffraction

The single crystal X-ray diffraction analysis for MUF-77-cat-1 were performed at 133 K. Individual crystals were selected under a microscope then mounted on a polymer mount with a minimum amount of Fomblin® Y oil. A Rigaku Spider diffractometer equipped with a MicroMax MM007 rotating anode generator (Cu_α radiation, 1.54178 Å), high-flux Osmic multilayer mirror optics, and a curved image-plate detector was used to collect the data. The data were integrated and scaled and averaged with FS Process.[182] Using Olex2[183], the structure was solved with the SHELXT[184] structure solution program using intrinsic phasing and refined with the ShelXL[185] refinement package using least squares minimization.

Crystallographic data details are summarized in Table 3.5. All zinc, oxygen and carbon atoms of the truxene ligands and bdc backbones were found in the electron density difference maps and refined anisotropically. Hydrogen atoms were calculated and refined as a riding model. The nitrogen, oxygen and carbon atoms of proline unit were found in the electron density difference map, despite their low occupancy due to disorder. These atoms were disordered over eight sites. Thus, their atomic occupancies were fixed at 0.125 with a fixed isotropic displacement parameter (0.05). All atoms in the carbazole ligand were found in the electron density difference map. However, nitrogen atom, and carbon atoms of the two rings

and ethyl group were also disordered over eight positions, so the corresponding atomic occupancies were fixed at 0.125 with a fixed isotropic displacement parameter (0.05). Phenyl rings were modelled as ideal hexagons.

Table 3. 5 Crystallographic data summary for MUF-77-cat-1

Compound	**MUF-77-cat-1**
Formula	$C_{62.5}H_{46}N_{1.5}O_{13.5}Zn_4$
Formula weight	1295.49
Crystal size (mm)	0.32 × 0.29 × 0.34
Temperature (K)	133
Wavelength (Å)	1.54178
Crystal system	cubic
Space group	*Pm*-3
Unit cell length (Å)	29.9479(4)
Unit cell volume ($Å^3$)	26859.6(11)
Z	6
D_{calc} (g cm^{-3})	0.481
μ (mm^{-1})	0.786
F (000)	3957.0
Reflns coll./unique, R_{int}	57072 / 7097, 0.078
Data range	8 Å > d > 0.89 Å
Completeness	100%
T_{min}, T_{max}	0.457, 1.00
R indices for data with I>2σ(I)	R_1 = 0.1037 wR_2 = 0.3200
R indices for all data	R_1 = 0.1387 wR_2 = 0.3511
Largest difference peak and hole (e $Å^{-3}$)	1.12/ −1.55

3.4.7 Catalysis

Experimental protocol A: A stock catalyst solution was prepared with p-nitrobenzaldehyde (181 mg, 1.20 mmol), acetone (30.0 mL), water (7.50 mL) and nitrobenzene

as an internal standard (121 μL, 1.20 mmol). In a typical experiment, 1.0 mL of stock solution was added to a 1.5 mL HPLC sample vial together with a pre-weighed quantity of desolvated catalyst. The mass of catalyst was chosen so that it contained 10 mol% of prolinyl groups relative to 4-nitrobenzaldehyde. The reaction mixture was allowed to stand in the autosampler of the HPLC at 20 °C. During the reaction, 2.5 μL of the supernatant was subjected to HPLC analysis every two hours over the initial 12 hours of the reaction and then again after 24 h. HPLC analysis was carried out under the following conditions: CHIRALCEL AS-H column; mixed solvent of hexane and isopropyl alcohol (70:30 v/v); flow rate of 0.8 ml/min. Products were detected according their absorption of 254 nm UV light. The conversion of 4-nitrobenzaldehyde was calculated by comparing the ratio of its peak area and that of the nitrobenzene standard. The ee value of each reaction is reported based on the excess of the *R* enantiomer after a reaction time of 24 h.

Experimental protocol B: A stock catalyst solution was prepared with p-nitrobenzaldehyde (158 mg, 1.05 mmol), acetone (30.0 mL), and nitrobenzene as an internal standard (100 μL). In a typical experiment, 1.0 mL of stock solution was added to a 1.5 mL HPLC sample vial together with a pre-weighed quantity of desolvated catalyst. The mass of catalyst was chosen so that it contained 10 mol% of prolinyl groups relative to 4-nitrobenzaldehyde. The reaction mixture was allowed to stand in the autosampler of the HPLC at 20 °C. During the reaction, 2.0 μL of the supernatant was subjected to reverse-phase HPLC analysis every two hours over the initial 12 hours of the reaction and then again after 24 h. HPLC analysis was carried out under the following conditions: Lux Amylose-1; mixed solvent of CH_3CN and deionized water (50:50 v/v); flow rate of 0.5 ml/min. Products were detected according their absorption of 254 nm UV light. The conversion of nitrobenzaldehyde was calculated by comparing the ratio of its peak area and that of the nitrobenzene standard. The ee value of each reaction is reported based on the excess of the enantiomer of short retention time after a reaction time of 24 h. Figure 10 shows typical HPLC chromatogram of a reaction mixture.

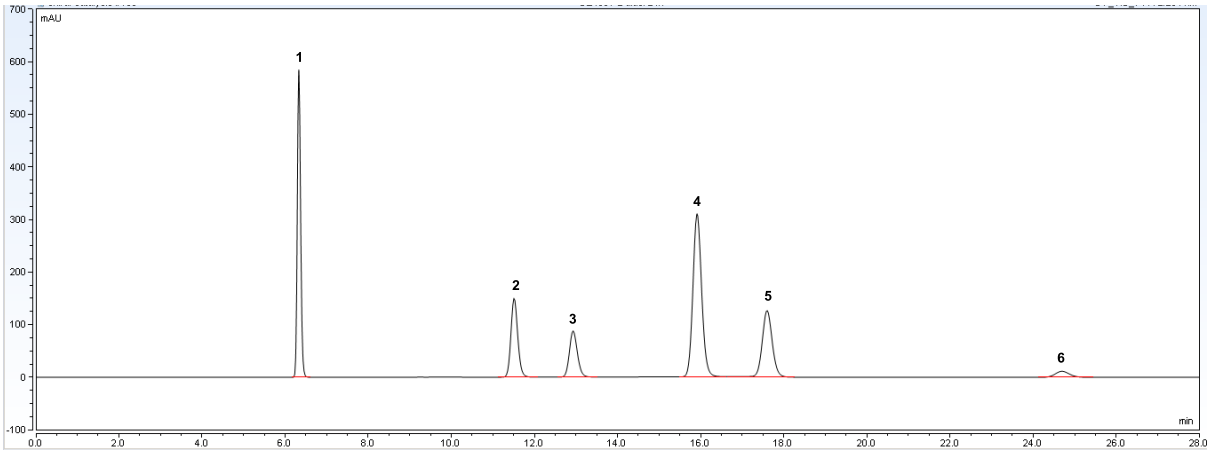

Figure 3. 13 A typical HPLC chromatogram (Lux amylose-1) of the p-aldol reaction mixture. Peak 1 (6.33 min): acetone; Peak 2 (11.51 min): enantiomer 1 of aldol adduct; Peak 3 (12.93 min): enantiomer 2 of aldol adduct; Peak 4 (15.91 min): nitrobenzene; Peak 5 (17.60 min): 4-nitrobenzaldehyde; Peak 6 (24.69 min): product of the elimination of H_2O from the initial aldol product.

Calculation of the observed rate constant for aldol reactions: The apparent rate constant was calculated as described previously.[84]

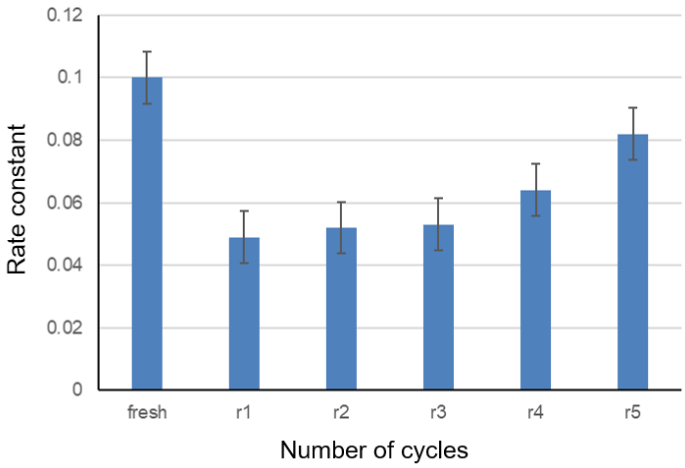

Figure 3. 14 A graph showing the recyclability of catalyst MUF-777-bdc-Pro based on the reaction rate constant (L mol^{-1} day^{-1}) measured under conditions in Entry 1 of Table 3.2.

Reaction kinetics plots

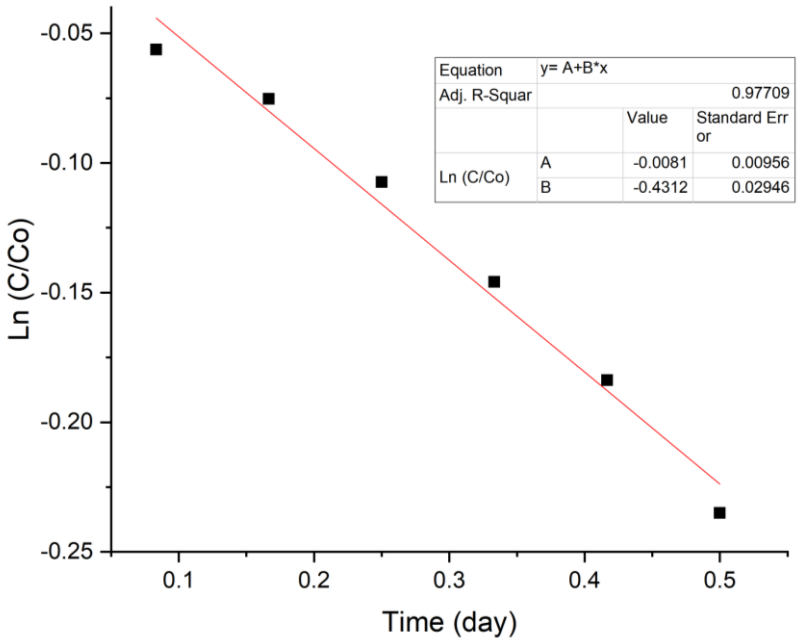

Figure 3. 15 Reaction kinetics plot for the aldol reaction catalyzed by MUF-777-bpdc-Pro.

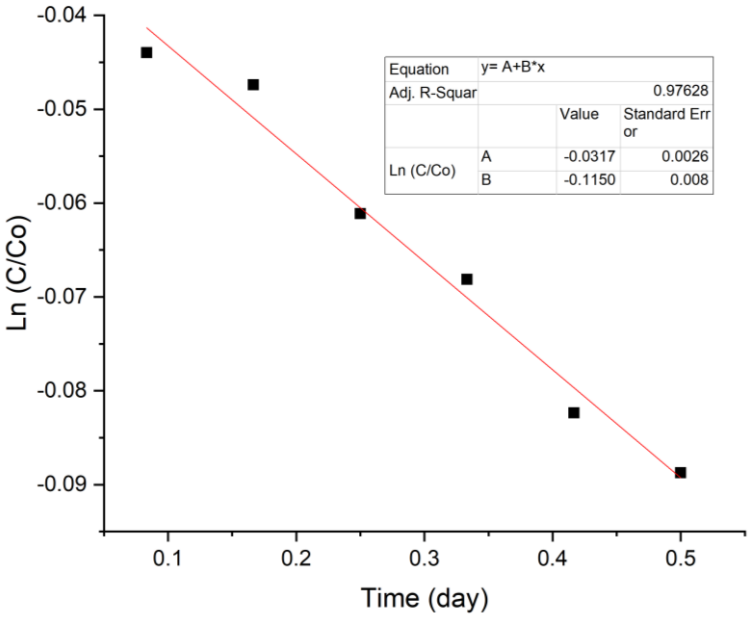

Figure 3. 16 Reaction kinetics plot for the aldol reaction catalyzed by MUF-777-bpc-Pro.

Chapter 4 Amino-functionalized Triazatruxene and Carbazole Derivatives for Catalytically Active MUF-777 and MUF-77 Systems

4.1 Introduction

Having demonstrated the use of tat and carbazole derivatives as modulators in MUF-77 and MUF-777 catalyst systems in Chapter 3, we next turned our efforts to multicomponent MOFs in which catalytic units are appended to tat or carbazole ligands. In previous MUF-77 and MUF-777 catalyst systems the activator was an enantiopure proline unit. In these systems, it was demonstrated that enantioselectivity of the catalyst can be tuned by changing the environment of the catalytic pore. This was achieved either by altering the position of the activator or by introducing achiral modulator groups into the catalytic pocket.[84] The pyrrolidine-type chiral amine catalysts have extensively been studied in MOF catalyst systems, due to availability of their enantiopure forms and stereoselective catalytic behaviour.[83-84, 206, 217-220] However, it may be possible to achieve stereoselectivity by using an achiral catalytic unit along with chiral modulators in a multicomponent MOF system. Therefore, in this study, achiral cyclic secondary amines such as piperidine and azetidine, and triethylamine were chosen as the catalytic unit for our target multicomponent MOF catalysts.

Another target of this study is to extend the use of multicomponent MOF catalysts beyond the aldol reaction which was previously studied by our group. Piperidine, azetidine and triethylamine are known to catalyse a wide range of reactions.[221-226] Here, two important carbon-carbon bond formation reactions, Michael reaction and Friedel Crafts reaction, are chosen.[227-229] The two reactions have previously been studied in binary MOF catalyst systems.[137, 218, 230]

In this chapter, I report syntheses of four new ligands that each bear either a secondary amine (piperidine or azetidine) or a tertiary amine (triethylamine) functionalities. Using these ligands, I then prepare new MUF-77 and MUF-777 analogues. Next, I investigate the catalytic activity of these new MOFs in the Michael addition reaction of dibenzoyl methane to β-nitrostyrene, and the Friedel Crafts reaction of indole with β-nitrostyrene.

4.2 Results and discussion

4.2.1 Synthesis and characterization of ligands

Three new carbazole derivatives were synthesized from Me_2cdc, using the synthetic protocol similar to that described in Chapter 3 (Scheme 4.1). Specifically, the reaction of Me_2cdc with 1-Boc-4-bromomethylpiperidine, 1-Boc-3-(bromomethyl)-azetidine and 2-chlorotriethylamine hydrochloride in DMSO at 70 °C afforded quantitative yields of Me_2pipcdc, Me_2azecdc-Boc and Me_2teacdc-Boc, respectively. These compounds were then hydrolyzed to obtain H_2pipcdc-Boc, H_2azecdc-Boc and H_2teacdc. Me_2pipcdc-Boc and Me_2azecd-Boc were Boc deprotected, by using trifluoroacetic acid, to obtain Me_2pipcdc-NH and Me_2azecdc-NH respectively. Me_2pipcdc and Me_2azecdc-Boc were purified by column chromatography. All other compounds were obtained in acceptable purity as shown by NMR spectroscopy and mass spectrometry.

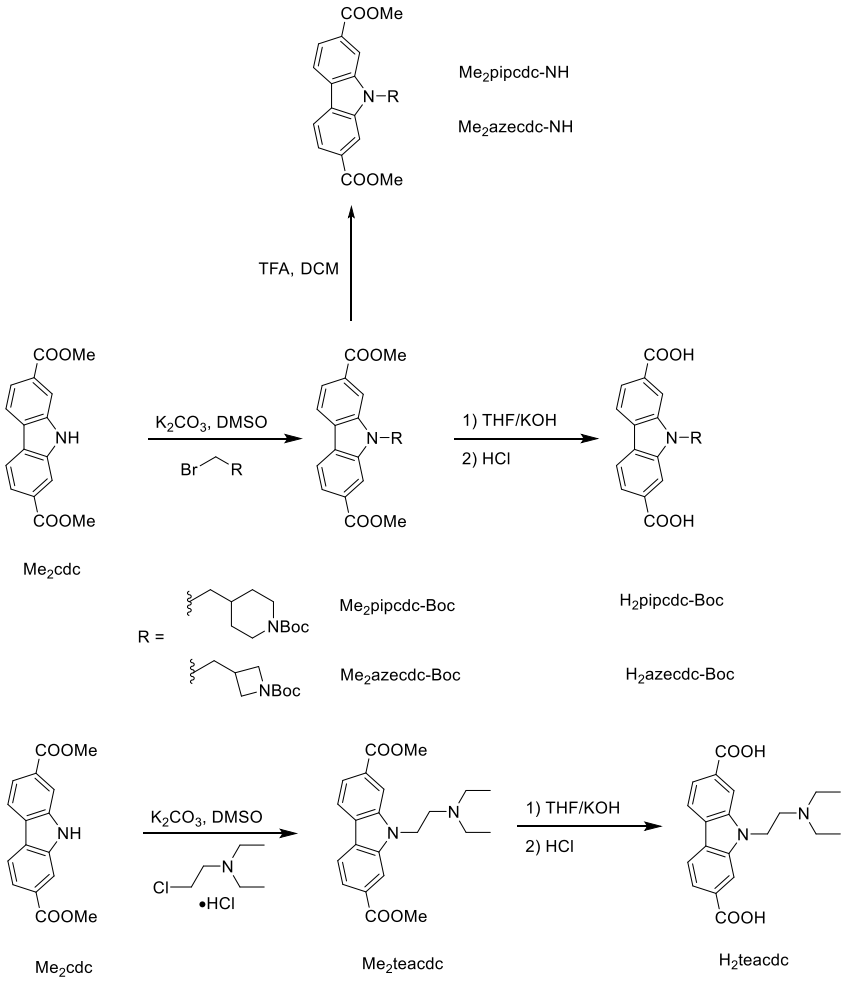

Scheme 4. 1 Synthetic route to the carbazole-based ligands.

In chapter 2, I developed a convenient method for the synthesis of triazatruxene derivatives. Using the same synthetic protocol, here, I prepared a new tritopic ligand, H_3tatpip-Boc. As illustrated in Scheme 4.2, Et_3tatpip-Boc was prepared by the alkylation reaction of Et_3tat with 1-Boc-4-bromomethylpiperidine. It was purified by column chromatography and then hydrolyzed to obtain the ligand H_3tatpip-Boc. Further, Et_3tat-Boc was converted into Et_3tat-NH using trifluoroacetic acid.

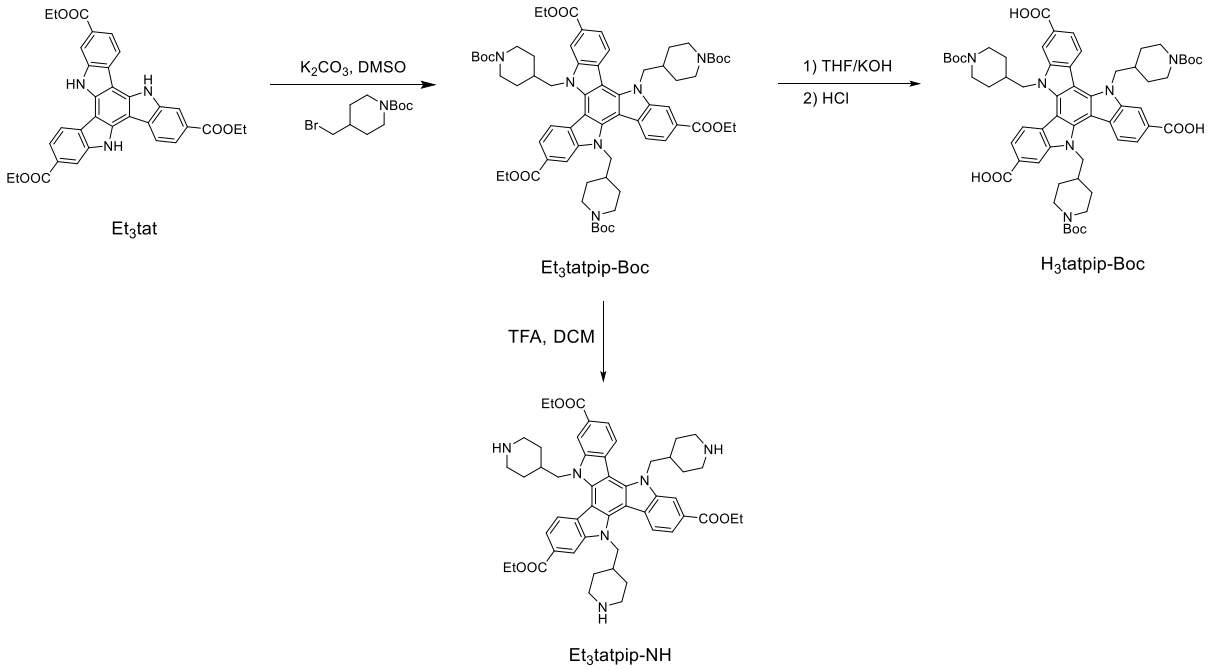

Scheme 4. 2 Synthetic route to tatpip derivatives.

4.2.2 Synthesis and characterization MUF-77 catalysts containing catalytically-active secondary and tertiary amine groups

In Chapter 3, the previously reported thermolabile protection group strategy was used to prepare MOFs containing catalytically-active proline unit. The strategy, initially, involved the preparation of a precursor MOF containing a Boc protected proline unit. Although during synthesis of this MOF some undesired phase formation was observed, this was eliminated by carefully adjusting the feed ratio of the three linkers. The precursor MOF was then thermolyzed to obtain the MOF containing Boc-free proline unit. Using the same strategy, here, I prepared MUF-77 and MUF-777 analogues in which the catalytically-active amino group is appended to the carbazole ligand.

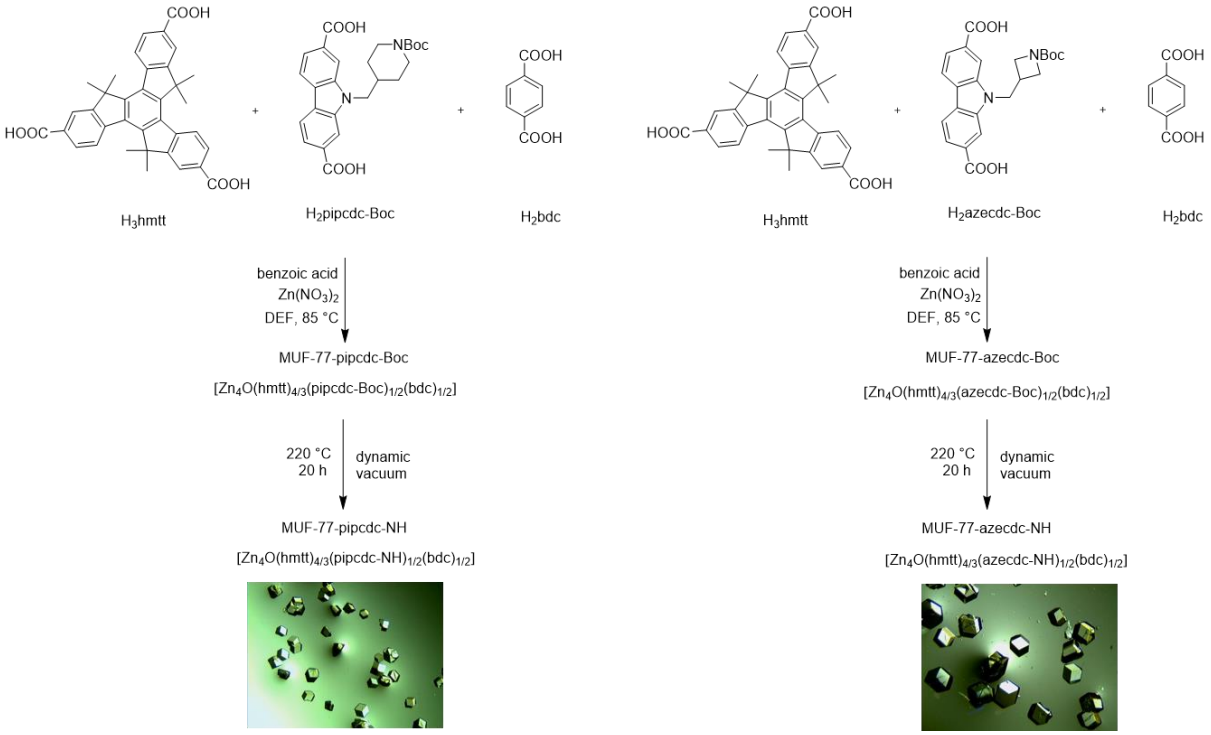

Figure 4. 1 Schematic illustration of syntheses of MUF-77-pipcdc-NH and MUF-77-azecdc-NH and their optical microscopy images.

As illustrated in Figure 4.1, MUF-77-pipcdc-Boc was prepared by a solvothermal reaction of H_3hmtt, H_2pipcdc-Boc, H_2bdc and zinc nitrate in DEF as colourless crystals. These crystals belong to a cubic crystal system as they are fully extinguished at all rotational positions under crossed polarizers on an optical microscope. The powder X-ray diffraction pattern of MUF-77-pipcdc-Boc is almost identical to that of MUF-77 indicating that this MOF has the same overall topology as MUF-77 (Figure 4.2a). The phase purity of this material was confirmed by ^{1}H NMR spectroscopic analysis. ^{1}H NMR spectrum of a digested sample shows a ratio of 8:3:3 of the three ligands which suggests that the framework has a formula of $[Zn_4O(hmtt)_{4/3}(pipcdc\text{-}Boc)_{1/2}(bdc)_{1/2}]$ (Figure 4.3). As a sensitive diagnostic tool for identifying the purity of multicomponent MOFs, NMR spectroscopy can clearly indicate the presence of any side products that do not share the stoichiometry of the framework. Further, thermogravimetric analysis (TGA) was done to investigate thermal stability of the framework and the temperature at which deprotection occurs. The first weight loss starts at room temperature and continues until around 80 °C. This weight loss is due to escape of the solvent (acetone). The TGA curve then shows a weight percent loss of 3.2% starting at about 220 °C (Figure 4.2b), which agrees

the expected weight loss of 3.7% attributable to the loss of the Boc protecting group as isobutylene and CO_2 gases.

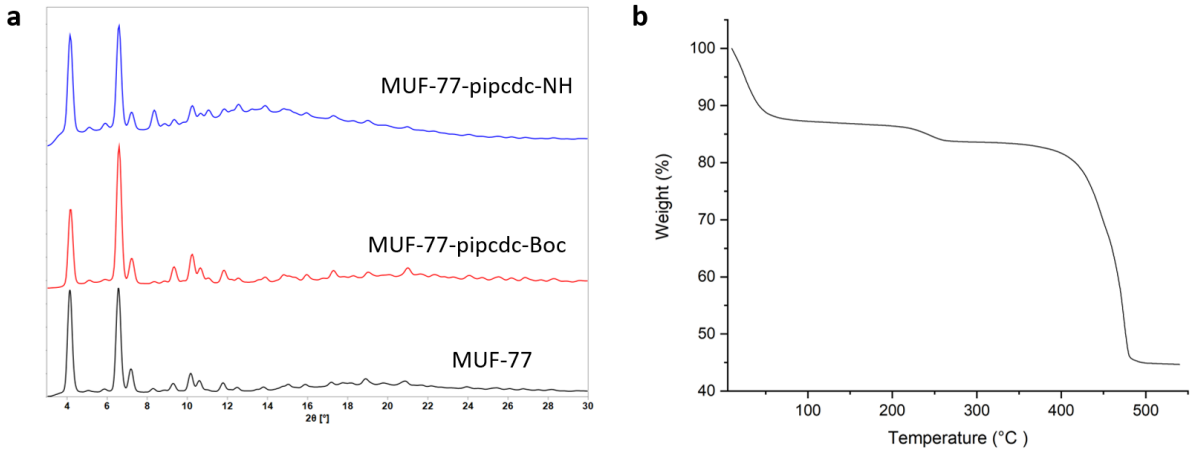

Figure 4. 2 a) PXRD patterns of MUF-77, MUF-77-pipcdc-Boc and MUF-77-pipcdc-NH. b) TGA trace of MUF-77-pipcdc-Boc.

To reveal the catalytically-active piperidinyl site, MUF-77-pipcdc-Boc was thermolyzed at 220 °C under a dynamic vacuum. The completeness of the thermolysis reaction was assessed by ^{1}H NMR spectroscopy on digested samples. A thermolysis time of 20 hours was sufficient to fully deprotect MUF-77-pipcdc-Boc. ^{1}H NMR spectroscopic analysis of digested sample of the thermolyzed MOF demonstrates that the peak at 1.11 ppm, which belong to the *tert*-butyl groups of H_2pipcdc-Boc, disappears (Figure 4.3). The PXRD pattern of MUF-77-pipcdc-NH is almost identical to that of MUF-77-pipcdc-Boc which suggest that the framework retains its crystallinity and phase-purity (Figure 4.2a).

As shown in Figure 4.1, the crystals of MUF-77-pipcdc-NH maintain their transparency after thermolysis. This indicates that the thermolysis of MUF-77-pipcdc-Boc is a single-crystal-to-single-crystal transformation. This allowed us to analyse the structure of MUF-77-pipcdc-NH by single crystal X-ray diffraction. The SCXRD data of MUF-77-pipcdc-NH was collected at 133 K. The data revealed that the framework displays a good diffraction pattern to a resolution of 0.81 Å. Such high resolution and the low R_{int} (5.09%) value of the model are indicative of the high quality of the data. This important for determining structural details accurately, especially the precise locations of activator and modulator sites.

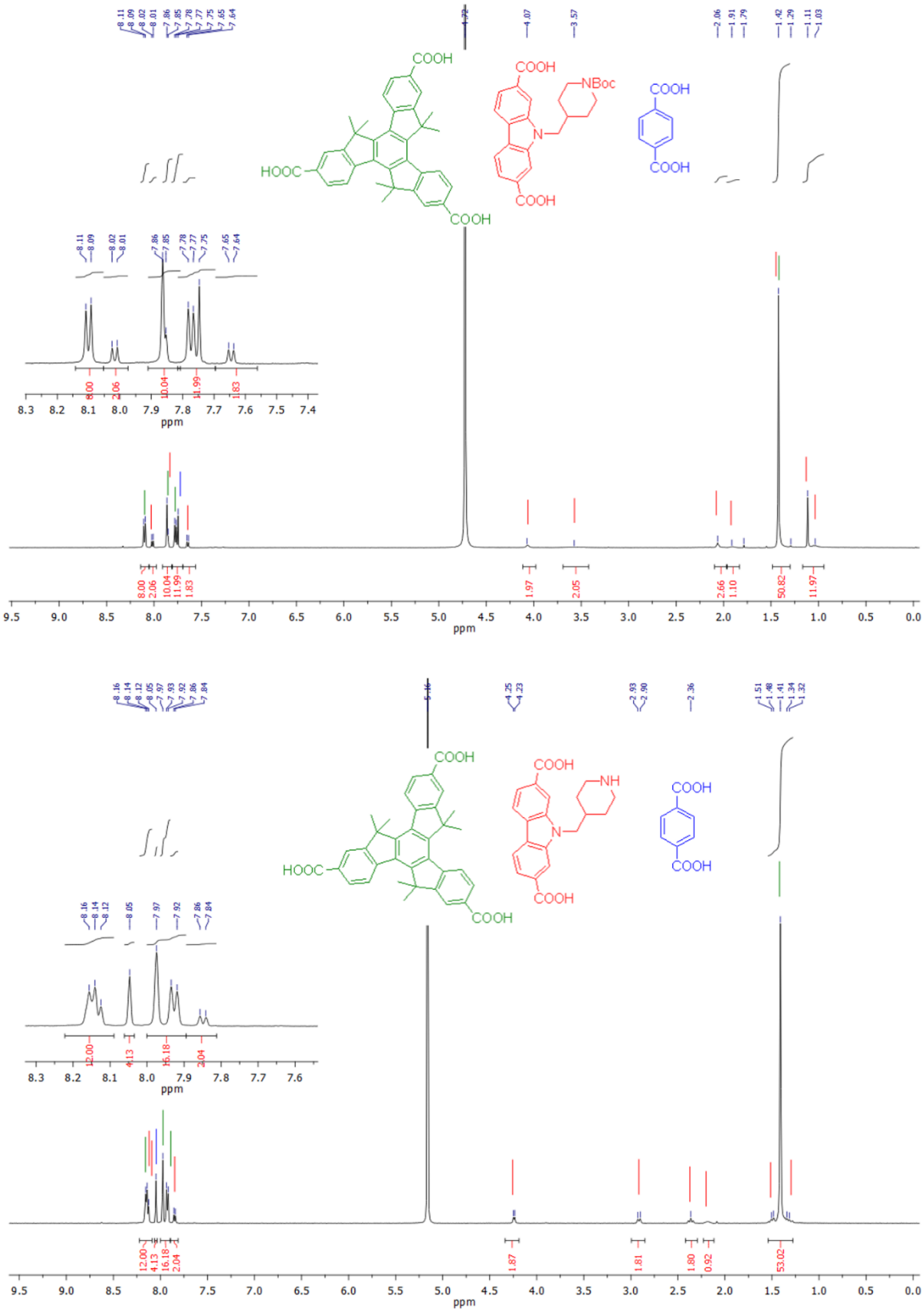

Figure 4. 3 Upper: The ^{1}H NMR spectrum of digested MUF-77-pipcdc-Boc (in KOH/D_2O) showing the integrals that match with the formula $[Zn_4O(hmtt)_{4/3}(pipcdc\text{-}Boc)_{1/2}(bdc)_{1/2}]$. Note that pipcdc-Boc shows a peak at 1.11 pm which belongs to the Boc group. This peak disappears after thermolysis. Lower: The ^{1}H NMR spectrum of digested MUF-77-pipcdc-NH showing the integrals that match with the formula $[Zn_4O(hmtt)_{4/3}(pipcdc\text{-}NH)_{1/2}(bdc)_{1/2}]$.

The crystallographic analysis revealed that MUF-77-pipcdc-NH crystallizes in the cubic space group *P*m-3. This is the same space group that other MUF-77 analogues also crystalize in. Initial refinements showed the overall framework structure of MUF-77-pipcdc-NH is nearly the same as MUF-77-cat-1 (described in Chapter 3), except for the piperidinyl group on the carbazole ligand and bare bdc ligand. A tetrahedral cavity in the framework is illustrated in Figure 4.4. This cavity is defined by four hmtt ligands, one bdc ligand and one carbazole ligand. The piperidinyl group is located inside the cavity and pointing towards the bdc ligand. A pair of methyl groups on each hmtt ligand are also positioned inside the same cavity. Similar to MUF-77-cat-1, the piperidine unit in the structure of MUF-77-pipcdc-NH can be considered as a single site catalyst.[201] Because, all piperidinyl units have the same well-defined microenvironment throughout the framework due to well-ordered and defect-free structure of MUF-77-pipcdc-NH.

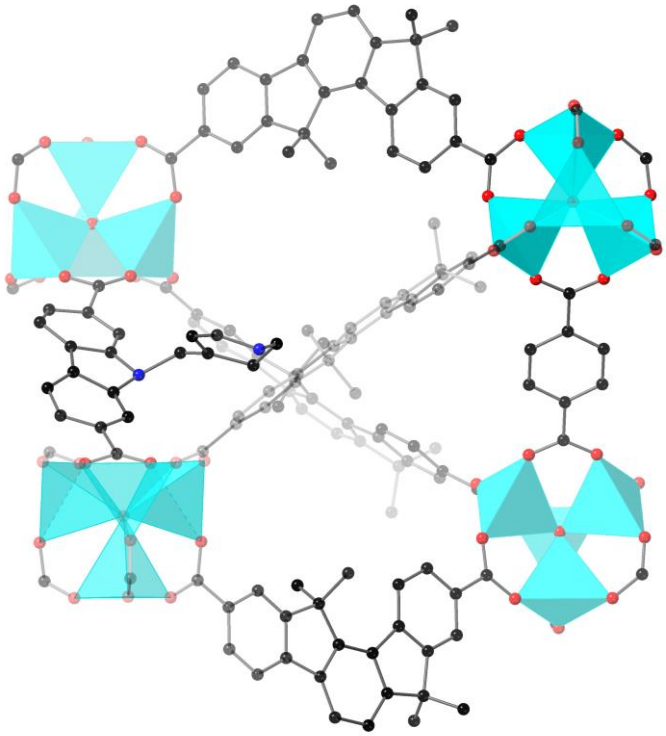

Figure 4. 4 A view illustrating the tetrahedral cavity and positions of catalytic-active piperidinyl group in the crystal structure MUF-77-pipcdc-NH. Atom colours: carbon: black, oxygen: red, nitrogen: blue, zinc: cyan. Hydrogen atoms are omitted for clarity.

Next, two MUF-77 variants with azetidine unit on the carbazole ligand were synthesized (Figure 4.1). The formula of MUF-77-azecdc-Boc was determined as $[Zn_4O(hmtt)_{4/3}$(azecdc-

Boc)$_{1/2}$(bdc)$_{1/2}$] by ^{1}H NMR spectroscopic analysis of a digested MOF sample (Figure 4.6). The PXRD pattern of MUF-77-azecdc-Boc is in good agreement with the PXRD pattern of the parent framework, MUF-77-methyl, indicating that the two frameworks have the same overall topology (Figure 4.5.a). It also confirms the bulk phase purity of the material.

The TGA curve of MUF-77-azecdc-Boc (Figure 4.5b) revealed a weight loss of 3.7% starting at about 220 °C, which agrees with the expected weight percent loss of 3.9% attributable to the loss of the Boc group. Therefore, to remove the Boc group, MUF-77-azecdc-Boc was heated at 220 °C for 20 hours under a dynamic vacuum. This process produced MUF-77-azecdc-NH with a formula of [Zn$_4$O(hmtt)$_{4/3}$(azecdc-NH)$_{1/2}$(bdc)$_{1/2}$] as confirmed by ^{1}H NMR spectroscopy (Figure 4.6). The PXRD pattern of MUF-77-azecdc-NH matches well with the pattern of MUF-77-azecdc-Boc which indicates that the crystallinity of the framework is retained (Figure 4.5a). It also confirms the bulk phase purity of the framework.

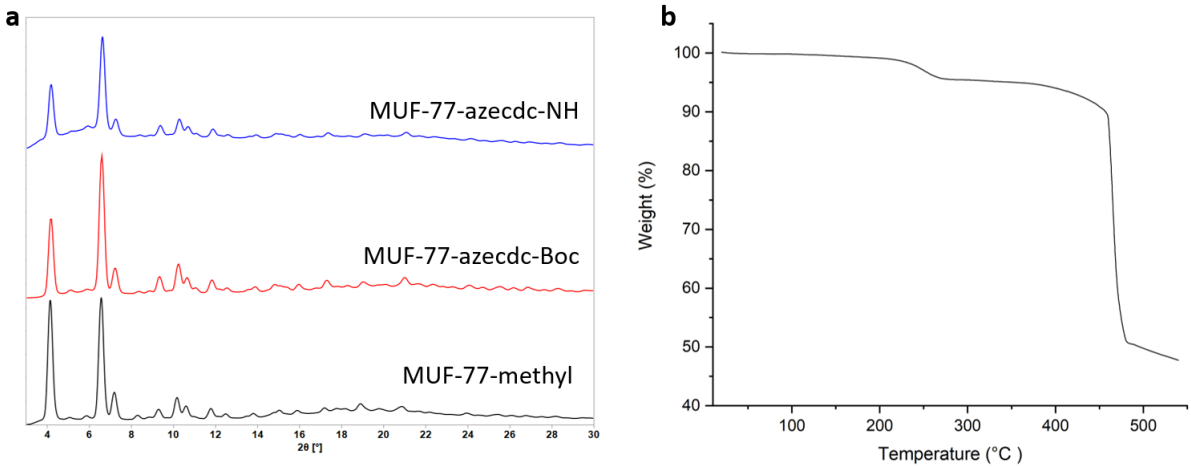

Figure 4. 5 a) PXRD patterns of MUF-77-methyl, MUF-77-azecdc-Boc and MUF-77-azecdc-NH. b) TGA trace of MUF-77-pipcdc-Boc.

Similar to the thermolysis of MUF-77-pipcdc-Boc, the thermolysis of MUF-77-azecdc-Boc is also occurs in a single-crystal-to-single-crystal manner (Figure 4.1). A good crystallographic dataset was obtained after performing single crystal X-ray diffraction analysis on a thermolyzed sample at 133 K. The structure of MUF-77-azecdc-NH was modelled similar to the structure of MUF-77-pipcdc-NH with good refinement statistics (Table 4.4). The position of the azetidinyl group in a tetrahedral pore of MUF-77-azecdc-NH is illustrated in Figure 4.7.

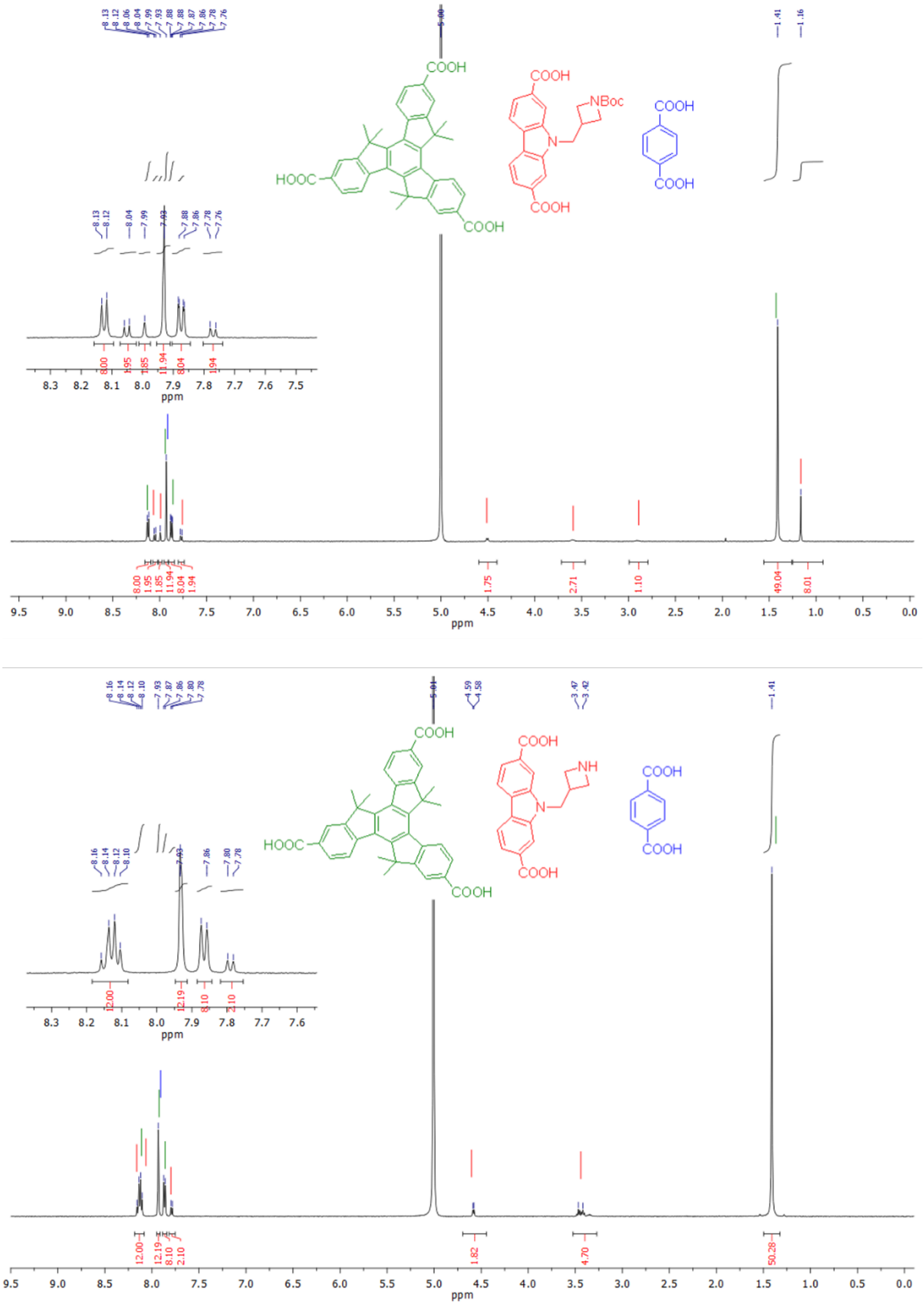

Figure 4. 6 Upper: The ^{1}H NMR spectrum of digested MUF-77-azecdc-Boc (in KOH/D_2O) showing the integrals that match with the formula $[Zn_4O(hmtt)_{4/3}(azecdc\text{-}Boc)_{1/2}(bdc)_{1/2}]$. Note that H_2azecdc-Boc shows a peak at 1.16 pm which belongs to the Boc group. This peak disappears after thermolysis. Lower: The ^{1}H NMR spectrum of digested MUF-77-azecdc-NH showing the integrals that match with the formula $[Zn_4O(hmtt)_{4/3}(azecdc\text{-}NH)_{1/2}(bdc)_{1/2}]$.

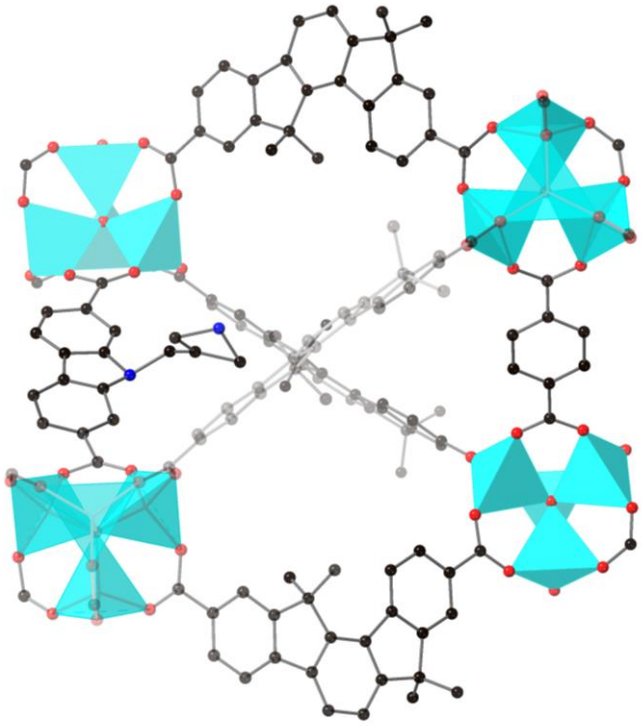

Figure 4. 7 A view illustrating the tetrahedral cavity and positions of catalytically-active azetidinyl group in the crystal structure MUF-77-pipcdc-NH. Atom colours: carbon: black, oxygen: red, nitrogen: blue, zinc: cyan. Hydrogen atoms are omitted for clarity.

As shown in Scheme 4.8, a solvothermal reaction of H_3hmtt, H_2teacdc, H_2bdc, benzoic acid and zinc nitrate produced MUF-77-teacdc. This material is isostructural to MUF-77-methyl and stable upon removal of solvent molecules as confirmed by PXRD analysis (Figure 4.9). ^{1}H NMR spectroscopic analysis showed that the integrals of the peaks corresponding to H_2teacdc ligand was around 50% lower than the expected value. Some additional peaks were also observed in the spectrum (Figure 4.10). These results indicate that some undesired reactions happen at the nitrogen of the triethylamine site under the solvothermal MOF synthesis conditions. One possible reaction is the protonation of the nitrogen of triethylamine to form a triethylammonium benzoate moiety on the carbazole ligand (Figure 4.11).

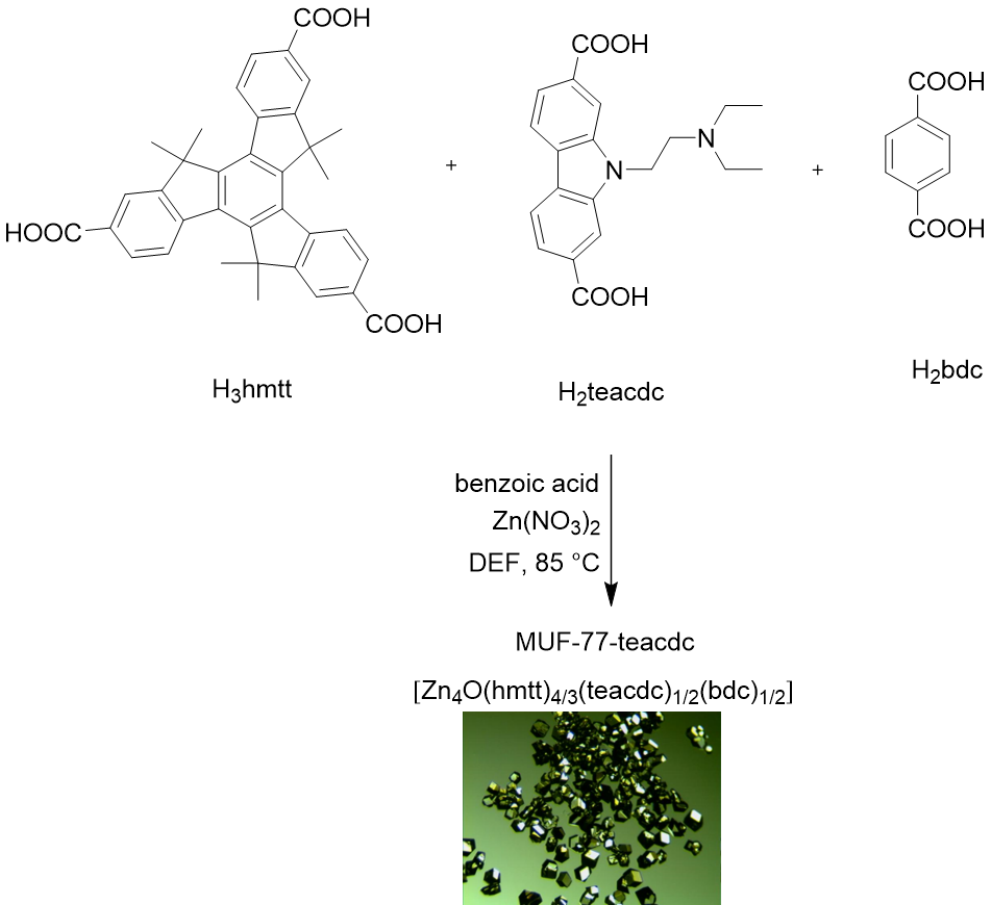

Figure 4. 8 Schematic illustration of synthesis of MUF-77-teacdc and its optical microscopy image.

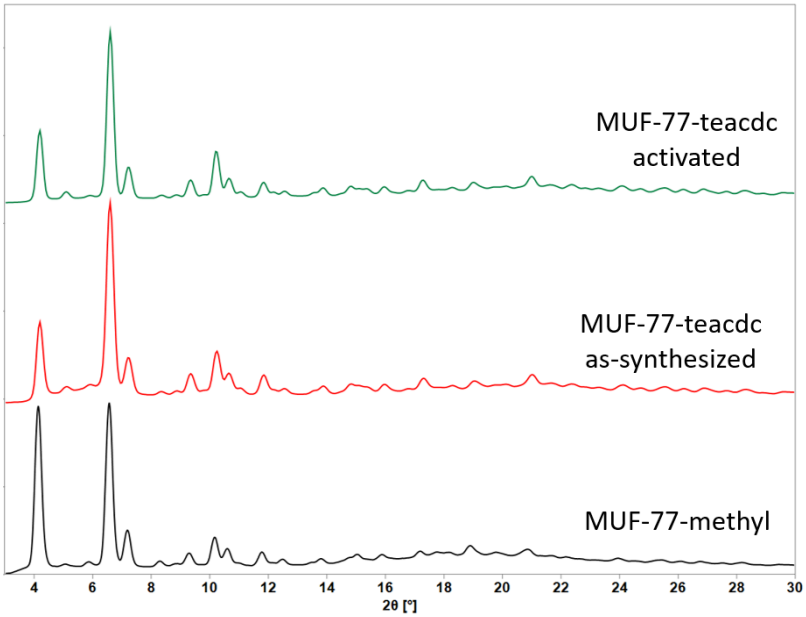

Figure 4. 9 PXRD patterns of MUF-77-methyl and MUF-77-teacdc (as-synthesized and activated samples)

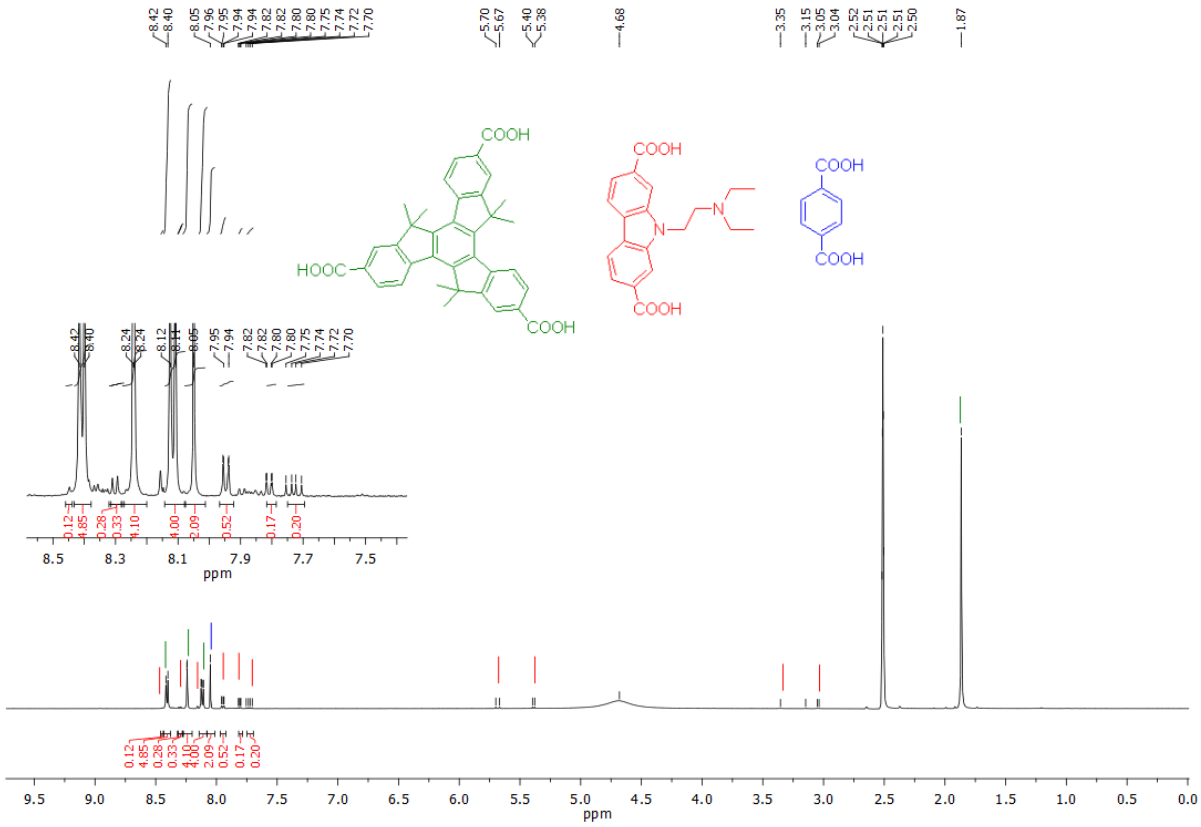

Figure 4. 10 The ^{1}H NMR spectrum of digested MUF-77-teacdc (in DCl/DMSO-d_6) showing the integrals that does not match with the formula $[(hmtt)_{4/3}(teacdc)_{1/2}(bdc)_{1/2}]$. The integrals belong to teacdc ligands shows lower values than expected. Some additional peaks are also present in the spectrum.

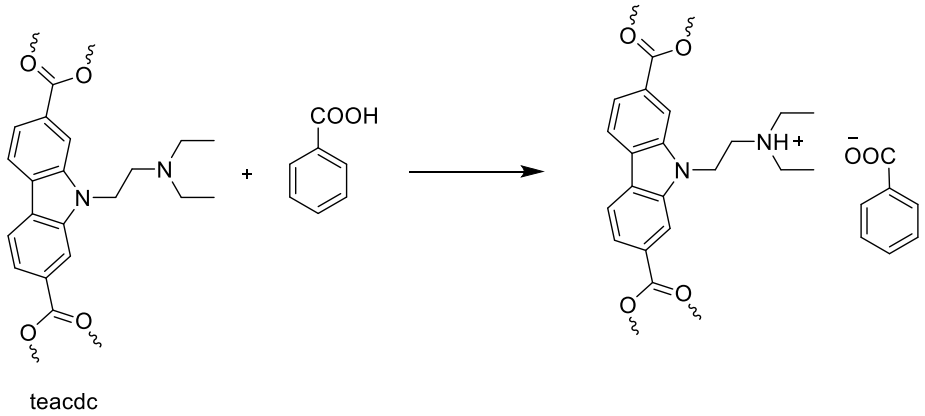

teacdc

Figure 4. 11 Schematic illustration of a possible reaction that may have occurred between the teacdc ligand and benzoic acid during MOF synthesis.

4.2.3 Synthesis and characterization MUF-777 catalysts containing catalytically-active secondary amine groups

MUF-777-tatpip-Boc, as illustrated in Scheme 4.12, was synthesized by a solvothermal reaction of H_3tatpip-Boc, H_2bpdc, H_2bdc, benzoic acid and zinc nitrate in DEF. The structure of this frameworks matches MUF-777-ethyl, as determined by PXRD (Figure 4.13a). ^{1}H NMR spectroscopic analysis of digested sample of this MOF revealed that the ratio of the ligand integrals matches the $[Zn_4O(tatpip\text{-}Boc)_{4/3}(bpdc)_{1/2}(bdc)_{1/2}]$ stoichiometry (Figure 4.14). This demonstrates the purity of MUF-777-tatpip-Boc. TGA plot, (Figure 4.13b), showed that the Boc group decomposes and escapes from the framework at about 200 °C. The weight loss observed at this temperature is 20.6%, which matches well the expected weight loss value, 21%. PXRD measurements of the thermolyzed framework, MUF-777-tatpip-NH, revealed the framework loses its crystallinity after deprotection process, indicating that the framework is not as stable as MUF-777-tatpip-Boc. This might be due to the high concentration of hydrophilic NH sites in the framework. This can make the framework more attractive to moisture and less stable towards water, compared to other members of this MOF family.

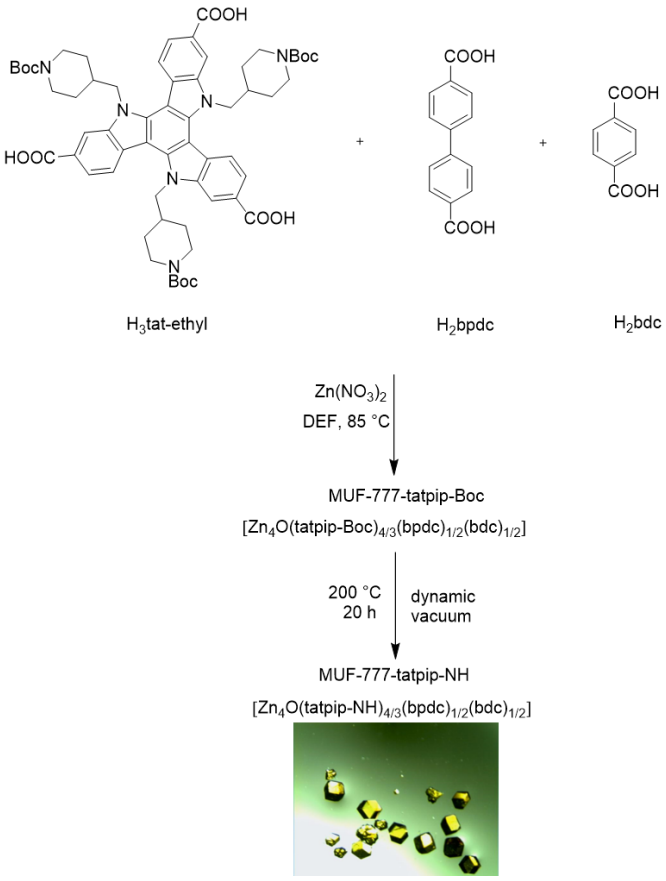

Figure 4. 12 Schematic illustration of synthesis of MUF-777-tatpip-NH and its optical microscopy image.

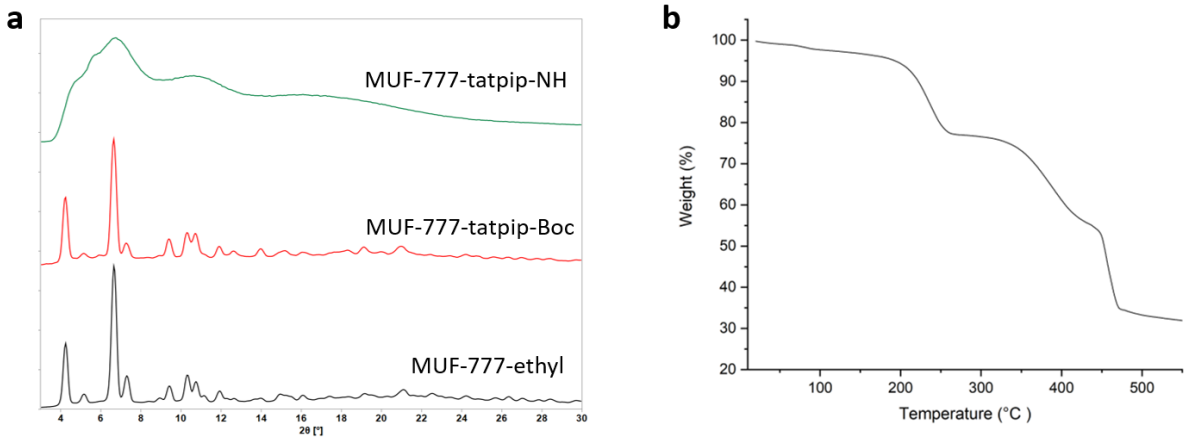

Figure 4. 13 a) PXRD patterns of MUF-777-ethyl, MUF-777-tatpip-Boc and MUF-77-tatpip-NH. b) TGA trace of MUF-777-tatpip-Boc.

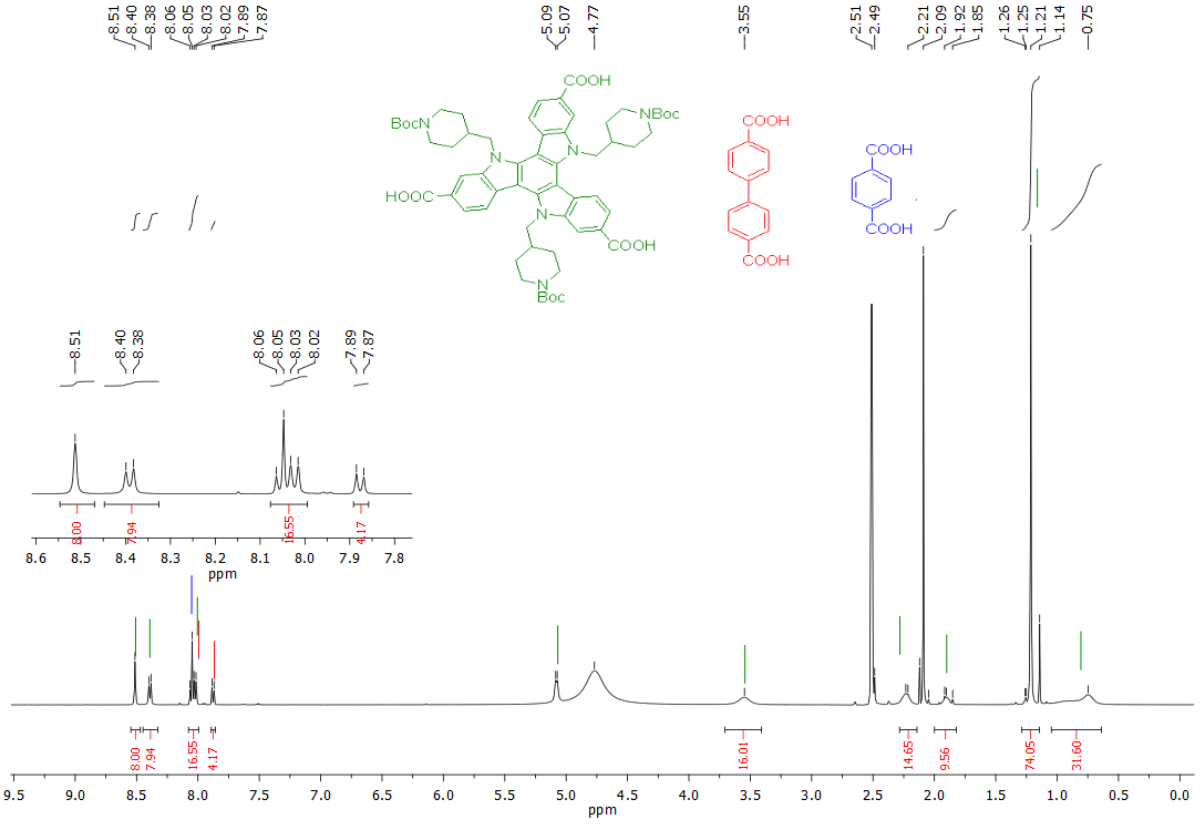

Figure 4. 14 The ^{1}H NMR spectrum of digested MUF-777-tatpip-Boc (in DCl/DMSO-d_6) showing the integrals that match with the formula $[Zn_4O(tatpip\text{-}Boc)_{4/3}(bpdc)_{1/2}(bdc)_{1/2}]$.

To minimize the exposure of the framework to the atmospheric water vapor, a solvothermal deprotection strategy was applied to convert MUF-777-tatpip-Boc into MUF-777-tatpip-NH. This was conducted by heating MUF-777-tatpip-Boc in DMF at 200 °C for 10 hours. PXRD analysis of the solvated MOF revealed that the framework retained its crystallinity after

thermolysis. However, ^{1}H NMR spectrum of the digested MOF showed some complications caused by the peaks belonging to the tat ligand. This result indicates that some undesired reactions occur at the NH site under solvothermal deprotection conditions. It is possible that the piperidinyl group is formylated during the solvothermal deprotection conditions (Figure 4.15).[231]

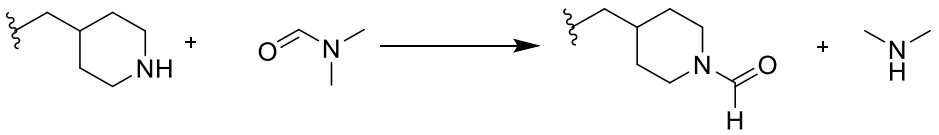

Figure 4. 15 Schematic illustration of a possible reaction that may have occurred between the piperidinyl group on the tat-pip ligand and DMF during solvothermal deprotection of MUF-777-tat-pip-Boc.

4.2.4 Catalysis studies

The catalytic activity of MUF-77-pipcdc-NH was studied in the asymmetric Michael reaction of dibenzoyl methane and β-nitrostyrene (Figure 4.16a), and the Friedel Crafts reaction between indole and β-nitrostyrene (Figure 4.16b). First, the Michael reaction was studied with $CHCl_3$ as the solvent. The use of $CHCl_3$ for the Michael reaction involving secondary amines as catalyst has previously been reported.[232] The catalytic reaction was conducted using a 210 mM stock solution (based on the concentration of β-nitrostyrene), in the presence of 5% catalyst (moles of piperidinyl group with respect to β-nitrostyrene) at room temperature. In the absence of the catalyst no adduct formation was observed over a period of 24 hours. Also, no product was detected when MUF-77-pipcdc-Boc was used as the catalyst. A 9.4% conversion was obtained in the case of MUF-77-pipcdc-NH after 24 hours, demonstrating the catalytic activity of MUF-77-pipcdc-NH originates from the Boc-free piperidinyl group and no dissolved or leached material from MUF-77-pipcdc-Boc is catalytically active. In addition, it was found that after filtering the catalyst from the reaction mixture, no further product formation takes place in the solution. This points out that the catalysis is heterogenous.

To compare this result with the homogeneous catalysis, we also tested the catalytic activity of the molecular catalyst, Me_2pipcdc-NH. Because of the poor solubility of Me_2pipcdc-NH in $CHCl_3$, homogeneous catalysis could not be performed under the conditions mentioned above. The best solubility was obtained in a mixture of $CHCl_3$ and DMSO. However, only trace amount of product was detected over a period of 24 hours at room temperature. Here, it is

possible that the hydrogen bonding between the NH site of the catalytic unit and DMSO prevents the catalytic reaction from happening.

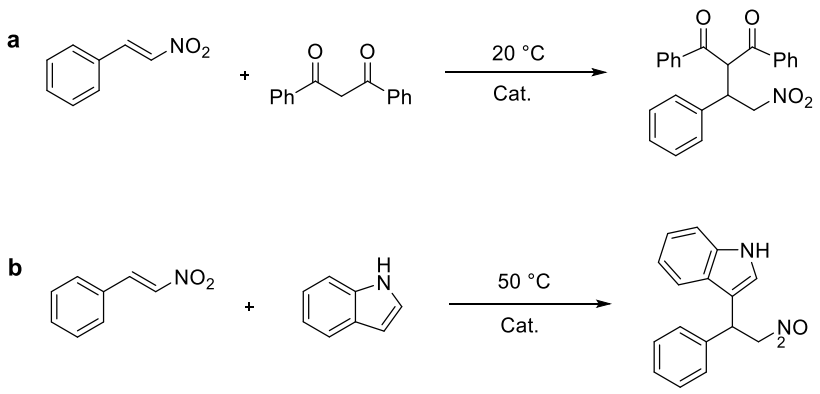

Figure 4. 16 Michael (a) and Friedel-Crafts (b) reactions catalysed by MUF-77-pipcdc-NH and MUF-77-azecdc-NH.

The catalytic activity of MUF-77-pipcdc-NH was further tested using toluene as the solvent. This change increased the conversion to 12.9%. Then, the reusability of the catalyst was investigated in both $CHCl_3$ and toluene. The recyclability experiments showed that the catalytic activity dropped dramatically in both solvents, resulting in 2.1% and 1.8% conversion respectively. The ^1H NMR spectra of digested MOF samples after catalysis (for both reactions in $CHCl_3$) revealed that no significant change had occured in the framework (Electronic Appendix C). Therefore, the decrease is possible due to the way the recyclability test was performed. The catalyst was washed with fresh solvent after the first run and then used for the second run without being completely dried in order to minimize the exposure of the catalyst to atmospheric water vapor. Because the volume of reaction mixture was relatively small, the solvent remained within the crystals can drop the concentration of solution and therefore decelerate the reaction.

Next, the Friedel Crafts reaction was studied. Firstly, the experiments were performed in $CHCl_3$, with a 210 mM stock solution (based on the concentration of β-nitrostyrene), in the presence of 5% catalyst (moles of piperidinyl group with respect to β-nitrostyrene) at 50 °C. A 55% conversion was obtained after 24 hours, when MUF-77-pipcdc-NH was used as catalyst. However, control experiments results showed that the reaction can progress without catalyst in $CHCl_3$, producing about 2% conversion at room temperature for 24 hours. After this result, toluene was used as the solvent and no product formation was observed in the stock solution at 50 °C for 24 hours. We also observed that the use MUF-77-pipcdc-Boc as catalyst does not

produce any products, indicating is MUF-77-pipcdc-Boc catalytically inactive and there is no catalytically-active species that dissolve or leach from this sample. The use of MUF-77-pipcdc-NH produced a 33.5% conversion at this condition. In addition, a conversion of 9.1% was obtained for the second run (Table 4.2).

Table 4. 1 Michael reaction catalysed by MUF-77-pipcdc-NH and Me_2pipcdc-NH.

Entry	Catalyst	Solvent	Conversion (%)
1	-	$CHCl_3$	-
2	MUF-pipcdc-Boc	$CHCl_3$	-
3	MUF-pipcdc-NH	$CHCl_3$	9.4
4	Cycle 1	$CHCl_3$	2.1
5	Me_2pipcdc-NH	$CHCl_3$/DMSO	Trace
6	MUF-pipcdc-NH	Toluene	12.9
7	Cycle 1	Toluene	1.8

Reaction conditions: 5 mol % catalyst (piperidinyl unit relative to amount of β-nitrostyrene), room temperature, 24 h.

Table 4. 2 Friedel-Crafts reaction catalysed by MUF-77-pipcdc-NH and Me2pipcdc-NH.

Entry	Catalyst	Solvent	Conversion (%)
1	-	Toluene	-
2	MUF-pipcdc-Boc	Toluene	-
3	MUF-pipcdc-NH	Toluene	33.5
4	Catalyst filtered	Toluene	-
5	Cycle 1	Toluene	9.1

Reaction conditions: 5 mol % catalyst (piperidinyl unit relative to amount of β-nitrostyrene), 50 °C, 24 h.

The catalysis study for MUF-77-azecdc-NH was performed using 5% catalyst (moles of azetidinyl group with respect to β-nitrostyrene) at room temperature for the Michael reaction, and at 50 °C for Friedel Crafts reaction. As shown in Table 4.3. MUF-77-azecdc-NH is catalytically active towards both reactions, producing 8.5% of conversion for Michael reaction and 43.7% of conversion for Friedel Crafts reaction. This was confirmed with control experiments. It was found that MUF-77-azecdc-Boc is catalytically inactive, and the progress of both reactions stops after filtering the catalyst. These control experiments imply that the Boc-free azetidinyl group is the only catalytically-active site, the catalysis is heterogenous in nature and no dissolved or leached components are catalytically active.

Table 4. 3 Michael and Friedel Crafts reaction catalysed by MUF-77-azecdc-NH.

Reaction	Catalyst	Temperature	Solvent	Conversion (%)
Michael	MUF-azecdc-NH	r.t.	Toluene	8.5
Michael	Cycle 1	r.t.	Toluene	Trace
Michael	MUF-azecdc-Boc	r.t.	Toluene	-
Friedel Crafts	MUF-azecdc-NH	50 °C	Toluene	43.7
Friedel Crafts	Cycle 1	50 °C	Toluene	9.7
Friedel Crafts	MUF-azecdc-Boc	50 °C	Toluene	-

Reaction conditions: 5 mol % catalyst (azetidinyl unit relative to amount of β-nitrostyrene), 24 h.

4.3 Conclusion

The synthesis of new MUF-77 analogues containing secondary amine functionalities, were successfully achieved by ligand functionalization followed by post-synthetic thermal deprotection. These frameworks showed catalytic activity for the Michael addition reaction of dibenzoyl methane to β-nitrostyrene, and the Friedel Crafts reaction of indole with β-nitrostyrene. By introducing chiral modulator groups in the pores of these materials, their analogues can be prepared for asymmetric catalysis. In addition, triethylamine functionalized MUF-77-teacdc was also synthesized. Its characterization results showed that the amino group is involved with some undesired reaction under solvothermal MOF synthesis conditions thus

the resulting framework is not phase-pure. This is possibly due to the reaction between the triethyl amino group and benzoic acid. Synthesis of phase-pure MUF-77-teacdc may be possible without the use of benzoic acid in future work. Moreover, it may be possible with room temperature synthesis method which was used for MUF-777 variants in Chapter 2. Finally, the preparation of MUF-777-tatpip-NH was not successful with thermal deprotection technique due to poor stability of this material. A solvothermal deprotection method was also tried using DMF as solvent. It was found that some side reaction occurs on the NH site under these conditions. This is likely due to the formylation of the piperidinyl group by DMF. A successful solvothermal deprotection of MUF-777-tatpip-Boc may be possible by using an inert solvent such as toluene.

4.4 Experimental section

4.4.1 General procedure

All starting materials and solvents were used as received from commercial sources without further purification unless otherwise noted. Column chromatography was carried out on silica gel (grade 60, mesh size 230-400, Scharlau). NMR spectra were recorded at room temperature (unless otherwise noted) on Bruker-400 and Bruker-500 Avance instruments, with the use of the solvent proton as an internal standard. High performance liquid chromatography (HPLC) was carried out using a Thermo Fisher Dionex Ultimate 3000 system equipped with a UV detector.

4.4.3 Ligand synthesis

Synthesis of Me_2pipcdc-Boc, H_2pipcdc-Boc and Me_2pipcdc-NH are presented below. Detailed synthetic procedures and spectroscopic data on other ligands and their intermediates are available in Electronic Appendix C.

Me_2pipcdc-Boc

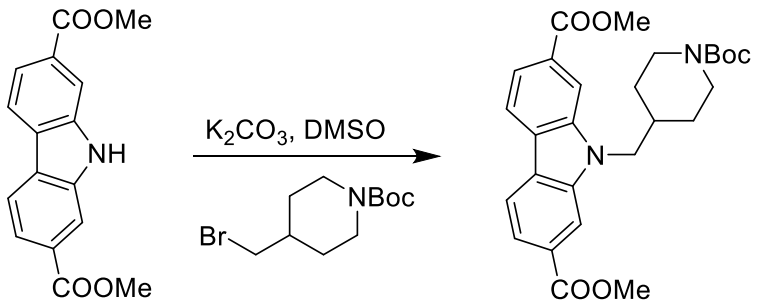

Dimethyl 9H-carbazole-2,7-dicarboxylate (142 mg, 0.5 mmol) and K_2CO_3 (500 mg) were combined in DMSO (3 mL) and stirred at RT for 15 minutes. Then, 1-Boc-4-bromomethylpiperidine (278 mg, 1 mmol) was added and the reaction mixture stirred at 70 °C overnight. After cooling to RT, the mixture was poured into cold water and stirred for half an hour. A white solid was filtered off, washed with water and dried. This material was purified by column chromatography on silica gel using EA/hexane (1:3) as eluent. Yield: 230 mg, 0.48 mmol, 96%. ^{1}H NMR (500 MHz, $CDCl_3$): δ 8.24-8.13 (m, 4H), 7.97 (d, *J* = 8.2 Hz, 2H), 4.32 (d, *J* = 7.4 Hz, 2H), 4.15 (br, 2H) 4.03 (s, 6H), 2.62 (t, *J* = 12.6 Hz, 2H) 2.22 (br, 1H), 1.61-1.59 (m, 3H), 1.44-1.31 (m, 12H) ppm. ^{13}C NMR (125 MHz, $CDCl_3$): δ 167.57, 154.67, 141.38, 128.48, 125.64, 120.87, 120.59, 111.04, 108.06, 79.59, 52.36, 48.86, 36.81, 30.24, 28.45 ppm. ESI (positive mode, CH_3OH): m/z = 503.2109 ($[C_{27}H_{32}N_2O_6Na]^+$, calcd. 503.2153).

H_2pipcdc-Boc

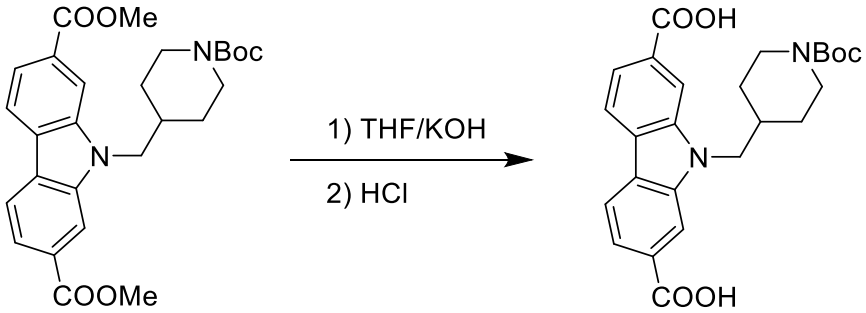

Me_2pipcdc (180 mg, 0.38 mmol) was dissolved in 20 mL 1:1 (V/V) THF/KOH (aq., 1M) and the solution was refluxed overnight. THF was removed under reduced pressure and the reaction mixture then was acidified with 1 M aqueous HCl while it was kept on an ice bath. pH was adjusted to around 4-5, and the mixture was stirred for 1 hour. A white solid was filtered off, washed with water and dried under vacuum. Yield: 160 mg, 0.35 mmol, 94%. ^{1}H NMR (500 MHz, DMSO-*d*6): δ 13.08 (br, 2H), 8.34-8.29 (m, 4H), 7.85 (d, *J* = 8.1 Hz, 2H), 4.47 (d, *J* = 7.1 Hz, 2H), 3.92 (br, 2H), 2.64-2.60 (m, 2H), 2.12 (m, 1H), 1.51-1.26 (m, 13H) ppm. ^{13}C NMR (125 MHz, DMSO-*d*6): 168.38, 154.16, 141.54, 129.75, 125.06, 121.38, 120.56, 111.86, 78.96, 47.95, 36.68, 29.84, 28.57 ppm. ESI (negative mode, CH_3OH): m/z = 451.1823 ($[C_{25}H_{27}N_2O_6]^-$, calcd. 451.1864).

Me_2pipcdc-NH

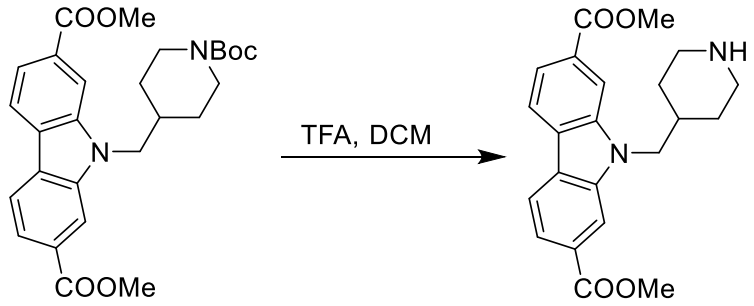

Me_2pipcdc (50 mg, 0.1 mmol) was dissolved in DCM (5 mL) and the solution was cooled on an ice-water bath. To this solution, TFA (1 mL) was added slowly. The solution then was stirred overnight. After addition of water (10 mL), solid K_2CO_3 was added to neutralize the acid. Then DCM was removed, and the white solid filtered off, washed with water and dried under vacuum. Yield: 38 mg, 0.1 mmol, 100%. ^{1}H NMR (500 MHz, DMSO-*d6*): δ 8.41 (d, *J* = 8.1 Hz, 2H), 8.32-8.28 (m, 3H), 7.89 (d, *J* = 8.2 Hz, 2H), 4.56 (d, *J* = 7.0 Hz, 2H), 3.94 (s, 6H) 3.22 (d, *J* = 12.2 Hz, 2H), 2.79 (t, *J* = 12.5 Hz, 2H), 2.27 (s, 1H), 1.61-1.24 (m, 4H) ppm. ESI (positive mode, CH_3OH): m/z = 381.1775 ($[C_{22}H_{25}N_2O_4]^+$, calcd. 381.1809).

4.4.3 MOF synthesis

$[Zn_4O(hmtt)_{4/3}(pipcdc\text{-}NH)_{1/2}(bdc)_{1/2}]$

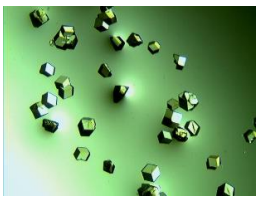

H_3hmtt (17.0 mg, 28.6 μmol), H_2pipcdc-Boc (14.4 mg, 31.8 μmol), terephthalic acid (6.5 mg, 39.1 μmol), benzoic acid (55.0 mg, 450 μmol) and $Zn(NO_3)_2{\cdot}4H_2O$ (74.0 mg, 283.2 μmol) were dissolved in a mixed solvent of dry DEF (5 mL) and water (0.100 mL). The reaction was carried out in an 85 °C isothermal oven for 19 hours to obtain colorless crystals. The mother liquor was replaced with anhydrous DMF and this process was repeated five times. The DMF was then replaced with fresh anhydrous acetone and the solvent replenished five times within an hour. The acetone-occluded crystals were thermolyzed to produce $[Zn_4O(hmtt)_{4/3}(pipcdc\text{-}NH)_{1/2}(bdc)_{1/2}]$ by heating the crystals at a rate of 20 °C / min and holding the temperature at 220 °C for 20 hours under a dynamic vacuum. Yield: 16.5 mg.

$[Zn_4O(hmtt)_{4/3}(azecdc\text{-}NH)_{1/2}(bdc)_{1/2}]$

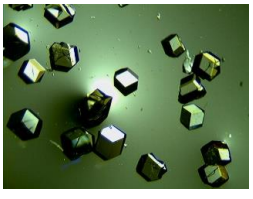

H_3hmtt (15.7 mg, 26.4 μmol), H_2azecdc-Boc (12.7 mg, 29.9 μmol), terephthalic acid (6.6 mg, 39.7 μmol), benzoic acid (50.5 mg, 413 μmol) and $Zn(NO_3)_2{\cdot}4H_2O$ (71.0 mg, 271.7 μmol) were dissolved in a mixed solvent of dry DEF (5 mL) and water (0.100 mL). The reaction was carried out in an 85 °C isothermal oven for 19 hours to obtain colorless crystals. The mother

liquor was replaced with anhydrous DMF and this process was repeated five times. The DMF was then replaced with fresh anhydrous acetone and the solvent replenished five times within an hour. The acetone-occluded crystals were thermolyzed to produce $[Zn_4O(hmtt)_{4/3}(azecdc\text{-}NH)_{1/2}(bdc)_{1/2}]$ by heating the crystals at a rate of 20 °C / min and holding the temperature at 220 °C for 20 hours under a dynamic vacuum. Yield: 14.5 mg.

4.4.4 ^{1}H NMR analysis of digested MOF samples

The following protocol was used for digestion of the MOFs for ^{1}H NMR spectroscopy: The sample was washed with dry acetone then soaked in dry acetone then desolvated *in vacuo*. As appropriate, 0.60 mL of either 0.15 M KOH/D_2O solution or DCl/DMSO-d_6 (10 µL/60 mL) solution was used to digest around 3 mg MOF. The NMR spectrum was acquired with the clear solution of the dissolved framework. The NMR spectrum was acquired with the clear solution of the digested framework.

4.4.5 Powder X-ray diffraction patterns

All powder X-ray diffraction measurements were carried out on a Rigaku Spider X-ray diffractometer with Cu K_α radiation (Rigaku MM007 microfocus rotating-anode generator), monochromated and focused with high-flux Osmic multilayer mirror optics, and a curved image plate detector. Samples were kept damp with solvent prior to and during measurements. The two-dimensional images of the Debye rings were integrated with 2DP to give 2θ vs I diffractograms. Predicted powder patterns were generated from single crystal structures using Mercury.

4.4.6 Single crystal X-ray diffraction

The single crystal X-ray diffraction analysis for MUF-77-pipcdc-NH and MUF-77-azecdc-NH were performed at 133 K. Individual crystals were selected under a microscope then mounted on a polymer mount with a minimum amount of Fomblin® Y oil. A Rigaku Spider diffractometer equipped with a MicroMax MM007 rotating anode generator (Cu_α radiation, 1.54178 Å), high-flux Osmic multilayer mirror optics, and a curved image-plate detector was used to collect the data. The data were integrated and scaled and averaged with FS Process.[182] Using Olex2[183], the structure was solved with the SHELXT[184] structure solution program using intrinsic phasing and refined with the ShelXL[185] refinement package using least squares minimization.

Crystallographic data details are summarized in Table 4.4. All zinc, oxygen and carbon atoms of the truxene ligands and bdc backbones were found in the electron density difference maps and refined anisotropically. Hydrogen atoms were calculated and refined as a riding model. All atoms in the carbazole ligand were found in the electron density difference map. However, nitrogen atom, and carbon atoms of the two rings and piperidinyl (and azetidinyl) group were also disordered over eight positions, so the corresponding atomic occupancies were fixed at 0.125 with a fixed isotropic displacement parameter (0.05). Phenyl rings were modelled as ideal hexagons.

Table 4. 4 Crystallographic data summary.

Compound	**MUF-77-pipcdc-NH**	**MUF-77-azecdc-NH**
Formula	$C_{62}H_{50}NO_{13}Zn_4$	$C_{61}H_{48}NO_{13}Zn_4$
Formula weight	1278.51	1264.48
Crystal size (mm)	0.32 × 0.28 × 0.26	0.23 × 0.22 × 0.19
Temperature (K)	133	133
Wavelength (Å)	1.54178	1.54178
Crystal system	cubic	cubic
Space group	*Pm*-3	*Pm*-3
Unit cell length (Å)	29.9415(5)	29.9559(13)
Unit cell volume ($Å^3$)	26842.4(13)	26881(3)
Z	6	6
D_{calc} (g cm^{-3})	0.475	0.469
μ (mm^{-1})	0.780	0.777
F(000)	3918.0	3870.0
Reflns coll./unique, R_{int}	63176 / 9102, 0.050	63111 / 9210, 0.069
Data range	8 Å > d > 0.81 Å	8 Å > d > 0.81 Å
Completeness	99%	99%
T_{min}, T_{max}	0.490, 1.00	0.506, 1.00
R indices for data with	R_1 = 0.0817	R_1 = 0.0753
I>2σ(I)	wR_2 = 0.2650	wR_2 = 0.2164
R indices for all data	R_1 = 0.0934 wR_2 = 0.2800	R_1 = 0.1225 wR_2 = 0.2473

Largest difference peak and hole (e $Å^{-3}$)	1.23/ −0.79	0.51/ −0.63

4.4.7 Catalysis

Experimental protocol for Michael reaction: A stock solution (210 mM) was prepared with *β*-nitrostyrene (limiting reagent, 156 mg, 1.05 mmol), dibenzoyl methane (471 mg, 2.1 mmol), nitrobenzene (standard, 30 µL) in $CHCl_3$ (5 mL) toluene (5 mL). In a typical experiment, 0.2 mL of stock solution was added to a 1.5 mL HPLC sample vial together with a pre-weighed quantity of desolvated catalyst. The mass of catalyst was chosen so that it contained 5 mol% of piperidinyl or azetidinyl group relative to *β*-nitrostyrene. The reaction mixture was allowed to stand at 20 °C for 24 hours. Then 75 µL of the supernatant was diluted with 425 µL of $CHCl_3$ or CH_3CN and 3 µL of diluted solution was subjected to HPLC analysis. HPLC analysis was carried out under the following conditions: Lux Cellulose-1; mixed solvent of MeOH and deionized water (87:13 v/v); flow rate of 0.7 ml/min. Products were detected according their absorption of 254 nm UV light. The conversion of *β*-nitrostyrene was calculated by comparing the ratio of its peak area and that of the nitrobenzene standard.

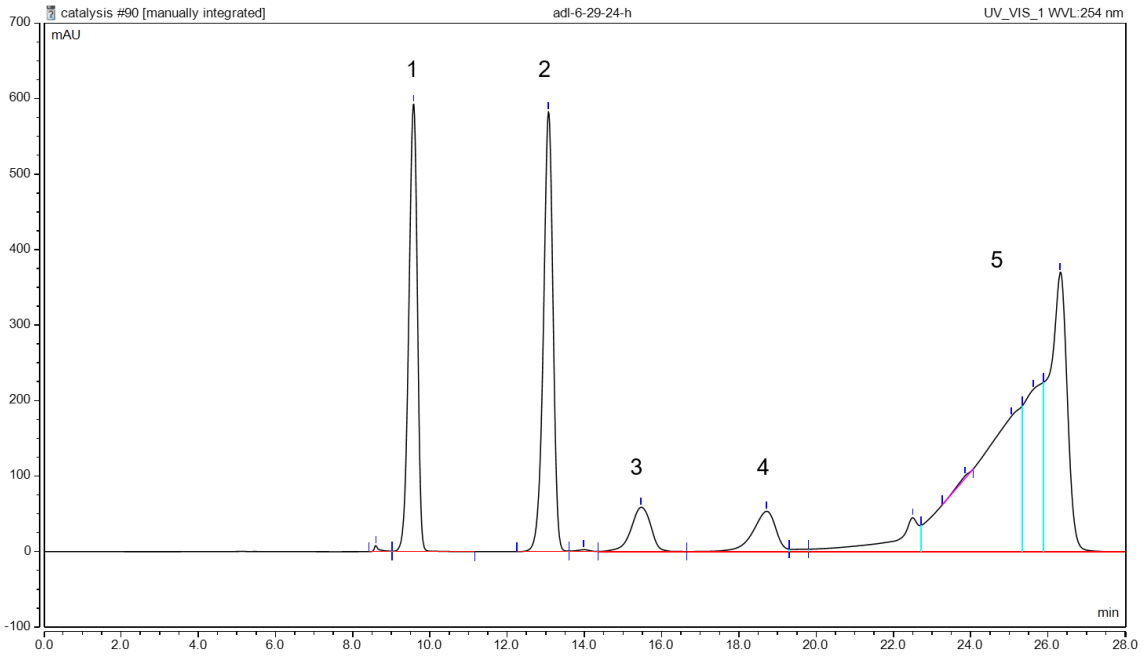

Figure 4. 17 A HPLC chromatogram of the reaction mixture (from a Michael reaction). Peak 1: nitrobenzene, peak 2: *β*-nitrostyrene, peak 3 and 4: two enantiomers of the product, peak 5: dibenzoyl methane.

Experimental protocol for Friedel Crafts reaction: A stock solution (210 mM) was prepared with β-nitrostyrene (limiting reagent, 313 mg, 2.1 mmol), indole (313 mg, 2.67 mmol), nitrobenzene (standard, 30 µL) in $CHCl_3$ (10 mL) toluene (10 mL). In a typical experiment, 0.2 mL of stock solution was added to a 1.5 mL HPLC sample vial together with a pre-weighed quantity of desolvated catalyst. The mass of catalyst was chosen so that it contained 5 mol% of piperidinyl or azetidinyl group relative to *β*-nitrostyrene. The reaction mixture was allowed to stand at 20 °C for 24 hours. Then 75 µL of the supernatant was diluted with 425 µL of $CHCl_3$ or CH_3CN and 3 µL of diluted solution was subjected to reverse-phase HPLC analysis. HPLC analysis was carried out under the following conditions: Lux Cellulose-1; mixed solvent of MeOH and deionized water (95:5 v/v); flow rate of 0.6 ml/min. Products were detected according their absorption of 254 nm UV light. The conversion of *β*-nitrostyrene was calculated by comparing the ratio of its peak area and that of the nitrobenzene standard. Figure 6 shows typical HPLC chromatograms of a mixture.

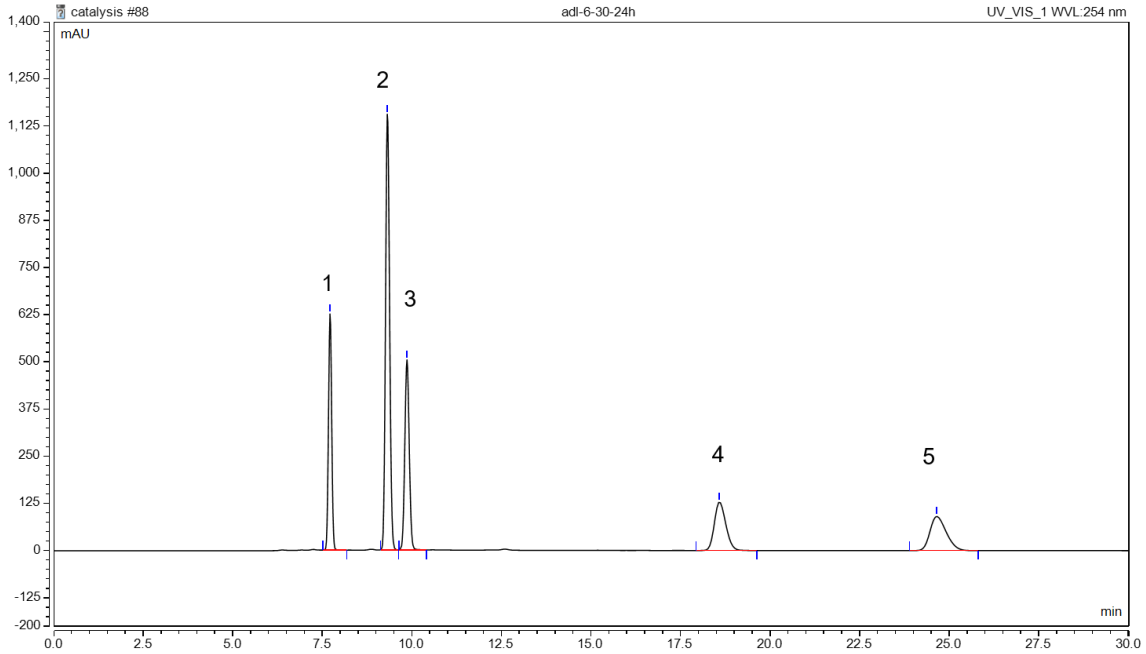

Figure 4. 18 A HPLC chromatograph of the reaction mixture (from a Friedel-Crafts reactions). Peak 1: nitrobenzene, peak 2: indole, peak 3: *β*-nitrostyrene, peak 4 and 5: two enantiomers of the product.

4.4.8 Thermogravimetric analysis (TGA)

Thermogravimetric analyses were performed on a TA Instruments Q50 instrument. Freshly prepared MOF samples were first washed with DMF and then with acetone. After acetone was

decanted, the samples were dried under vacuum. Samples were then transferred to an aluminium sample pan and then measurements were performed under an N_2 flow with a heating rate of 5 °C/min.

Chapter 5 Synthesis and Characterization of Zn-carboxylate MOFs Containing Triazatruxene Ligands

5.1 Introduction

The structural and chemical features of organic ligands have an important role in the properties and potential uses of MOFs. Introducing functional groups onto ligands is a common strategy for tuning the chemical and physical properties of the pores of the resulting frameworks. This requires designing ligand backbones which can be easily derivatized. Symmetrically-substituted ligands are also generally desired as they can lead to uniform crystal growth that is free from symmetry-related disorder. Ligand functionalization has been extensively studied in MOFs containing ditopic linkers for a variety of applications, such as gas sorption,[233] separation,[234] catalysis[235] and photoluminescence.[181, 236]

Tritopic carboxylate ligands are commonly used organic linkers in the chemistry of MOFs.[56-57] Researchers have used tritopic linkers to construct MOFs with great stability as well as ultrahigh porosity.[16, 237] Moreover, chiral frameworks containing achiral tritopic linkers have been reported.[238-239] Chiral MOFs have potential applications in chiral separation,[240-241] asymmetric catalysis[217, 242-243] and nonlinear optics.[244] However, common tritopic linkers[16, 61-62, 245] used in the field of MOFs are usually unsubstituted, perhaps, due to the difficult and costly preparation of their symmetrically-substituted derivatives. In Chapter 2, I developed a convenient method for the synthesis of H_3tat derivatives and used them to prepare a series of quaternary multicomponent MOFs. In this chapter, I will focus on the use of these ligands in making binary Zn-carboxylate MOFs. Different functional groups on triazatruxene ligands may help to systematically tune the pore sizes and shapes of resulting binary MOFs.

5.2 Results and discussion

5.2.1 Synthesis and characterization of ligands

In this chapter, six triazatruxene ligands are used for constructing new MOFs. The syntheses of five of these ligands were described in Chapter 2, Scheme 2.1. The synthetic procedure for these ligands initially involved the trimerization of 1*H*-indole-6-carboxylic acid ethyl ester. These ligands were isolated after substitution of the ester (Et_3tat) followed by hydrolysis of the resulting compound. For the synthesis of H_3tat-benzyl, another synthetic procedure was developed. As illustrated in Scheme 5.1, H_3tat-benzyl was synthesized starting

from the previously reported compound, Br_3tat.[167] Br_3tat-benzyl was prepared by alkylation of Br_3tat with benzyl bromide, and purified by column chromatography. A similar synthetic procedure for the benzylation of triazatruxene and its derivatives has previously been reported.[246-247] H_3tat-benzyl was obtained by carboxylation of Br_3tat-benzyl. Although this procedure worked well for the synthesis H_3tat-benzyl, it is not ideal for some functional groups that might be sensitive to the carboxylation step. Because the procedure described in Chapter 2 does not involve a carboxylation step, it can be used for preparation more diverse triazatruxene derivatives. Detailed synthetic procedure and characterization of Br_3tat-benzyl and H_3tat-benzyl are available in the experimental section.

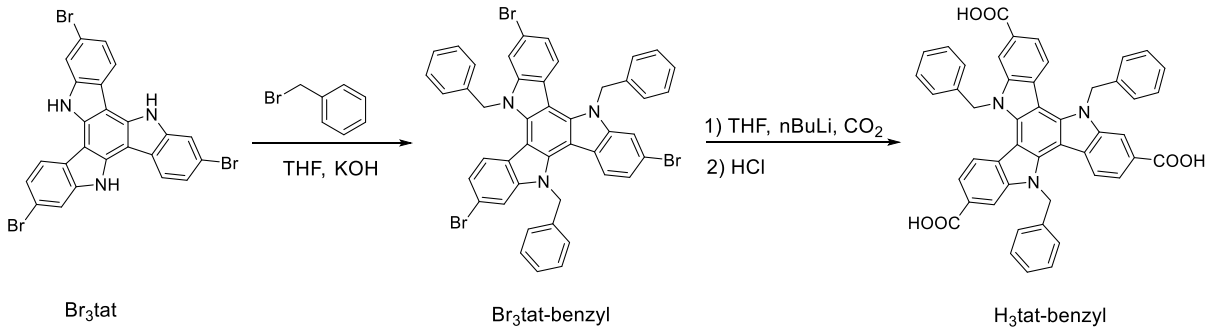

Scheme 5. 1 Synthetic route to H_3tat-benzyl.

5.2.2 Synthesis and characterization of MUF-tat-benzyl

A solvothermal reaction of H_3tat-benzyl with $Zn(NO_3)_2$ in DMF at 85 °C afforded yellow crystals of MUF-tat-benzyl, $[Zn_3(tatbenzyl)_2(H_2O)_2]$ (Figure 5.1). Benzoic acid (BA) was used as a modulator to grow big crystals. The structure of MUF-tat-benzyl was determined by single crystal X-ray diffraction (SCXRD), which was carried on a solvated crystal (in DBF) at room temperature. The data revealed that MUF-tat-benzyl crystallizes in the cubic chiral space group $P4_132$ with a Flack parameter of 0.04(5), indicating the enantiomeric purity of the single crystal although achiral precursors were used. As shown in Figure 5.1, the ligand pairs are connected through a linear trinuclear zinc cluster to form a three-dimensional chiral **(10,3)-a** network. Each asymmetric unit contains three Zn(II) ions, a third of the tat-benzyl ligand and two water molecules. The two peripheral metal ions of trinuclear cluster are tetrahedrally coordinated to three carboxylate oxygen atoms and one water molecule each, while the central metal ion is octahedrally coordinated to six carboxylate oxygen atoms (Figure 5.1c). MOFs containing this type of cluster have been reported in the literature.[76, 156, 248-251]

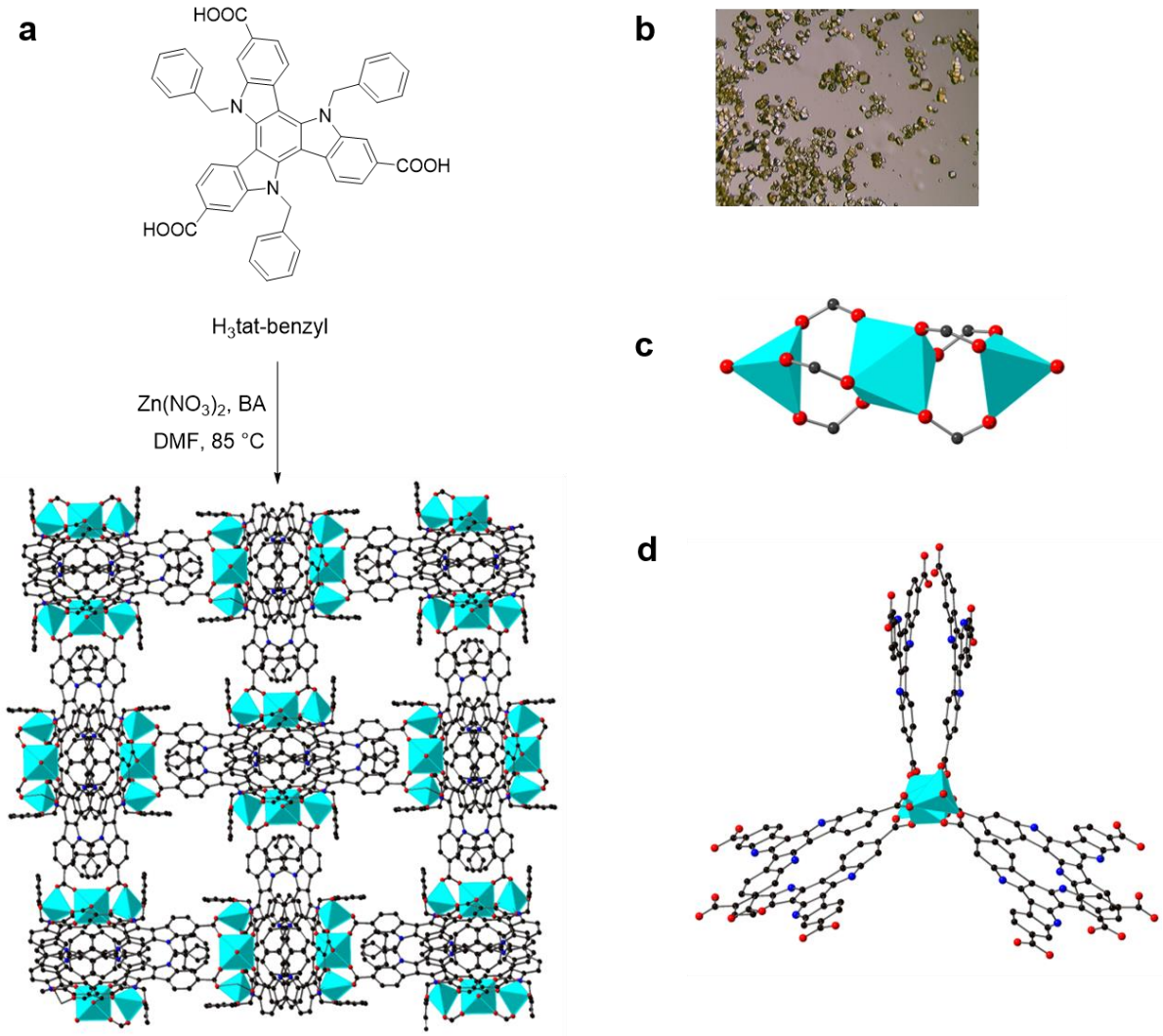

Figure 5. 1 a) Synthetic route to MUF-tat-benzyl and its single crystal structure, b) optical microscopy image of MUF-tat-benzyl crystals c) the trinuclear cluster and d) three pairs of ligands connected to a cluster. Atom colours: carbon: black, oxygen: red, nitrogen: blue, zinc: cyan. Hydrogen atoms, and benzyl groups on ligand pairs are omitted for clarity.

MUF-tat-benzyl has a low crystallographic density (0.70 g/cm^{-3}) and high calculated[168] porosity (void fraction of 69%). As shown in Figure 5.2, the framework possesses two different types of channels. The helical channel extends in the crystallographic *b* axis direction and is 12 Å across (including van der Waals radii) (Figure 5.2a). The length of each side of the triangular channel, along the [111] direction, is approximately 21 Å (distance between two zinc atoms at the corner of triangle) (Figure 5.2b). In the structure of MUF-tat-benzyl, tat-benzyl ligands are nearly planar. The distance between the centroids of the central phenyl rings of pair ligands is about 3.95 Å, which is the range of π-π interaction distance.[252] Also, the two ligands in a pair

do not have a perfect alignment, instead they are offset with a rotational angle of about 30°. The three benzyl groups of each ligand are oriented in the opposite site of stacking face of the ligand and are therefore located in the pores of the framework (Figure 5.2).

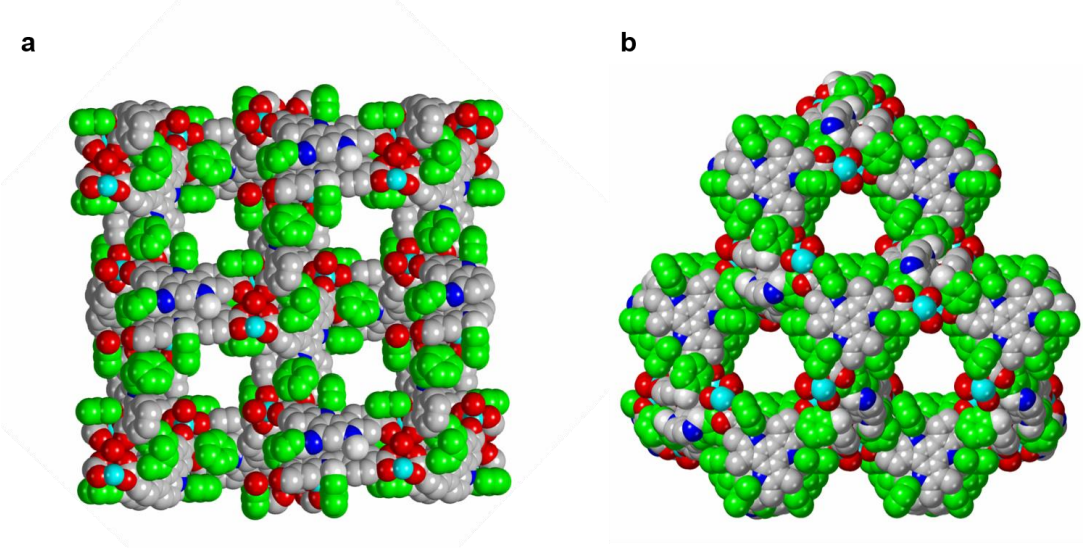

Figure 5. 2 Helical cannels viewed along the b-axis (a) and triangular channels viewed along [111] direction. Atom colours: carbon: black, oxygen: red, nitrogen: blue, zinc: cyan. Benzyl groups are highlighted in green. Hydrogens are omitted for clarity.

The chiral structure of MUF-tat-benzyl is a result of two possible assembly modes of the H_3tat-benzyl ligand pair. The two ligands can stack together in either a clockwise or counter-clockwise fashion, which results in the formation of two enantiomers (Figure 5.3). Although each single crystal MUF-tat-benzyl is constituted by only one of these enantiomers, the bulk sample is a racemic mixture because during the framework formation each of the two enantiomers has an equal chance of crystallization. However, preparation of homochiral MUF-tat-benzyl may be possible by using a chiral additive (modulating agent) during synthesis.[253] Researchers have also reported homochiral frameworks that can be formed through spontaneous symmetry-breaking crystallization without using any chiral additives.[81]

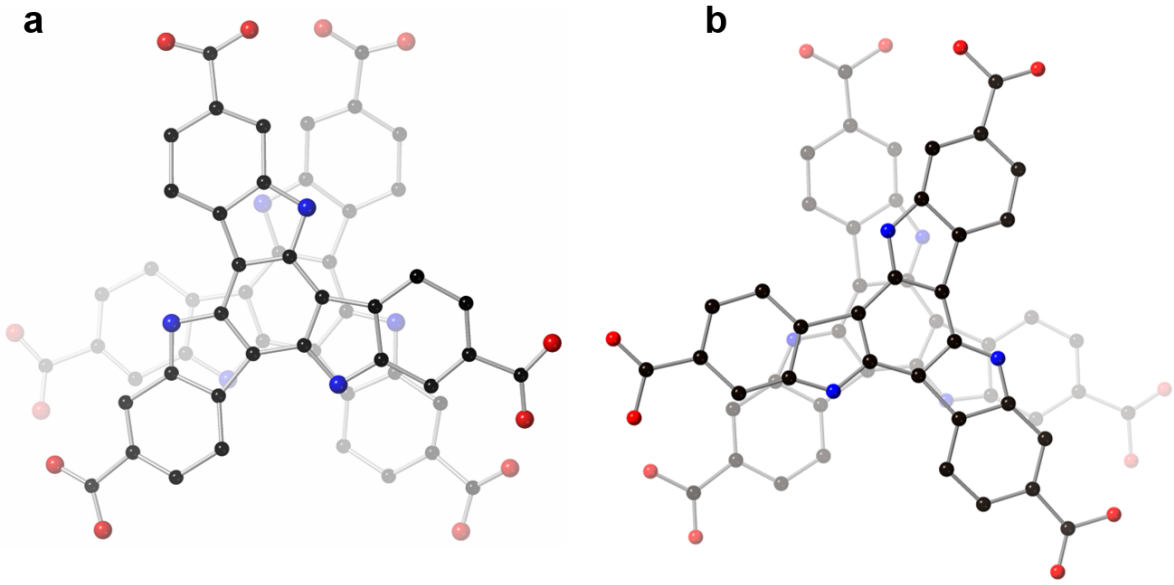

Figure 5. 3 Two possible stacking modes for tat-benzyl ligand pair: a) clockwise, b) counter-clockwise. Atom colours: carbon: black, oxygen: red, nitrogen: blue. Benzyl groups and hydrogens are omitted for clarity.

The bulk identity and thermal stability of MUF-tat-benzyl were investigated by powder X-ray diffraction (PXRD) measurements and thermogravimetric analysis (TGA). All major peaks in the experimental PXRD pattern of MUF-tat-benzyl match well with the simulated pattern from SCXRD model (Figure 5.4a). This result indicates that the single crystal is representative of the pure bulk sample. The desolvated crystals become opaque when exposed to air and lose their crystallinity (Figure 5.4a). This result suggests that desolvated MUF-tat-benzyl has a poor stability towards atmospheric water vapor. The TGA curve shows that MUF-tat-benzyl has a weight loss of 3% from 20 to 100 °C, corresponding the loss of free solvent molecules in the pores. The weight loss between 100 and 200 °C has a value of 2% which matches the percentages of two coordinated water molecules (2.08%) (Figure 5.4b). After this point the curve does not plateau, and the weight loss becomes more pronounced, indicating that the framework is not thermally stable. Poor stability was also observed in some other frameworks containing trinuclear zinc(II) clusters and tritopic linkers.[249] Zhou *et al.* reported that the stability of this type of frameworks can be improved by replacing coordinated aqua ligands with formate or acetate ligands, but this avenue was not pursued in this case.[156]

The porous nature of MUF-tat-benzyl was investigated by carrying out adsorption studies with different gaseous adsorbates at different temperatures. Prior to the adsorption measurements MUF-tat-benzyl was washed with dichloromethane to remove DMF. Then, the sample was activated at a temperature of 80 °C under vacuum for 20 hours to generate a

solvent-free framework. First, the adsorption experiments for N_2 at low temperatures were performed. The experimental data show a type-II isotherm with a low uptake for N_2 at 77 K (Figure 5.5). This is an unexpected result, considering that the structural features of MUF-tat-benzyl indicated high porosity. It might be due to diffusion limitations that arise from strong interactions between N_2 and the aperture of the 1D pore which prevents other molecules from passing through at low temperature.[254-256] Alternatively, it might be due to complete collapse of the framework.

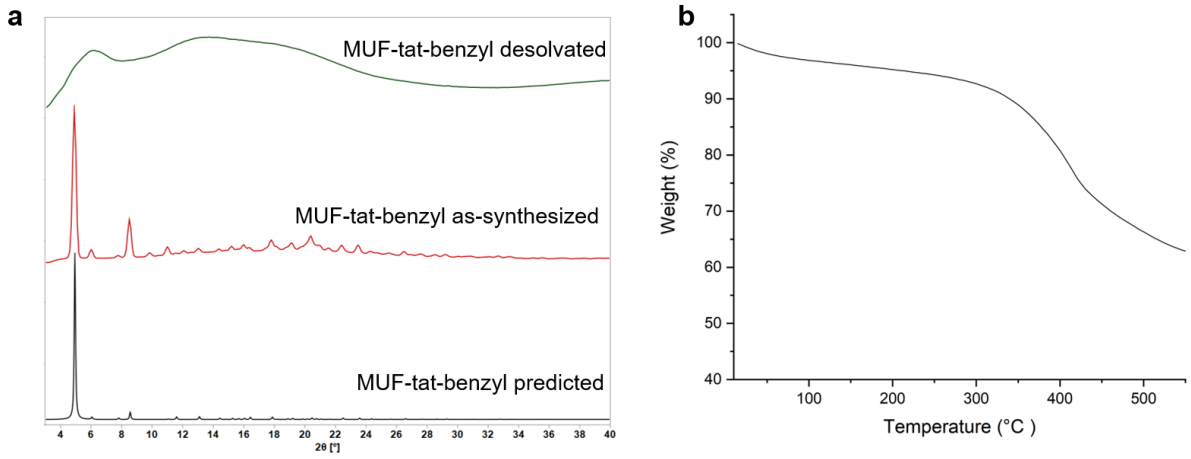

Figure 5. 4 a) PXRD patterns of as-synthesized and desolvated samples of MUF-tat-benzyl and its calculated pattern from its single crystal X-ray structure. b) TGA trace of MUF-tat-benzyl.

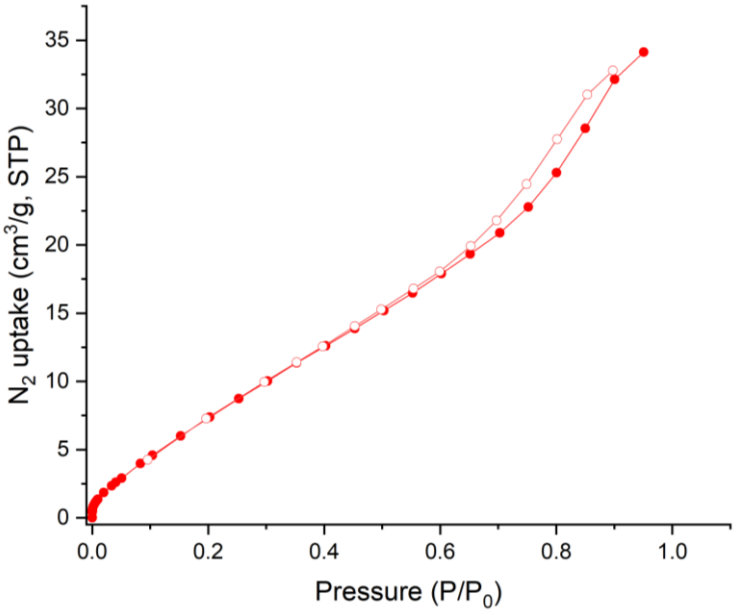

Figure 5. 5 N_2 adsorption (filled circles) and desorption (open circles) isotherms of MUF-tat-benzyl measured at 77 K.

Next, the CO_2 isotherm of MUF-tat-benzyl was measured at 195 K. The isotherm shows a semi-steep rise at low pressure region followed by a gradual increase which reaches a maximum amount of 70 cm^3/g. This result indicates that MUF-tat-benzyl retains its porosity upon removal of solvent molecules and the structure does not collapse. As can be seen in Figure 5.6, there is a significant degree of hysteresis between the adsorption and desorption isotherms. This will be discussed in the following section.

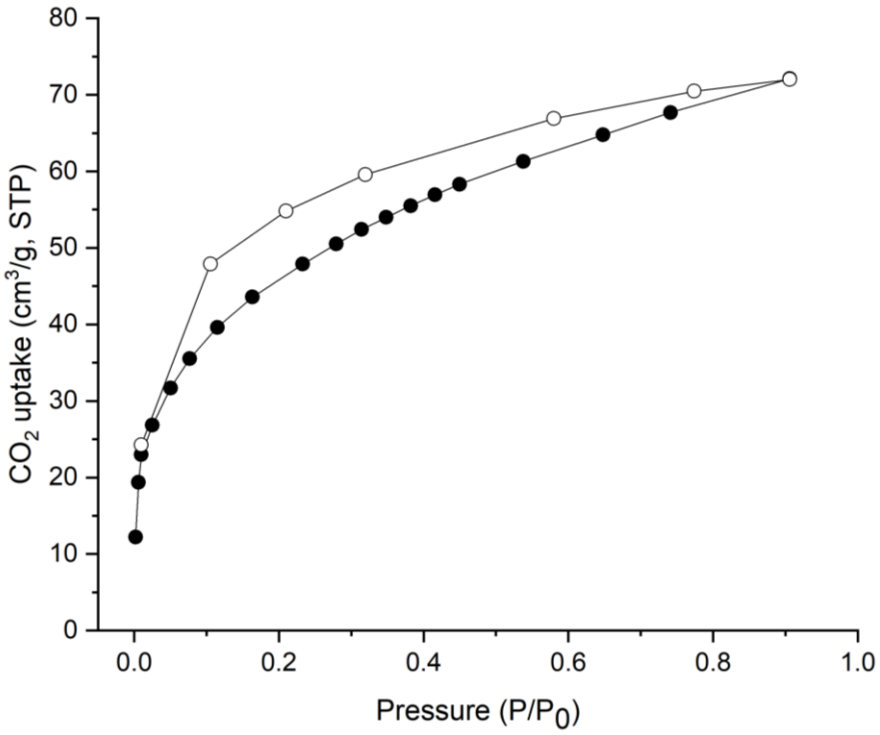

Figure 5. 6 CO_2 adsorption (filled circle) and desorption (open circle) isotherms of MUF-tat-benzyl measured at 195 K.

Further, CO_2, CH_4, C_2H_6 and C_2H_4 isotherms were measured at both 273 K and 293 K (Figures 5.7 and 5.8). As it was observed in the adsorption isotherm of CO_2 at 195 K, hysteresis was also observed in adsorption isotherms of CO_2, C_2H_4 and C_2H_6 at 273 and 293 K. The hysteresis may be related to insufficient equilibration time.[257] Therefore, we investigated the optimal equilibration time for gas sorption measurements by conducting some tests on MUF-tat-benzyl at 293 K using CO_2 as the adsorbate. We performed CO_2 adsorption measurement with 4, 6, 8 and 12 minutes of equilibration time respectively. Although some improvement was observed as the equilibration time was increased, a completely reversible isotherm could not be obtained. Based on this observation it is clear that longer times are needed to completely

remove the hysteresis. To collect a data set in a reasonable amount of time, we decided to perform sorption measurements with six-minutes equilibration time.

The adsorption isotherms of CO_2 show a gradual increase and reach a maximal amount of 22 and 13 cm^3/g at 273 and 293 K, respectively. MUF-tat-benzyl takes up similar amounts of C_2H_6 and C_2H_4 at 293 K, while the adsorption amount of C_2H_4 is slightly higher than that of C_2H_6 at 273 K. At both temperatures, the adsorption amounts of CH_4 is found to be lower than that of other gases. The high C_2H_6 and C_2H_4 adsorption capacity of MUF-tat-benzyl as compared to CH_4 is compatible with the larger size and polarizability of C_2H_6 and C_2H_4 relative to CH_4.[170-172]

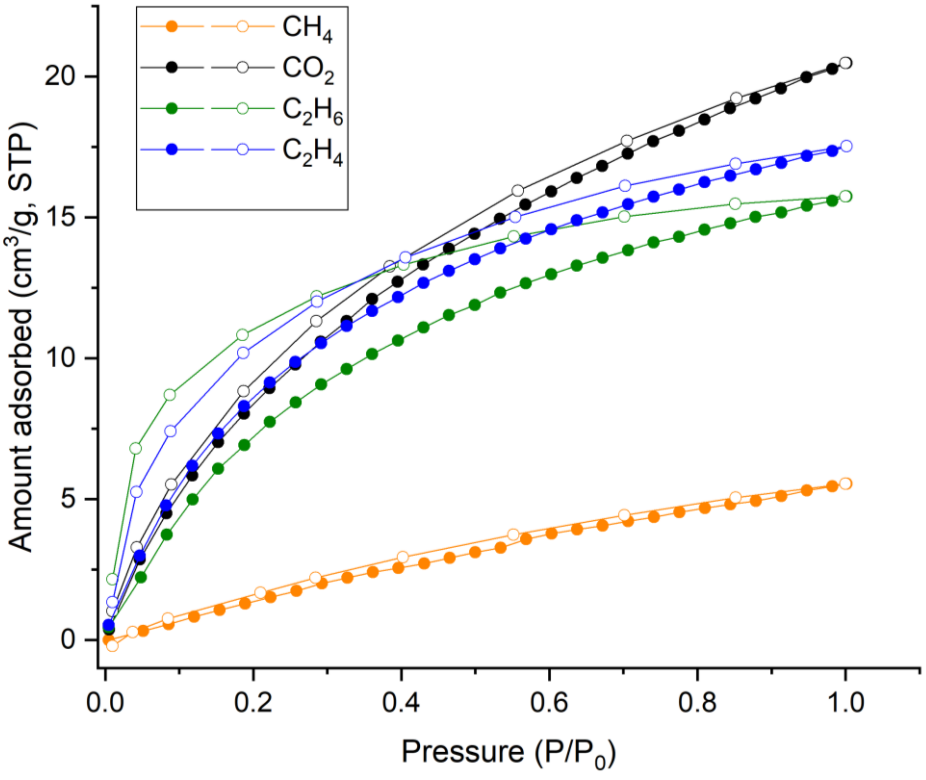

Figure 5. 7 CO_2, CH_4, C_2H_6 and C_2H_4 adsorption (filled circles) and desorption (open circles) isotherms of MUF-tat-benzyl at 273 K.

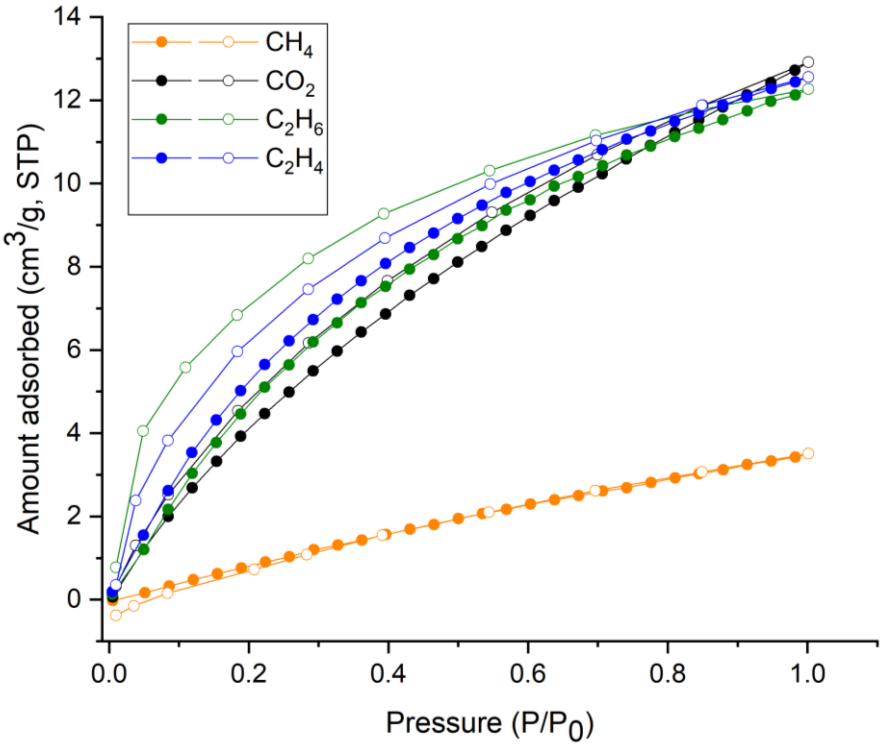

Figure 5. 8 CO_2, CH_4, C_2H_6 and C_2H_4 adsorption (filled circles) and desorption (open circles) isotherms of MUF-tat-benzyl at 293 K.

5.2.2 Synthesis and characterization of MUF-tat

MUF-tat, $[Zn_3(tat)_2(H_2O)_2]$, was obtained by a solvothermal reaction of H_3tat with $Zn(NO_3)_2$ in DMF at 85 °C as orange crystals (Figure 5.9). SCXRD data reveal that MUF-tat crystallizes in the cubic chiral space group $P4_332$. The diffraction pattern simulated from the single crystal model is in agreement with the experimental pattern, demonstrating the phase purity of the bulk sample. The PXRD pattern of MUF-tat also matches the pattern of MUF-tat-benzyl (Figure 5.10). This result indicates that these two MOFs are isostructural. MUF-tat has a much lower crystallographic density (0.47 g/cm^{-3}) and higher porosity (void fraction of 81%) relative to MUF-tat-benzyl. This is because the pores of MUF-tat-benzyl are partially occupied by benzyl groups. Another difference between these two frameworks is the distance that separate the two ligands in a pair. In the case of MUF-tat-benzyl this distance is 3.95 Å. This might be the shortest distance allowed due to the orientation of methylene carbons on benzyl group, which are not planar to the triazatruxene core. On the other hand, in the structure of MUF-tat, substituent-free ligands have a stacking distance of 3.43 Å.

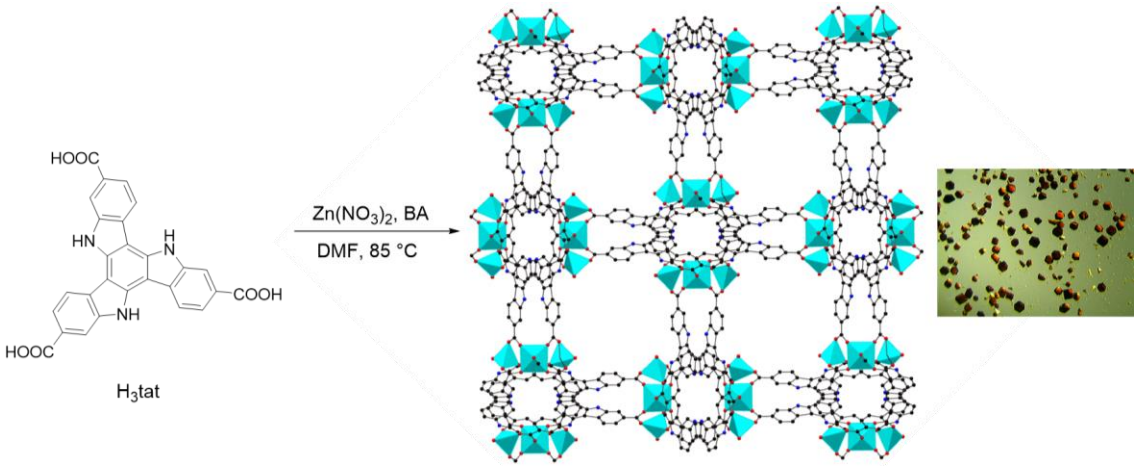

Figure 5. 9 Synthetic route to MUF-tat-benzyl and its single crystal structure. Atom colours: carbon: black, oxygen: red, nitrogen: blue, zinc: cyan. Hydrogen atoms are omitted for clarity.

To obtain solvent-free MUF-tat, the crystals were washed with dichloromethane or acetone before being heated at 80 °C under vacuum for 20 hours. Activated samples were then used for gas sorption measurements. Unlike MUF-tat-benzyl, MUF-tat could only take up a negligible amount of gas (CO_2, CH_4, C_2H_4 and C_2H_6) at both 273 and 293 K which suggests that the framework does not retain its porosity after removal of solvent. As mentioned above, MUF-tat has a greater porosity compared to MUF-tat-benzyl, which could make it more fragile after being desolvated. The PXRD pattern of activated sample shows some weak peaks which are at different positions relative to the pattern of freshly synthesized sample (Figure 5.10). Although, this result does not suggest a complete loss of crystallinity, it is clear that the framework does not remain in its original phase.

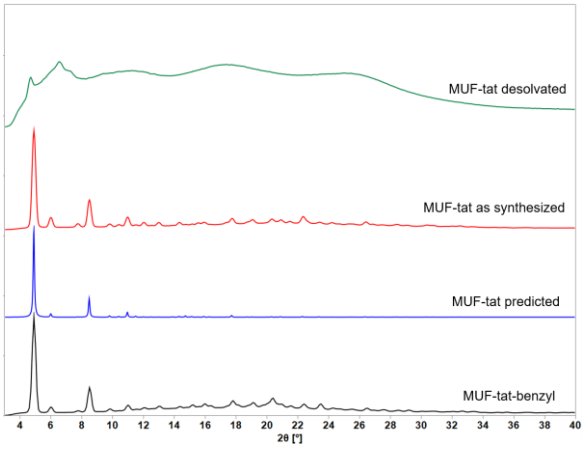

Figure 5. 10 PXRD patterns of MUF-tat-benzyl and MUF-tat (as-synthesized and desolvated samples of MUF-tat and its calculated pattern from its single crystal X-ray structure).

5.2.2 Syntheses and characterization of MUF-tat-butyl, MUF-tat-hexyl, MUF-tat-allyl and MUF-tat-cyclohexyl

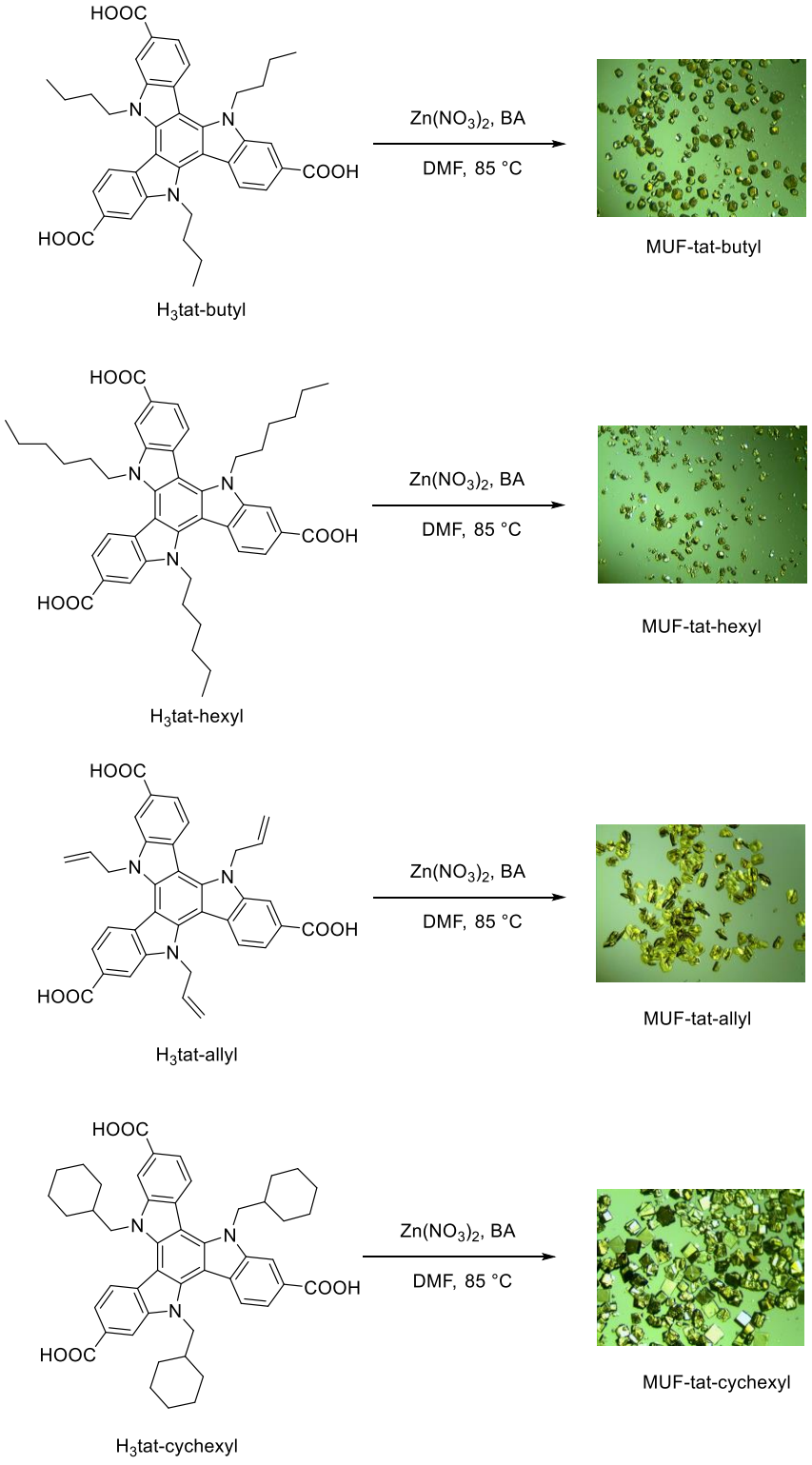

Figure 5. 11 Generalized synthetic route to MUF-tat-butyl, MUF-tat-hexyl, MUF-tat-allyl and MUF-tat-cyclohexyl.

Synthesis of MUF-tat-butyl produced two morphologically different type of crystals with different sizes. The smaller crystals had a rectangular prismatic shape, and they were termed MUF-tat-butyl-**1**. The bigger crystals had a pseudo-cubic shape, and they were termed MUF-tat-butyl-**2**. Both phases did not extinguish at some rotational positions under crossed polarizers on an optical microscope, indicating that they do not belong to a cubic crystal system. PXRD measurements of these crystals showed two distinct patterns, indicating that they are not identical frameworks (Figure 5.12). These patterns also do not match the PXRD pattern of MUF-tat-benzyl (Figure 5.12). We observed that increasing the amount of zinc nitrate and modulator (benzoic acid) increased the formation of phase **1**, yet neither of the two phases could be synthesized in pure form. Both types of crystals become opaque shortly after exposed to air even when immersed in solvent (DMF).

Single crystal X-ray diffraction analysis of MUF-tat-butyl-**1** and MUF-tat-butyl-**2** were not easy due to the fragile nature of their structures. The first data collection for MUF-tat-butyl-1 was performed using a solvated crystal (in DMF). The crystal started to demonstrate poor diffraction shortly after the measurement started. Similar behaviour was also observed for a DBF solvated crystal. Next, the crystal was mounted with a sleeve which has a small amount of solvent (DBF) in it. Using a sleeve prevents air exposure, while the solvent in the sleeve creates a solvent atmosphere, which prevents the evaporation of the solvent in the pores of the crystal. However, even with a sleeve the sample started to lose its crystallinity after about three hours, therefore a complete data set could not be collected. Using the available amount of data, we were able to identify the structure of MUF-tat-butyl-**1**. The PXRD pattern calculated from this data set match the experimental pattern (Figure 5.12). The structure shows similarities to the structure of MUF-tat-benzyl as in this structure ligand pairs are also connected through a linear trinuclear zinc cluster (Figure 5.13). Crystallographic details of the unit cells of MUF-tat-butyl-**1** are given in Table 5.2. Similar procedures were also used for the SCXRD analysis of MUF-tat-butyl-**2.** However, the data collected was not enough for solving it structure.

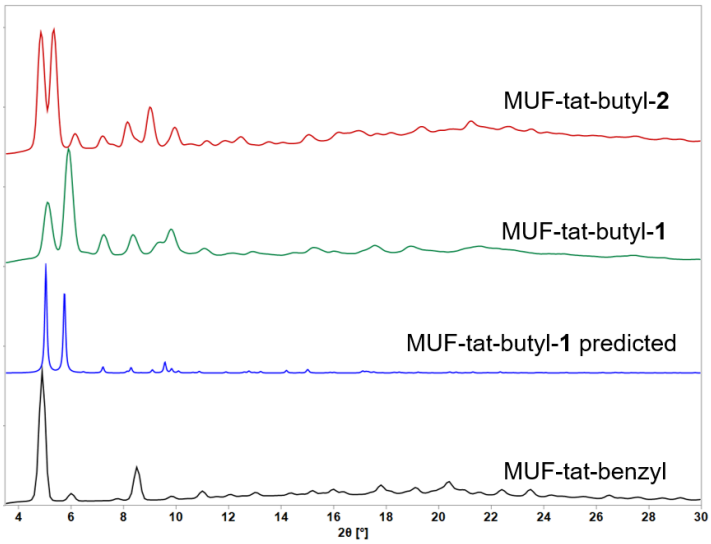

Figure 5. 12 PXRD patterns of MUF-tat-butyl-**1** and MUF-tat-butyl-**2** compared to the pattern calculated from the single crystal X-ray structure of MUF-tat-butyl-**1**.

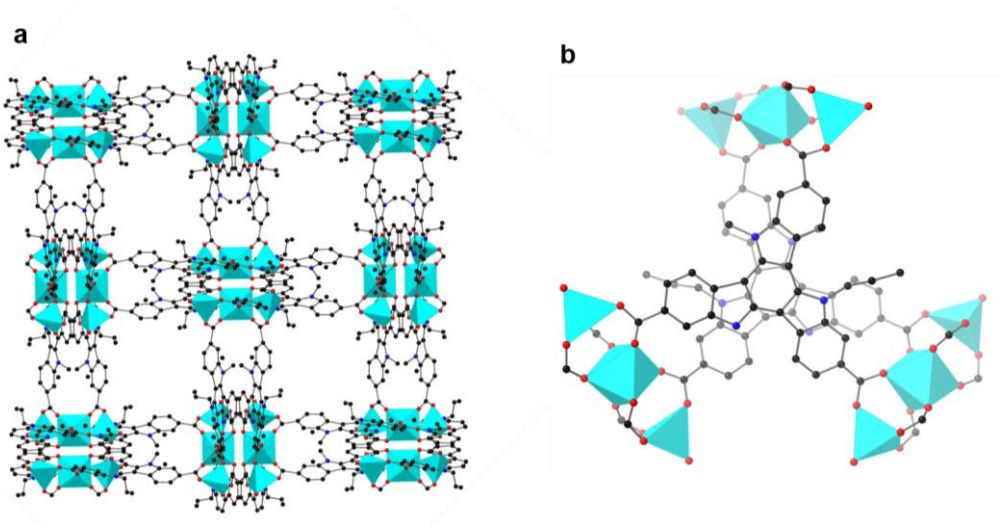

Figure 5. 13 a) Single crystal X-ray structure of MUF-tat-butyl-1. b) A pair of tat-butyl ligand connected to three trinuclear zinc clusters. Atom colours: carbon: black, oxygen: red, nitrogen: blue, zinc: cyan. Hydrogen atoms are omitted for clarity. Some of carbons of butyl group are not present in the model due to poor data quality.

Unlike MUF-tat-butyl, MUF-tat-hexyl produced only one type of crystal (Figure 5.11). MUF-tat-hexyl crystals have a rectangular prismatic shape and do not extinguish at some rotational positions under crossed polarizers on an optical microscope. The PXRD pattern of these crystals is different than that of MUF-tat-benzyl (Figure 5.13). However, the pattern shows similarities to the pattern of MUF-tat-butyl-**2** (Figure 5.13). The stability of MUF-tat-hexyl was also not good enough for collecting a complete data set for SCXRD analysis. Its structure was solved using a part of the data collected. The PXRD pattern calculated from this

data matches with the experimental pattern (Figure 5.13). Crystallographic details of the unit cells of MUF-tat-hexyl are given in Table 5.2.

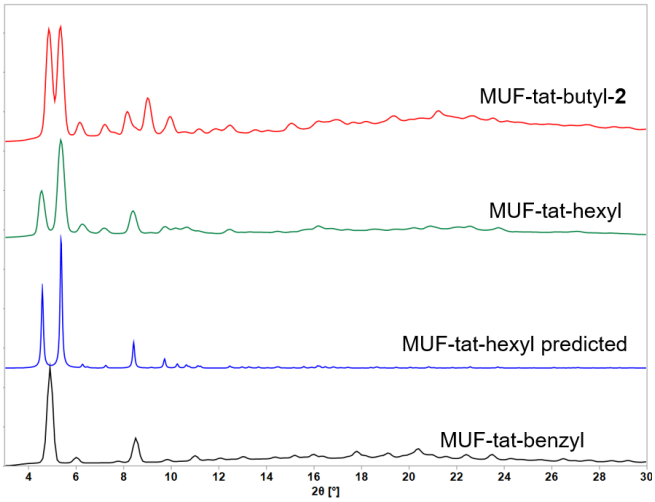

Figure 5. 14 PXRD patterns of MUF-tat-hexyl and MUF-tat-butyl-**2** and MUF-tat-benzyl compared to the pattern calculated from the single crystal structure of MUF-tat-hexyl.

MUF-tat-allyl was obtained as yellow plate-like crystals (Figure 5.11). The crystals are poorly extinguishable under crossed polarizers on an optical microscope, indicating that they belong to a low symmetry crystal system. Its PXRD pattern is different than all the above-mentioned frameworks. To activate MUF-tat-allyl the crystals were washed with acetone and then heated at 100 °C under vacuum for 20 hours. The activated sample was then subjected to gas adsorption measurements, which resulted in insignificant amounts of uptake. This might be due to either the collapse of the framework or insufficient activation. The PXRD pattern of the desolvated sample is different than that of an as-synthesized sample, indicating that a phase transition occurred, or a new material formed (Figure 5.15). SCXRD analysis were done on both as-synthesized and desolvated samples. The desolvated sample diffracted poorly, while the solvated sample had a good diffraction only at the beginning of measurement. Unfortunately, good quality SCXRD data could not be collected for this sample as the crystal diffracted for only a short period of time.

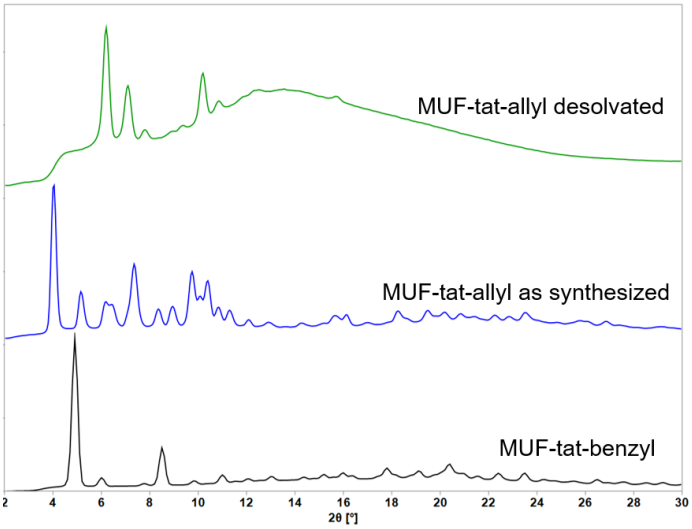

Figure 5. 15 PXRD patterns of as-synthesized and desolvated MUF-tat-allyl samples compared to the pattern of MUF-tat-benzyl.

MUF-tat-cyclohexyl obtained as colourless cube-like crystals. Indeed, these crystals belong to a cubic crystal system as they are fully extinguished at all rotational positions under crossed polarizers on an optical microscope. Although its PXRD pattern shows some similarities with the structure of MUF-benzyl, it has some additional peaks (Figure 5.16). Therefore, it might be either a mixture of two phases or a completely different phase. In addition, all single crystal samples of this MOF showed nearly no diffraction during SCXRD measurements. No further analysis was done on this framework.

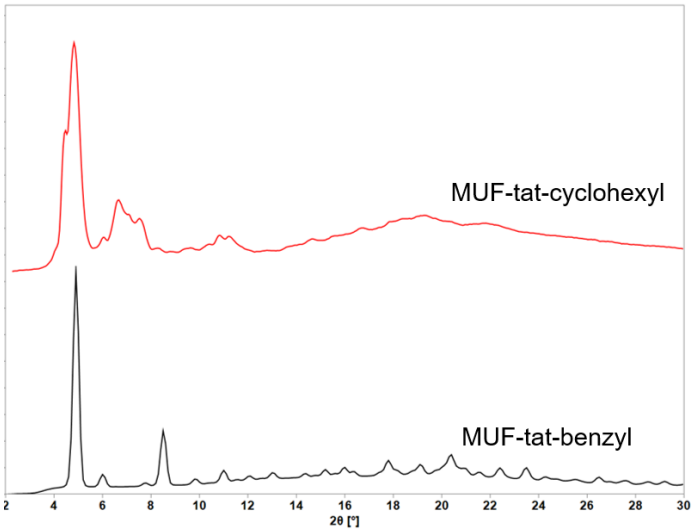

Figure 5. 16 PXRD patterns of MUF-tat-benzyl and MUF-tat-cyclohexyl.

It is interesting that these ligands with similar geometries can produce MOFs with distinct phases. The different behaviour of these ligands might be related to the size and orientation of side groups on each ligand. These groups can cause a certain degree of bending in the triazatruxene core. They can also have an effect on the face-to-face interaction of the ligand pair which can produce dimers with different stacking modes (Figure 5.17). Each stacking mode may then lead to formation of a different phase. In addition, the trinuclear zinc cluster is not the only possible cluster. Formation of different clusters will also give rise to formation of new phases.

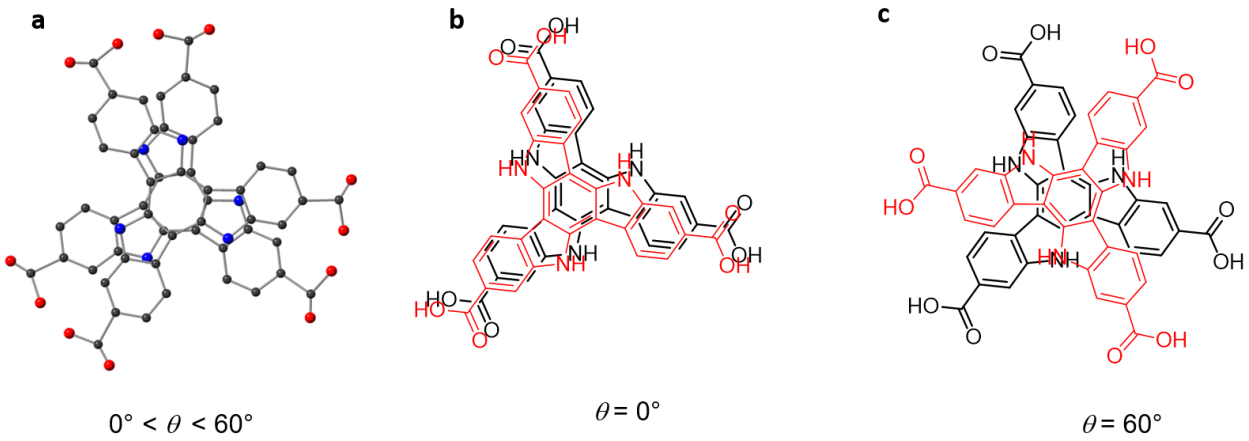

Figure 5. 17 Some possible stacking modes of a triazatruxene ligand pair differ by stacking angle (θ): a) gauche (observed in the structures of MUF-tat, MUF-tat-benzyl, MUF-tat-butyl-**1** and MUF-tat-hexyl), b) eclipsed and c) staggered.

5.3 Conclusion

In conclusion, the synthesis of H_3tat-benzyl was achieved, as well as the syntheses of six new MOFs. The structures of MUF-tat and MUF-tat-benzyl were determined by SCXRD analysis. These frameworks are isostructural and have chiral networks. Gas sorption measurements revealed that MUF-tat-benzyl retains its porosity after removal of guest molecules, although PXRD analysis showed that it exhibits poor stability under ambient conditions. The structure of MUF-tat collapsed upon activation possibly due to its high porosity. MUF-tat-butyl-**1** and MUF-tat-hexyl both are highly unstable when exposed to air. This made difficulties for their structural characterization. A phase transition was observed in the structure of MUF-allyl after activation and the structures of both solvated and activated could not be solved due to the loss of crystallinity during measurements.

5.4 Experimental section

5.4.1 General procedure

All starting materials and solvents were used as received from commercial sources without further purification unless otherwise noted. Column chromatography was carried out on silica gel (grade 60, mesh size 230-400, Scharlau). NMR spectra were recorded at room temperature (unless otherwise noted) on Bruker-400 and Bruker-500 Avance instruments, with the use of the solvent proton as an internal standard. Thermogravimetric analysis (TGA) was performed on a TA Instruments Q50 instrument.

5.4.2 Ligands synthesis

Br_3tat-benzyl

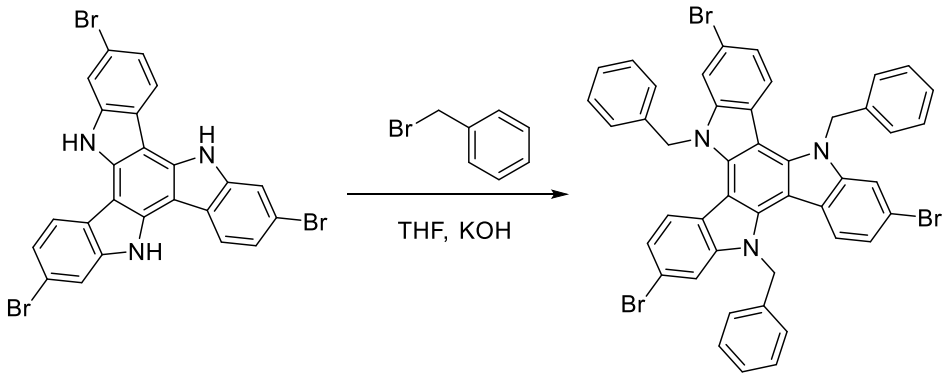

Br_3tat (438 mg, 0.75 mmol) and KOH (1.3 g) were combined in THF (50 mL). To this mixture benzyl bromide (400 µL, 3.4 mmol) was added and the mixture was refluxed overnight. After cooling to room temperature, the suspension was filtered. The solvent was removed from the collected filtrate under vacuum, and the residue was dissolved in dichloromethane (50 mL) and washed with 10 % aqueous HCl (40 mL) and then with water (40 mL). The organic layer was separated, dried over $MgSO_4$ and filtered through silica. The solvent was removed under reduced pressure and the crude material was purified on a silica column eluting with a gradient from hexane to 2:3 DCM/hexane. Yield: 468 mg (73%). ^{1}H NMR: (500 MHz, $CDCl_3$): δ 7.80 (d, *J* = 7.8 Hz, 3H), 7.48-7.41 (m, 18H), 7.15 (d, *J* = 7.7 Hz, 3H), 6.03 (s, 6H).

H_3tat-benzyl

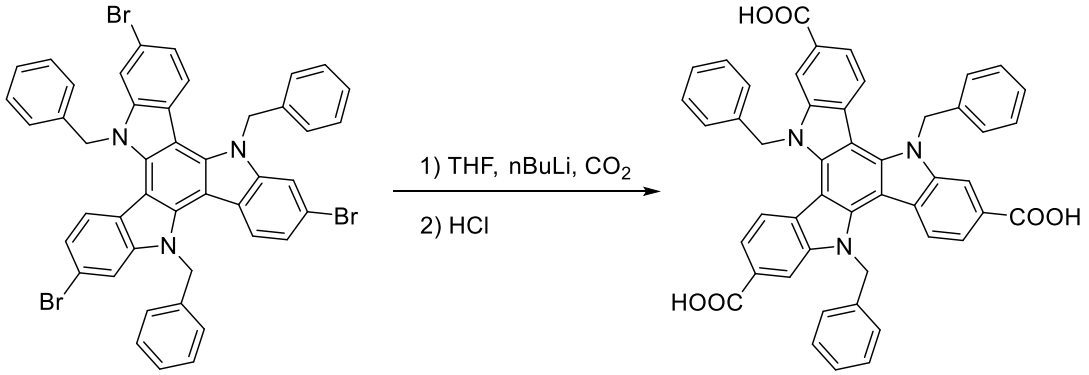

A mixture of Br_3tat-benzyl (820 mg, 0.96 mmol) and dry THF (200 mL) were degassed and stirred on liquid nitrogen-acetone bath (-70 ˚C) for 15 minutes. To this mixture n-BuLi (2.2 M in hexane, 10 mL, 22 mmol) was added dropwise. The mixture was slowly warmed to -10 ˚C over a period of 4 hours and an orange solution was observed. The mixture was cooled to -78 ˚C, and dry CO_2 was passed through the solution for 20 minutes. The reaction mixture was warmed to room temperature and quenched with water (20 mL). Then 1 M HCl (30 mL) was added and the mixture stirred for 2 hours. THF was removed and a yellow solid was filtered, washed with water and dried. The crude product was further recrystallized in MeOH. Yield: 575 mg (80%). ^{1}H NMR: (500 MHz, DMSO-d_6): δ 12.83 (br, 3H), 8.08 (d, J = 8.5 Hz, 3H), 8.02 (s, 3H), 7.62 (d, J = 8.4 Hz, 3H), 7.43-7.40 (m, 6H), 7.36-7.32 (m, 9H), 6.28 (s, 6H). ^{13}C NMR: (125 MHz, DMSO): 167.91, 141.48, 140.66, 138.08, 129.61, 128.11, 126.62, 126.02, 125.92, 121.84, 121.46, 112.82, 102.92, 50.92. ESI (negative mode, CH_3OH): m/z = 746.2319 ($[C_{48}H_{32}N_3O_6]^-$, calcd. 746.2369).

5.4.3 General method for MOFs synthesis

The ligand (10 μmol), benzoic acid (12 mg, 98 μmol) and $Zn(NO_3)_2{\cdot}4H_2O$ (14 mg, 53 μmol) were dissolved in a mixed solvent of dry DMF (1 mL) and water (35 μL) in a 4 mL vial. The reaction was carried out in an 85 °C isothermal oven for 20-30 hours to obtain MOF crystals. The mother liquor was replaced with anhydrous DMF. For SCXRD measurements DMF was replaced with DBF.

5.4.4 Powder X-ray diffraction patterns

All powder X-ray diffraction measurements were carried out on a Rigaku Spider X-ray diffractometer with Cu K_α radiation (Rigaku MM007 microfocus rotating-anode generator), monochromated and focused with high-flux Osmic multilayer mirror optics, and a curved image plate detector. Samples were kept damp with solvent prior to and during measurements. The two-dimensional images of the Debye rings were integrated with 2DP to give 2θ vs I diffractograms.

5.4.5 Single crystal X-ray diffraction

The single crystal X-ray diffraction analyses for MUF-tat-benzyl and MUF-tat-allyl were performed on crystals in fresh DBF at room temperature. Individual crystals were selected under a microscope then mounted on a polymer mount with a minimum amount of Fomblin® Y oil. A Rigaku Spider diffractometer equipped with a MicroMax MM007 rotating anode generator (Cu_α radiation, 1.54178 Å), high-flux Osmic multilayer mirror optics, and a curved image-plate detector was used to collect the data. The data were integrated and scaled and averaged with FS Process.[182] Using Olex2[183], the structure was solved with the SHELXT[184] structure solution program using intrinsic phasing and refined with the ShelXL[185] refinement package using least squares minimisation.

All zinc, oxygen and carbon atoms were found in the electron density difference maps and refined anisotropically except for carbons of the benzyl ring on MUF-tat-benzyl. Unrestrained atomic displacement parameters sometimes produced high U_{eq} values during the refinement thus RIGU, SADI, ISOR, DELU and SIMU commands were introduced as appropriate with careful adjustments of the standard deviations. In MUF-tat-benzyl, DFIX restrains were employed for the bond between bridging carbon and the ring carbon. All phenyl rings were modelled as ideal hexagons. Hydrogen atoms were calculated and refined as a riding model.

Table 5. 1 Crystallographic data summary of MUF-tat-benzyl and MUF-tat.

Compound	**MUF-tat-benzyl**	**MUF-tat**
Formula	$C_{96}H_{60}N_6O_{14}Zn_3$	$C_{54}H_{28}N_6O_{14}Zn_3$
Formula weight	1717.61	1180.93
Crystal size (mm)	0.22 × 0.19 × 0.20	0.24 × 0.28 × 0.21
Temperature (K)	293	293
Wavelength (Å)	1.54178	1.54178
Crystal system	cubic	cubic
Space group	$P4_132$	$P4_332$
Unit cell length (Å)	25.279(3)	25.5171(17)
Unit cell volume ($Å^3$)	16155(6)	16615(3)
Z	4	4
Dcalc (g cm-3)	0.706	0.472
μ (mm-1)	0.813	0.699
F(000)	3520.0	2384.0
Reflns coll./unique, Rint	6547/1291, 0.0729	10121/1299, 0.042
Data range	8 Å > d > 1.3 Å	8 Å > d > 1.3 Å
Completeness	100%	100%
Tmin, Tmax	0.388, 1.00	0.40, 1.00
R indices for data with I>2σ(I)	R1 = 0.1236 wR2 = 0.2965	R1 = 0.1493 wR2 = 0.3534
R indices for all data	R1 = 0.1431 wR2 = 0.3157	R1 = 0.1566 wR2 = 0.3598
Largest difference peak and hole (e Å-3)	0.39/ −0.33	0.59 / −0.31

Table 5. 2 Crystallographic details of the unit cells of MUF-tat-butyl-1 and MUF-tat-hexyl.

MOF	**Crystal system**	**Unit cell length (Å)**	**Unit cell angle (°)**	**Unit cell volume ($Å^3$)**
MUF-tat-butyl-**1**	tetragonal	a = b = 21.718 c = 29.629	a = b = c = 90	13976
MUF-tat-hexyl	tetragonal	a = b = 27.105 c = 20.631	a = b = c = 90	15157

Chapter 6 Synthesis and Thermolysis of a Multicomponent MOF Containing a Cyclobutyl-substituted Truxene Ligand

6.1 Introduction

Incorporating functional groups into MOFs is an attractive strategy as it provides the ability to rationally design materials for specific applications. This can be achieved through direct assembly of metal ions and organic ligands with appropriate functionalities. However, direct synthesis may not be possible when the functional group shows high sensitivity to the reaction conditions required. In such cases, as an alternative strategy, researchers have developed post-synthetic modification (PSM)[258-259] for installing functional groups in MOFs. By this strategy the framework can be modified after its formation to create desired pore characteristic and chemical feature in the structure of framework.

Thermally promoted post-synthetic modifications generally involve expulsion of small molecules and, are efficient to create functionalities in the framework and enlarge their pore sizes. In addition, such modifications require no reagents, and can be easily achieved by simple heating. The Telfer group introduced primary amine and catalytically-active prolinyl groups into IRMOF-10 and MUF-77-type frameworks through thermal decomposition of tert-butoxycarbamate protecting groups into isobutylene and carbon dioxide.[83-84, 173] This strategy later was used by other groups for the modification of various MOFs.[219, 260-261] Thermolysis involving carboxylic acids,[262] and azides[263-264] have also been reported. Recently, Richardson *et al*. demonstrated quantitative thermolysis of a sulfoxide group to a vinyl functionality in an analogue of IRMOF-9.[175] Vinyl groups are attractive post-synthetic targets due to their potential use for further functionalization. Kitagawa *et al*. reported a highly ordered vinyl polymer prepared through cross-polymerization of a divinyl embedded MOF and a vinyl monomer.[265] In addition, researchers have demonstrated polymerization on vinyl-tagged MOF to fabricate composite materials such as mixed-matrix membranes (MMM).[266]

Cyclobutane derivatives can be formed photochemically from alkenes by [2 + 2] cycloaddition reactions, and in some cases cycloreversion of the resulting cyclobutane species can be achieved by microwave irradiation or heating.[267-271] Although, there are many reports on cyclobutane formation via [2 + 2] cycloaddition reactions involving MOFs,[272-282] only a small number of studies have been reported on the reverse reaction. The first example of thermal cleavage of cyclobutane rings in a MOF structure was reported by the Vittal group.[283] In another study, the group could perform such transformation in a single-crystal-to-single-

crystal manner and analyze the resulting framework by single crystal X-ray diffraction (Figure 6.1).[284] Recently, researchers have demonstrated that cyclobutane can be converted into its corresponding furan derivative via solvothermal cleavage followed oxidation of the resulting biradicalic intermeditate.[285]

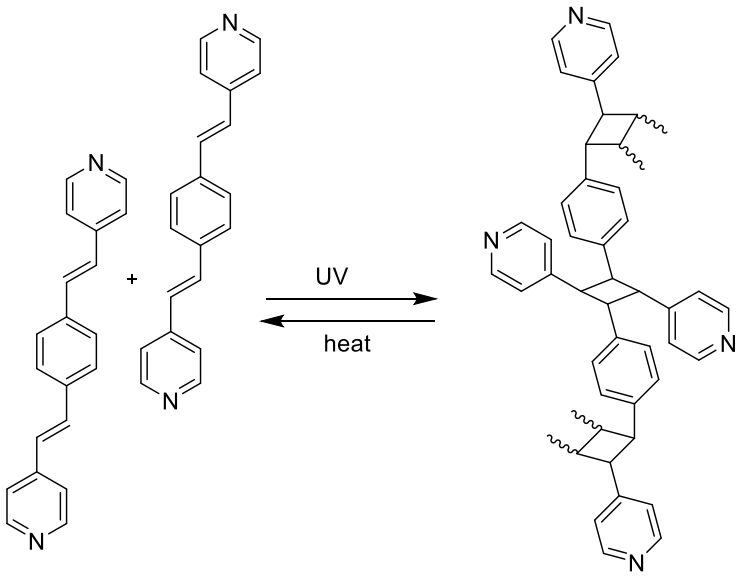

Figure 6. 1 Schematic illustration of polymerization of 1,4-bis[2-(4'-pyridyl)ethenyl]benzene by UV light and cleavage of cyclobutane rings upon heating.[284]

In this chapter, we focus on the synthesis of a new truxene-based tritopic ligand, H_3cbtt, and its use in constructing multicomponent MOFs. This ligand is functionalized with cyclobutane groups through the methylene bridges on truxene. Previously, truxene derivatives have been used to construct quaternary frameworks, MUF-77s.[48] These frameworks show great water stability due the hydrophobic alkyl groups appended to truxene linkers. Here, using H_3cbtt along with two ditopic linkers, we prepare a highly porous and thermally stable zinc-based quaternary framework, which is termed MUF-88-cb. Further, we thermolyze this framework to obtain vinyl-tagged MUF-88-v.

6.2 Results and discussion

6.2.1 Synthesis and characterization of ligands

Synthesis of [truxene-5,1':10,1":15,1"'-tris(cyclobutane)][286] (**1**) is described as two separate steps in the literature. Here, by modifying the reported conditions, compound **1** was prepared in a one-pot reaction from truxene (Scheme 6.1). Although this strategy eliminates one

purification step, it decreases the overall yield to 38%. Compound **1** was then converted into H_3cbtt via Friedel-Crafts acylation reaction followed by hydrolysis of the resulting acyl chloride compound. Some side products were also formed during acylation reaction. These are presumably truxene-core involved polymers, because $AlCl_3$ can act as an coupling agent and polymerize truxene under these conditions.[287] The crude material was esterified to obtain Me_3cbtt which then was purified by column chromatography. Hydrolysis of the ester produced H_3cbtt in high yield and good purity.

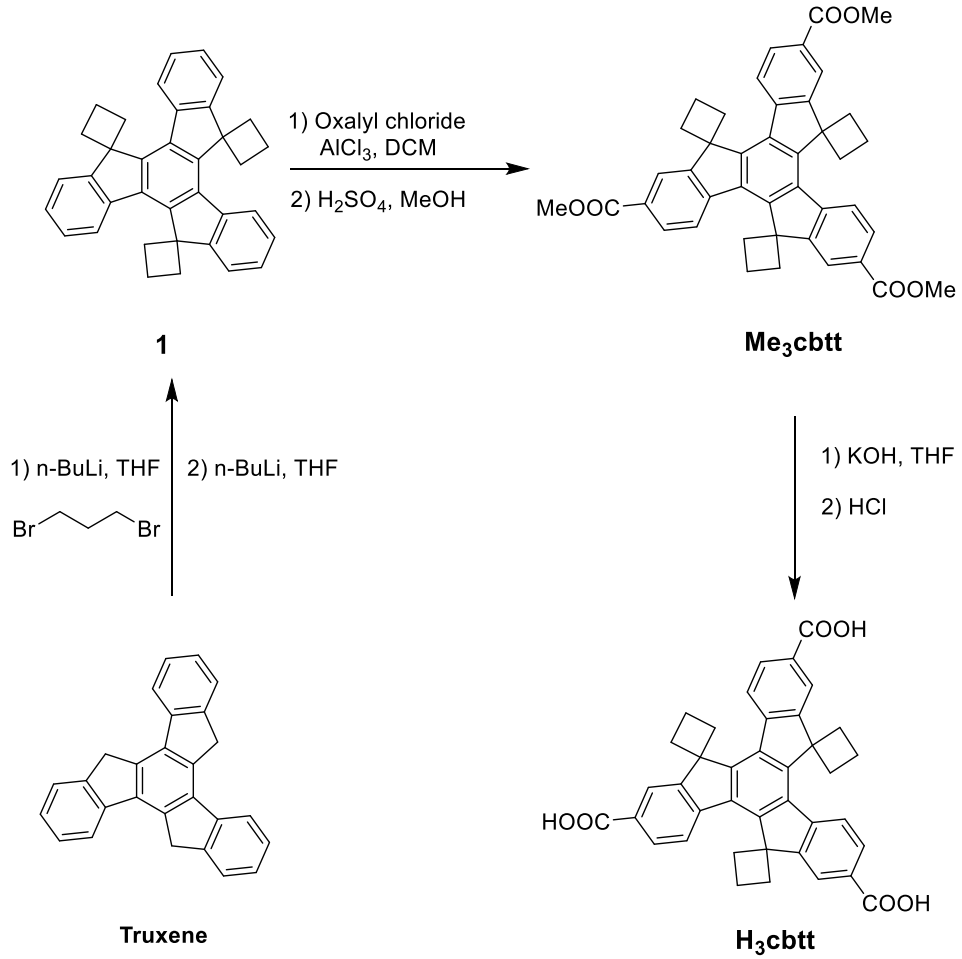

Scheme 6. 1 Synthetic route to H_3cbtt.

6.2.2 Synthesis and characterization of MUF-88-cb and MUF-88-v

Reacting H_3cbtt, H_2bpdc, H_2bdc with $Zn(NO_3)_2$ in DEF produced a quaternary metal-organic framework with the formula $[Zn_4O(cbtt)_{4/3}(bpdc)_{1/2}(bdc)_{1/2}]$. To characterize MUF-88-cb, single crystal X-ray diffraction was carried out on a desolvated crystal at room temperature. A good X-ray diffraction pattern was obtained to a resolution of 0.85 Å. The data showed that

MUF-88-cb crystalizes in the cubic space group *I*-43*d* and has an **ith-d** topology which is the same overall network type observed in structures of MUF-7, MUF-77 and MUF-777. The powder X-ray diffraction pattern of an as-synthesized MUF-88 sample matches well with the pattern calculated from the single crystal X-ray diffraction data (Figure 6.3). This confirms the bulk phase purity of MUF-88-cb. The bulk phase purity of the framework was further confirmed by ^{1}H NMR spectroscopy of a digested sample (Figure 6.4). The ^{1}H NMR spectrum of digested MUF-88-cb shows only the presence of the three ligands with their expected integral ratios.

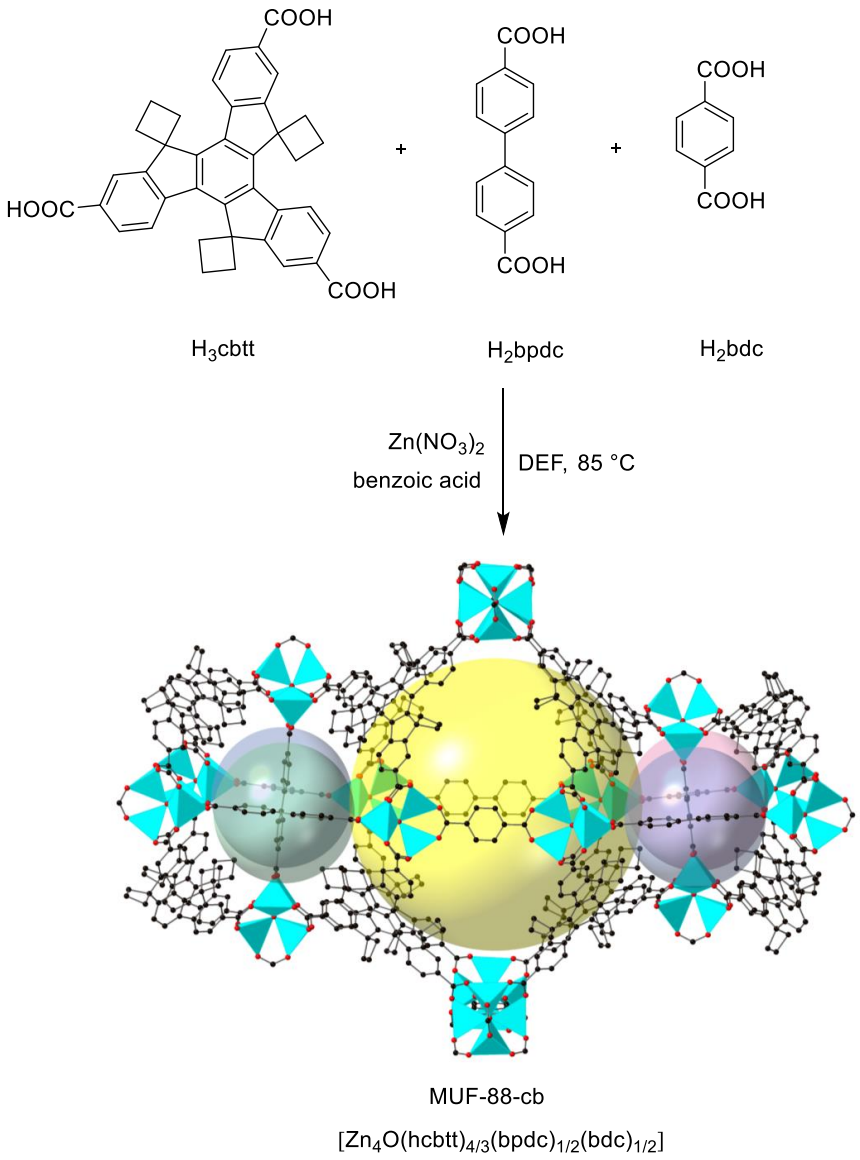

Figure 6. 2 Synthetic route to MUF-88-cb and its structure determined by SCXRD. Cavities in the structure are highlighted with coloured spheres. Atom colours: carbon: black, oxygen: red and zinc: cyan. Hydrogen atoms are omitted for clarity.

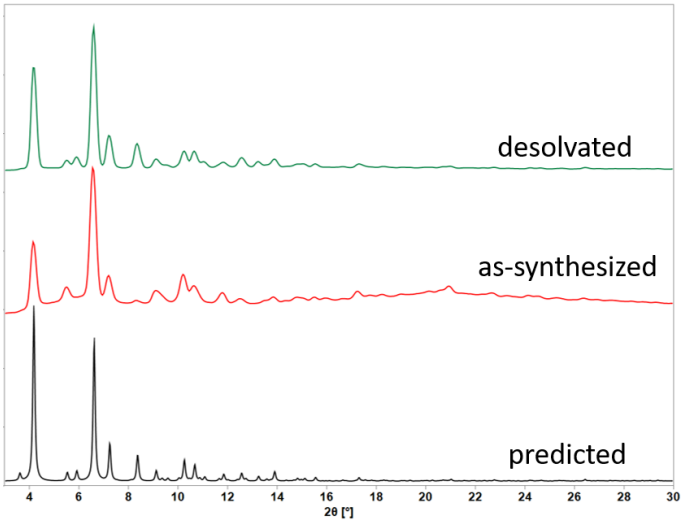

Figure 6. 3 Experimental and calculated PXRD patterns of MUF-88-cb.

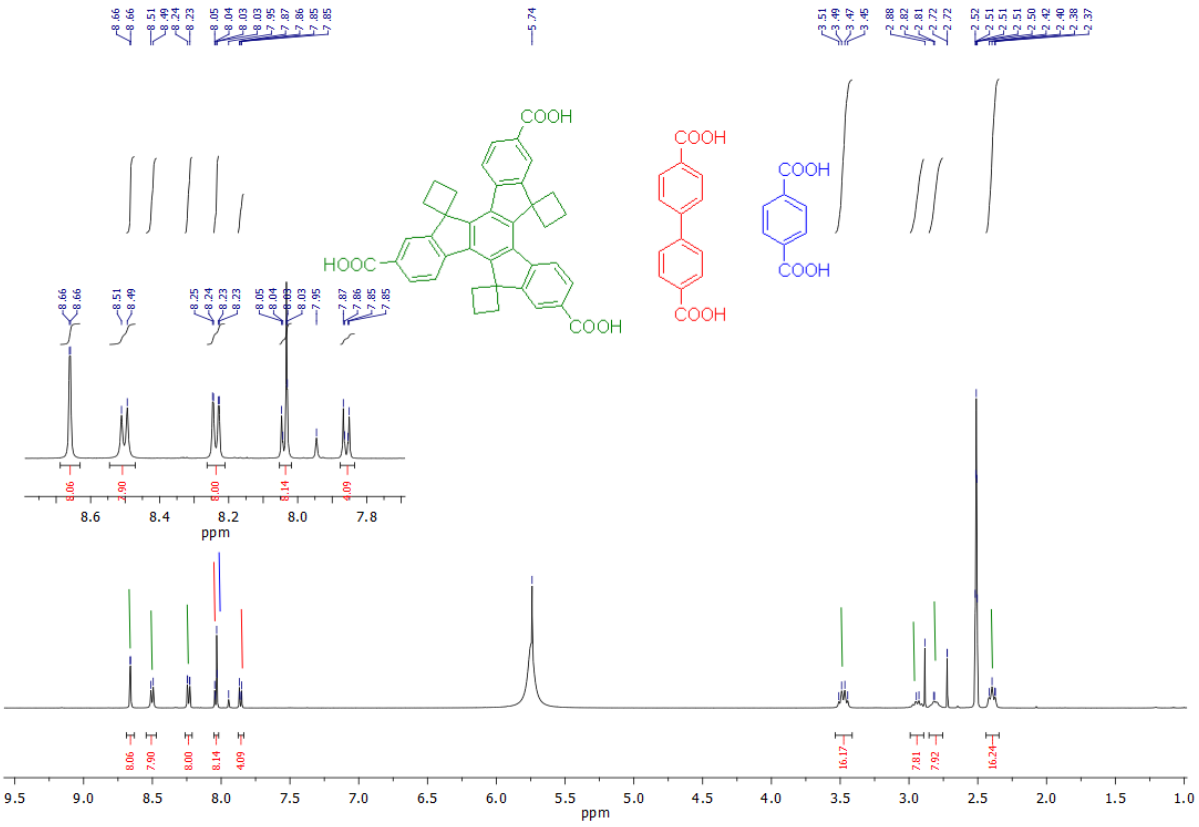

Figure 6. 4 ^{1}H NMR spectrum of MUF-88-cb digested in DCl/DMSO-d_6 showing the integrals that match with the formula $[Zn_4O(cbtt)_{4/3}(bpdc)_{1/2}(bdc)_{1/2}]$.

In the structure of MUF-88-cb, the three ligands are linked by six connected Zn_4O nodes. The framework has one type of dodecahedral and three types of tetrahedral cavities.

Dodecahedral cavities are defined by 12 Zn_4O clusters, eight cbtt linkers, three bpdc linkers, and three bdc linkers (Figure 6.5). Tetrahedral cavities, on the other hand, are constructed with four Zn_4O nodes, four cbtt linkers and two linear linkers. The three tetrahedral cavities differ by the identities of the two ditopic ligands that define them as shown in Figure 6.6: a) two bpdc linkers, b) one bpdc and one bpdc linker and c) two bdc linkers.

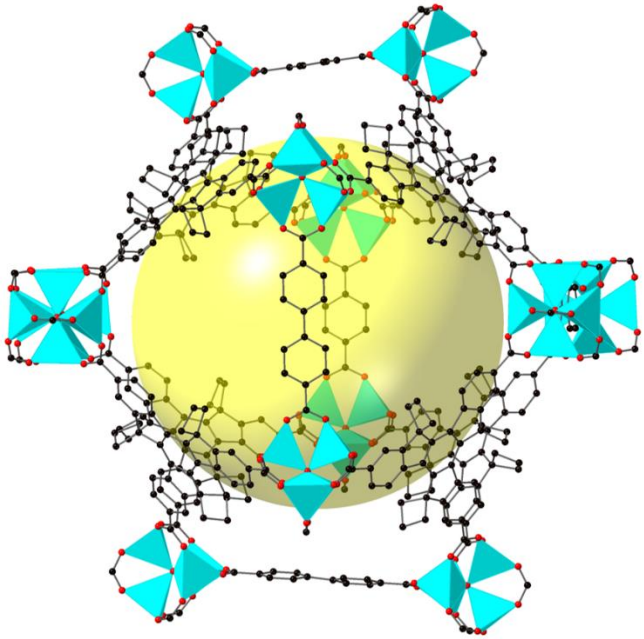

Figure 6. 5 Single crystal X-ray structure of MUF-88-cb highlighting the dodecahedral cavity as a yellow sphere.

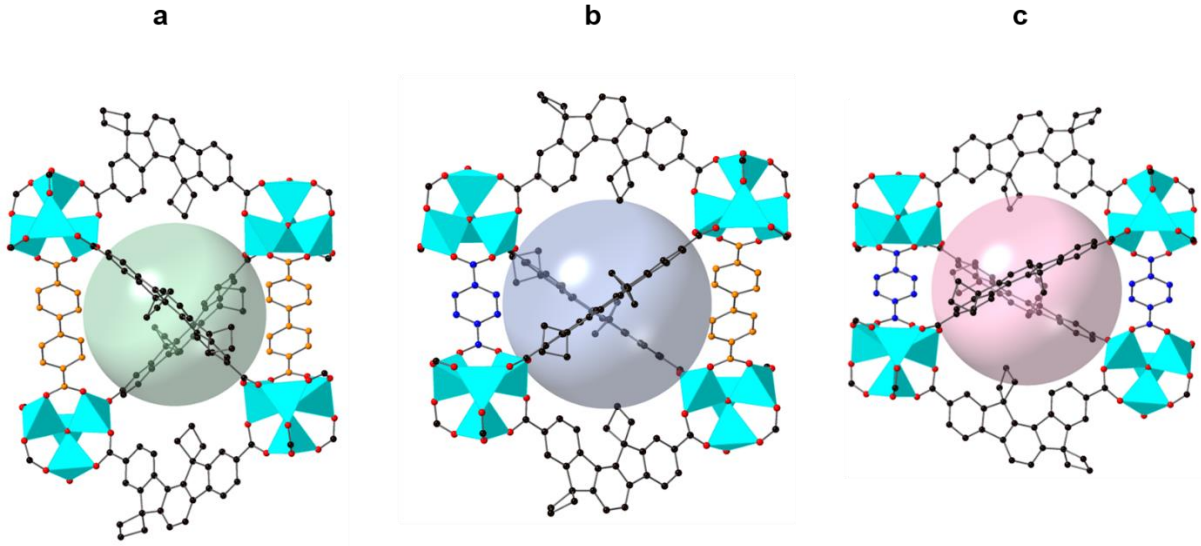

Figure 6. 6 Single crystal X-ray structure of MUF-88-cb highlighting three distinct tetrahedral cavities defined with four Zn_4O nodes, four cbtt linkers and a) two bpdc, b) one bpdc and bdc and c) two bdc linkers. Ligand colour code: cbtt: black, bpdc: orange, bdc: blue.

As mentioned above, MUF-88-cb has the same overall topology as MUF-77-ethyl and MUF-7. In these MOFs the three ligands are linked by six-connected Zn_4O SBUs to form a framework with **ith-d** topology. Four tritopic linkers occupy the equatorial positions of each SBU while one bpdc and one bdc ligand fill the axial sites. MUF-77-ethyl crystallized in the primitive cubic space group *P*m-3 with a unit cell dimension length of 29.9508 Å. On the other hand, similar to MUF-7, MUF-88-cb crystallizes in the face-centred cubic space group *I*-43*d* with a unit cell dimension length of 59.7565 Å. Although the overall network topology of the two frameworks are the same, due to their different cell symmetries the alignment of the three linkers throughout the framework is different. As illustrated in Figure 6.7, the ditopic linkers are arranged differently in the two lattices. This results in the formation of three cavities with different sizes and environments in MUF-77 (Figure 6.9). The larger dodecahedral cavity is defined by 12 Zn_4O cluster, eight truxene linkers and three pairs of bpdc linkers, while in the smaller dodecahedral cavity bdc ligands replace bpdc ligands. The smallest cavity has a tetrahedral shape and is defined by four Zn_4O cluster, four truxene ligands, one bpdc ligand and one bdc ligand. MUF-88-cb, on the other hand possesses one large dodecahedral and three distinct tetrahedral cavities (Figure 6.8). The environment of these cavities is discussed in section 6.2.2.

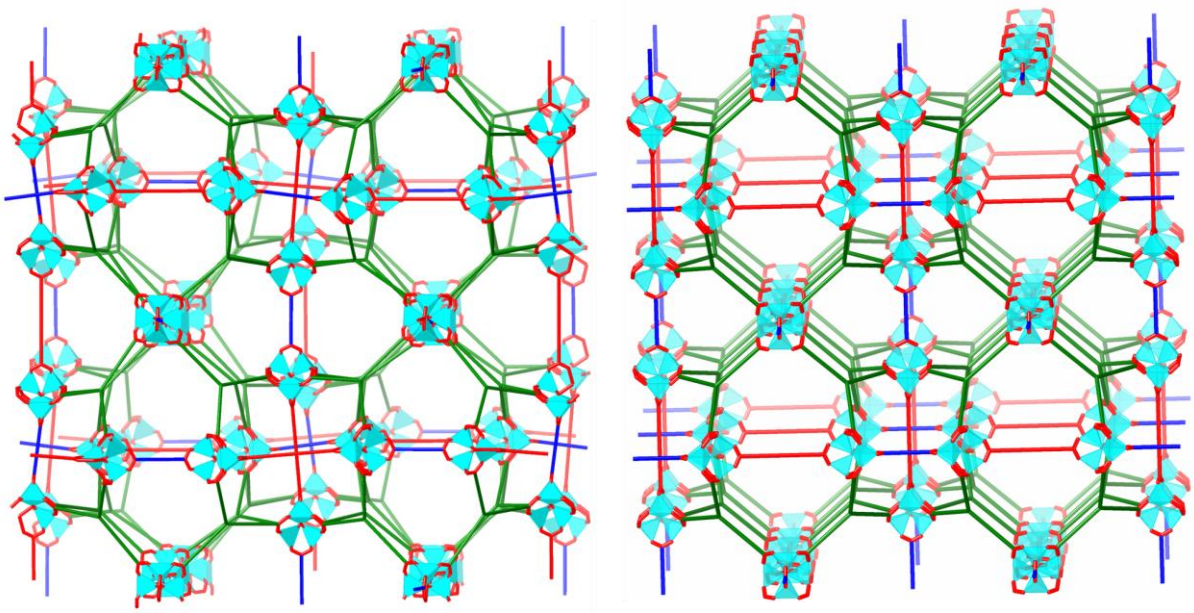

Figure 6. 7 Simplified views of single crystal X-ray structures of MUF-88 (left) and MUF-77 (right) viewed from the b and c crystallographic axes, respectively. Ligand colours: truxene ligands: green, bdc: blue and bpdc: red.

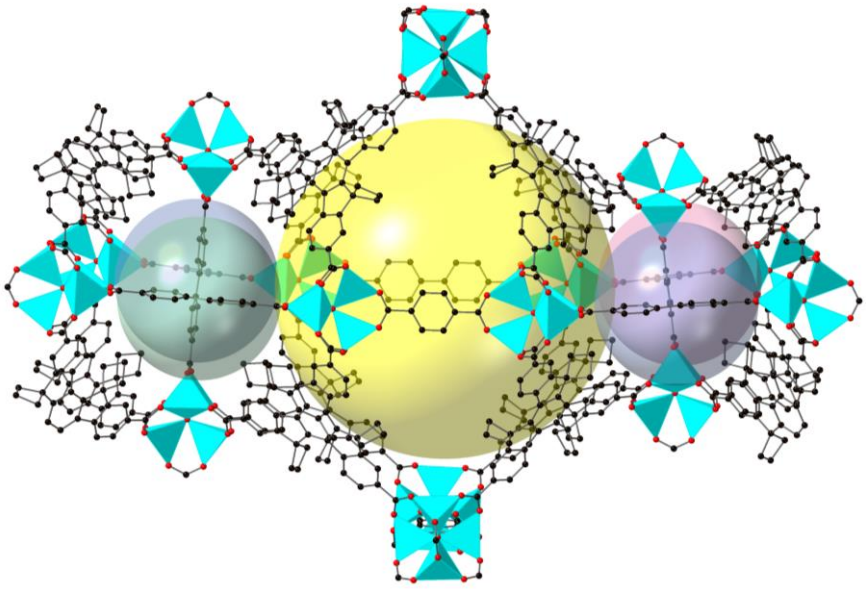

Figure 6. 8 A view of the single crystal X-ray structure of MUF-88-cb highlighting the positions of different cavities in the frameworks with coloured spheres. Large dodecahedral cavity: yellow and three different tetrahedral cavities: pastel blue, pastel green and pasted magenta. Atom colours: carbon: black, oxygen: red and zinc: cyan. Hydrogen atoms are omitted for clarity.

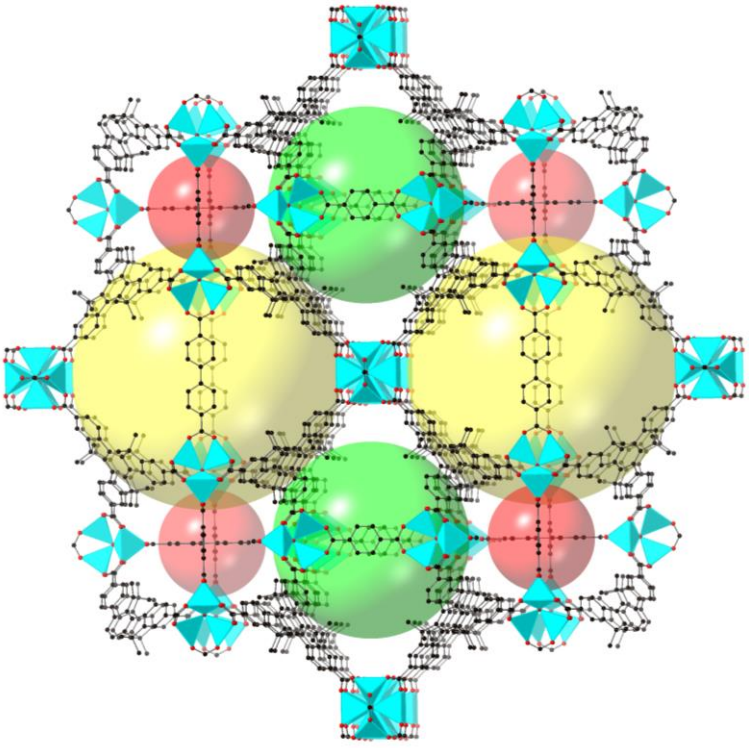

Figure 6. 9 A view of the single crystal X-ray structure of MUF-77 highlighting the positions of different cavities in the frameworks with coloured spheres. Larger dodecahedral cavity: yellow, smaller dodecahedral cavity: green and tetrahedral cavity: red. Atom colours: carbon: black, oxygen: red and zinc: cyan. Hydrogen atoms are omitted for clarity.

The porous nature of MUF-88-cb was examined by conducting gas adsorption measurements. To do this, first, MUF-88-cb crystals were activated by removing the solvent occluded in its pores during synthesis. To obtain an activated MOF sample, the solvent of an as-synthesized sample was exchanged with fresh DMF and then dry dichloromethane. After dichloromethane was decanted, the sample was heated at 80 °C under dynamic vacuum for 20 hours. Then, a low-pressure N_2 adsorption isotherm was measured at 77 K. The capacity of MUF-88-cb for taking up N_2 at 77 K is 1065 cm^3/g (Figure 6.10). Its BET surface area and pore volume based on this isotherm were calculated to be 3290 cm^2/g and 1.65 cm^3/g respectively. These values are lower than those reported for MUF-7a. This is due to the bulky groups on the cbtt ligand in MUF-88-cb compared substituent-free btb linker in the structure of MUF-7a. The surface area of MUF-88-cb is closer to the surface are of MUF-77-ethyl, because of the similar size of groups on their tritopic linkers. The truxene ligand in MUF-77-ethyl is substituted with six ethyl groups, while the two ditopic linker are the same as in MUF-88-cb.

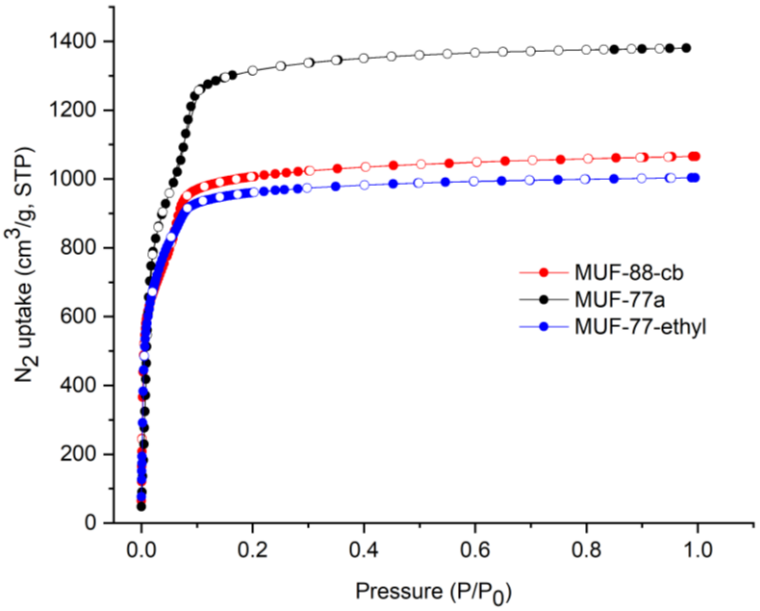

Figure 6. 10 N_2 adsorption (filled circles) and desorption (open circles) isotherms measured at 77 K for MUF-88-cb, MUF-7a and MUF-77-ethyl.

Gas adsorption isotherms of CO_2, CH_4, C_2H_4 and C_2H_6 were measured at both 273 K and 293 K. Due to its large pore windows, MUF-88-cb demonstrates a near-linear adsorptions behavior with no noticeable hysteresis for these gases (Figure 6.20-21).

Next, the stability of MUF-88-cb was investigated. MUF-88-cb, is fairly stable towards atmospheric water vapor. Desolvated MUF-88-cb crystals retain their crystallinity after air exposure for about 4 weeks (Figure 6.18). This is a greater stability than MUF-7a demonstrates,[82] and is in line with the effect of rigid truxene linker on the stability of MUF-77 materials.[48] In addition to its high porosity and stability at ambient conditions, MUF-88-cb exhibits a very interesting thermal profile. Thermogravimetric analysis of desolvated MUF-88-cb shows no weight loss up to 240 °C (Figure 6.11a). A weight loss of 9% was observed between 250 and 275 °C, which agrees with the expected weight percent loss of 8.8% attributable to the loss of ethylene released by fragmentation of cyclobutyl groups (Figure 6.12). After this point the framework remains stable up to around 450 °C. The mass loss observed beyond this temperature is due to framework decomposition.

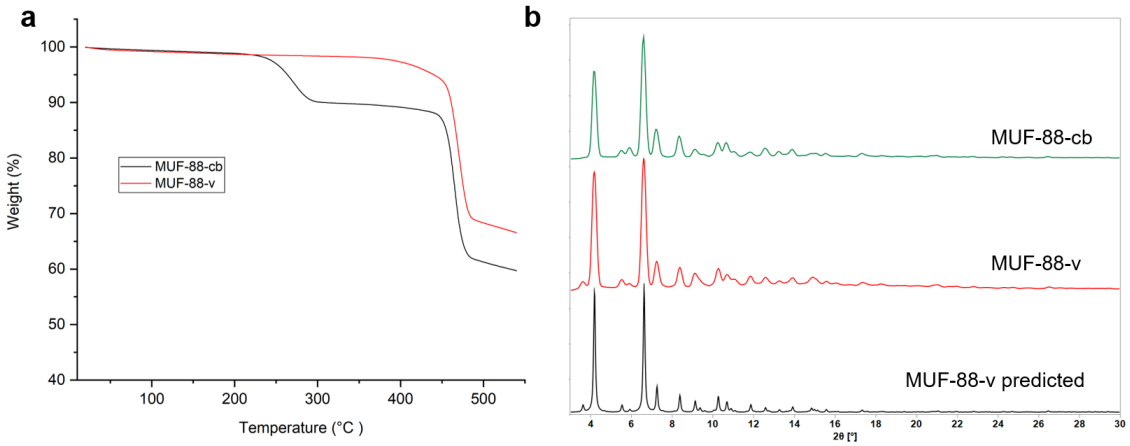

Figure 6. 11 a) TGA curves of MUF-88-cb and MUF-88-v, b) PXRD patterns of MUF-88-cb and MUF-88-v.

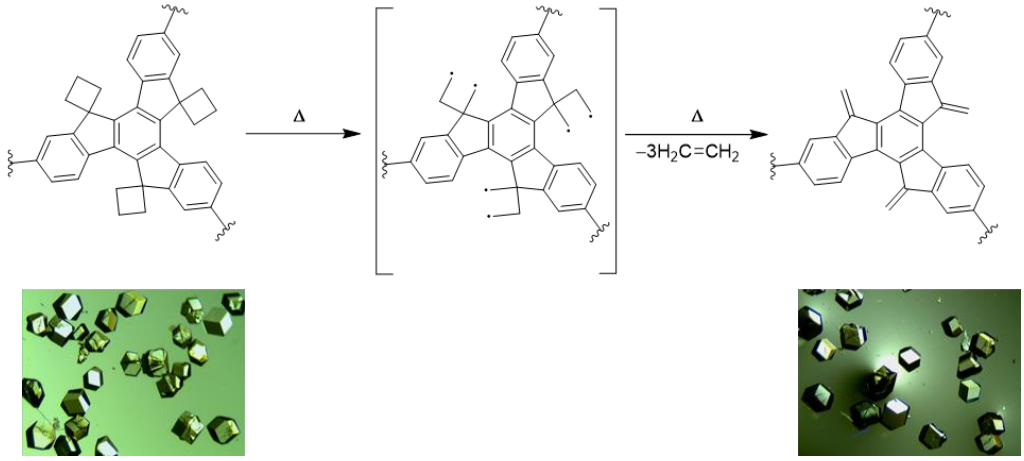

Figure 6. 12 Schematic illustration of decomposition of cyclobutyl groups on the cbtt ligand, and optical microscopy images of the crystals before and after thermolysis.

The reaction mechanism for thermal decomposition of cyclobutanes is thought to be a stepwise fragmentation via the biradical intermediates.[210] An indirect proof for this mechanism was reported by Zewail *et al*. The proof involved monitoring the decarboxylation of cyclopentanone by femtosecond mass spectroscopy which produce tetramethylene-biradicals forming two ethylene molecules by fragmentation or a cyclobutane ring by ring closure (Figure 6.13a).[288] Researchers, later, reported direct proof for the existence of biradical intermediate species in thermal decomposition of some cyclobutane derivatives through radical scavenging reactions and electron paramagnetic resonance experiments (Figure 6.13b).[289] In addition, researchers have isolated and analyzed organic species derived from cleavage of some cyclobutane derivatives (Figure 6.13c).[285] Based on these findings, it is in line with literature precedent that the thermal reaction of MUF-88-cb results in the decomposition of the cyclobutyl groups on the truxene ligand to form two olefinic products. TGA results suggests that one product is ethylene which escapes the framework during the thermolysis process. The second product, on the other hand, is likely to be a vinyl group on the truxene ligand (Figure 6.13). Therefore, we decided to conduct further analysis on the thermolysis of MUF-88-cb.

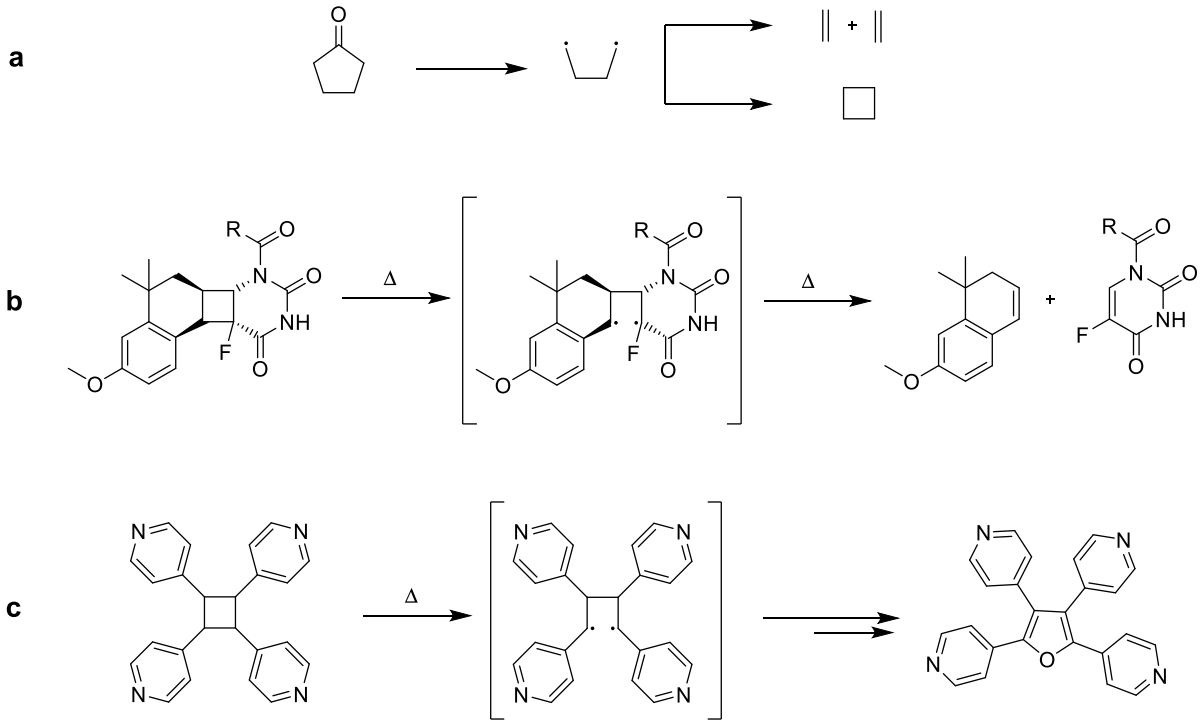

Figure 6. 13 Schematic illustrations of a) formation of ethylene and cyclobutane through decarbonylation of cyclopentanone,[288] b) formation of two alkene species through decomposition of a cyclobutane derivative,[289] c) conversion of a cyclobutane ring into a furan derivative via oxidation of biradical intermediate.[285]

For a bulk thermolysis study, the solvent of freshly-synthesized MUF-88-cb crystals were exchanged with dry DMF then dichloromethane. The dichloromethane was decanted, and the crystals were heated at 260 °C under dynamic vacuum for 20 hours. The resulting thermolyzed material was termed MUF-88-v. The PXRD pattern of MUF-88-v is in agreement with the pattern of MUF-88-cb, indicating that thermolysis process neither destroys the structure nor causes a major structural transformation (Figure 6.11b). It also confirms the phase purity of the thermolyzed material. In addition, the TGA curve of MUF-88-v does not show any weight loss until rapid decomposition of the framework around 450 °C (Figure 6.11a). This result demonstrates that the expulsion of ethylene is completed during thermolysis at 260 °C.

Interestingly, the transparency of crystals did not change during the thermolysis process. This was indicative of a single-crystal-to-single-crystal transformation (Figure 6.12). Indeed, a thermolyzed crystal of MUF-88-v displayed an excellent diffraction pattern to a resolution of 0.95 Å (Figure 6.14). This is evident with high intensities at high Bragg angles. The high-resolution along with initial low R_{int} value (6.02%) indicate that a good quality data was obtained. Moreover, after refinements low R-factor (4.93%) was obtained, which is indicative of a good agreement between the model and the data collected. To the best of my knowledge there is only one report on a single-crystal-to-single-crystal transformation via cyclobutane cleavage in a MOF structure.[284] The molecular structure of the linker of this MOF and its thermolytic transformation is illustrated in Figure 6.1.

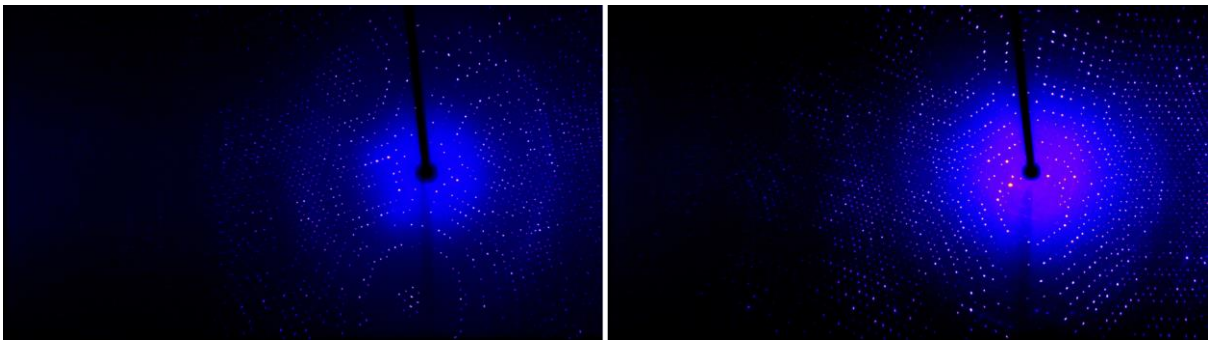

Figure 6. 14 Representative diffraction images of MUF-88-cb (left) and MUF-88-v (right).

The structure of MUF-88-v was found to belong to the centrosymmetric *I*-43*d* space group. The overall framework of MUF-88-v is almost the same as the parent framework, MUF-88-cb, except for the substituents on the truxene ligand. In the structure of MUF-88-cb the carbon atoms of the cyclobutyl ring were found in the electron density difference map. Following thermolysis, in MUF-88-v, two carbons of a vinyl group were visible on electron density

difference map and they could be refined sensibly (Figure 6.15). The distance for the double bond between vinyl carbons was found to be 1.38 Å. In addition, no significant additional electron density was observed around the location of these atoms. This implies that the cleavage of cyclobutane groups was completed.

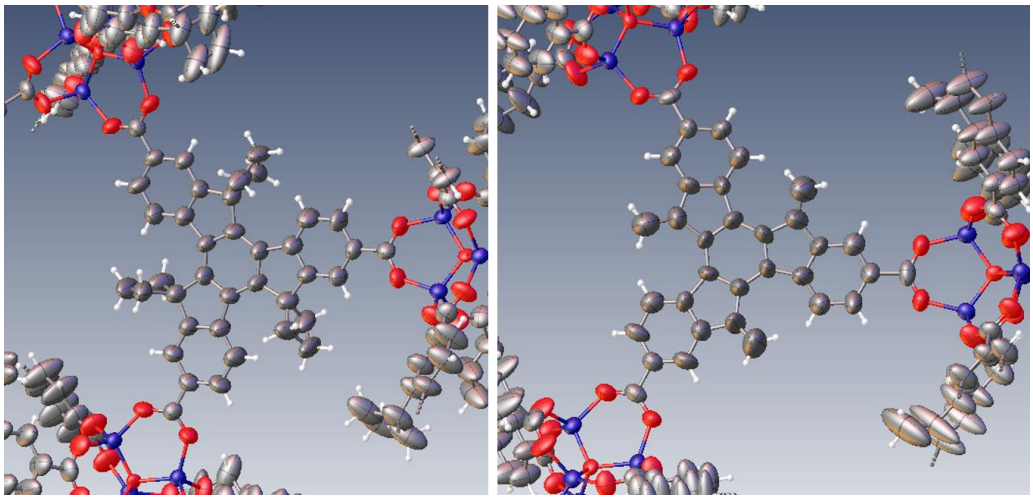

Figure 6. 15 ORTEP diagrams of the structures of MUF-88-cb (right) and MUF-88-v (left), determined by SCXRD, showing 50% probability of the atomic displacement ellipsoids.

Next, we wanted to confirm the presence of the vinyl groups by ^{1}H NMR spectroscopy. The analysis of a sample digested in DCl/d_6-DMSO revealed that the peaks between 2.2 and 3.5 ppm which belong to cyclobutyl group disappear (Figure 6.16). Also, we observed that two singlet peaks appear around 6.9 and 6.8 ppm which belong to the two protons on vinylic carbon, which confirms the identity of this group (Figure 6.16). However, the integrals of the peaks corresponding to the H_3cbtt linker was lower than the expected values. Moreover, the integrals showed a decrease over time. When MOF crystals were digested in an alternative solvent system comprising NaOD/D_2O, a yellow precipitate was observed and the ^{1}H NMR spectrum of this sample did not show any peaks belong to the H_3cbtt ligand. This may be the result of a polymerization reaction happening through the vinyl group. Reports on polymerization reactions for truxenene[290] (a precursor for H_3vtt ligand) are not available in the literature. Truxenene can be considered as a derivative of dibenzofulvene (Figure 6.17). Researchers have demonstrated that dibenzofulvene can polymerize with cationic, anionic, and radical initiators.[291-294] Therefore, it is possible that the acid or base used for MOF digestion catalyse or initiate the polymerization of the H_3vtt ligand.

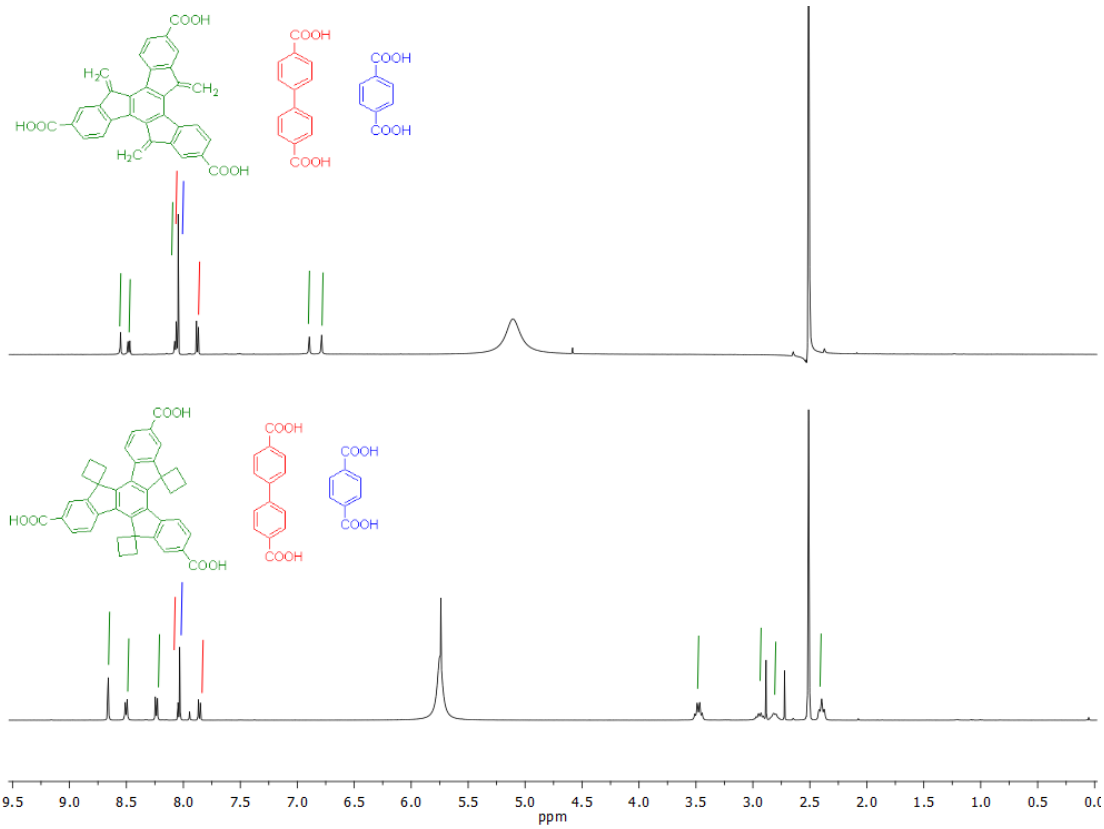

Figure 6. 16 Comparison of ^{1}H NMR spectra of MUF-88-cb and MUF-88-v samples digested in DCl/d_6-DMSO.

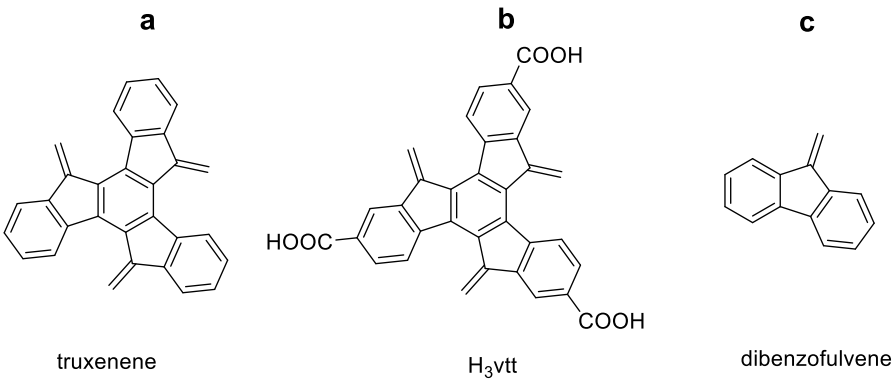

Figure 6. 17 Molecular structures of a) truxenene, b) H_3vtt and c) dibenzofulvene.

6.3 Conclusion

In conclusion, the synthesis of the cyclobutyl-functionalized truxene based tritopic ligand, H_3cbtt, was achieved. Using this ligand along with bpdc and bdc a new multicomponent MOF was synthesized. MUF-88-cb was prepared under solvothermal conditions, and its structure was confirmed by SCXRD analysis. The framework is isostructural to MUF-7a and exhibits

similar high porosity. Due to the rigidity of the truxene linker and hydrophobicity of the cyclobutyl groups, MUF-88-cb has a greater stability than MUF-7a towards atmospheric water vapor. MUF-88-cb was converted into MUF-88-v under high temperature thermolysis conditions. The thermal reaction of MUF-88-cb resulted in expulsion of ethylene from the cyclobutane groups to form vinyl tags on the truxene ligand without damaging its crystallinity. This single-crystal-to-single-crystal transformation was confirmed by SCXRD analysis. Although, the reactivity of vinyl groups causes some problems for ^{1}H NMR spectroscopic analysis, this behaviour may be useful for further modification of MUF-88-v. In addition, incorporating vinyl groups in a MOF structure under conditions that require elevated temperature or involve the use of acids is not very easy, because of the reactivity of vinyl groups under such conditions. To the best of our knowledge, there is no reported synthetic procedure for H_3vtt. Due to its reactivity, it clear that the direct synthesis of H_3vtt would be challenging. Therefore, introducing vinyl groups into a multicomponent MOF structure at precise locations via thermal decomposition of cyclobutane group is an exciting strategy as it provides an opportunity for further derivatization which may be useful to tune the physical and chemical features of pores of a multicomponent MOF. Some possible post-synthetic modifications of MUF-88-v will be discussed in Chapter 7.

6.4 Experimental section

6.4.1 General procedure

All starting materials and solvents were used as received from commercial sources without further purification unless otherwise noted. Column chromatography was carried out on silica gel (grade 60, mesh size 230-400, Scharlau). NMR spectra were recorded at room temperature (unless otherwise noted) on Bruker-400 and Bruker-500 Avance instruments, with the use of the solvent proton as an internal standard. Thermogravimetric analysis (TGA) was performed on a TA Instruments Q50 instrument.

6.4.2 Ligand synthesis

Trispiro[truxene-5,1':10,1'':15,1'''-tris(cyclobutane)][286]

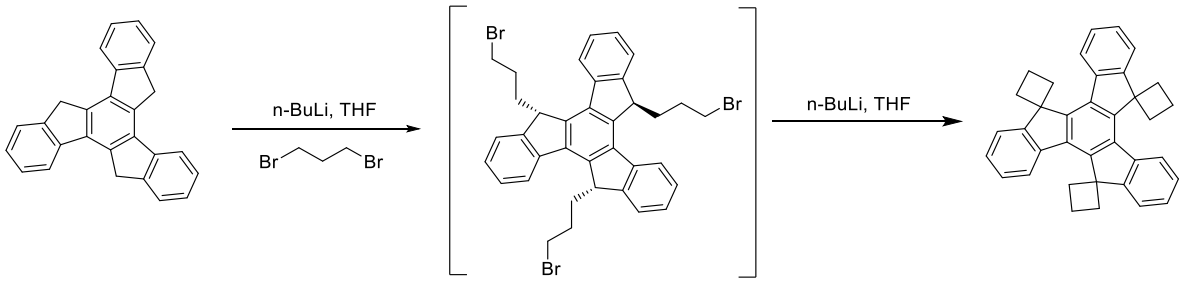

To a solution of truxene (171 mg, 0.5 mmol) in THF (10 mL) was added a solution of n-BuLi in cyclohexane (2 M, 0.75 mL, 3 eq.) at 0 °C and the mixture was stirred at this temperature for 0.5 h, then slowly warmed to room temperature. To the reaction mixture was added 1,3-dibromopropane (152 µL, 1.5 mmol) at room temperature, and the mixture stirred for 0.5 h. The mixture was cooled to 0 °C and 6 eq. of n-BuLi was added, and the mixture allowed to warm to room temperature and stirred overnight. After diluting with EA, organic phase was washed water and brine. Organic phase then was separated, dried over magnesium sulfate and concentrated. This material was further chromatographed on a silica column eluting with a mixture of DCM/hexane, 1:5, to afford the product as white solid. Yield: 88 mg (38%). ^{1}H NMR spectrum agree well with literature values. (500 MHz, $CDCl_3$): δ 8.51 (d, *J* = 7.6 Hz, 3H), 8.13 (d, *J* = 6.6 Hz, 3H), 7.55-7.51 (m, 6H), 3.72-3.65 (m, 6H), 2.97-2.91 (m, 3H), 2.71-2.67 (m, 3H), 2.49-2.45 (m, 6H) ppm.

H_3cbtt

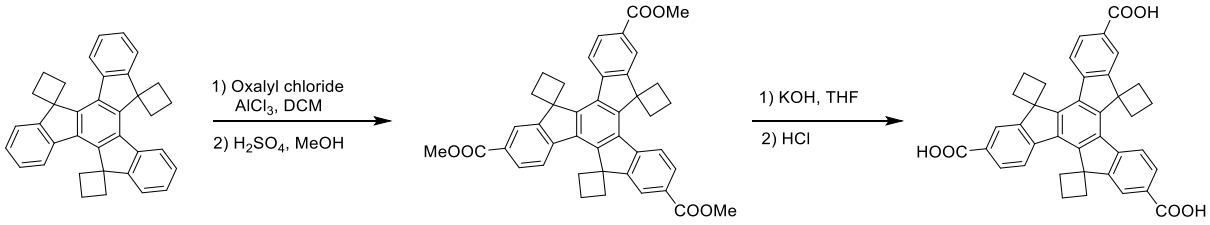

$AlCl_3$ (2.11 g, 15 mmol) in dichloromethane (15 mL) was cooled on ice under nitrogen atmosphere. To this mixture oxalyl chloride (950 µL, 11 mmol) was added and the suspension was stirred for 15 minutes. Trispiro[truxene-5,1':10,1":15,1"'-tris(cyclobutane)] (370 mg, 0.8 mmol) in dichloromethane (10 mL) was added to previous suspension and the mixture was refluxed for 3 hours. The mixture then, was poured onto ice-water slurry and stirred overnight. Then, dichloromethane was removed, and a yellow solid was collected by filtration, washed with water and dried under vacuum. The crude material was refluxed in MeOH (25 mL) in presence of H_2SO_4 (1 mL). After cooling to room temperature, solid K_2CO_3 was added and the mixture was stirred for 1 hour to neutralize excess H_2SO_4. MeOH was removed under reduced pressure. 100 mL of cold water was added to reaction mixture and a yellow solid was filtered and dried under vacuum. This material was further chromatographed on a silica column eluting

with a mixture of ethyl acetate/hexane, 2:3, to afford the product as pale-yellow solid. Yield: 341 mg, (67%). ^{1}H NMR (400 MHz, $CDCl_3$): δ 8.75 (s, 3H), 8.56 (d, *J* = 8.4 Hz, 3H), 8.23 (d, *J* = 8.2 Hz, 3H), 4.01 (s, 9H), 3.67-3.59 (m, 6H), 3.09-3.03 (m, 3H), 2.74-2.71 (m, 3H), 2.54-2.49 (m, 6H) ppm. The ester (320 mg, 0.5 mmol) was dissolved in 20 mL 1:1 (V/V) THF/KOH (aq., 1M) and the solution was refluxed overnight. THF was removed under reduced pressure and the reaction mixture then was acidified with 3 M aqueous HCl while it was kept on an ice bath. pH was adjusted to around 1, and the mixture was stirred for 3 hours. The yellow solid formed was filtered, washed with water and dried under vacuum. Yield: 270 mg (91%). ^{1}H NMR: (500 MHz, DMSO-*d*6): δ 13.3 (br, 3H), 8.68 (s, 3H), 8.52 (d, *J* = 8.3 Hz, 3H), 8.26 (d, *J* = 8.2 Hz, 3H), 3.53-3.49 (m, 6H), 2.99-2.93 (m, 3H), 2.86-2.80 (m, 3H), 2.44-2.40 (m, 6H) ppm. ^{13}C NMR: (125 MHz, DMSO-*d*6): δ 167.83, 156.41, 146.92, 140.66, 136.96, 130.93, 129.29, 123.63, 122.95, 51.48, 30.03, 16.47 ppm. ESI (negative mode, CH_3OH): m/z = 593.1974 ($[C_{39}H_{29}O_6]^-$, calcd. 593.1959).

6.4.3 MOF synthesis

MUF-88-cb, $[Zn_4O(cbtt)_{4/3}(bpdc)_{1/2}(bdc)_{1/2}]$

H_3cbtt (12.5 mg, 21 μmol), biphenyl-4,4'-dicarboxylic acid (9.5 mg, 43.7 μmol), terephthalic acid (6.9 mg, 40.5 μmol), benzoic acid (50 mg, 416 μmol) and $Zn(NO_3)_2{\cdot}4H_2O$ (74 mg, 283 μmol) were dissolved in anhydrous DEF (5 mL) and water (120 μL) in a 20 mL vial. The reaction mixture was sonicated for 1 minute, then heated in an 85 °C isothermal oven for 23 hours to obtain pale yellow crystals. For yield calculation, TGA and NMR analysis, the mother liquor was decanted and replaced with anhydrous DMF. The solvent was then replaced with fresh anhydrous DMF (2 times) and dichloromethane (5 times). After dichloromethane was decanted, the crystals were dried under vacuum. Yield: 13 mg.

To obtain MUF-88-v, dichloromethane washed MUF-88-cb crystals were heated at 260 °C under a dynamic vacuum for 20 hours.

6.4.4 Single crystal X-ray diffraction

The single crystal X-ray diffraction analyses for MUF-88-cb and MUF-88-v were performed on desolvated crystals at room temperature. Individual crystals were selected under a microscope then mounted on a polymer mount with a minimum amount of Fomblin® Y oil. A Rigaku Spider diffractometer equipped with a MicroMax MM007 rotating anode generator

(Cu_{α} radiation, 1.54178 Å), high-flux Osmic multilayer mirror optics, and a curved image-plate detector was used to collect the data. The data were integrated and scaled and averaged with FS Process.[182] Using Olex2[183], the structure was solved with the SHELXS[295] structure solution program using intrinsic phasing and refined with the ShelXL[185] refinement package using least squares minimization.

All zinc, oxygen and carbon atoms were found in the electron density difference maps and refined anisotropically. Unrestrained atomic displacement parameters sometimes produced high U_{eq} values during the refinement thus ISOR and SADI commands were introduced as appropriate with careful adjustments of the standard deviations. All phenyl rings were modeled as ideal hexagons. Hydrogen atoms were calculated and refined as a riding model.

Table 6. 1 Crystallographic data summary for MUF-88-cb and MUF-88-v.

Compound	**MUF-88-cb**	**MUF-88-v**
Formula	$C_{63}H_{42}O_{13}Zn_4$	$C_{55}H_{26}O_{13}Zn_4$
Formula weight	1268.44	1156.24
Crystal size (mm)	0.28 × 0.25 × 0.31	0.22 × 0.26 × 0.19
Temperature (K)	293	293
Wavelength (Å)	1.54178	1.54178
Crystal system	cubic	cubic
Space group	*I*-43*d*	*I*-43*d*
Unit cell length (Å)	59.7565(6)	59.6327(18)
Unit cell volume ($Å^3$)	213381(6)	212057(19)
Z	48	48
Dcalc (g cm-3)	0.474	0.435
μ (mm-1)	0.783	0.771
F (000)	30912.0	27840.0
Reflns coll./unique, Rint	233227/30150, 0.0670	105069/20390, 0.0602
Data range	8 Å > d > 0.85 Å	8 Å > d > 0.95 Å
Completeness	99%	94%
Tmin, Tmax	0.63, 1.00	0.39, 1.00
R indices for data with I>2σ(I)	R1 = 0.0647 wR2 = 0.1521	R1 = 0.049 wR2 = 0.1189
R indices for all data	R1 = 0.1045 wR2 = 0.1790	R1 = 0.0671 wR2 = 0.1278
Largest difference peak and hole (e Å-3)	0.24/ −0.32	0.24 / −0.21

6.4.5 Powder x-ray diffraction patterns

All powder X-ray diffraction measurements were carried out on a Rigaku Spider X-ray diffractometer with Cu K_α radiation (Rigaku MM007 microfocus rotating-anode generator), monochromated and focused with high-flux Osmic multilayer mirror optics, and a curved image plate detector. Samples were kept damp with solvent prior to and during measurements.

The two-dimensional images of the Debye rings were integrated with 2DP to give 2θ vs I diffractograms.

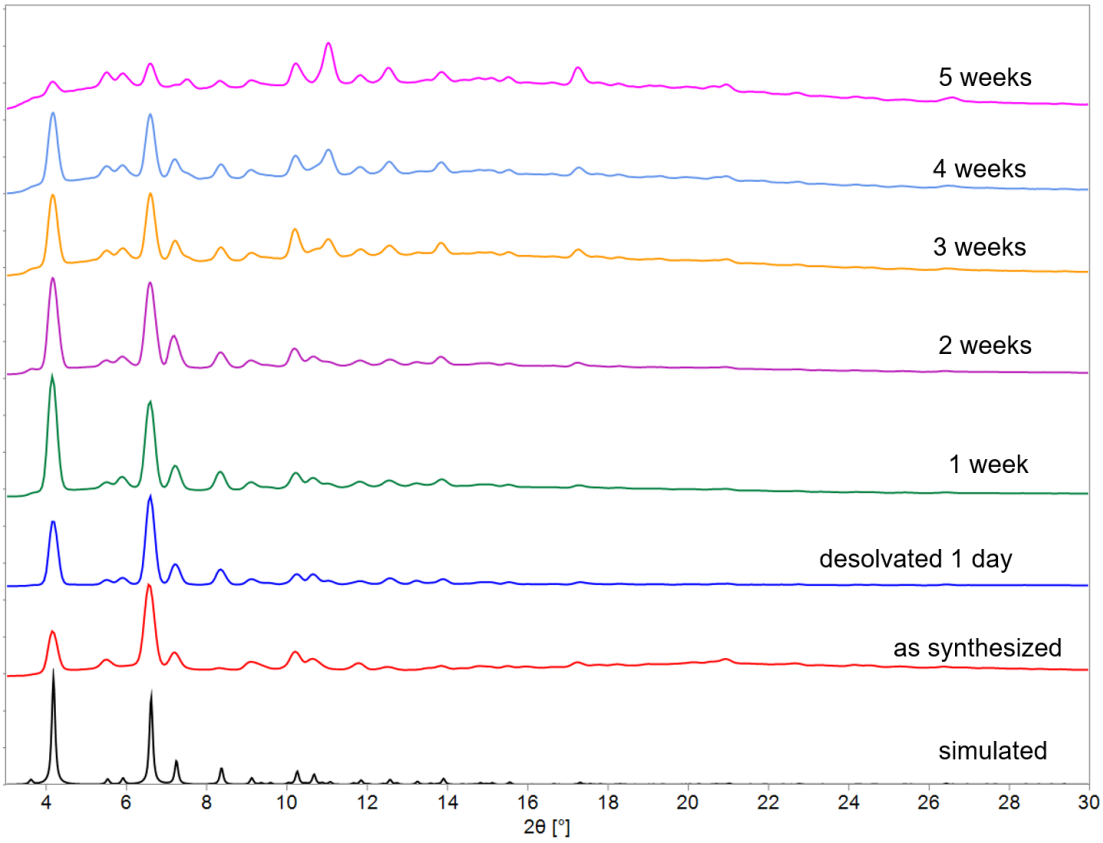

Figure 6. 18 PXRD patterns of MUF-88-cb; as synthesized, activated and aged samples exposed to air for the stated period.

6.4.6 Gas adsorptions measurements

Low pressure gas adsorption isotherms were measured by a volumetric method using a Quantachrome Autosorb iQ2 instrument. All adsorption measurements used ultra-high purity gases. Freshly prepared MOF samples were washed four times with acetone and soaked in dry dichloromethane for two hours. The samples were then transferred to a pre-dried and weighed analysis tube. Excess dichloromethane was removed under vacuum and the tube back filled with argon before being heated at 1 °C per minute to 80 °C under vacuum. The sample was then held under a dynamic vacuum at 10^{-6} Torr for 20 hours. Accurate sample masses were calculated using activated samples after backfilling with nitrogen. BET surface areas were calculated from N_2 adsorption isotherms at 77 K as described in Chapter 2.

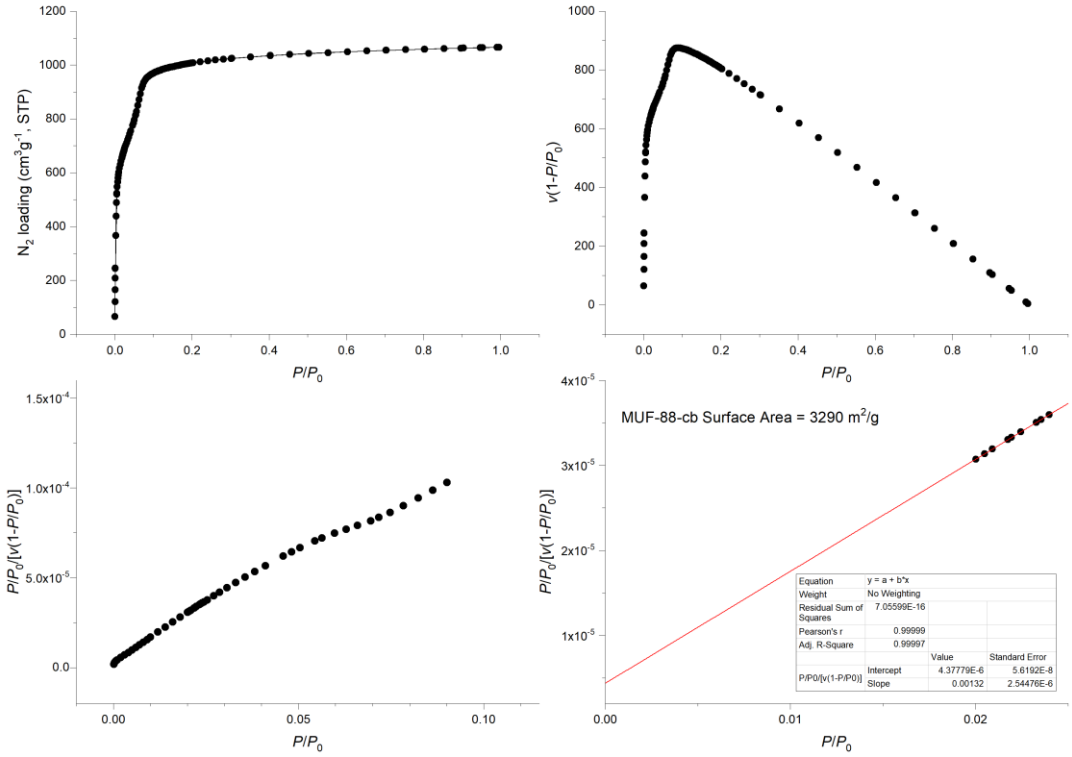

Figure 6. 19 N_2 adsorption isotherm at 77 K and BET surface area plots of MUF-88-cb.

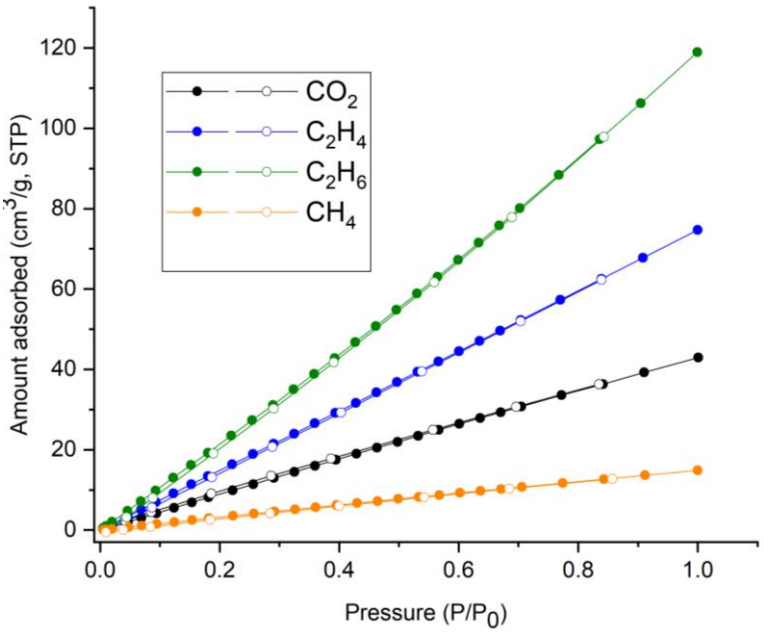

Figure 6. 20 CO_2, C_2H_6. C_2H_4 and CH_4 adsorption (filled circles) and desorption (open circles) isotherms at 273 K for MUF-88-cb.

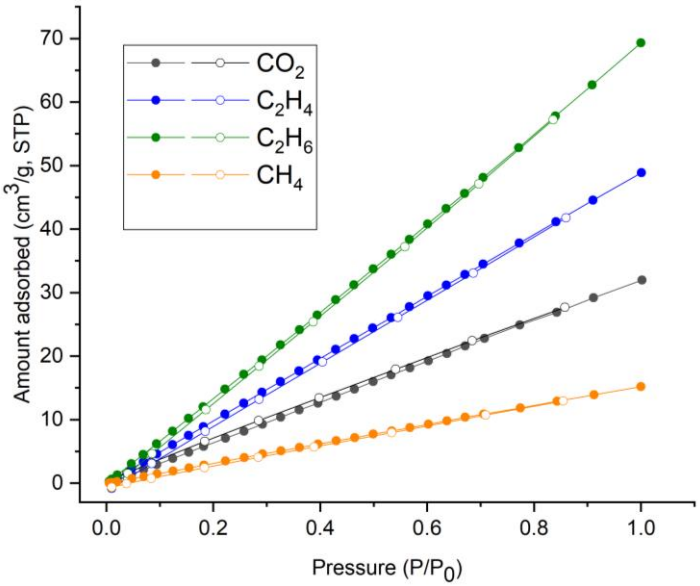

Figure 6. 21 CO_2, C_2H_6. C_2H_4 and CH_4 adsorption (filled circles) and desorption (open circles) isotherms at 293 K for MUF-88-cb.

Chapter 7 Summary and Perspectives

7.1. Thesis summary

The study presented in this thesis was initially focused on design and synthesis of new linkers. Firstly, a series of triazatruxene based ligands was synthesized (Chapters 2, 4 and 5). Prior to the study, to the best of our knowledge there were no reports on triazatruxene based ligands in which carboxylic acid groups occupy the 2-, 7- and 12- positions. Secondly, a series of novel carbazole derivatives was prepared (Chapter 3 and 4). Further, a spiro-truxene derivative was synthesized (Chapter 6) which had not previously been reported in the literature.

The study then covered the preparation of a number of quaternary (Chapter 2, 3, 4 and 6) and binary (Chapter 5) MOFs. Furthermore, the study was focused on the physical and chemical properties of these MOFs, such as their catalytic activity, gas adsorption and fluorescence behaviors.

In Chapter 2, using triazatruxene ligands along with bpdc and bdc a series of isostructural multicomponent MOFs was synthesized. MUF-777, MUF-777-ethyl and MUF-777-allyl were prepared under solvothermal conditions and their structures were determined by SCXRD analysis. Gas adsorption measurements on these MOFs revealed that they have different pore size and volumes. This observation is in line with the programmable pore approach.[82] Because other members of the series could not be obtained in a phase pure form by solvothermal conditions, a new synthetic procedure was developed. Based on the new procedure MUF-777, MUF-777-butyl, MUF-777-hexyl and MUF-777-cychexyl were synthesized at room temperature by using zinc acetate instead of zinc nitrate. This method resulted in nanocrystals rather than the large single crystals obtained under typical conditions. Further, fluorescence measurements were conducted on MUF-777 and MUF-777-hexyl. The results showed that MUF-777 is able to form hydrogen bonds with guest molecules through its NH sites. This behavior of MUF-777 may be useful for the detection of proton acceptors by luminescence quenching.[192]

In Chapter 3, new MUF-777 and MUF-77 derivatives containing homochiral activator sites were prepared. The catalytic pores of these materials were further tuned by introducing modulator sites on the tat (in MUF-777) and carbazole (in MUF-77) ligands. The catalytic activity of these materials was studied on the asymmetric aldol reaction of 4-nitrobenzaldehyde and acetone. It was observed that in MUF-777 system, the relocation of the active site from the bpdc ligand to the bdc ligand has a significant effect on the catalysis reaction. The relocation

results in a reversed enantioselectivity and a decreased reaction rate. This observation is in agreement with the previously reported results for MUF-77 catalyst system for the same reaction.[84] Moreover, the catalysis results of MUF-77 system revealed that the reaction rate and enantioselectivity of a catalytic aldol reaction can be tuned by modulator sites on the carbazole ligand. This observation suggests that modulator groups in the catalytic pore are positioned in a way that they can interact beneficially with the reactants as they pass through this 'active site'.[84, 202]

In Chapter 4, two new MUF-77 analogues containing secondary amine functionalities as activator sites were synthesized. These frameworks were used as catalysts for the Michael addition reaction of dibenzoyl methane to β-nitrostyrene, and the Friedel Crafts reaction of indole with β-nitrostyrene. It was observed that these MOFs were able to accelerate both reactions even with relatively low catalyst loading. It would be interesting to introduce chiral modulator groups into these frameworks. If the modulator sites are chiral, it might be possible to achieve enantioselectivity even using an achiral catalytic unit. In addition, MUF-777-tatpip-NH exhibited poor stability under ambient conditions. This might be due to the high concentration of hydrophilic NH sites in the framework. Triethylamine functionalized MUF-77-teacdc was also synthesized. This material was not obtained phase pure as the characterization results showed that the amino group underwent with some undesired reactions under the solvothermal MOF synthesis conditions. Room temperature synthesis method which was used for MUF-777 derivatives in Chapter 2 might be a convenient procedure for the synthesis of phase-pure MUF-77-teacdc.

The study in Chapter 5 was focused on the synthesis of zinc-carboxylate MOFs containing triazatruxene ligands. Although the structures of MUF-tat and MUF-tat-benzyl were determined by SCXRD analysis, these materials exhibited poor stability under ambient conditions possibly due to their high porosity. MUF-tat-butyl, MUF-tat-hexyl, MUF-tat-allyl and MUF-tat-cychexyl were highly unstable when exposed to air even in solvent. This resulted in difficulties for their structural characterization.

In Chapter 6, using the cyclobutyl functionalized truxene based tritopic ligand along with bpdc and bdc a new multicomponent MOF, MUF-88-cb, was synthesized, and its structure was confirmed by SCXRD analysis. The framework is isostructural to MUF-7a and exhibits similarly high porosity. MUF-88-cb has a greater hydrolytic stability than MUF-7a due to the hydrophobic nature of cyclobutyl groups. High temperature thermolysis of MUF-88-cb under vacuum produced a new framework, MUF-88-v. This is a single-crystal-to-single-crystal

transformation that occurs by thermolysis of the cyclobutyl groups. A vinyl tag is left behind on the truxene ligand and ethylene gas escapes from the framework without damaging its crystallinity. The structure of MUF-88-v was determined by SCXRD analysis. Single-crystal-to-single-crystal transformation by thermal cleavage of cyclobutane ring has rarely been observed in the field of MOFs.[284] Due to its reactive nature vinyl group on MUF-88-v provides an opportunity for further modification in the pores of the framework. Some possible post-synthetic modifications on this material will be discussed in section 7.4.

7.2. Exploring new triazatruxene based MOFs

In this thesis, I only studied zinc-based MOFs containing triazatruxene ligands. Although multicomponent MOFs presented in early chapters exhibited fair stability, the binary MOFs prepared in Chapter 5 showed poor hydrolytic stability. In future work, it would be interesting to explore frameworks constructed from triazatruxene ligands and other metals (Figure 7.1). Triazatruxene based tricarboxylate ligands may form stable MOFs with high valent metal ions. Researchers have reported Fe(III) and Cr(III) based MOFs containing the prototype tricarboxylate linker, H_3btc.[296-297] Highly stable Zr(IV)-MOFs constructed from extended tricarboxylate ligands are also available in the literature.[298-300] Here, the advantage of using triazatruxene ligand is that it can be symmetrically functionalized with a variety of groups to systematically construct MOFs featuring different pore shapes, sizes and chemical properties. It would also be interesting to expand triazatruxene derivatives beyond tricarboxylates. Using extended triazatruxene-tripyrazolate ligands along with divalent metal ions, it may be possible to build up stable MOFs with large pore volumes.

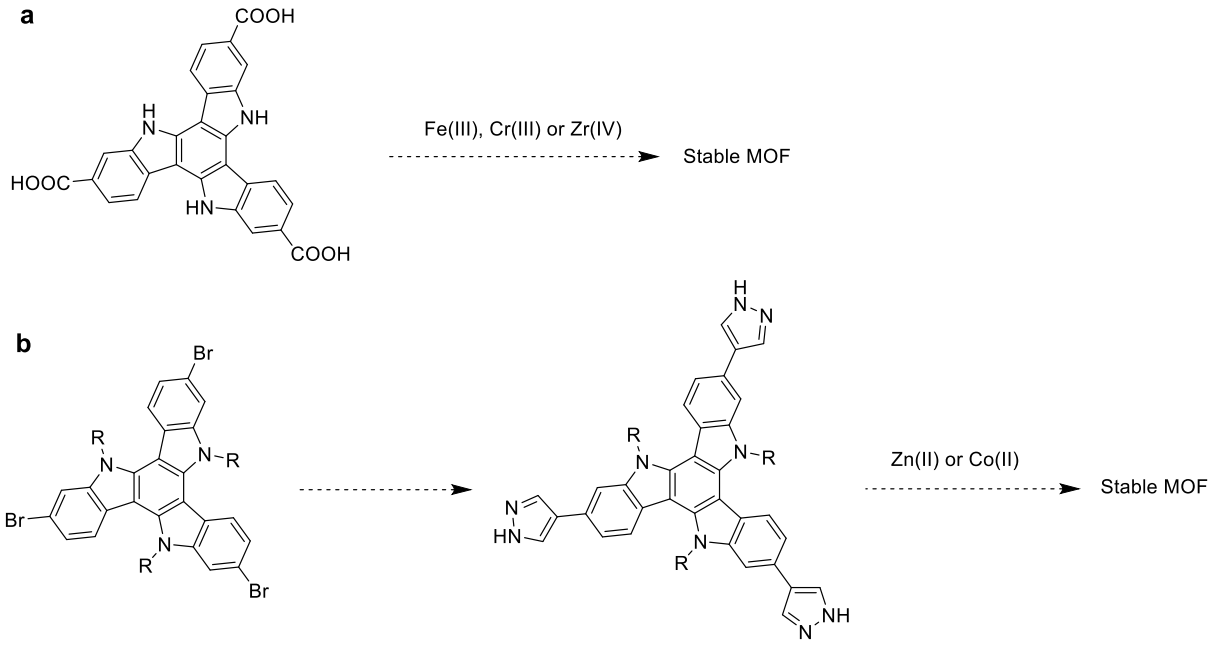

Figure 7. 1 Synthetic schemes to a) MOFs containing triazatruxene and high valent metal ions, b) triazatruxene-tripyrazolate ligands and their MOFs with divalent metal ions.

7.3. Exploring new truxene derivatives

In this thesis, by preparing two new truxene derivatives, triazatruxene and cyclobutyl-substituted truxene ligands, I introduced new functionalities into multicomponent MOFs, MUF-777 and MUF-88 respectively. It would be interesting to explore new truxene ligands by which additional functionalities could be introduced into quaternary MOFs. This could be achieved by converting known truxene derivatives, **A**,[301-302] **B**,[303] **C**,[304] **D**,[305-307] **E**[302] and **F**[308] to their corresponding tricarboxylate ligands (Figure 7.2). These ligands will expand the library of MUF-77 type quaternary MOFs with members featuring pores with different physical and chemical properties such as catalytic activity, selective adsorption, and optical behaviour.

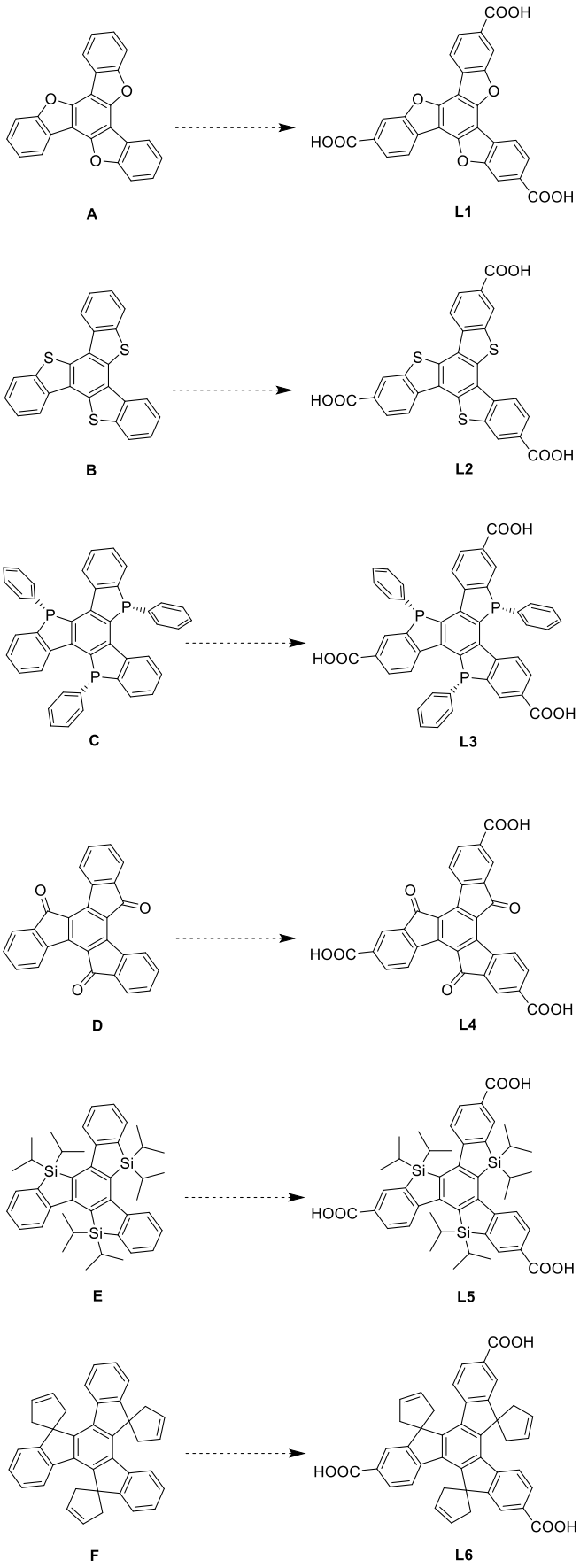

Figure 7. 2 Schematic illustration showing the hypothetical conversion of some known truxenes to their corresponding tricarboxylic acid derivatives.

D could be further functionalized with various functionalities through its carbonyl moiety (Figure 7.3).[306-307, 309-312] Choosing substituents with different sizes may help to tune the shape and size of pores of the resulting MOF. Groups with different polarities, on the other hand, could be useful for tuning selective adsorption behavior of MOFs. In addition, the optical properties of some of these compounds[305-306] may be useful for tuning the luminescence profile of the resulting MOFs.[181]

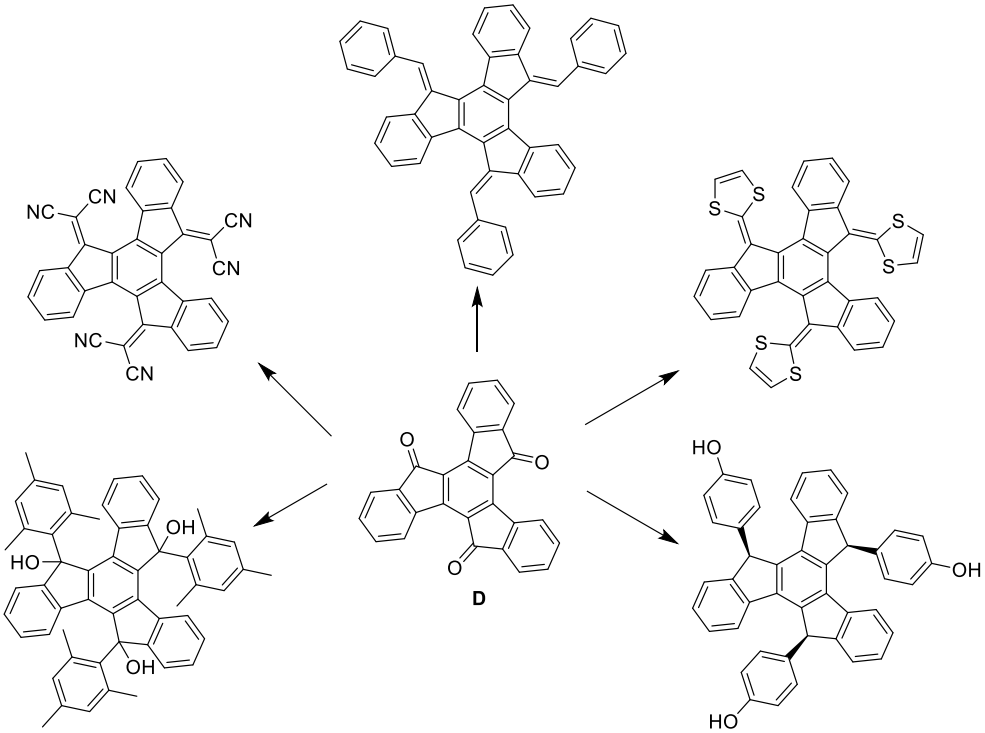

Figure 7. 3 Schematic illustration of derivatization of D into intermediates that may be appended with carboxyl groups to become MOF ligands.

MUF-77 variants that containing metallo-ligands have not been reported previously. Here, **L2** and **L3** provide an opportunity to prepare tritopic metallo-ligands, which will expand the library of MUF-77 catalysts. Metalation **L2** of **L3** may be possible by complexation of the ligand with an appropriate metal (e.g., Au(I), Ru(II)) before MOF synthesis or by post-synthetic modification of the MOF. Catalytically-active MOFs containing triphenylphosphine-based gold and ruthenium complexes have been reported in the literature.[313-314]

Synthetic procedures for tri-substituted chiral truxene derivatives illustrated in Figure 7.4 are available in the literature.[315-316] A series of chiral truxene ligands could be prepared by converting these compounds into their corresponding tricarboxylates. It is important to note that these compounds will be obtained as a racemic mixture. To separate their enantiomers,

they can be converted to a mixture of diastereomeric salt using some chiral bases. Since the physical properties of diastereomers will be different, it might be easy to separate them via physical methods, such as crystallization. Moreover, the separation of enantiomers may be possible by direct crystallization techniques.[317] By using enantiopure chiral truxene ligands, homochiral MUF-77 variants could be prepared. Homochiral MOFs could be useful for chiral separation and asymmetric catalysis. Using chiral truxenes, two types of catalyst systems could be prepared. The first type could feature achiral or racemic activator sites with homochiral modulator sites. In this catalyst system enantioselectivity could be generated via remote modulator sites rather than the activator sites. In the second type of catalyst system homochiral activator sites could be used along with modulator sites that have the same or inverted chirality which could either enhance or suppress the enantioselectivity of the chiral activator sites.

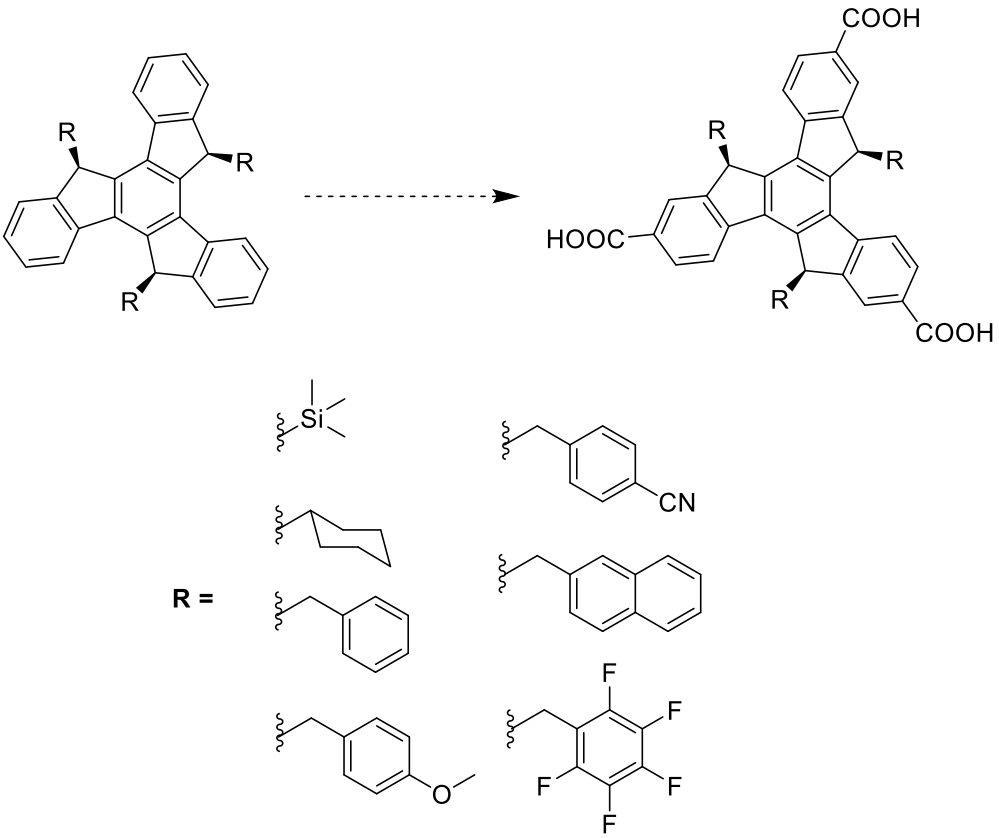

Figure 7. 4 Schematic illustration of known trisubstituted chiral truxene derivatives and their corresponding tricarboxylic acid ligands.

7.4. Post-synthetic modification of MUF-88-v

In Chapter 6, a truxene derivative in which cyclobutyl moieties are spiro-anneulated at the 5-, 10- and 15- positions was prepared. This ligand was successfully introduced into the

structure of MUF-88-cb which was then thermolyzed to generate vinyl groups on the truxene ligand. Due to their reactive nature, it is not easy to incorporate vinyl groups into MOF structure by direct synthesis. However, their reactivity may be useful for post-synthetic modifications by which additional functionalities could be introduced into MUF-88-v to tune its pores shape and chemical properties.

One target modification on the vinyl group could be done by an addition reaction with a halogen (Figure 7.5a). Researchers have performed such reaction on a vinyl-tagged MOF under mild conditions.[318-319] Similarly, thiol-ene click reactions[320] could be useful for post-synthetic modification of MUF-88-v (Figure 7.5b). These reactions can easily be performed in the presence of a radical initiator under mild conditions to introduce interesting functionalities into MOF structure.[266] In addition, it is also possible to generate a substituted cyclobutyl ring via cycloaddition reaction of vinyl group with another alkene compound (Figure 7.5c).[272]

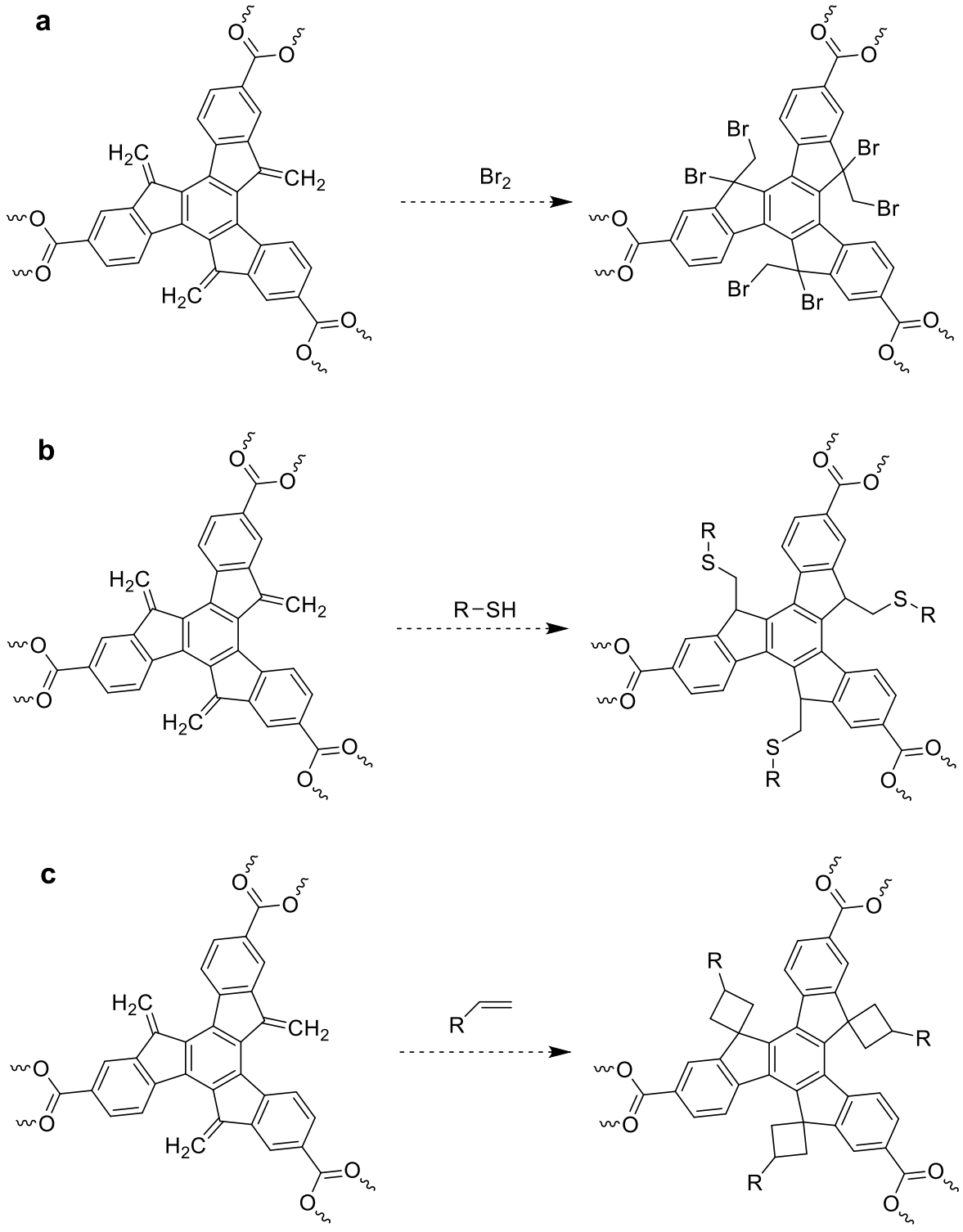

Figure 7. 5 Schematic illustrations of different proposed post-synthetic modifications of MUF-88-v.

7.5. Introducing carbene into a quaternary MOF

The number of spiro-truxene ligands can be expanded by preparing new members with different cycloalkane groups. According to synthetic scheme described in Chapter 6, a truxene ligand with cyclopropyl groups could be synthesized. It would be interesting to explore the thermolytic transformation of the MOF containing this ligand. The thermolysis of this MOF may result in decomposition of the cyclopropyl group which may lead to formation of carbene on the truxene ligand by releasing ethylene gas (Figure 7.6a). Although such transformations have not been reported in MOFs, it has been observed after photolysis of some small molecules containing cyclopropyl derivatives.[321-322]

Carbenes are neutral compounds containing a divalent carbon atom that has just six electrons. The divalent carbon atom in a carbene compound can have either two singly occupied orbitals (triplet state) or both a lone pair and a vacant orbital (singlet state).[323] Although most of carbenes are too reactive to be isolated in laboratory conditions, some carbenes are stable and isolable for characterization and further transformations.[324] The key for the synthesis of stable carbenes is careful design of its electronic and steric environments.[325-328] Therefore, embedding carbenes in a MOF will add steric bulk to their structures, hence stabilizing them. Moreover, introducing such reactive functionality into a MOF structure would be an exciting target considering its potential interactions with guest molecules and scope for further derivatization to prepare a range of new MOFs.

MOFs containing free carbenes have been reported previously.[329-330] However, the structures of these materials were not fully characterized. For our target MOF, if the thermolysis proceeds in a single-crystal-to-single-crystal manner, the structure of resulting MOF containing carbene can be determined by SCXRD analysis. In addition, TGA will be informative for determining the amount of ethylene gas that will be released during thermolysis. For ^{1}H NMR spectroscopic analysis of a digested MOF sample, the carbene ligand can be converted in its corresponding ylide compound.[321] The putative formation of a pyridinium ylide and its possible resonance structures are presented in Figure 7.6b.

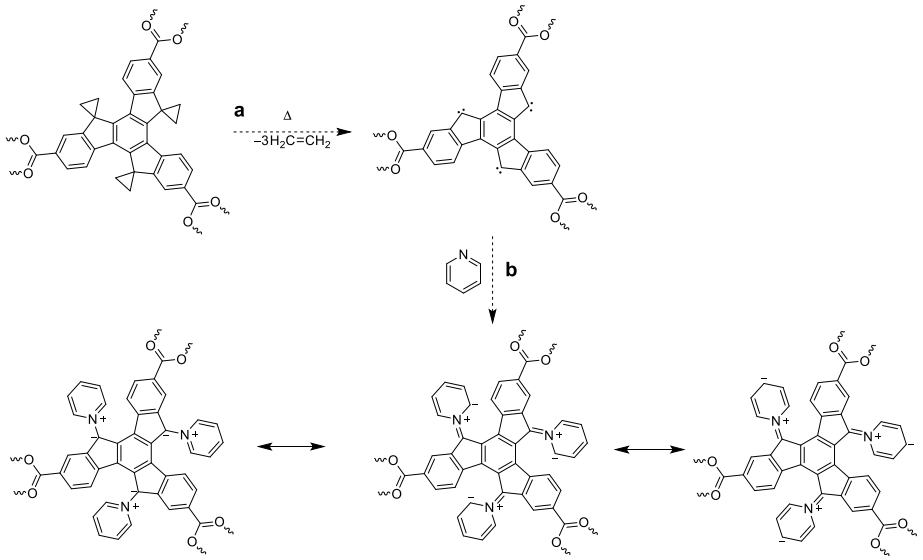

Figure 7. 6 Schematic illustrations of a) a proposed thermolytic reaction of a MOF containing a cyclopropyl-substituted truxene ligand to form a carbene by the release of ethylene gas, b) trapping of the carbene for further analysis by formation of a pyridinium ylide and its resonance structures.

References

1. Batten Stuart, R.; Champness Neil, R.; Chen, X.-M.; Garcia-Martinez, J.; Kitagawa, S.; Öhrström, L.; O'Keeffe, M.; Paik Suh, M.; Reedijk, J., Terminology of metal–organic frameworks and coordination polymers. In *Pure Appl. Chem.*, 2013; Vol. 85, p 1715.
2. Kitagawa, S.; Kitaura, R.; Noro, S.-i., Functional Porous Coordination Polymers. *Angew. Chem. Int. Ed.* **2004,** *43* (18), 2334-2375.
3. Ahmad, R.; Wong-Foy, A. G.; Matzger, A. J., Microporous Coordination Polymers As Selective Sorbents for Liquid Chromatography. *Langmuir* **2009,** *25* (20), 11977-11979.
4. Zhang, M.; Chen, Y.-P.; Zhou, H.-C., Structural design of porous coordination networks from tetrahedral building units. *CrystEngComm* **2013,** *15* (45), 9544-9552.
5. Li, H.; Eddaoudi, M.; O'Keeffe, M.; Yaghi, O. M., Design and synthesis of an exceptionally stable and highly porous metal-organic framework. *Nature* **1999,** *402*, 276.
6. Xue, M.; Liu, Y.; Schaffino, R. M.; Xiang, S.; Zhao, X.; Zhu, G.-S.; Qiu, S.-L.; Chen, B., New Prototype Isoreticular Metal−Organic Framework $Zn_4O(FMA)_3$ for Gas Storage. *Inorg. Chem.* **2009,** *48* (11), 4649-4651.
7. Farha, O. K.; Özgür Yazaydın, A.; Eryazici, I.; Malliakas, C. D.; Hauser, B. G.; Kanatzidis, M. G.; Nguyen, S. T.; Snurr, R. Q.; Hupp, J. T., De novo synthesis of a metal–organic framework material featuring ultrahigh surface area and gas storage capacities. *Nature Chem.* **2010,** *2*, 944.
8. Lee, S. J.; Doussot, C.; Baux, A.; Liu, L.; Jameson, G. B.; Richardson, C.; Pak, J. J.; Trousselet, F.; Coudert, F.-X.; Telfer, S. G., Multicomponent Metal–Organic Frameworks as Defect-Tolerant Materials. *Chem. Mater.* **2016,** *28* (1), 368-375.
9. Buser, H. J.; Schwarzenbach, D.; Petter, W.; Ludi, A., The crystal structure of Prussian Blue: $Fe_4[Fe(CN)_6]_3.xH_2O$. *Inorg. Chem.* **1977,** *16* (11), 2704-2710.
10. Hoskins, B. F.; Robson, R., Infinite polymeric frameworks consisting of three dimensionally linked rod-like segments. *J. Am. Chem. Soc.* **1989,** *111* (15), 5962-5964.
11. Hoskins, B. F.; Robson, R., Design and construction of a new class of scaffolding-like materials comprising infinite polymeric frameworks of 3D-linked molecular rods. A reappraisal of the zinc cyanide and cadmium cyanide structures and the synthesis and structure of the diamond-related frameworks $[N(CH_3)_4][CuIZnII(CN)_4]$ and CuI[4,4',4'',4'''-tetracyanotetraphenylmethane]BF4.xC6H5NO2. *J. Am. Chem. Soc.* **1990,** *112* (4), 1546-1554.
12. Yaghi, O. M.; Li, H., Hydrothermal Synthesis of a Metal-Organic Framework Containing Large Rectangular Channels. *J. Am. Chem. Soc.* **1995,** *117* (41), 10401-10402.
13. Yaghi, O. M.; Li, G.; Li, H., Selective binding and removal of guests in a microporous metal–organic framework. *Nature* **1995,** *378*, 703.

14. Kondo, M.; Yoshitomi, T.; Matsuzaka, H.; Kitagawa, S.; Seki, K., Three-Dimensional Framework with Channeling Cavities for Small Molecules: {[M_2(4,4′-bpy)$_3$(NO_3)$_4$] • xH_2O}n (M = Co, Ni, Zn). *Angew. Chem. Int. Ed. Engl.* **1997,** *36* (16), 1725-1727.

15. Li, H.; Eddaoudi, M.; Groy, T. L.; Yaghi, O. M., Establishing Microporosity in Open Metal−Organic Frameworks: Gas Sorption Isotherms for Zn(BDC) (BDC = 1,4-Benzenedicarboxylate). *J. Am. Chem. Soc.* **1998,** *120* (33), 8571-8572.

16. Chui, S. S.-Y.; Lo, S. M.-F.; Charmant, J. P. H.; Orpen, A. G.; Williams, I. D., A Chemically Functionalizable Nanoporous Material [Cu_3(TMA)$_2$(H_2O)$_3$]n. *Science* **1999,** *283* (5405), 1148-1150.

17. Brunauer, S.; Emmett, P. H.; Teller, E., Adsorption of Gases in Multimolecular Layers. *J. Am. Chem. Soc.* **1938,** *60* (2), 309-319.

18. Kaye, S. S.; Dailly, A.; Yaghi, O. M.; Long, J. R., Impact of Preparation and Handling on the Hydrogen Storage Properties of Zn_4O(1,4-benzenedicarboxylate)$_3$ (MOF-5). *J. Am. Chem. Soc.* **2007,** *129* (46), 14176-14177.

19. Eddaoudi, M.; Kim, J.; Rosi, N.; Vodak, D.; Wachter, J.; O'Keeffe, M.; Yaghi, O. M., Systematic Design of Pore Size and Functionality in Isoreticular MOFs and Their Application in Methane Storage. *Science* **2002,** *295* (5554), 469-472.

20. Yaghi, O. M.; O'Keeffe, M.; Ockwig, N. W.; Chae, H. K.; Eddaoudi, M.; Kim, J., Reticular synthesis and the design of new materials. *Nature* **2003,** *423*, 705.

21. Férey, G.; Mellot-Draznieks, C.; Serre, C.; Millange, F.; Dutour, J.; Surblé, S.; Margiolaki, I., A Chromium Terephthalate-Based Solid with Unusually Large Pore Volumes and Surface Area. *Science* **2005,** *309* (5743), 2040-2042.

22. Lin, Y.; Yan, Q.; Kong, C.; Chen, L., Polyethyleneimine Incorporated Metal-Organic Frameworks Adsorbent for Highly Selective CO_2 Capture. *Sci. Rep.* **2013,** *3*, 1859.

23. Yan, Q.; Lin, Y.; Kong, C.; Chen, L., Remarkable CO_2/CH_4 selectivity and CO_2 adsorption capacity exhibited by polyamine-decorated metal–organic framework adsorbents. *Chem. Commun.* **2013,** *49* (61), 6873-6875.

24. Yoon, M.; Srirambalaji, R.; Kim, K., Homochiral Metal–Organic Frameworks for Asymmetric Heterogeneous Catalysis. *Chem. Rev.* **2012,** *112* (2), 1196-1231.

25. Serra-Crespo, P.; Ramos-Fernandez, E. V.; Gascon, J.; Kapteijn, F., Synthesis and Characterization of an Amino Functionalized MIL-101(Al): Separation and Catalytic Properties. *Chem. Mater.* **2011,** *23* (10), 2565-2572.

26. Carson, F.; Su, J.; Platero-Prats, A. E.; Wan, W.; Yun, Y.; Samain, L.; Zou, X., Framework Isomerism in Vanadium Metal–Organic Frameworks: MIL-88B(V) and MIL-101(V). *Cryst. Growth Des.* **2013,** *13* (11), 5036-5044.

27. Sonnauer, A.; Hoffmann, F.; Fröba, M.; Kienle, L.; Duppel, V.; Thommes, M.; Serre, C.; Férey, G.; Stock, N., Giant Pores in a Chromium 2,6-Naphthalenedicarboxylate Open-

Framework Structure with MIL-101 Topology. *Angew. Chem. Int. Ed.* **2009,** *48* (21), 3791-3794.

28. Stock, N.; Biswas, S., Synthesis of Metal-Organic Frameworks (MOFs): Routes to Various MOF Topologies, Morphologies, and Composites. *Chem. Rev.* **2012,** *112* (2), 933-969.

29. Howarth, A. J.; Peters, A. W.; Vermeulen, N. A.; Wang, T. C.; Hupp, J. T.; Farha, O. K., Best Practices for the Synthesis, Activation, and Characterization of Metal–Organic Frameworks. *Chem. Mater.* **2017,** *29* (1), 26-39.

30. Schaate, A.; Roy, P.; Godt, A.; Lippke, J.; Waltz, F.; Wiebcke, M.; Behrens, P., Modulated Synthesis of Zr-Based Metal–Organic Frameworks: From Nano to Single Crystals. *Chem. Eur. J.* **2011,** *17* (24), 6643-6651.

31. Mondloch, J. E.; Karagiaridi, O.; Farha, O. K.; Hupp, J. T., Activation of metal–organic framework materials. *CrystEngComm* **2013,** *15* (45), 9258-9264.

32. Ma, J.; Kalenak, A. P.; Wong-Foy, A. G.; Matzger, A. J., Rapid Guest Exchange and Ultra-Low Surface Tension Solvents Optimize Metal–Organic Framework Activation. *Angew. Chem. Int. Ed.* **2017,** *56* (46), 14618-14621.

33. Nelson, A. P.; Farha, O. K.; Mulfort, K. L.; Hupp, J. T., Supercritical Processing as a Route to High Internal Surface Areas and Permanent Microporosity in Metal−Organic Framework Materials. *J. Am. Chem. Soc.* **2009,** *131* (2), 458-460.

34. Burtch, N. C.; Jasuja, H.; Walton, K. S., Water Stability and Adsorption in Metal–Organic Frameworks. *Chem. Rev.* **2014,** *114* (20), 10575-10612.

35. Wang, C.; Liu, X.; Keser Demir, N.; Chen, J. P.; Li, K., Applications of water stable metal–organic frameworks. *Chem. Soc. Rev.* **2016,** *45* (18), 5107-5134.

36. Canivet, J.; Fateeva, A.; Guo, Y.; Coasne, B.; Farrusseng, D., Water adsorption in MOFs: fundamentals and applications. *Chem. Soc. Rev.* **2014,** *43* (16), 5594-5617.

37. Bosch, M.; Zhang, M.; Zhou, H.-C., Increasing the Stability of Metal-Organic Frameworks. *Adv. Chem.* **2014,** *2014*, 8.

38. Yuan, S.; Feng, L.; Wang, K.; Pang, J.; Bosch, M.; Lollar, C.; Sun, Y.; Qin, J.; Yang, X.; Zhang, P.; Wang, Q.; Zou, L.; Zhang, Y.; Zhang, L.; Fang, Y.; Li, J.; Zhou, H.-C., Stable Metal–Organic Frameworks: Design, Synthesis, and Applications. *Adv. Mater.* **2018,** *30* (37), 1704303.

39. Taylor-Pashow, K. M. L.; Della Rocca, J.; Xie, Z.; Tran, S.; Lin, W., Postsynthetic Modifications of Iron-Carboxylate Nanoscale Metal−Organic Frameworks for Imaging and Drug Delivery. *J. Am. Chem. Soc.* **2009,** *131* (40), 14261-14263.

40. Cavka, J. H.; Jakobsen, S.; Olsbye, U.; Guillou, N.; Lamberti, C.; Bordiga, S.; Lillerud, K. P., A New Zirconium Inorganic Building Brick Forming Metal Organic Frameworks with Exceptional Stability. *J. Am. Chem. Soc.* **2008,** *130* (42), 13850-13851.

41. DeCoste, J. B.; Peterson, G. W.; Jasuja, H.; Glover, T. G.; Huang, Y.-g.; Walton, K. S., Stability and degradation mechanisms of metal–organic frameworks containing the Zr6O4(OH)4 secondary building unit. *J. Mater. Chem. A* **2013,** *1* (18), 5642-5650.

42. Mondloch, J. E.; Katz, M. J.; Planas, N.; Semrouni, D.; Gagliardi, L.; Hupp, J. T.; Farha, O. K., Are Zr6-based MOFs water stable? Linker hydrolysis vs. capillary-force-driven channel collapse. *Chem. Commun.* **2014,** *50* (64), 8944-8946.

43. Park, K. S.; Ni, Z.; Côté, A. P.; Choi, J. Y.; Huang, R.; Uribe-Romo, F. J.; Chae, H. K.; O'Keeffe, M.; Yaghi, O. M., Exceptional chemical and thermal stability of zeolitic imidazolate frameworks. *Proc. Natl. Acad. Sci. U.S.A.* **2006,** *103* (27), 10186-10191.

44. Huang, X.-C.; Lin, Y.-Y.; Zhang, J.-P.; Chen, X.-M., Ligand-Directed Strategy for Zeolite-Type Metal–Organic Frameworks: Zinc(II) Imidazolates with Unusual Zeolitic Topologies. *Angew. Chem. Int. Ed.* **2006,** *45* (10), 1557-1559.

45. Kalidindi, S. B.; Nayak, S.; Briggs, M. E.; Jansat, S.; Katsoulidis, A. P.; Miller, G. J.; Warren, J. E.; Antypov, D.; Corà, F.; Slater, B.; Prestly, M. R.; Martí-Gastaldo, C.; Rosseinsky, M. J., Chemical and Structural Stability of Zirconium-based Metal–Organic Frameworks with Large Three-Dimensional Pores by Linker Engineering. *Angew. Chem. Int. Ed.* **2015,** *54* (1), 221-226.

46. Yang, C.; Kaipa, U.; Mather, Q. Z.; Wang, X.; Nesterov, V.; Venero, A. F.; Omary, M. A., Fluorous Metal–Organic Frameworks with Superior Adsorption and Hydrophobic Properties toward Oil Spill Cleanup and Hydrocarbon Storage. *J. Am. Chem. Soc.* **2011,** *133* (45), 18094-18097.

47. Nijem, N.; Canepa, P.; Kaipa, U.; Tan, K.; Roodenko, K.; Tekarli, S.; Halbert, J.; Oswald, I. W. H.; Arvapally, R. K.; Yang, C.; Thonhauser, T.; Omary, M. A.; Chabal, Y. J., Water Cluster Confinement and Methane Adsorption in the Hydrophobic Cavities of a Fluorinated Metal–Organic Framework. *J. Am. Chem. Soc.* **2013,** *135* (34), 12615-12626.

48. Liu, L.; Telfer, S. G., Systematic Ligand Modulation Enhances the Moisture Stability and Gas Sorption Characteristics of Quaternary Metal–Organic Frameworks. *J. Am. Chem. Soc.* **2015,** *137* (11), 3901-3909.

49. Tranchemontagne, D. J.; Mendoza-Cortés, J. L.; O'Keeffe, M.; Yaghi, O. M., Secondary building units, nets and bonding in the chemistry of metal–organic frameworks. *Chem. Soc. Rev.* **2009,** *38* (5), 1257-1283.

50. Koyama, H.; Saito, Y., The Crystal Structure of Zinc Oxyacetate, $Zn_4O(CH_3COO)_6$. *Bull. Chem. Soc. Jpn.* **1954,** *27* (2), 112-114.

51. Tulinsky, A.; Worthington, C. R.; Pignataro, F., Basic beryllium acetate. I. The collection of intensity data. *Acta Cryst.* **1959,** *12* (9), 623-626.

52. Jaitner, P.; Rieker, C.; Wurst, K., Aggregation of carbamato ligands around the $[Co_4O]_6^+$ core. Synthesis and structure of the cluster $[Co_4O(O_2CNC_9H_{18})_6]$ prepared by a novel

oxo-transfer reaction of the nitroxyl free radical 2,2,6,6-tetramethylpiperidin-1-oxyl with [$Co_2(CO)_8$]. *Chem. Commun.* **1997,** (13), 1245-1246.

53. Kalmutzki, M. J.; Hanikel, N.; Yaghi, O. M., Secondary building units as the turning point in the development of the reticular chemistry of MOFs. *Sci. Adv.* **2018,** *4* (10).

54. Rowsell, J. L. C.; Yaghi, O. M., Metal–organic frameworks: a new class of porous materials. *Microporous Mesoporous Mater.* **2004,** *73* (1), 3-14.

55. Li, M.; Li, D.; O'Keeffe, M.; Yaghi, O. M., Topological Analysis of Metal–Organic Frameworks with Polytopic Linkers and/or Multiple Building Units and the Minimal Transitivity Principle. *Chem. Rev.* **2014,** *114* (2), 1343-1370.

56. Lu, W.; Wei, Z.; Gu, Z.-Y.; Liu, T.-F.; Park, J.; Park, J.; Tian, J.; Zhang, M.; Zhang, Q.; Gentle III, T.; Bosch, M.; Zhou, H.-C., Tuning the structure and function of metal–organic frameworks via linker design. *Chem. Soc. Rev.* **2014,** *43* (16), 5561-5593.

57. Furukawa, H.; Cordova, K. E.; O'Keeffe, M.; Yaghi, O. M., The Chemistry and Applications of Metal-Organic Frameworks. *Science* **2013,** *341* (6149).

58. Almeida Paz, F. A.; Klinowski, J.; Vilela, S. M. F.; Tomé, J. P. C.; Cavaleiro, J. A. S.; Rocha, J., Ligand design for functional metal–organic frameworks. *Chem. Soc. Rev.* **2012,** *41* (3), 1088-1110.

59. Wang, X.-S.; Ma, S.; Sun, D.; Parkin, S.; Zhou, H.-C., A Mesoporous Metal−Organic Framework with Permanent Porosity. *J. Am. Chem. Soc.* **2006,** *128* (51), 16474-16475.

60. Ma, S.; Sun, D.; Ambrogio, M.; Fillinger, J. A.; Parkin, S.; Zhou, H.-C., Framework-Catenation Isomerism in Metal−Organic Frameworks and Its Impact on Hydrogen Uptake. *J. Am. Chem. Soc.* **2007,** *129* (7), 1858-1859.

61. Furukawa, H.; Miller, M. A.; Yaghi, O. M., Independent verification of the saturation hydrogen uptake in MOF-177 and establishment of a benchmark for hydrogen adsorption in metal–organic frameworks. *J. Mater. Chem.* **2007,** *17* (30), 3197-3204.

62. Furukawa, H.; Ko, N.; Go, Y. B.; Aratani, N.; Choi, S. B.; Choi, E.; Yazaydin, A. Ö.; Snurr, R. Q.; O'Keeffe, M.; Kim, J.; Yaghi, O. M., Ultrahigh Porosity in Metal-Organic Frameworks. *Science* **2010,** *329* (5990), 424-428.

63. Furukawa, H.; Go, Y. B.; Ko, N.; Park, Y. K.; Uribe-Romo, F. J.; Kim, J.; O'Keeffe, M.; Yaghi, O. M., Isoreticular Expansion of Metal–Organic Frameworks with Triangular and Square Building Units and the Lowest Calculated Density for Porous Crystals. *Inorg. Chem.* **2011,** *50* (18), 9147-9152.

64. Wong-Foy, A. G.; Lebel, O.; Matzger, A. J., Porous Crystal Derived from a Tricarboxylate Linker with Two Distinct Binding Motifs. *J. Am. Chem. Soc.* **2007,** *129* (51), 15740-15741.

65. Duan, J.; Yang, Z.; Bai, J.; Zheng, B.; Li, Y.; Li, S., Highly selective CO_2 capture of an agw-type metal–organic framework with inserted amides: experimental and theoretical studies. *Chem. Commun.* **2012,** *48* (25), 3058-3060.

66. Colombo, V.; Galli, S.; Choi, H. J.; Han, G. D.; Maspero, A.; Palmisano, G.; Masciocchi, N.; Long, J. R., High thermal and chemical stability in pyrazolate-bridged metal–organic frameworks with exposed metal sites. *Chem. Sci.* **2011,** *2* (7), 1311-1319.

67. Xiao, D. J.; Gonzalez, M. I.; Darago, L. E.; Vogiatzis, K. D.; Haldoupis, E.; Gagliardi, L.; Long, J. R., Selective, Tunable O_2 Binding in Cobalt(II)–Triazolate/Pyrazolate Metal–Organic Frameworks. *J. Am. Chem. Soc.* **2016,** *138* (22), 7161-7170.

68. Sumida, K.; Horike, S.; Kaye, S. S.; Herm, Z. R.; Queen, W. L.; Brown, C. M.; Grandjean, F.; Long, G. J.; Dailly, A.; Long, J. R., Hydrogen storage and carbon dioxide capture in an iron-based sodalite-type metal–organic framework (Fe-BTT) discovered via high-throughput methods. *Chem. Sci.* **2010,** *1* (2), 184-191.

69. Dincă, M.; Han, W. S.; Liu, Y.; Dailly, A.; Brown, C. M.; Long, J. R., Observation of Cu2+–H2 Interactions in a Fully Desolvated Sodalite-Type Metal–Organic Framework. *Angew. Chem. Int. Ed.* **2007,** *46* (9), 1419-1422.

70. Dincă, M.; Dailly, A.; Liu, Y.; Brown, C. M.; Neumann, D. A.; Long, J. R., Hydrogen Storage in a Microporous Metal−Organic Framework with Exposed Mn2+ Coordination Sites. *J. Am. Chem. Soc.* **2006,** *128* (51), 16876-16883.

71. Sumida, K.; Stück, D.; Mino, L.; Chai, J.-D.; Bloch, E. D.; Zavorotynska, O.; Murray, L. J.; Dincă, M.; Chavan, S.; Bordiga, S.; Head-Gordon, M.; Long, J. R., Impact of Metal and Anion Substitutions on the Hydrogen Storage Properties of M-BTT Metal–Organic Frameworks. *J. Am. Chem. Soc.* **2013,** *135* (3), 1083-1091.

72. Deng, H.; Doonan, C. J.; Furukawa, H.; Ferreira, R. B.; Towne, J.; Knobler, C. B.; Wang, B.; Yaghi, O. M., Multiple Functional Groups of Varying Ratios in Metal-Organic Frameworks. *Science* **2010,** *327* (5967), 846-850.

73. Kong, X.; Deng, H.; Yan, F.; Kim, J.; Swisher, J. A.; Smit, B.; Yaghi, O. M.; Reimer, J. A., Mapping of Functional Groups in Metal-Organic Frameworks. *Science* **2013,** *341* (6148), 882-885.

74. Cozzi, P. G., Metal–Salen Schiff base complexes in catalysis: practical aspects. *Chem. Soc. Rev.* **2004,** *33* (7), 410-421.

75. Xia, Q.; Li, Z.; Tan, C.; Liu, Y.; Gong, W.; Cui, Y., Multivariate Metal–Organic Frameworks as Multifunctional Heterogeneous Asymmetric Catalysts for Sequential Reactions. *J. Am. Chem. Soc.* **2017,** *139* (24), 8259-8266.

76. Chen, W.; Wang, J.-Y.; Chen, C.; Yue, Q.; Yuan, H.-M.; Chen, J.-S.; Wang, S.-N., Photoluminescent Metal−Organic Polymer Constructed from Trimetallic Clusters and Mixed Carboxylates. *Inorg. Chem.* **2003,** *42* (4), 944-946.

77. Koh, K.; Wong-Foy, A. G.; Matzger, A. J., A Crystalline Mesoporous Coordination Copolymer with High Microporosity. *Angew. Chem. Int. Ed.* **2008,** *47* (4), 677-680.

78. Koh, K.; Wong-Foy, A. G.; Matzger, A. J., A Porous Coordination Copolymer with over 5000 m2/g BET Surface Area. *J. Am. Chem. Soc.* **2009,** *131* (12), 4184-4185.

79. Koh, K.; Wong-Foy, A. G.; Matzger, A. J., Coordination Copolymerization Mediated by Zn4O(CO2R)6 Metal Clusters: a Balancing Act between Statistics and Geometry. *J. Am. Chem. Soc.* **2010,** *132* (42), 15005-15010.

80. Yao, Q.; Su, J.; Cheung, O.; Liu, Q.; Hedin, N.; Zou, X., Interpenetrated metal–organic frameworks and their uptake of CO_2 at relatively low pressures. *J. Mater. Chem.* **2012,** *22* (20), 10345-10351.

81. Zhang, Q.; Lei, M.; Kong, F.; Yang, Y., A water-stable homochiral luminescent MOF constructed from an achiral acylamide-containing dicarboxylate ligand for enantioselective sensing of penicillamine. *Chem. Commun.* **2018,** *54* (77), 10901-10904.

82. Liu, L.; Konstas, K.; Hill, M. R.; Telfer, S. G., Programmed Pore Architectures in Modular Quaternary Metal–Organic Frameworks. *J. Am. Chem. Soc.* **2013,** *135* (47), 17731-17734.

83. Lun, D. J.; Waterhouse, G. I. N.; Telfer, S. G., A General Thermolabile Protecting Group Strategy for Organocatalytic Metal−Organic Frameworks. *J. Am. Chem. Soc.* **2011,** *133* (15), 5806-5809.

84. Liu, L.; Zhou, T.-Y.; Telfer, S. G., Modulating the Performance of an Asymmetric Organocatalyst by Tuning Its Spatial Environment in a Metal–Organic Framework. *J. Am. Chem. Soc.* **2017,** *139* (39), 13936-13943.

85. Liang, C.-C.; Shi, Z.-L.; He, C.-T.; Tan, J.; Zhou, H.-D.; Zhou, H.-L.; Lee, Y.; Zhang, Y.-B., Engineering of Pore Geometry for Ultrahigh Capacity Methane Storage in Mesoporous Metal–Organic Frameworks. *J. Am. Chem. Soc.* **2017,** *139* (38), 13300-13303.

86. Dutta, A.; Wong-Foy, A. G.; Matzger, A. J., Coordination copolymerization of three carboxylate linkers into a pillared layer framework. *Chem. Sci.* **2014,** *5* (10), 3729-3734.

87. Pang, J.; Yuan, S.; Qin, J.; Wu, M.; Lollar, C. T.; Li, J.; Huang, N.; Li, B.; Zhang, P.; Zhou, H.-C., Enhancing Pore-Environment Complexity Using a Trapezoidal Linker: Toward Stepwise Assembly of Multivariate Quinary Metal–Organic Frameworks. *J. Am. Chem. Soc.* **2018,** *140* (39), 12328-12332.

88. Ma, S.; Zhou, H.-C., Gas storage in porous metal–organic frameworks for clean energy applications. *Chem. Commun.* **2010,** *46* (1), 44-53.

89. Li, H.; Wang, K.; Sun, Y.; Lollar, C. T.; Li, J.; Zhou, H.-C., Recent advances in gas storage and separation using metal–organic frameworks. *Mater. Today* **2018,** *21* (2), 108-121.

90. Gascon, J.; Corma, A.; Kapteijn, F.; Llabrés i Xamena, F. X., Metal Organic Framework Catalysis: Quo vadis? *ACS Catal.* **2014,** *4* (2), 361-378.

91. Abánades Lázaro, I.; Forgan, R. S., Application of zirconium MOFs in drug delivery and biomedicine. *Coord. Chem. Rev.* **2019,** *380*, 230-259.

92. Guo, Y.; Feng, X.; Han, T.; Wang, S.; Lin, Z.; Dong, Y.; Wang, B., Tuning the Luminescence of Metal–Organic Frameworks for Detection of Energetic Heterocyclic Compounds. *J. Am. Chem. Soc.* **2014,** *136* (44), 15485-15488.

93. Zhang, C.; Sun, L.; Yan, Y.; Li, J.; Song, X.; Liu, Y.; Liang, Z., A luminescent cadmium metal–organic framework for sensing of nitroaromatic explosives. *Dalton Trans.* **2015,** *44* (1), 230-236.

94. Chen, M.; Xu, W.-M.; Tian, J.-Y.; Cui, H.; Zhang, J.-X.; Liu, C.-S.; Du, M., A terbium(iii) lanthanide–organic framework as a platform for a recyclable multi-responsive luminescent sensor. *J. Mater. Chem. C* **2017,** *5* (8), 2015-2021.

95. Talin, A. A.; Centrone, A.; Ford, A. C.; Foster, M. E.; Stavila, V.; Haney, P.; Kinney, R. A.; Szalai, V.; El Gabaly, F.; Yoon, H. P.; Léonard, F.; Allendorf, M. D., Tunable Electrical Conductivity in Metal-Organic Framework Thin-Film Devices. *Science* **2014,** *343* (6166), 66-69.

96. Della Rocca, J.; Liu, D.; Lin, W., Nanoscale Metal–Organic Frameworks for Biomedical Imaging and Drug Delivery. *Acc. Chem. Res.* **2011,** *44* (10), 957-968.

97. Sheberla, D.; Sun, L.; Blood-Forsythe, M. A.; Er, S.; Wade, C. R.; Brozek, C. K.; Aspuru-Guzik, A.; Dincă, M., High Electrical Conductivity in Ni3(2,3,6,7,10,11-hexaiminotriphenylene)2, a Semiconducting Metal–Organic Graphene Analogue. *J. Am. Chem. Soc.* **2014,** *136* (25), 8859-8862.

98. van den Berg, A. W. C.; Areán, C. O., Materials for hydrogen storage: current research trends and perspectives. *Chem. Commun.* **2008,** (6), 668-681.

99. Rowsell, J. L. C.; Yaghi, O. M., Strategies for Hydrogen Storage in Metal–Organic Frameworks. *Angew. Chem. Int. Ed.* **2005,** *44* (30), 4670-4679.

100. Zhou, W.; Wu, H.; Yildirim, T., Enhanced H2 Adsorption in Isostructural Metal−Organic Frameworks with Open Metal Sites: Strong Dependence of the Binding Strength on Metal Ions. *J. Am. Chem. Soc.* **2008,** *130* (46), 15268-15269.

101. Vitillo, J. G.; Regli, L.; Chavan, S.; Ricchiardi, G.; Spoto, G.; Dietzel, P. D. C.; Bordiga, S.; Zecchina, A., Role of Exposed Metal Sites in Hydrogen Storage in MOFs. *J. Am. Chem. Soc.* **2008,** *130* (26), 8386-8396.

102. Dietzel, P. D. C.; Georgiev, P. A.; Eckert, J.; Blom, R.; Strässle, T.; Unruh, T., Interaction of hydrogen with accessible metal sites in the metal–organic frameworks M2(dhtp) (CPO-27-M; M = Ni, Co, Mg). *Chem. Commun.* **2010,** *46* (27), 4962-4964.

103. Nijem, N.; Veyan, J.-F.; Kong, L.; Wu, H.; Zhao, Y.; Li, J.; Langreth, D. C.; Chabal, Y. J., Molecular Hydrogen "Pairing" Interaction in a Metal Organic Framework System with Unsaturated Metal Centers (MOF-74). *J. Am. Chem. Soc.* **2010,** *132* (42), 14834-14848.

104. Wang, X.-S.; Ma, S.; Forster, P. M.; Yuan, D.; Eckert, J.; López, J. J.; Murphy, B. J.; Parise, J. B.; Zhou, H.-C., Enhancing H2 Uptake by "Close-Packing" Alignment of Open Copper Sites in Metal–Organic Frameworks. *Angew. Chem. Int. Ed.* **2008,** *47* (38), 7263-7266.

105. Wang, X.-S.; Ma, S.; Rauch, K.; Simmons, J. M.; Yuan, D.; Wang, X.; Yildirim, T.; Cole, W. C.; López, J. J.; de Meijere, A.; Zhou, H.-C., Metal−Organic Frameworks Based on

Double-Bond-Coupled Di-Isophthalate Linkers with High Hydrogen and Methane Uptakes. *Chem. Mater.* **2008,** *20* (9), 3145-3152.

106. Tan, C.; Yang, S.; Champness, N. R.; Lin, X.; Blake, A. J.; Lewis, W.; Schröder, M., High capacity gas storage by a 4,8-connected metal–organic polyhedral framework. *Chem. Commun.* **2011,** *47* (15), 4487-4489.

107. Sun, D.; Ma, S.; Ke, Y.; Collins, D. J.; Zhou, H.-C., An Interweaving MOF with High Hydrogen Uptake. *J. Am. Chem. Soc.* **2006,** *128* (12), 3896-3897.

108. Mason, J. A.; Veenstra, M.; Long, J. R., Evaluating metal–organic frameworks for natural gas storage. *Chem. Sci.* **2014,** *5* (1), 32-51.

109. Celzard, A.; Fierro, V., Preparing a Suitable Material Designed for Methane Storage: A Comprehensive Report. *Energy Fuels* **2005,** *19* (2), 573-583.

110. He, Y.; Zhou, W.; Qian, G.; Chen, B., Methane storage in metal–organic frameworks. *Chem. Soc. Rev.* **2014,** *43* (16), 5657-5678.

111. Schoedel, A.; Ji, Z.; Yaghi, O. M., The role of metal–organic frameworks in a carbon-neutral energy cycle. *Nat. Energy* **2016,** *1*, 16034.

112. Lin, J.-M.; He, C.-T.; Liu, Y.; Liao, P.-Q.; Zhou, D.-D.; Zhang, J.-P.; Chen, X.-M., A Metal–Organic Framework with a Pore Size/Shape Suitable for Strong Binding and Close Packing of Methane. *Angew. Chem. Int. Ed.* **2016,** *55* (15), 4674-4678.

113. Mason, J. A.; Oktawiec, J.; Taylor, M. K.; Hudson, M. R.; Rodriguez, J.; Bachman, J. E.; Gonzalez, M. I.; Cervellino, A.; Guagliardi, A.; Brown, C. M.; Llewellyn, P. L.; Masciocchi, N.; Long, J. R., Methane storage in flexible metal–organic frameworks with intrinsic thermal management. *Nature* **2015,** *527*, 357.

114. Sumida, K.; Rogow, D. L.; Mason, J. A.; McDonald, T. M.; Bloch, E. D.; Herm, Z. R.; Bae, T.-H.; Long, J. R., Carbon Dioxide Capture in Metal–Organic Frameworks. *Chem. Rev.* **2012,** *112* (2), 724-781.

115. Olajire, A. A., Synthesis of bare and functionalized porous adsorbent materials for CO_2 capture. *Greenhouse Gas Sci Technol.* **2017,** *7* (3), 399-459.

116. Caskey, S. R.; Wong-Foy, A. G.; Matzger, A. J., Dramatic Tuning of Carbon Dioxide Uptake via Metal Substitution in a Coordination Polymer with Cylindrical Pores. *J. Am. Chem. Soc.* **2008,** *130* (33), 10870-10871.

117. McDonald, T. M.; Lee, W. R.; Mason, J. A.; Wiers, B. M.; Hong, C. S.; Long, J. R., Capture of Carbon Dioxide from Air and Flue Gas in the Alkylamine-Appended Metal–Organic Framework mmen-Mg2(dobpdc). *J. Am. Chem. Soc.* **2012,** *134* (16), 7056-7065.

118. Liao, P.-Q.; Chen, H.; Zhou, D.-D.; Liu, S.-Y.; He, C.-T.; Rui, Z.; Ji, H.; Zhang, J.-P.; Chen, X.-M., Monodentate hydroxide as a super strong yet reversible active site for CO_2 capture from high-humidity flue gas. *Energy Environ. Sci.* **2015,** *8* (3), 1011-1016.

119. Nugent, P.; Belmabkhout, Y.; Burd, S. D.; Cairns, A. J.; Luebke, R.; Forrest, K.; Pham, T.; Ma, S.; Space, B.; Wojtas, L.; Eddaoudi, M.; Zaworotko, M. J., Porous materials with optimal adsorption thermodynamics and kinetics for CO_2 separation. *Nature* **2013,** *495*, 80.

120. Smeets, S.; Berkson, Z. J.; Xie, D.; Zones, S. I.; Wan, W.; Zou, X.; Hsieh, M.-F.; Chmelka, B. F.; McCusker, L. B.; Baerlocher, C., Well-Defined Silanols in the Structure of the Calcined High-Silica Zeolite SSZ-70: New Understanding of a Successful Catalytic Material. *J. Am. Chem. Soc.* **2017,** *139* (46), 16803-16812.

121. Corma, A., From Microporous to Mesoporous Molecular Sieve Materials and Their Use in Catalysis. *Chem. Rev.* **1997,** *97* (6), 2373-2420.

122. Wight, A. P.; Davis, M. E., Design and Preparation of Organic−Inorganic Hybrid Catalysts. *Chem. Rev.* **2002,** *102* (10), 3589-3614.

123. Taguchi, A.; Schüth, F., Ordered mesoporous materials in catalysis. *Microporous Mesoporous Mater.* **2005,** *77* (1), 1-45.

124. Zhu, L.; Liu, X.-Q.; Jiang, H.-L.; Sun, L.-B., Metal–Organic Frameworks for Heterogeneous Basic Catalysis. *Chem. Rev.* **2017,** *117* (12), 8129-8176.

125. Jiang, J.; Yaghi, O. M., Brønsted Acidity in Metal–Organic Frameworks. *Chem. Rev.* **2015,** *115* (14), 6966-6997.

126. Majewski, M. B.; Howarth, A. J.; Li, P.; Wasielewski, M. R.; Hupp, J. T.; Farha, O. K., Enzyme encapsulation in metal–organic frameworks for applications in catalysis. *CrystEngComm* **2017,** *19* (29), 4082-4091.

127. Huang, Y.-B.; Liang, J.; Wang, X.-S.; Cao, R., Multifunctional metal–organic framework catalysts: synergistic catalysis and tandem reactions. *Chem. Soc. Rev.* **2017,** *46* (1), 126-157.

128. Nath, I.; Chakraborty, J.; Verpoort, F., Metal organic frameworks mimicking natural enzymes: a structural and functional analogy. *Chem. Soc. Rev.* **2016,** *45* (15), 4127-4170.

129. Zou, C.; Zhang, T.; Xie, M.-H.; Yan, L.; Kong, G.-Q.; Yang, X.-L.; Ma, A.; Wu, C.-D., Four Metalloporphyrinic Frameworks as Heterogeneous Catalysts for Selective Oxidation and Aldol Reaction. *Inorg. Chem.* **2013,** *52* (7), 3620-3626.

130. Meng, L.; Cheng, Q.; Kim, C.; Gao, W.-Y.; Wojtas, L.; Chen, Y.-S.; Zaworotko, M. J.; Zhang, X. P.; Ma, S., Crystal Engineering of a Microporous, Catalytically Active fcu Topology MOF Using a Custom-Designed Metalloporphyrin Linker. *Angew. Chem. Int. Ed.* **2012,** *51* (40), 10082-10085.

131. Sasan, K.; Lin, Q.; Mao, C.; Feng, P., Incorporation of iron hydrogenase active sites into a highly stable metal–organic framework for photocatalytic hydrogen generation. *Chem. Commun.* **2014,** *50* (72), 10390-10393.

132. Fateeva, A.; Chater, P. A.; Ireland, C. P.; Tahir, A. A.; Khimyak, Y. Z.; Wiper, P. V.; Darwent, J. R.; Rosseinsky, M. J., A Water-Stable Porphyrin-Based Metal–Organic

Framework Active for Visible-Light Photocatalysis. *Angew. Chem. Int. Ed.* **2012,** *51* (30), 7440-7444.

133. Yang, X.-L.; Wu, C.-D., Metalloporphyrinic Framework Containing Multiple Pores for Highly Efficient and Selective Epoxidation. *Inorg. Chem.* **2014,** *53* (10), 4797-4799.

134. Xu, L.; Wang, J.; Xu, Y.; Zhang, Z.; Lu, P.; Fang, M.; Li, S.; Sun, P.; Liu, H.-K., A new strategy to construct metal–organic frameworks with ultrahigh chemical stability. *CrystEngComm* **2014,** *16* (37), 8656-8659.

135. Xiao, D. J.; Oktawiec, J.; Milner, P. J.; Long, J. R., Pore Environment Effects on Catalytic Cyclohexane Oxidation in Expanded Fe2(dobdc) Analogues. *J. Am. Chem. Soc.* **2016,** *138* (43), 14371-14379.

136. Schreiner, P. R.; Wittkopp, A., H-Bonding Additives Act Like Lewis Acid Catalysts. *Org. Lett.* **2002,** *4* (2), 217-220.

137. McGuirk, C. M.; Katz, M. J.; Stern, C. L.; Sarjeant, A. A.; Hupp, J. T.; Farha, O. K.; Mirkin, C. A., Turning On Catalysis: Incorporation of a Hydrogen-Bond-Donating Squaramide Moiety into a Zr Metal–Organic Framework. *J. Am. Chem. Soc.* **2015,** *137* (2), 919-925.

138. Han, Y.-H.; Zhou, Z.-Y.; Tian, C.-B.; Du, S.-W., A dual-walled cage MOF as an efficient heterogeneous catalyst for the conversion of CO_2 under mild and co-catalyst free conditions. *Green Chem.* **2016,** *18* (14), 4086-4091.

139. Zhang, G.; Wei, G.; Liu, Z.; Oliver, S. R. J.; Fei, H., A Robust Sulfonate-Based Metal–Organic Framework with Permanent Porosity for Efficient CO_2 Capture and Conversion. *Chem. Mater.* **2016,** *28* (17), 6276-6281.

140. Beyzavi, M. H.; Stephenson, C. J.; Liu, Y.; Karagiaridi, O.; Hupp, J. T.; Farha, O. K., Metal–Organic Framework-Based Catalysts: Chemical Fixation of CO_2 with Epoxides Leading to Cyclic Organic Carbonates. *Front. Energy Res.* **2015,** *2* (63).

141. Kim, J.; Kim, S.-N.; Jang, H.-G.; Seo, G.; Ahn, W.-S., CO_2 cycloaddition of styrene oxide over MOF catalysts. *Appl. Catal., A* **2013,** *453*, 175-180.

142. Kang, D.-W.; Han, X.; Ma, X.-J.; Liu, Y.-Y.; Ma, J.-F., Two cyclotriveratrylene metal–organic frameworks as effective catalysts for Knoevenagel condensation and CO_2 cycloaddition with epoxides. *Dalton Trans.* **2018**.

143. Kim, H.-C.; Huh, S.; Kim, S.-J.; Kim, Y., Selective carbon dioxide sorption and heterogeneous catalysis by a new 3D Zn-MOF with nitrogen-rich 1D channels. *Sci. Rep.* **2017,** *7* (1), 17185.

144. Du, J.-J.; Zhang, X.; Zhou, X.-P.; Li, D., Robust heterometallic MOF catalysts for the cyanosilylation of aldehydes. *Inorg. Chem. Front.* **2018**.

145. Hu, A.; Ngo, H. L.; Lin, W., Chiral Porous Hybrid Solids for Practical Heterogeneous Asymmetric Hydrogenation of Aromatic Ketones. *J. Am. Chem. Soc.* **2003,** *125* (38), 11490-11491.

146. Zhang, Y.; Li, G.; Kong, L.; Lu, H., Deep oxidative desulfurization catalyzed by Ti-based metal-organic frameworks. *Fuel* **2018,** *219*, 103-110.

147. Fei, H.; Shin, J.; Meng, Y. S.; Adelhardt, M.; Sutter, J.; Meyer, K.; Cohen, S. M., Reusable Oxidation Catalysis Using Metal-Monocatecholato Species in a Robust Metal–Organic Framework. *J. Am. Chem. Soc.* **2014,** *136* (13), 4965-4973.

148. Dhakshinamoorthy, A.; Asiri, A. M.; Garcia, H., Metal–organic frameworks catalyzed C–C and C–heteroatom coupling reactions. *Chem. Soc. Rev.* **2015,** *44* (7), 1922-1947.

149. Nguyen, L. T. L.; Le, K. K. A.; Truong, H. X.; Phan, N. T. S., Metal–organic frameworks for catalysis: the Knoevenagel reaction using zeolite imidazolate framework ZIF-9 as an efficient heterogeneous catalyst. *Catal. Sci. Technol.* **2012,** *2* (3), 521-528.

150. Miao, Z.; Luan, Y.; Qi, C.; Ramella, D., The synthesis of a bifunctional copper metal organic framework and its application in the aerobic oxidation/Knoevenagel condensation sequential reaction. *Dalton Trans.* **2016,** *45* (35), 13917-13924.

151. Lin, A.; Ibrahim, A. A.; Arab, P.; El-Kaderi, H. M.; El-Shall, M. S., Palladium Nanoparticles Supported on Ce-Metal–Organic Framework for Efficient CO Oxidation and Low-Temperature CO_2 Capture. *ACS Appl. Mater. Interfaces* **2017,** *9* (21), 17961-17968.

152. Noei, H.; Amirjalayer, S.; Müller, M.; Zhang, X.; Schmid, R.; Muhler, M.; Fischer, R. A.; Wang, Y., Low-Temperature CO Oxidation over Cu-Based Metal–Organic Frameworks Monitored by using FTIR Spectroscopy. *ChemCatChem* **2012,** *4* (6), 755-759.

153. Li, B.; Wen, H.-M.; Cui, Y.; Zhou, W.; Qian, G.; Chen, B., Emerging Multifunctional Metal–Organic Framework Materials. *Adv. Mater.* **2016,** *28* (40), 8819-8860.

154. Li, B.; Wen, H.-M.; Zhou, W.; Chen, B., Porous Metal–Organic Frameworks for Gas Storage and Separation: What, How, and Why? *J. Phys. Chem. Lett.* **2014,** *5* (20), 3468-3479.

155. Chughtai, A. H.; Ahmad, N.; Younus, H. A.; Laypkov, A.; Verpoort, F., Metal–organic frameworks: versatile heterogeneous catalysts for efficient catalytic organic transformations. *Chem. Soc. Rev.* **2015,** *44* (19), 6804-6849.

156. Sun, D.; Ke, Y.; Collins, D. J.; Lorigan, G. A.; Zhou, H.-C., Construction of Robust Open Metal−Organic Frameworks with Chiral Channels and Permanent Porosity. *Inorg. Chem.* **2007,** *46* (7), 2725-2734.

157. Goubard, F.; Dumur, F., Truxene: a promising scaffold for future materials. *RSC Adv.* **2015,** *5* (5), 3521-3551.

158. Yonghwi, K.; Sunirban, D.; Saurav, B.; Soonsang, H.; Gyu, K. M.; Minyoung, Y.; Srinivasan, N.; Kimoon, K., Metal‐Ion Metathesis in Metal‐Organic Frameworks: A Synthetic Route to New Metal‐Organic Frameworks. *Chem. Eur. J.* **2012,** *18* (52), 16642-16648.

159. Li, X.-C.; Wang, C.-Y.; Lai, W.-Y.; Huang, W., Triazatruxene-based materials for organic electronics and optoelectronics. *J. Mater. Chem. C* **2016,** *4* (45), 10574-10587.

160. Lu, Z.; Li, C.; Fang, T.; Li, G.; Bo, Z., Triindole-cored star-shaped molecules for organic solar cells. *J. Mater. Chem. A* **2013,** *1* (26), 7657-7665.

161. Lai, W.-Y.; Zhu, R.; Fan, Q.-L.; Hou, L.-T.; Cao, Y.; Huang, W., Monodisperse Six-Armed Triazatruxenes: Microwave-Enhanced Synthesis and Highly Efficient Pure-Deep-Blue Electroluminescence. *Macromolecules* **2006,** *39* (11), 3707-3709.

162. Lai, W. Y.; He, Q. Y.; Zhu, R.; Chen, Q. Q.; Huang, W., Kinked Star‐Shaped Fluorene/ Triazatruxene Co‐oligomer Hybrids with Enhanced Functional Properties for High‐Performance, Solution‐Processed, Blue Organic Light‐Emitting Diodes. *Adv. Funct. Mater.* **2008,** *18* (2), 265-276.

163. Xie, Y.-F.; Ding, S.-Y.; Liu, J.-M.; Wang, W.; Zheng, Q.-Y., Triazatruxene based covalent organic framework and its quick-response fluorescence-on nature towards electron rich arenes. *J. Mater. Chem. C* **2015,** *3* (39), 10066-10069.

164. Zhang, P.; Wang, X.; Xuan, W.; Peng, P.; Li, Z.; Lu, R.; Wu, S.; Tian, Z.; Cao, X., Chiral separation and characterization of triazatruxene-based face-rotating polyhedra: the role of non-covalent facial interactions. *Chem. Commun.* **2018**.

165. Wang, X.; Lu, W.; Gu, Z.-Y.; Wei, Z.; Zhou, H.-C., Topology-guided design of an anionic bor-network for photocatalytic [Ru(bpy)3]2+ encapsulation. *Chem. Commun.* **2016,** *52* (9), 1926-1929.

166. Tu, B.; Pang, Q.; Xu, H.; Li, X.; Wang, Y.; Ma, Z.; Weng, L.; Li, Q., Reversible Redox Activity in Multicomponent Metal–Organic Frameworks Constructed from Trinuclear Copper Pyrazolate Building Blocks. *J. Am. Chem. Soc.* **2017,** *139* (23), 7998-8007.

167. Valentine, R. A.; Whyte, A.; Awaga, K.; Robertson, N., New indole trimers as precursors for molecular electronic materials. *Tetrahedron Lett.* **2012,** *53* (6), 657-660.

168. Willems, T. F.; Rycroft, C. H.; Kazi, M.; Meza, J. C.; Haranczyk, M., Algorithms and tools for high-throughput geometry-based analysis of crystalline porous materials. *Microporous Mesoporous Mater.* **2012,** *149* (1), 134-141.

169. Rouquerol, J.; Avnir, D.; Fairbridge, C. W.; Everett, D. H.; Haynes, J. M.; Pernicone, N.; Ramsay, J. D. F.; Sing, K. S. W.; Unger, K. K., Recommendations for the characterization of porous solids (Technical Report). In *Pure Appl. Chem.*, 1994; Vol. 66, p 1739.

170. Li, J.-R.; Kuppler, R. J.; Zhou, H.-C., Selective gas adsorption and separation in metal–organic frameworks. *Chem. Soc. Rev.* **2009,** *38* (5), 1477-1504.

171. Geier, S. J.; Mason, J. A.; Bloch, E. D.; Queen, W. L.; Hudson, M. R.; Brown, C. M.; Long, J. R., Selective adsorption of ethylene over ethane and propylene over propane in the metal–organic frameworks M_2(dobdc) (M = Mg, Mn, Fe, Co, Ni, Zn). *Chem. Sci.* **2013,** *4* (5), 2054-2061.

172. Wang, D.; Liu, B.; Yao, S.; Wang, T.; Li, G.; Huo, Q.; Liu, Y., A polyhedral metal–organic framework based on the supermolecular building block strategy exhibiting high

performance for carbon dioxide capture and separation of light hydrocarbons. *Chem. Commun.* **2015,** *51* (83), 15287-15289.

173. Deshpande, R. K.; Minnaar, J. L.; Telfer, S. G., Thermolabile Groups in Metal–Organic Frameworks: Suppression of Network Interpenetration, Post-Synthetic Cavity Expansion, and Protection of Reactive Functional Groups. *Angew. Chem. Int. Ed.* **2010,** *49* (27), 4598-4602.

174. Gupta, A. S.; Deshpande, R. K.; Liu, L.; Waterhouse, G. I. N.; Telfer, S. G., Porosity in metal–organic frameworks following thermolytic postsynthetic deprotection: gas sorption, dye uptake and covalent derivatisation. *CrystEngComm* **2012,** *14* (18), 5701-5704.

175. Bryant, M. R.; Ablott, T. A.; Telfer, S. G.; Liu, L.; Richardson, C., High temperature expulsion of thermolabile groups for pore-space expansion in metal–organic frameworks. *CrystEngComm* **2019,** *21* (1), 60-64.

176. Liu, X.; Xu, Y.; Jiang, D., Conjugated Microporous Polymers as Molecular Sensing Devices: Microporous Architecture Enables Rapid Response and Enhances Sensitivity in Fluorescence-On and Fluorescence-Off Sensing. *J. Am. Chem. Soc.* **2012,** *134* (21), 8738-8741.

177. Xu, Y.; Wu, X.; Chen, Y.; Hang, H.; Tong, H.; Wang, L., Star-shaped triazatruxene derivatives for rapid fluorescence fiber-optic detection of nitroaromatic explosive vapors. *RSC Adv.* **2016,** *6* (38), 31915-31918.

178. Lustig, W. P.; Mukherjee, S.; Rudd, N. D.; Desai, A. V.; Li, J.; Ghosh, S. K., Metal–organic frameworks: functional luminescent and photonic materials for sensing applications. *Chem. Soc. Rev.* **2017,** *46* (11), 3242-3285.

179. Steiner, T., Donor and acceptor strengths in C–H···O hydrogen bonds quantified from crystallographic data of small solvent molecules. *New J. Chem.* **1998,** *22* (10), 1099-1103.

180. Graton, J.; Le Questel, J.-Y.; Maxwell, P.; Popelier, P., Hydrogen-Bond Accepting Properties of New Heteroaromatic Ring Chemical Motifs: A Theoretical Study. *J. Chem. Inf. Model.* **2016,** *56* (2), 322-334.

181. Cornelio, J.; Zhou, T.-Y.; Alkaş, A.; Telfer, S. G., Systematic Tuning of the Luminescence Output of Multicomponent Metal–Organic Frameworks. *J. Am. Chem. Soc.* **2018,** *140* (45), 15470-15476.

182. *FS Process*, Rigaku Corporation, Tokyo, Japan: 1996.

183. Dolomanov, O. V.; Bourhis, L. J.; Gildea, R. J.; Howard, J. A. K.; Puschmann, H., OLEX2: a complete structure solution, refinement and analysis program. *J. Appl. Crystallogr.* **2009,** *42* (2), 339-341.

184. Sheldrick, G., SHELXT - Integrated space-group and crystal-structure determination. *Acta Crystallogr. A* **2015,** *71* (1), 3-8.

185. Sheldrick, G., Crystal structure refinement with SHELXL. *Acta Crystallogr. C* **2015,** *71* (1), 3-8.

186. Walton, K. S.; Snurr, R. Q., Applicability of the BET Method for Determining Surface Areas of Microporous Metal−Organic Frameworks. *J. Am. Chem. Soc.* **2007,** *129* (27), 8552-8556.

187. Fujita, M.; Kwon, Y. J.; Washizu, S.; Ogura, K., Preparation, Clathration Ability, and Catalysis of a Two-Dimensional Square Network Material Composed of Cadmium(II) and 4,4'-Bipyridine. *J. Am. Chem. Soc.* **1994,** *116* (3), 1151-1152.

188. Corma, A.; García, H.; Llabrés i Xamena, F. X., Engineering Metal Organic Frameworks for Heterogeneous Catalysis. *Chem. Rev.* **2010,** *110* (8), 4606-4655.

189. Liu, J.; Chen, L.; Cui, H.; Zhang, J.; Zhang, L.; Su, C.-Y., Applications of metal–organic frameworks in heterogeneous supramolecular catalysis. *Chem. Soc. Rev.* **2014,** *43* (16), 6011-6061.

190. Farrusseng, D.; Aguado, S.; Pinel, C., Metal–Organic Frameworks: Opportunities for Catalysis. *Angew. Chem. Int. Ed.* **2009,** *48* (41), 7502-7513.

191. Jiao, L.; Wang, Y.; Jiang, H.-L.; Xu, Q., Metal–Organic Frameworks as Platforms for Catalytic Applications. *Adv. Mater.* **2018,** *30* (37), 1703663.

192. Alkaş, A.; Cornelio, J.; Telfer, S. G., Tritopic Triazatruxene Ligands for Multicomponent Metal-Organic Frameworks. *Chem. Asian J.* **2019,** *14* (8), 1167-1174.

193. Dydio, P.; Reek, J. N. H., Supramolecular control of selectivity in transition-metal catalysis through substrate preorganization. *Chem. Sci.* **2014,** *5* (6), 2135-2145.

194. Raynal, M.; Ballester, P.; Vidal-Ferran, A.; van Leeuwen, P. W. N. M., Supramolecular catalysis. Part 2: artificial enzyme mimics. *Chem. Soc. Rev.* **2014,** *43* (5), 1734-1787.

195. Gruttadauria, M.; Giacalone, F.; Noto, R., Supported proline and proline-derivatives as recyclable organocatalysts. *Chem. Soc. Rev.* **2008,** *37* (8), 1666-1688.

196. MacMillan, D. W. C., The advent and development of organocatalysis. *Nature* **2008,** *455*, 304.

197. Mohr, J. T.; Krout, M. R.; Stoltz, B. M., Natural products as inspiration for the development of asymmetric catalysis. *Nature* **2008,** *455*, 323.

198. Que Jr, L.; Tolman, W. B., Biologically inspired oxidation catalysis. *Nature* **2008,** *455*, 333.

199. Bartlett, G. J.; Porter, C. T.; Borkakoti, N.; Thornton, J. M., Analysis of Catalytic Residues in Enzyme Active Sites. *J. Mol. Biol.* **2002,** *324* (1), 105-121.

200. Rogge, S. M. J.; Bavykina, A.; Hajek, J.; Garcia, H.; Olivos-Suarez, A. I.; Sepúlveda-Escribano, A.; Vimont, A.; Clet, G.; Bazin, P.; Kapteijn, F.; Daturi, M.; Ramos-Fernandez, E. V.; Llabrés i Xamena, F. X.; Van Speybroeck, V.; Gascon, J., Metal–organic and covalent organic frameworks as single-site catalysts. *Chem. Soc. Rev.* **2017,** *46* (11), 3134-3184.

201. Cohen, S. M.; Zhang, Z.; Boissonnault, J. A., Toward "metalloMOFzymes": Metal–Organic Frameworks with Single-Site Metal Catalysts for Small-Molecule Transformations. *Inorg. Chem.* **2016,** *55* (15), 7281-7290.

202. Zhou, T.-Y.; Auer, B.; Lee, S. J.; Telfer, S. G., Catalysts Confined in Programmed Framework Pores Enable New Transformations and Tune Reaction Efficiency and Selectivity. *J. Am. Chem. Soc.* **2019,** *141* (4), 1577-1582.

203. Notz, W.; Tanaka, F.; Barbas, C. F., Enamine-Based Organocatalysis with Proline and Diamines: The Development of Direct Catalytic Asymmetric Aldol, Mannich, Michael, and Diels−Alder Reactions. *Acc. Chem. Res.* **2004,** *37* (8), 580-591.

204. List, B.; Lerner, R. A.; Barbas, C. F., Proline-Catalyzed Direct Asymmetric Aldol Reactions. *J. Am. Chem. Soc.* **2000,** *122* (10), 2395-2396.

205. Yang, J. W.; Chandler, C.; Stadler, M.; Kampen, D.; List, B., Proline-catalysed Mannich reactions of acetaldehyde. *Nature* **2008,** *452*, 453.

206. Banerjee, M.; Das, S.; Yoon, M.; Choi, H. J.; Hyun, M. H.; Park, S. M.; Seo, G.; Kim, K., Postsynthetic Modification Switches an Achiral Framework to Catalytically Active Homochiral Metal−Organic Porous Materials. *J. Am. Chem. Soc.* **2009,** *131* (22), 7524-7525.

207. Zhu, W.; He, C.; Wu, X.; Duan, C., "Click" post-synthetic modification of metal−organic frameworks for asymmetric aldol catalysis. *Inorg. Chem. Commun.* **2014,** *39*, 83-85.

208. Lili, L.; Xin, Z.; Shumin, R.; Ying, Y.; Xiaoping, D.; Jinsen, G.; Chunming, X.; Jing, H., Catalysis by metal–organic frameworks: proline and gold functionalized MOFs for the aldol and three-component coupling reactions. *RSC Adv.* **2014,** *4* (25), 13093-13107.

209. Olkhovik, V. K.; Vasilevskii, D. A.; Pap, A. A.; Kalechyts, G. V.; Matveienko, Y. V.; Baran, A. G.; Halinouski, N. A.; Petushok, V. G., Synthesis of new polyconjugated molecules with biphenyl, dibenzothiophene, carbazole and phenanthrene units. *ARKIVOC* **2008,** *(ix)* 69-93.

210. Stolle, A.; Ondruschka, B.; Hopf, H., Thermal Rearrangements of Monoterpenes and Monoterpenoids. *Helv. Chim. Acta* **2009,** *92* (9), 1673-1719.

211. Yuan, S.; Chen, Y.-P.; Qin, J.-S.; Lu, W.; Zou, L.; Zhang, Q.; Wang, X.; Sun, X.; Zhou, H.-C., Linker Installation: Engineering Pore Environment with Precisely Placed Functionalities in Zirconium MOFs. *J. Am. Chem. Soc.* **2016,** *138* (28), 8912-8919.

212. Fracaroli, A. M.; Siman, P.; Nagib, D. A.; Suzuki, M.; Furukawa, H.; Toste, F. D.; Yaghi, O. M., Seven Post-synthetic Covalent Reactions in Tandem Leading to Enzyme-like Complexity within Metal–Organic Framework Crystals. *J. Am. Chem. Soc.* **2016,** *138* (27), 8352-8355.

213. Bartók, M., Unexpected Inversions in Asymmetric Reactions: Reactions with Chiral Metal Complexes, Chiral Organocatalysts, and Heterogeneous Chiral Catalysts. *Chem. Rev.* **2010,** *110* (3), 1663-1705.

214. Zheng, M.; Liu, Y.; Wang, C.; Liu, S.; Lin, W., Cavity-induced enantioselectivity reversal in a chiral metal–organic framework Brønsted acid catalyst. *Chem. Sci.* **2012,** *3* (8), 2623-2627.

215. Nießing, S.; Czekelius, C.; Janiak, C., Immobilisation of catalytically active proline on H2N-MIL-101(Al) accompanied with reversal in enantioselectivity. *Catal. Commun.* **2017,** *95*, 12-15.

216. Barrero, A. F.; Herrador, M. M.; Quílez del Moral, J. F.; Arteaga, P.; Arteaga, J. F.; Diéguez, H. R.; Sánchez, E. M., Mild TiIII- and Mn/ZrIV-Catalytic Reductive Coupling of Allylic Halides: Efficient Synthesis of Symmetric Terpenes. *J. Org. Chem.* **2007,** *72* (8), 2988-2995.

217. Dang, D.; Wu, P.; He, C.; Xie, Z.; Duan, C., Homochiral Metal−Organic Frameworks for Heterogeneous Asymmetric Catalysis. *J. Am. Chem. Soc.* **2010,** *132* (41), 14321-14323.

218. Nguyen, K. D.; Kutzscher, C.; Drache, F.; Senkovska, I.; Kaskel, S., Chiral Functionalization of a Zirconium Metal–Organic Framework (DUT-67) as a Heterogeneous Catalyst in Asymmetric Michael Addition Reaction. *Inorg. Chem.* **2018,** *57* (3), 1483-1489.

219. Kutzscher, C.; Nickerl, G.; Senkovska, I.; Bon, V.; Kaskel, S., Proline Functionalized UiO-67 and UiO-68 Type Metal–Organic Frameworks Showing Reversed Diastereoselectivity in Aldol Addition Reactions. *Chem. Mater.* **2016,** *28* (8), 2573-2580.

220. Canivet, J.; Farrusseng, D., Proline-functionalized metal–organic frameworks and their use in asymmetric catalysis: pitfalls in the MOFs rush. *RSC Adv.* **2015,** *5* (15), 11254-11256.

221. Dalessandro, E. V.; Collin, H. P.; Guimarães, L. G. L.; Valle, M. S.; Pliego, J. R., Mechanism of the Piperidine-Catalyzed Knoevenagel Condensation Reaction in Methanol: The Role of Iminium and Enolate Ions. *J. Phys. Chem. B* **2017,** *121* (20), 5300-5307.

222. Huang, J.; Wu, M.; Hu, L.; Guo, H.; Sun, S., Piperidine-Catalyzed 1,3-Dipolar Cycloaddition of Diazoesters to Enones. *Asian J. Org. Chem.* **2016,** *5* (4), 462-465.

223. Wang, Y.-G.; Cui, S.-L.; Lin, X.-F., A Highly Selective Cascade Approach to Diverse Aromatic Ring Systems from Simple Aromatic Aldehydes and Propiolates. *Org. Lett.* **2006,** *8* (6), 1241-1244.

224. Shu, S.; Liu, Z.; Li, Y.; Ke, Z.; Liu, Y., Diastereoselectivity in a cyclic secondary amine catalyzed asymmetric Mannich reaction: a model rationalization from DFT studies. *Org Chem Front.* **2018,** *5* (14), 2148-2157.

225. Ramesh, R.; Madhesh, R.; Malecki, J. G.; Lalitha, A., Piperidine Catalyzed Four–component Strategy for the Facile Access of Polyfunctionalized 1,4-Dihydropyridines at Ambient Conditions. *ChemistrySelect* **2016,** *1* (16), 5196-5200.

226. Yavari, I.; Ghazanfarpour-Darjani, M.; Solgi, Y.; Ahmadian, S., Triethylamine-Catalyzed Efficient Synthesis of Oxathiolanes Containing a Highly Polarized Carbon-Carbon Double Bond from Reaction of Malononitrile, Carbon Disulfide (CS2), and Oxiranes. *Helv. Chim. Acta* **2011,** *94* (4), 639-642.

227. Mukherjee, S.; Yang, J. W.; Hoffmann, S.; List, B., Asymmetric Enamine Catalysis. *Chem. Rev.* **2007,** *107* (12), 5471-5569.

228. Enders, D.; Wang, C.; Liebich, J. X., Organocatalytic Asymmetric Aza-Michael Additions. *Chem. Eur. J.* **2009,** *15* (42), 11058-11076.

229. Lancianesi, S.; Palmieri, A.; Petrini, M., Synthetic Approaches to 3-(2-Nitroalkyl) Indoles and Their Use to Access Tryptamines and Related Bioactive Compounds. *Chem. Rev.* **2014,** *114* (14), 7108-7149.

230. Tanaka, K.; Sakuragi, K.; Ozaki, H.; Takada, Y., Highly enantioselective Friedel-Crafts alkylation of N,N-dialkylanilines with trans-β-nitrostyrene catalyzed by a homochiral metal-organic framework. *Chem. Commun.* **2018,** *54* (49), 6328-6331.

231. Sonawane, R. B.; Rasal, N. K.; Jagtap, S. V., Nickel-(II)-Catalyzed N-Formylation and N-Acylation of Amines. *Org. Lett.* **2017,** *19* (8), 2078-2081.

232. Ishii, T.; Fujioka, S.; Sekiguchi, Y.; Kotsuki, H., A New Class of Chiral Pyrrolidine−Pyridine Conjugate Base Catalysts for Use in Asymmetric Michael Addition Reactions. *J. Am. Chem. Soc.* **2004,** *126* (31), 9558-9559.

233. Zhang, J.; Yao, S.; Liu, S.; Liu, B.; Sun, X.; Zheng, B.; Li, G.; Li, Y.; Huo, Q.; Liu, Y., Enhancement of Gas Sorption and Separation Performance via Ligand Functionalization within Highly Stable Zirconium-Based Metal–Organic Frameworks. *Cryst. Growth Des.* **2017,** *17* (4), 2131-2139.

234. Wu, Y.; Chen, H.; Liu, D.; Xiao, J.; Qian, Y.; Xi, H., Effective Ligand Functionalization of Zirconium-Based Metal–Organic Frameworks for the Adsorption and Separation of Benzene and Toluene: A Multiscale Computational Study. *ACS Appl. Mater. Interfaces* **2015,** *7* (10), 5775-5787.

235. Herbst, A.; Khutia, A.; Janiak, C., Brønsted Instead of Lewis Acidity in Functionalized MIL-101Cr MOFs for Efficient Heterogeneous (nano-MOF) Catalysis in the Condensation Reaction of Aldehydes with Alcohols. *Inorg. Chem.* **2014,** *53* (14), 7319-7333.

236. Marshall, R. J.; Kalinovskyy, Y.; Griffin, S. L.; Wilson, C.; Blight, B. A.; Forgan, R. S., Functional Versatility of a Series of Zr Metal–Organic Frameworks Probed by Solid-State Photoluminescence Spectroscopy. *J. Am. Chem. Soc.* **2017,** *139* (17), 6253-6260.

237. Chae, H. K.; Siberio-Pérez, D. Y.; Kim, J.; Go, Y.; Eddaoudi, M.; Matzger, A. J.; O'Keeffe, M.; Yaghi, O. M., A route to high surface area, porosity and inclusion of large molecules in crystals. *Nature* **2004,** *427*, 523.

238. Prior, T. J.; Rosseinsky, M. J., Chiral Direction and Interconnection of Helical Three-Connected Networks in Metal-Organic Frameworks. *Inorg. Chem.* **2003,** *42* (5), 1564-1575.

239. Kepert, C. J.; Prior, T. J.; Rosseinsky, M. J., A Versatile Family of Interconvertible Microporous Chiral Molecular Frameworks: The First Example of Ligand Control of Network Chirality. *J. Am. Chem. Soc.* **2000,** *122* (21), 5158-5168.

240. Peng, Y.; Gong, T.; Zhang, K.; Lin, X.; Liu, Y.; Jiang, J.; Cui, Y., Engineering chiral porous metal-organic frameworks for enantioselective adsorption and separation. *Nat. Commun.* **2014,** *5*, 4406.

241. Navarro-Sánchez, J.; Argente-García, A. I.; Moliner-Martínez, Y.; Roca-Sanjuán, D.; Antypov, D.; Campíns-Falcó, P.; Rosseinsky, M. J.; Martí-Gastaldo, C., Peptide Metal–Organic Frameworks for Enantioselective Separation of Chiral Drugs. *J. Am. Chem. Soc.* **2017,** *139* (12), 4294-4297.

242. Zhu, C.; Xia, Q.; Chen, X.; Liu, Y.; Du, X.; Cui, Y., Chiral Metal–Organic Framework as a Platform for Cooperative Catalysis in Asymmetric Cyanosilylation of Aldehydes. *ACS Catal.* **2016,** *6* (11), 7590-7596.

243. Song, F.; Wang, C.; Falkowski, J. M.; Ma, L.; Lin, W., Isoreticular Chiral Metal−Organic Frameworks for Asymmetric Alkene Epoxidation: Tuning Catalytic Activity by Controlling Framework Catenation and Varying Open Channel Sizes. *J. Am. Chem. Soc.* **2010,** *132* (43), 15390-15398.

244. Huang, X.; Li, Q.; Xiao, X.; Jia, S.; Li, Y.; Duan, Z.; Bai, L.; Yuan, Z.; Li, L.; Lin, Z.; Zhao, Y., Nonlinear-Optical Behaviors of a Chiral Metal–Organic Framework Comprised of an Unusual Multioriented Double-Helix Structure. *Inorg. Chem.* **2018,** *57* (11), 6210-6213.

245. Zhao, D.; Timmons, D. J.; Yuan, D.; Zhou, H.-C., Tuning the Topology and Functionality of Metal−Organic Frameworks by Ligand Design. *Acc. Chem. Res.* **2011,** *44* (2), 123-133.

246. Techajaroonjit, T.; Namuangruk, S.; Prachumrak, N.; Promarak, V.; Sukwattanasinitt, M.; Rashatasakhon, P., Synthesis, characterization, and hole-transporting properties of pyrenyl N-substituted triazatruxenes. *RSC Adv.* **2016,** *6* (61), 56392-56398.

247. García-Frutos, E. M.; Gómez-Lor, B.; Monge, Á.; Gutiérrez-Puebla, E.; Alkorta, I.; Elguero, J., Synthesis and Preferred All-syn Conformation of C3-Symmetrical N-(Hetero)arylmethyl Triindoles. *Chem. Eur. J.* **2008,** *14* (28), 8555-8561.

248. Lee, J. Y.; Pan, L.; Kelly, S. P.; Jagiello, J.; Emge, T. J.; Li, J., Achieving High Density of Adsorbed Hydrogen in Microporous Metal Organic Frameworks. *Adv. Mater.* **2005,** *17* (22), 2703-2706.

249. Ke, Y.; Collins, D. J.; Sun, D.; Zhou, H.-C., (10,3)-a Noninterpenetrated Network Built from a Piedfort Ligand Pair. *Inorg. Chem.* **2006,** *45* (5), 1897-1899.

250. Gao, F.-X.; Ye, Y.-J.; Zhao, L.-T.; Liu, D.-H.; Li, Y., A porous Zn-based metal-organic framework with an expanded tricarboxylic acid ligand for effective CO_2 capture and CO_2/CH_4 separation. *Inorg. Chem. Commun.* **2018,** *94*, 39-42.

251. Lin, X.-M.; Li, T.-T.; Wang, Y.-W.; Zhang, L.; Su, C.-Y., Two ZnII Metal-Organic Frameworks with Coordinatively Unsaturated Metal Sites: Structures, Adsorption, and Catalysis. *Chem. Asian J.* **2012,** *7* (12), 2796-2804.

252. Janiak, C., A critical account on π–π stacking in metal complexes with aromatic nitrogen-containing ligands. *J. Chem. Soc., Dalton Trans.* **2000,** (21), 3885-3896.

253. Zhang, S.-Y.; Li, D.; Guo, D.; Zhang, H.; Shi, W.; Cheng, P.; Wojtas, L.; Zaworotko, M. J., Synthesis of a Chiral Crystal Form of MOF-5, CMOF-5, by Chiral Induction. *J. Am. Chem. Soc.* **2015,** *137* (49), 15406-15409.

254. Parshamoni, S.; Sanda, S.; Jena, H. S.; Konar, S., A copper based pillared-bilayer metal organic framework: its synthesis, sorption properties and catalytic performance. *Dalton Trans.* **2014,** *43* (19), 7191-7199.

255. Parshamoni, S.; Sanda, S.; Jena, H. S.; Konar, S., Tuning CO_2 Uptake and Reversible Iodine Adsorption in Two Isoreticular MOFs through Ligand Functionalization. *Chem. Asian J.* **2015,** *10* (3), 653-660.

256. Maji, T. K.; Matsuda, R.; Kitagawa, S., A flexible interpenetrating coordination framework with a bimodal porous functionality. *Nat. Mater.* **2007,** *6*, 142.

257. Silvestre-Albero, A. M.; Juárez-Galán, J. M.; Silvestre-Albero, J.; Rodríguez-Reinoso, F., Low-Pressure Hysteresis in Adsorption: An Artifact? *J. Phys. Chem. C* **2012,** *116* (31), 16652-16655.

258. Cohen, S. M., Postsynthetic Methods for the Functionalization of Metal–Organic Frameworks. *Chem. Rev.* **2012,** *112* (2), 970-1000.

259. Zhu, W.; He, C.; Wu, P.; Wu, X.; Duan, C., "Click" post-synthetic modification of metal–organic frameworks with chiral functional adduct for heterogeneous asymmetric catalysis. *Dalton Trans.* **2012,** *41* (10), 3072-3077.

260. Kutzscher, C.; Hoffmann, H. C.; Krause, S.; Stoeck, U.; Senkovska, I.; Brunner, E.; Kaskel, S., Proline Functionalization of the Mesoporous Metal−Organic Framework DUT-32. *Inorg. Chem.* **2015,** *54* (3), 1003-1009.

261. Fracaroli, A. M.; Furukawa, H.; Suzuki, M.; Dodd, M.; Okajima, S.; Gándara, F.; Reimer, J. A.; Yaghi, O. M., Metal–Organic Frameworks with Precisely Designed Interior for Carbon Dioxide Capture in the Presence of Water. *J. Am. Chem. Soc.* **2014,** *136* (25), 8863-8866.

262. Reimer, N.; Gil, B.; Marszalek, B.; Stock, N., Thermal post-synthetic modification of Al-MIL-53–COOH: systematic investigation of the decarboxylation and condensation reaction. *CrystEngComm* **2012,** *14* (12), 4119-4125.

263. Ganguly, S.; Pachfule, P.; Bala, S.; Goswami, A.; Bhattacharya, S.; Mondal, R., Azide-Functionalized Lanthanide-Based Metal–Organic Frameworks Showing Selective CO2 Gas Adsorption and Postsynthetic Cavity Expansion. *Inorg. Chem.* **2013,** *52* (7), 3588-3590.

264. Vitillo, J. G.; Lescouet, T.; Savonnet, M.; Farrusseng, D.; Bordiga, S., Soft synthesis of isocyanate-functionalised metal–organic frameworks. *Dalton Trans.* **2012,** *41* (47), 14236-14238.

265. Distefano, G.; Suzuki, H.; Tsujimoto, M.; Isoda, S.; Bracco, S.; Comotti, A.; Sozzani, P.; Uemura, T.; Kitagawa, S., Highly ordered alignment of a vinyl polymer by host–guest cross-polymerization. *Nature Chem.* **2013,** *5*, 335.

266. Satheeshkumar, C.; Yu, H. J.; Park, H.; Kim, M.; Lee, J. S.; Seo, M., Thiol–ene photopolymerization of vinyl-functionalized metal–organic frameworks towards mixed-matrix membranes. *J. Mater. Chem. A* **2018,** *6* (44), 21961-21968.

267. Li, F.; Zhuang, J.; Jiang, G.; Tang, H.; Xia, A.; Jiang, L.; Song, Y.; Li, Y.; Zhu, D., A Rewritable Optical Data Storage Material System by [2 + 2] Photocycloreversion−Photocycloaddition. *Chem. Mater.* **2008,** *20* (4), 1194-1196.

268. Novak, K.; Enkelmann, V.; Wegner, G.; Wagener, K. B., Crystallographic Study of a Single Crystal to Single Crystal Photodimerization and Its Thermal Reverse Reaction. *Angew. Chem. Int. Ed. Engl.* **1993,** *32* (11), 1614-1616.

269. Sonoda, Y., Solid-State [2+2] Photodimerization and Photopolymerization of α,ω-Diarylpolyene Monomers: Effective Utilization of Noncovalent Intermolecular Interactions in Crystals. *Molecules* **2011,** *16* (1), 119.

270. Papagni, A.; Buttero, P. D.; Bertarelli, C.; Miozzo, L.; Moret, M.; Pryce, M. T.; Rizzato, S., Novel fluorinated amino-stilbenes and their solid-state photodimerization. *New J. Chem.* **2010,** *34* (11), 2612-2621.

271. Poplata, S.; Tröster, A.; Zou, Y.-Q.; Bach, T., Recent Advances in the Synthesis of Cyclobutanes by Olefin [2 + 2] Photocycloaddition Reactions. *Chem. Rev.* **2016,** *116* (17), 9748-9815.

272. Medishetty, R.; Park, I.-H.; Lee, S. S.; Vittal, J. J., Solid-state polymerisation via [2+2] cycloaddition reaction involving coordination polymers. *Chem. Commun.* **2016,** *52* (21), 3989-4001.

273. Sinnwell, M. A.; Baltrusaitis, J.; MacGillivray, L. R., Combination of Argentophilic and Perfluorophenyl-Perfluorophenyl Interactions Supports a Head-to-Head [2 + 2] Photodimerization in the Solid State. *Cryst. Growth Des.* **2015,** *15* (2), 538-541.

274. Claassens, I. E.; Nikolayenko, V. I.; Haynes, D. A.; Barbour, L. J., Solvent-Mediated Synthesis of Cyclobutane Isomers in a Photoactive Cadmium(II) Porous Coordination Polymer. *Angew. Chem. Int. Ed.* **2018,** *57* (47), 15563-15566.

275. Zhang, Y.-J.; Chen, C.; Cai, L.-X.; Tan, B.; Yang, X.-D.; Zhang, J.; Ji, M., Post-cycloaddition modification of a porous MOF for improved GC separation of ethanol and water. *Dalton Trans.* **2017,** *46* (21), 7092-7097.

276. Papaefstathiou, G. S.; MacGillivray, L. R., An Inverted Metal-Organic Framework with Compartmentalized Cavities Constructed by Using an Organic Bridging Unit Derived from the Solid State. *Angew. Chem. Int. Ed.* **2002,** *41* (12), 2070-2073.

277. Medishetty, R.; Tandiana, R.; Koh, L. L.; Vittal, J. J., Assembly of 3D Coordination Polymers from 2D Sheets by [2+2] Cycloaddition Reaction. *Chem. Eur. J.* **2014,** *20* (5), 1231-1236.

278. Kole, G. K.; Koh, L. L.; Lee, S. Y.; Lee, S. S.; Vittal, J. J., A new ligand for metal–organic framework and co-crystal synthesis: mechanochemical route to rctt-1,2,3,4-tetrakis-(4′-carboxyphenyl)-cyclobutane. *Chem. Commun.* **2010,** *46* (21), 3660-3662.

279. Peedikakkal, A. M. P.; Peh, C. S. Y.; Koh, L. L.; Vittal, J. J., Metal−Organic Frameworks Containing a Tetrapyridylcyclobutane Ligand Derived from Isomerization Reaction. *Inorg. Chem.* **2010,** *49* (15), 6775-6777.

280. Papaefstathiou, G. S.; Milios, C.; MacGillivray, L. R., A 2D metal-organic framework with two different rhombus-shaped cavities: a rare example of a (4,4)-net with alternating metal and organic nodes. *Microporous Mesoporous Mater.* **2004,** *71* (1), 11-15.

281. Hamilton, T. D.; Bučar, D.-K.; Atkinson, M. B. J.; Papaefstathiou, G. S.; MacGillivray, L. R., 1D and 2D metal–organic frameworks functionalized with free pyridyl groups. *J. Mol. Struct.* **2006,** *796* (1), 58-62.

282. Xie, M.-H.; Yang, X.-L.; Wu, C.-D., From 2D to 3D: A Single-Crystal-to-Single-Crystal Photochemical Framework Transformation and Phenylmethanol Oxidation Catalytic Activity. *Chem. Eur. J.* **2011,** *17* (41), 11424-11427.

283. Chanthapally, A.; Kole, G. K.; Qian, K.; Tan, G. K.; Gao, S.; Vittal, J. J., Thermal Cleavage of Cyclobutane Rings in Photodimerized Coordination-Polymeric Sheets. *Chem. Eur. J.* **2012,** *18* (25), 7869-7877.

284. Park, I.-H.; Medishetty, R.; Lee, H.-H.; Mulijanto, C. E.; Quah, H. S.; Lee, S. S.; Vittal, J. J., Formation of a Syndiotactic Organic Polymer Inside a MOF by a [2+2] Photo-Polymerization Reaction. *Angew. Chem. Int. Ed.* **2015,** *54* (25), 7313-7317.

285. Chen, L.; Li, H.-X.; Dai, M.; Li, H.-Y.; Lang, J.-P., Capturing the Organic Species Derived from the C–C Cleavage and in Situ Oxidation of 1,2,3,4-Tetra(pyridin-4-yl)cyclobutane by [CuCN]n-Based MOFs. *Inorg. Chem.* **2018,** *57* (15), 9160-9166.

286. Hiroyasu, S.; Gaku, Y.; Yasuhiro, M., Synthesis and Properties of Trispiro[truxenetris(cycloalkane)]s. *Bull. Chem. Soc. Jpn.* **2006,** *79* (6), 938-943.

287. Guadalupe, J.; Ray, A. M.; Maya, E. M.; Gómez-Lor, B.; Iglesias, M., Truxene-based porous polymers: from synthesis to catalytic activity. *Polym. Chem.* **2018,** *9* (36), 4585-4595.

288. Pedersen, S.; Herek, J. L.; Zewail, A. H., The Validity of the "Diradical" Hypothesis: Direct Femtoscond Studies of the Transition-State Structures. *Science* **1994,** *266* (5189), 1359-1364.

289. Liese, J.; Hampp, N., Thermal [2 + 2] Cycloreversion of a Cyclobutane Moiety via a Biradical Reaction. *J. Phys. Chem. A* **2011,** *115* (14), 2927-2932.

290. Sbrogiò, F.; Fabris, F.; De Lucchi, O.; Lucchini, V., 5,10,15-Trimethylenetribenzo[a,f,k]trindene (Truxenene). *Synlett* **1994,** *1994* (09), 761-762.

291. Nakano, T.; Yade, T., Synthesis, Structure, and Photophysical and Electrochemical Properties of a π-Stacked Polymer. *J. Am. Chem. Soc.* **2003,** *125* (50), 15474-15484.

292. Nakano, T.; Takewaki, K.; Yade, T.; Okamoto, Y., Dibenzofulvene, a 1,1-Diphenylethylene Analogue, Gives a π-Stacked Polymer by Anionic, Free-Radical, and Cationic Catalysts. *J. Am. Chem. Soc.* **2001,** *123* (37), 9182-9183.

293. Nageh, H.; Wang, Y.; Nakano, T., Cationic polymerization of dibenzofulvene leading to a π-stacked polymer. *Polymer* **2018,** *144*, 51-56.

294. Nakano, T.; Yade, T.; Fukuda, Y.; Yamaguchi, T.; Okumura, S., Free-Radical Polymerization of Dibenzofulvene Leading to a π-Stacked Polymer: Structure and Properties of the Polymer and Proposed Reaction Mechanism. *Macromolecules* **2005,** *38* (20), 8140-8148.

295. Sheldrick, G., A short history of SHELX. *Acta Crystallogr. A* **2008,** *64* (1), 112-122.

296. Férey, G.; Serre, C.; Mellot-Draznieks, C.; Millange, F.; Surblé, S.; Dutour, J.; Margiolaki, I., A Hybrid Solid with Giant Pores Prepared by a Combination of Targeted Chemistry, Simulation, and Powder Diffraction. *Angew. Chem. Int. Ed.* **2004,** *43* (46), 6296-6301.

297. Yang, J.; Du, B.; Liu, J.; Krishna, R.; Zhang, F.; Zhou, W.; Wang, Y.; Li, J.; Chen, B., MIL-100Cr with open Cr sites for a record N2O capture. *Chem. Commun.* **2018,** *54* (100), 14061-14064.

298. Wang, B.; Lv, X.-L.; Feng, D.; Xie, L.-H.; Zhang, J.; Li, M.; Xie, Y.; Li, J.-R.; Zhou, H.-C., Highly Stable Zr(IV)-Based Metal–Organic Frameworks for the Detection and Removal of Antibiotics and Organic Explosives in Water. *J. Am. Chem. Soc.* **2016,** *138* (19), 6204-6216.

299. Feng, D.; Wang, K.; Su, J.; Liu, T.-F.; Park, J.; Wei, Z.; Bosch, M.; Yakovenko, A.; Zou, X.; Zhou, H.-C., A Highly Stable Zeotype Mesoporous Zirconium Metal–Organic Framework with Ultralarge Pores. *Angew. Chem. Int. Ed.* **2015,** *54* (1), 149-154.

300. Liu, H.; Chen, F.; Bai, D.; Jiao, J.; Zhou, W.; Yildirim, T.; He, Y., High-Pressure Methane Adsorption in Two Isoreticular Zr-Based Metal–Organic Frameworks Constructed from C3-Symmetrical Tricarboxylates. *Cryst. Growth Des.* **2017,** *17* (1), 248-254.

301. Kaida, H.; Satoh, T.; Nishii, Y.; Hirano, K.; Miura, M., Synthesis of Benzobis- and Benzotrisbenzofurans by Palladium-Catalyzed Multiple Intramolecular C–H/C–H Coupling. *Chem. Lett.* **2016,** *45* (9), 1069-1071.

302. Ogaki, T.; Ohta, E.; Oda, Y.; Sato, H.; Matsui, Y.; Kumeda, M.; Ikeda, H., Intramolecular Triple Cyclization Strategy for Sila- and Oxa-Analogues of Truxene with Long-Lived Phosphorescence. *Asian J. Org. Chem.* **2017,** *6* (3), 290-296.

303. Bergman, J.; Egestad, B., Cyclocondensation of 3(2H)-benzo[b]thiophenone and oxidation products obtained during these reactions. *Tetrahedron* **1986,** *42* (2), 763-773.

304. Kojima, T.; Furukawa, S.; Tsuji, H.; Nakamura, E., Synthesis of Triphosphatruxene via Sextuple Aromatic Nucleophilic Substitution and Simple Isolation of Stereoisomers. *Chem. Lett.* **2014,** *43* (5), 676-677.

305. Sanguinet, L.; Williams, J. C.; Yang, Z.; Twieg, R. J.; Mao, G.; Singer, K. D.; Wiggers, G.; Petschek, R. G., Synthesis and Characterization of New Truxenones for Nonlinear Optical Applications. *Chem. Mater.* **2006,** *18* (18), 4259-4269.

306. Isla, H.; Grimm, B.; Pérez, E. M.; Rosario Torres, M.; Ángeles Herranz, M.; Viruela, R.; Aragó, J.; Ortí, E.; M. Guldi, D.; Martín, N., Bowl-shape electron donors with absorptions in the visible range of the solar spectrum and their supramolecular assemblies with C60. *Chem. Sci.* **2012,** *3* (2), 498-508.

307. Frantz, D. K.; Walish, J. J.; Swager, T. M., Synthesis and Properties of the 5,10,15-Trimesityltruxen-5-yl Radical. *Org. Lett.* **2013,** *15* (18), 4782-4785.

308. Kotha, S.; Ali, R.; Panguluri, N. R.; Datta, A.; Kannaujiya, K. K., Synthesis and photophysical properties of star-shaped blue green emitting π-conjugated spirotruxenes. *Tetrahedron Lett.* **2018,** *59* (46), 4080-4085.

309. González-Cantalapiedra, E.; Ruiz, M.; Gómez-Lor, B.; Alonso, B.; García-Cuadrado, D.; Cárdenas, D. J.; Echavarren, A. M., New Building Blocks Based on Truxene Cores: Synthesis of Functionalized syn-Tri- and -Hexasubstituted Derivatives. *Eur. J. Org. Chem.* **2005,** (19), 4127-4140.

310. Gómez-Lor, B.; Frutos, Óscar d.; Ceballos, Plácido A.; Granier, T.; Echavarren, Antonio M., Synthesis of New C3h and C3v Truxene Derivatives. *Eur. J. Org. Chem.* **2001,** (11), 2107-2114.

311. Ruiz, M.; Gómez-Lor, B.; Santos, A.; Echavarren, Antonio M., Overcrowded 5,10,15-Trisubstituted Derivatives: Synthesis of 5,10,15-Tri(fluorenylidene)truxene. *Eur. J. Org. Chem.* **2004,** (4), 858-866.

312. Jacob, K.; Becker, J. Y.; Ellern, A.; Khodorkovsky, V., Synthesis of novel truxenequinone based electron acceptors. *Tetrahedron Lett.* **1999,** *40* (49), 8625-8628.

313. Beloqui Redondo, A.; Morel, F. L.; Ranocchiari, M.; van Bokhoven, J. A., Functionalized Ruthenium–Phosphine Metal–Organic Framework for Continuous Vapor-Phase Dehydrogenation of Formic Acid. *ACS Catal.* **2015,** *5* (12), 7099-7103.

314. Václavík, J.; Servalli, M.; Lothschütz, C.; Szlachetko, J.; Ranocchiari, M.; van Bokhoven, J. A., AuI Catalysis on a Coordination Polymer: A Solid Porous Ligand with Free Phosphine Sites. *ChemCatChem* **2013,** *5* (3), 692-696.

315. de Frutos, Ó.; Gómez-Lor, B.; Granier, T.; Monge, M. Á.; Gutiérrez-Puebla, E.; Echavarren, A. M., syn-Trialkylated Truxenes: Building Blocks That Self-Associate by Arene Stacking. *Angew. Chem. Int. Ed.* **1999,** *38* (1‐2), 204-207.

316. Óscar, d. F.; Thierry, G.; Berta, G. L.; Jesús, J. B.; Ángeles, M.; Enrique, G. P.; M., E. A., Synthesis and Self‐Association of syn‐5,10,15‐Trialkylated Truxenes. *Chem. Eur. J.* **2002,** *8* (13), 2879-2890.

317. Pálovics, E.; Faigl, F.; Fogassy, E., Separation of the Mixtures of Chiral Compounds by Crystallization, Advances in Crystallization Processes. In *Advances in Crystallization Processes*, Mastai, D. Y., Ed. Rijeka, Croatia, InTech:2012.

318. Sun, F.; Yin, Z.; Wang, Q.-Q.; Sun, D.; Zeng, M.-H.; Kurmoo, M., Tandem Postsynthetic Modification of a Metal–Organic Framework by Thermal Elimination and Subsequent Bromination: Effects on Absorption Properties and Photoluminescence. *Angew. Chem. Int. Ed.* **2013,** *52* (17), 4538-4543.

319. Jones, S. C.; Bauer, C. A., Diastereoselective Heterogeneous Bromination of Stilbene in a Porous Metal−Organic Framework. *J. Am. Chem. Soc.* **2009,** *131* (35), 12516-12517.

320. Hoyle, C. E.; Bowman, C. N., Thiol–Ene Click Chemistry. *Angew. Chem. Int. Ed.* **2010,** *49* (9), 1540-1573.

321. Presolski, S. I.; Zorba, A.; Thamattoor, D. M.; Tippmann, E. M.; Platz, M. S., A search for dichlorocarbene ether solvent interactions. *Tetrahedron Lett.* **2004,** *45* (3), 485-486.

322. Hare, S. R.; Orman, M.; Dewan, F.; Dalchand, E.; Buzard, C.; Ahmed, S.; Tolentino, J. C.; Sethi, U.; Terlizzi, K.; Houferak, C.; Stein, A. M.; Stedronsky, A.; Thamattoor, D. M.; Tantillo, D. J.; Merrer, D. C., Experimental and Computational Mechanistic Investigation of Chlorocarbene Additions to Bridgehead Carbene–Anti-Bredt Systems: Noradamantylcarbene–Adamantene and Adamantylcarbene–Homoadamantene. *J. Org. Chem.* **2015,** *80* (10), 5049-5065.

323. de Frémont, P.; Marion, N.; Nolan, S. P., Carbenes: Synthesis, properties, and organometallic chemistry. *Coord. Chem. Rev.* **2009,** *253* (7), 862-892.

324. Melaimi, M.; Jazzar, R.; Soleilhavoup, M.; Bertrand, G., Cyclic (Alkyl)(amino)carbenes (CAACs): Recent Developments. *Angew. Chem. Int. Ed.* **2017,** *56* (34), 10046-10068.

325. Hopkinson, M. N.; Richter, C.; Schedler, M.; Glorius, F., An overview of N-heterocyclic carbenes. *Nature* **2014,** *510*, 485.

326. Nakano, R.; Jazzar, R.; Bertrand, G., A crystalline monosubstituted carbene. *Nature Chem.* **2018,** *10* (12), 1196-1200.

327. Lavallo, V.; Canac, Y.; Präsang, C.; Donnadieu, B.; Bertrand, G., Stable Cyclic (Alkyl)(Amino)Carbenes as Rigid or Flexible, Bulky, Electron-Rich Ligands for Transition-Metal Catalysts: A Quaternary Carbon Atom Makes the Difference. *Angew. Chem. Int. Ed.* **2005,** *44* (35), 5705-5709.

328. Ezugwu, C. I.; Kabir, N. A.; Yusubov, M.; Verpoort, F., Metal–organic frameworks containing N-heterocyclic carbenes and their precursors. *Coord. Chem. Rev.* **2016,** *307*, 188-210.

329. Lalonde, M. B.; Farha, O. K.; Scheidt, K. A.; Hupp, J. T., N-Heterocyclic Carbene-Like Catalysis by a Metal–Organic Framework Material. *ACS Catal.* **2012,** *2* (8), 1550-1554.

330. Zhang, X.; Sun, J.; Wei, G.; Liu, Z.; Yang, H.; Wang, K.; Fei, H., In Situ Generation of an N-Heterocyclic Carbene Functionalized Metal–Organic Framework by Postsynthetic Ligand Exchange: Efficient and Selective Hydrosilylation of CO2. *Angew. Chem. Int. Ed.* **2019,** *58* (9), 2844-2849.

DRC 16 Form

Electronic Appendices

MASSEY UNIVERSITY
GRADUATE RESEARCH SCHOOL

STATEMENT OF CONTRIBUTION
DOCTORATE WITH PUBLICATIONS/MANUSCRIPTS

We, the candidate and the candidate's Primary Supervisor, certify that all co-authors have consented to their work being included in the thesis and they have accepted the candidate's contribution as indicated below in the *Statement of Originality*.

Name of candidate:	Adil Alkas
Name/title of Primary Supervisor:	Prof. Shane G. Telfer
Name of Research Output and full reference:	
A. Alkaş, J. Cornelio, S. G. Telfer, Tritopic Triazatruxene Ligands for Multicomponent Metal-Organic Frameworks, Chem. Asian J. 2018, In Press.	
In which Chapter is the Manuscript /Published work:	Chapter 2
Please indicate:	
• The percentage of the manuscript/Published Work that was contributed by the candidate:	60%
and	
• Describe the contribution that the candidate has made to the Manuscript/Published Work:	
The candidate carried out the experimental and computational work, put together the electronic supporting information, and wrote the first draft of this paper.	
For manuscripts intended for publication please indicate target journal:	
Candidate's Signature:	
Date:	22/3/19
Primary Supervisor's Signature:	Shane Telfer Digitally signed by Shane Telfer Date: 2019.03.22 10:26:19 +13'00'
Date:	22/3/19

(This form should appear at the end of each thesis chapter/section/appendix submitted as a manuscript/ publication or collected as an appendix at the end of the thesis)

Electronic Appendices

Table of Contents

Appendix A for Chapter 2

Experimental Details and Supporting Information for Chapter 2

1. Ligand synthesis and characterization

Indole 6-carboxylic acid ethyl ester[1]

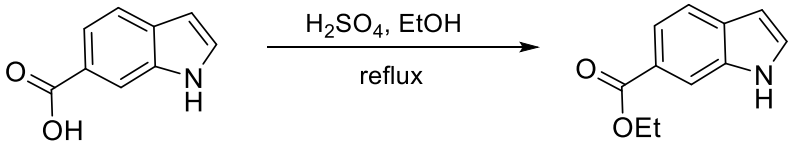

Indole 6-carboxylic acid (5.00 g, 31.03 mmol) and EtOH (150 mL) was combined and the mixture cooled on an ice-water bath. Concentrated H_2SO_4 (1 mL) was added dropwise, then the reaction mixture was refluxed for 24 hours. After cooling to RT, solid K_2CO_3 was added and the mixture was stirred for 1 hour to neutralize excess H_2SO_4. Ethanol was removed under reduced pressure. 100 ml of cold water was added to reaction mixture and a brown solid was filtered and dried under vacuum. This material was further chromatographed on a silica column eluting with a mixture of ethyl acetate/hexane, 1:5, to afford the product as a white crystalline solid. Yield: 5.1 g, (87%). ^{1}H NMR (500 MHz, $CDCl_3$) δ 8.48 (s, 1H), 8.21 (s, 1H), 7.86 (d, *J* = 8.3 Hz, 1H), 7.69 (d, *J* = 8.3 Hz, 1H), 7.40 (s, 1H), 6.63 (s, 1H), 4.43 (q, *J* = 7.1 Hz, 2H), 1.45 (t, *J* = 7.1 Hz, 3H) ppm. ^{13}C NMR: (125 MHz, DMSO-*d*6): δ 168.03, 135.23, 131.60, 127.71, 123.90, 120.79, 120.25, 113.57, 102.87, 60.82, 14.45 ppm. ESI (positive mode, CH_3OH): m/z = 212.0678 ($[C_{11}H_{11}N_1O_2Na]^+$ calcd. 212.0682).

Et_3tat-ethyl

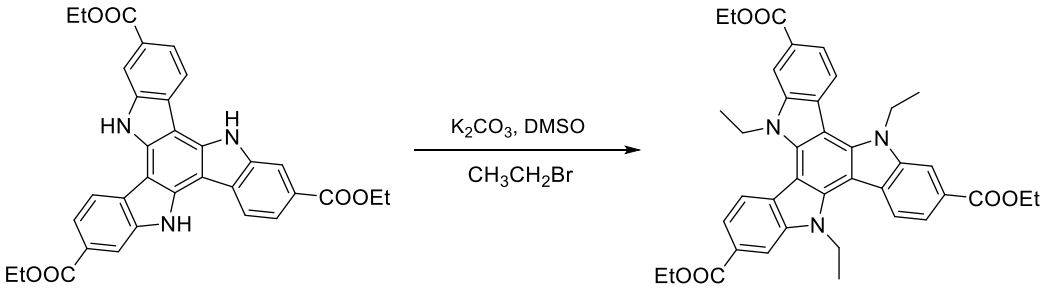

Et_3tat (562 mg, 1 mmol) and K_2CO_3 (2.07 g) were combined in DMSO (5 mL) under an argon atmosphere and stirred at room temperature for 15 minutes. Ethyl bromide (746µL, 10 mmol) was then added and the reaction mixture stirred at room temperature overnight. The mixture was poured into cold water and stirred for 30 mins. The yellow solid was filtered off, washed with water and dried under vacuum. This crude product was recrystallized from a mixture of ethyl acetate and hexane (1:3). Yield: 538 mg (83%). ^{1}H NMR: (500 MHz, $CDCl_3$): δ 8.39 (s, 3H), 8.33 (d, *J* = 8.5 Hz, 3H), 8.10 (d, *J* = 8.4 Hz, 3H), 5.07 (q, *J* = 6.9 Hz, 6H), 4.53 (q, *J* = 7.1 Hz, 6H), 1.65 (t, *J* = 7.1 Hz, 9H), 1.52 (t, *J* = 7.1 Hz, 9H). ^{13}C NMR: (125 MHz, $CDCl_3$): 167.29, 140.80, 139.94, 126.74, 124.94, 121.52, 120.80, 112.03, 103.15, 61.01, 41.91, 15.68, 14.53. ESI (positive mode, CH_3OH): m/z = 668.2721 ($[C_{39}H_{39}N_3O_6Na]^+$, calcd. 668.2731).

H_3tat-ethyl

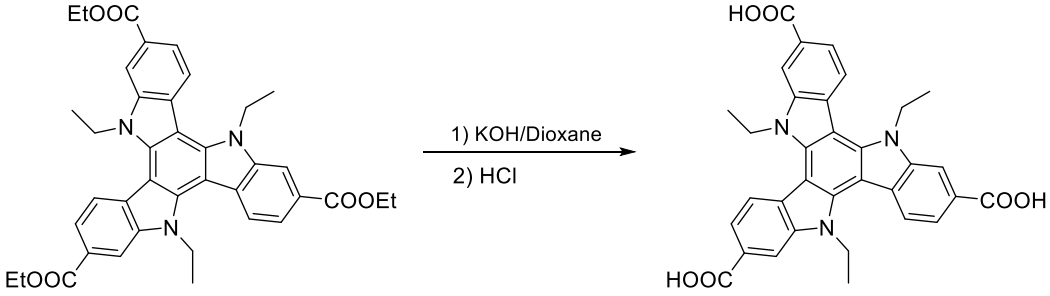

Et_3tat-ethyl (527 mg, 0.82 mmol) was dissolved in 20 mL of 1:1 (V/V) dioxane/KOH (aq., 1 M) and the solution was refluxed overnight. Dioxane was removed under reduced pressure and the reaction mixture then was acidified with aqueous 1 M HCl while it was kept on an ice bath. The pH was adjusted to around 1, and the mixture was stirred for one hour. The yellow solid was filtered off, washed with water and dried under vacuum. Yield: 451 mg (98%). ^{1}H NMR: (500 MHz,

DMSO-*d*6): δ 12.83 (br, 3H), 8.42-8.40 (m, 6H), 8.01 (d, *J* = 8.8 Hz, 3H), 5.11 (q, *J* = 6.7 Hz, 6H), 1.50 (t, *J* = 7.0 Hz, 9H). ^{13}C NMR: (125 MHz, DMSO-*d*6): 168.33, 140.41, 139.85, 126.15, 125.83, 122.03, 121.56, 112.51, 102.87, 41.97, 15.76. ESI (negative mode, CH_3OH): m/z = 560.1838 ($[C_{33}H_{26}N_3O_6]^-$, calcd. 560.1900).

Et$_3$tat-allyl

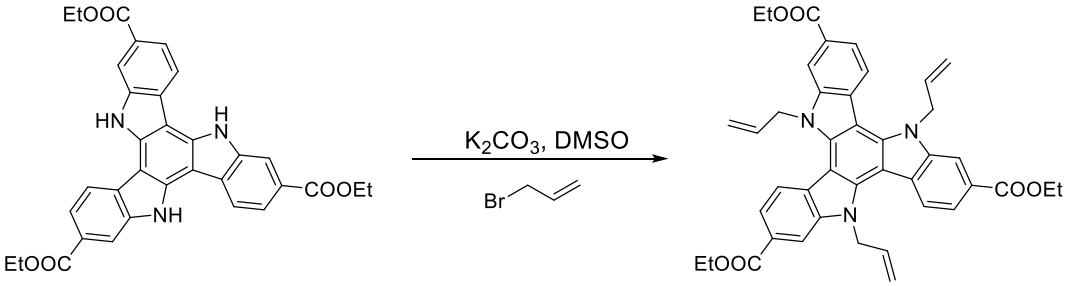

Et$_3$tat (300 mg, 0.53 mmol) and K_2CO_3 (1.12 g) were combined in DMSO (5 mL) under argon atmosphere and stirred at room temperature for 15 minutes. Then, allyl bromide (459 µL, 5.3 mmol) was added and the reaction mixture stirred at room temperature overnight. The mixture was poured into cold water and stirred for half an hour. The yellow solid formed was filtered, washed with water and dried under vacuum. This material was further recrystallized from a mixture of (1:1) ethyl acetate and hexane. Yield: 254 mg, (70%). ^{1}H NMR: (500 MHz, $CDCl_3$): δ 8.42 (d, *J* = 8.5 Hz, 3H), 8.29 (s, 3H), 8.07 (dd, *J* = 8.5, 1.2 Hz, 3H), 6.50 (ddt, *J* = 17.6, 10.6, 3.6 Hz, 3H), 5.62 (d, *J* = 10.7 Hz, 3H), 5.57 – 5.43 (m, 9H), 4.49 (q, *J* = 7.1 Hz, 6H), 1.49 (t, *J* = 7.1 Hz, 9H) ppm. ^{13}C NMR: (125 MHz, $CDCl_3$): δ 167.20, 141.57, 141.04, 133.81, 126.59, 125.36, 121.85, 121.17, 118.47, 112.55, 103.16, 60.97, 50.01, 14.48 ppm. ESI (positive mode, CH_3OH): m/z = 681.2822 ($[C_{42}H_{39}N_3O_6]^+$, calcd. 681.2833).

H$_3$tat-allyl

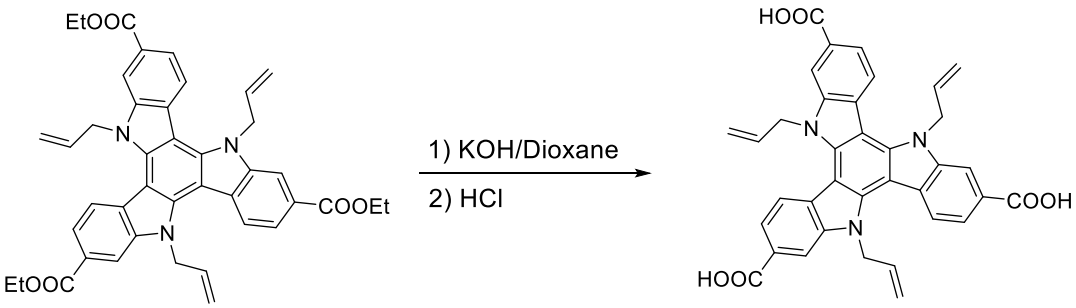

Et_3tat-allyl (220 mg, 0.32 mmol) was dissolved in 20 mL 1:1 (V/V) dioxane/KOH (aq., 1M) and the solution was refluxed overnight. Dioxane was removed under reduced pressure and the reaction mixture then was acidified with 3 M aqueous HCl while it was kept on an ice bath. pH was adjusted to around 1, and the mixture was stirred for 3 hours. The yellow solid fromed was filtered, washed with water and dried under vacuum. Yield: 181 mg (94%). ^{1}H NMR: (500 MHz, DMSO-*d*6): δ 12.92 (s, 3H), 8.40 (d, *J* = 8.5 Hz, 3H), 8.23 (s, 3H), 7.93 (d, *J* = 8.5 Hz, 3H), 6.54 (ddt, *J* = 17.5, 10.6, 3.6 Hz, 3H), 5.53 (s, 6H), 5.49 (d, *J* = 10.8 Hz, 3H), 5.24 (d, *J* = 17.1 Hz, 3H) ppm. ^{13}C NMR: (125 MHz, DMSO-*d*6): δ 168.19, 141.20, 140.79, 135.25, 126.03, 125.92, 122.00, 121.69, 117.68, 112.89, 102.75, 49.96 ppm. ESI (negative mode, CH_3OH): m/z = 596.1842 ($[C_{36}H_{26}N_3O_6]^-$, calcd. 596.1900).

Et_3tat-butyl

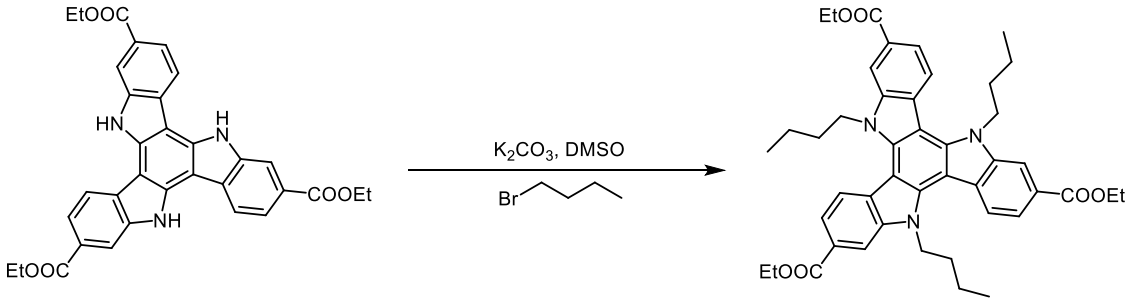

Et_3tat (281 mg, 0.5 mmol) and K_2CO_3 (1.17 g) were combined in DMSO (3 mL) and stirred at RT for 15 minutes. Then, 1-bromobutane (537μL, 5 mmol) was added and the reaction mixture stirred at 70 ℃ overnight. After cooling to RT, the mixture was poured into cold water and stirred for half an hour. The yellow solid formed was filtered, washed with water and dried under vacuum. This material was further recrystallized from a mixture of ethyl acetate and hexane. Yield: 248 mg (68%). ^{1}H NMR: (500 MHz, $CDCl_3$): δ 8.40 (s, 3H), 8.31 (d, *J* = 8.5 Hz, 3H), 8.10 (d, *J* = 8.4 Hz, 3H), 5.10 – 4.96 (m, 6H), 4.53 (q, *J* = 7.1 Hz, 6H), 2.15 – 1.80 (m, 6H), 1.54 (dd, *J* = 18.3, 11.1 Hz, 6H), 1.53 (t, *J* = 7.1 Hz, 9H), 1.30 (dd, *J* = 15.0, 7.5 Hz, 6H), 0.89 (t, *J* = 7.4 Hz, 9H) ppm. ^{13}C NMR: (125 MHz, $CDCl_3$): δ 167.35, 141.11, 140.21, 126.69, 124.79, 121.32, 120.86, 112.36, 103.15, 61.01, 46.98, 32.03, 19.91, 14.53, 13.74 ppm. ESI (positive mode, CH_3OH): m/z = 752.3661 ($[C_{45}H_{51}N_3O_6Na]^+$, calcd. 752.3670).

H_3tat-butyl

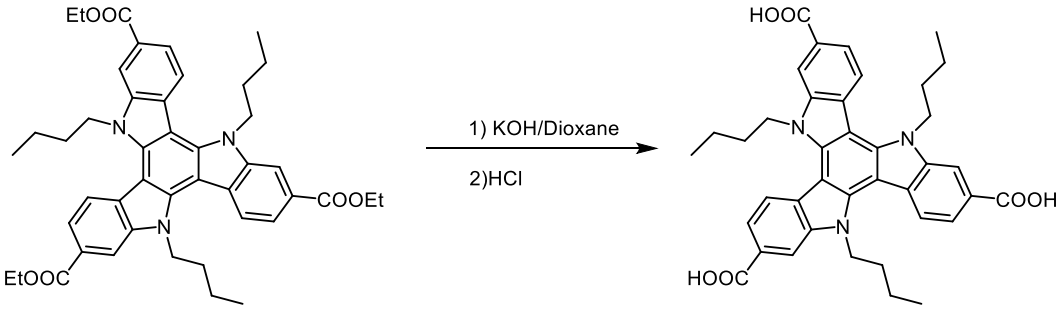

Et_3tat-butyl (452 mg, 0.62 mmol) was dissolved in 20 mL 1:1 (V/V) dioxane/KOH (aq., 1M) and the solution was refluxed overnight. Dioxane was removed under reduced pressure and the reaction mixture then was acidified with 3 M aqueous HCl while it was kept on an ice bath. pH was adjusted to around 1, and the mixture was stirred overnight. The yellow solid formed was filtered, washed with water and dried at 80 ℃ under vacuum. Yield: 384 mg (96%). ^{1}H NMR: (500 MHz, DMSO-*d*6): δ 12.94 (br, 3H), 8.36 (s, 3H), 8.30 (d, *J* = 8.5 Hz, 3H), 7.97 (d, *J* = 8.6 Hz, 3H), 4.99 (t, *J* = 7.1 Hz, 6H), 1.87 – 1.64 (m, 6H), 1.13 – 0.92 (m, 6H), 0.69 (t, *J* = 7.4 Hz, 9H) ppm. ^{13}C NMR: (125 MHz, DMSO-*d*6): δ 168.34, 140.71, 140.22, 126.09, 125.74, 121.81, 121.53, 112.86, 102.94, 46.65, 31.73, 19.58, 13.88 ppm. ESI (negative mode, CH_3OH): m/z = 644.2772 ($[C_{39}H_{38}N_3O_6]^-$, calcd. 644.2755).

Et_3tat-hexyl

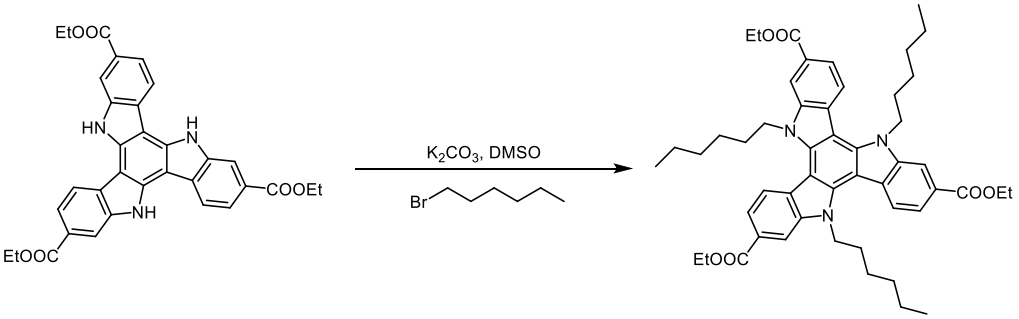

Et_3tat (562 mg, 1 mmol) and K_2CO_3 (2.07 g) were combined in DMSO (6 mL) and stirred at RT for 15 minutes. Then, 1-bromohexane (561µL, 4 mmol) was added and the reaction mixture stirred at 70 ℃ overnight. After cooling to RT, the mixture was poured into cold water and stirred for half an hour. The yellow solid formed was filtered, washed with water and dried under vacuum. The product was obtained as a yellowish solid after purification by column with hexane/ethyl acetate

(from 1:0 to 5:1). Yield: 582 mg (72%). ^{1}H NMR: (500 MHz, $CDCl_3$): δ 8.37 (s, 3H), 8.28 (d, *J* = 8.5 Hz, 3H), 8.08 (d, *J* = 8.5 Hz, 3H), 5.03 – 4.91 (m, 6H), 4.53 (q, *J* = 7.1 Hz, 6H), 2.07 – 1.90 (m, 6H), 1.53 (t, *J* = 7.1 Hz, 9H), 1.41 – 1.06 (m, 18H), 0.81 (t, *J* = 7.0 Hz, 9H) ppm. ^{13}C NMR: (125 MHz, $CDCl_3$): δ 167.35, 141.08, 140.21, 126.70, 124.79, 121.32, 120.84, 112.32, 103.15, 61.00, 47.18, 31.29, 29.86, 26.22, 22.39, 14.52, 13.86 ppm. ESI (positive mode, CH_3OH): m/z = 836.4595 ($[C_{51}H_{63}N_3O_6Na]^+$, calcd. 836.4609).

H_3tat-hexyl

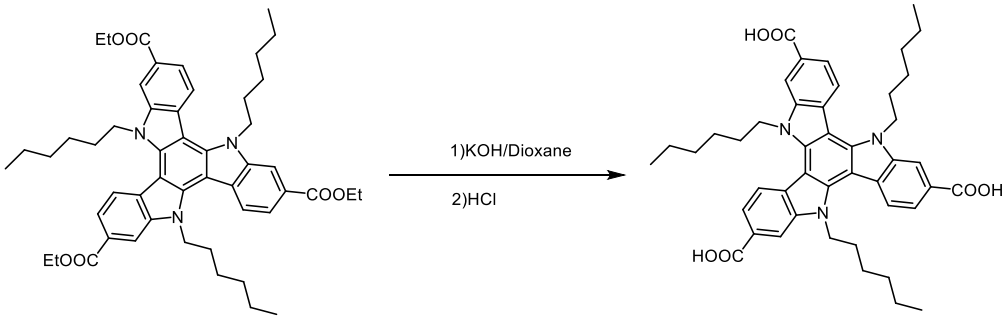

Et_3tat-hexyl (560 mg, 0.68 mmol) was dissolved in 20 mL 1:1 (V/V) dioxane/KOH (aq., 1M) and the solution was refluxed overnight. Dioxane was removed under reduced pressure and the reaction mixture then was acidified with 3 M aqueous HCl while it was kept on an ice bath. pH was adjusted to around 1, and the mixture was stirred for 3 hours. The yellowish solid fromed was filtered, washed with water and dried under vacuum. Yield: 447 mg (89%). ^{1}H NMR: (500 MHz, DMSO-*d6*): δ 12.89 (br, 3H), 8.35 (s, 3H), 8.29 (d, *J* = 8.5 Hz, 3H), 7.96 (d, *J* = 8.4 Hz, 3H), 4.96 (t, *J* = 6.6 Hz, 6H), 1.79-1.69 (m, 6H), 1.14 – 0.82 (m, 18H), 0.62 (t, *J* = 6.9 Hz, 9H) ppm. ^{13}C NMR: (125 MHz, DMSO): δ 168.33, 140.65, 140.22, 126.07, 125.74, 121.76, 121.47, 112.83, 102.97, 46.71, 30.95, 29.39, 25.70, 22.15, 13.99 ppm. ESI (negative mode, CH_3OH): m/z = 728.3714 ($[C_{45}H_{50}N_3O_6]^-$, calcd. 728.3694).

Et_3tat-cychexyl

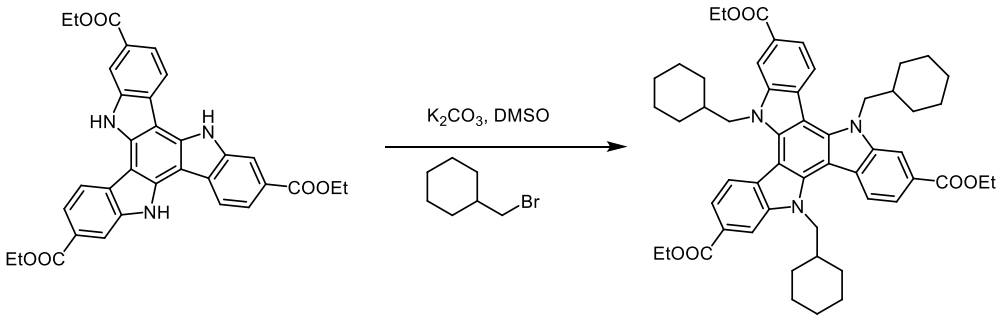

Et_3tat (281 mg, 0.5 mmol) and K_2CO_3 (1.5 g) were combined in DMSO (5 mL) and stirred at RT for 15 minutes. Then, bromomethyl cyclohexane (700 µL, 5 mmol) was added and the reaction mixture stirred at 70 ℃ overnight. The mixture was poured into cold water and stirred for half an hour. The product was extracted with ethyl acetate. Organic layer was dried over magnesium sulfate and ethyl acetate removed under reduced pressure. The product was recrystallized in a mixture of ethyl acetate and hexane to obtain a yellow solid. Yield: 345 mg, (81%). ^{1}H NMR: (500 MHz, $CDCl_3$): δ 8.41 (s, 3H), 8.30 (d, *J* = 8.5 Hz, 3H), 8.11 (d, *J* = 8.4 Hz, 3H), 4.94 (d, *J* = 8.4 Hz, 6H), 4.54 (q, *J* = 7.1 Hz, 6H), 1.90 – 1.85 (m, 6H), 1.53 (t, *J* = 7.1 Hz, 9H), 1.37 – 1.30 (m, 9H), 1.05 0.95 (m, 6H), 0.90 0.75 (m, 9H), 0.72 0.65 (m, 6H) ppm. ^{13}C NMR: (125 MHz, $CDCl_3$): δ 167.50, 141.44, 140.71, 126.72, 124.61, 121.38, 121.22, 113.16, 103.62, 61.02, 52.98, 37.65, 30.16, 25.96, 25.34, 14.55 ppm. ESI (positive mode, CH_3OH): m/z = 851.2490 ($[C_{54}H_{64}N_3O_6]^+$, calcd. 851.4823).

H_3tat-cychexyl

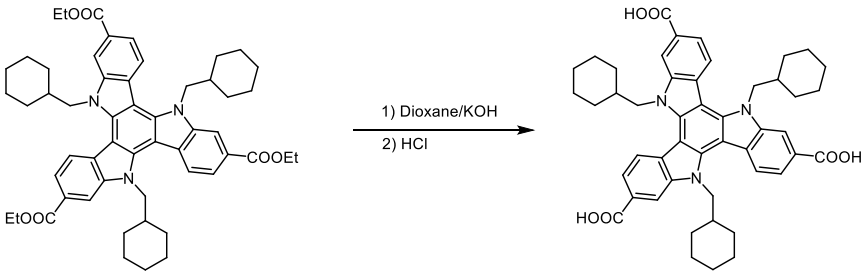

Et_3tat-cychexyl (335 mg, 0.40 mmol) was dissolved in 20 mL 1:1 (V/V) dioxane/KOH (aq., 1M) and the solution was refluxed overnight. Dioxane was removed under reduced pressure and the reaction mixture then was acidified with 1 M aqueous HCl while it was kept on an ice bath. pH was adjusted to around 1, and the mixture was stirred for 1 hour. The yellow solid formed was filtered, washed with water and dried under vacuum. 290 mg, 0.39 mmol, 96%. ^{1}H NMR: (500 MHz, DMSO-*d*6): δ 12.97 (br, 3H), 8.45 (s, 3H), 8.39 (d, *J* = 8.5 Hz, 3H), 8.01 (d, *J* = 8.4 Hz, 3H), 4.99 (d, *J* = 7.2 Hz, 6H), 1.79-1.69 (m, 3H), 1.32 – 1.25 (m, 9H), 0.94-0.57 (m, 21H) ppm. ^{13}C NMR: (125 MHz, DMSO-*d*6): δ 168.47, 141.00, 140.98, 126.16, 125.74, 121.98, 121.82, 113.62, 103.53, 52.54, 37.61, 29.88, 25.95, 25.30 ppm. ESI (negative mode, CH_3OH): m/z = 764.3697 ($[C_{48}H_{50}N_3O_6]^-$, calcd. 764.3694).

2. MOF synthesis and characterization

MUF-777 nanocrystals, $[Zn_4O(tat)_{4/3}(bpdc)_{1/2}(bdc)_{1/2}]$

To a solution of H_3tat (27.6 mg, 57.81 μmol), H_2bpdc (2.6 mg, 10.73 μmol) and H_2bdc (1.4 mg, 8.43 μmol) in 3 mL of DMF/H_2O (50:1, v/v) was added a solution of $Zn(OAc)_2{\cdot}2H_2O$ (27.5 mg, 0.15 mmol) in 0.5 mL DMF. The mixture was stirred at room temperature for 30 minutes. The resulting suspension was centrifuged thrice with fresh DMF and placed in an isothermal oven at 85 °C overnight. The crystals were centrifuged again with fresh dry DMF. For yield calculation, TGA and NMR analysis, the solvent was replaced with anhydrous acetone (5 times). After acetone was decanted, the crystals were dried under vacuum. Yield: 18 mg.

MUF-777-butyl nanocrystals, $[Zn_4O(tat\text{-}butyl)_{4/3}(bpdc)_{1/2}(bdc)_{1/2}]$

To a solution of H_3tat-butyl (15.0 mg, 23.23 μmol), H_2bpdc (2.3 mg, 9.49 μmol) and H_2bdc (1.3 mg, 7.73 μmol) in 2 mL of DMF/H_2O (50:1, v/v) was added a solution of $Zn(OAc)_2{\cdot}2H_2O$ (27.5 mg, 0.15 mmol) in 0.5 mL DMF. The mixture was stirred at room temperature for 30 minutes. The resulting suspension was centrifuged thrice with fresh DMF and placed in an isothermal oven at 85 °C overnight. The crystals were centrifuged again with fresh dry DMF. For yield calculation, TGA and NMR analysis, the solvent was replaced with anhydrous acetone (5 times). After acetone was decanted, the crystals were dried under vacuum. Yield: 15 mg.

MUF-777-hexyl nanoscrystals, [Zn_4O(tat-hexyl)$_{4/3}$(bpdc)$_{1/2}$(bdc)$_{1/2}$]

To a solution of H_3tat-hexyl (17.8 mg, 24.39 µmol), H_2bpdc (2.4 mg, 9.90 µmol) and H_2bdc (1.4 mg, 8.43 µmol) in 2 mL of DMF/H_2O (50:1, v/v) was added a solution of $Zn(OAc)_2 \cdot 2H_2O$ (27.5 mg, 0.15 mmol) in 0.5 mL DMF. The mixture was stirred at room temperature for 30 minutes. The resulting suspension was centrifuged thrice with fresh DMF and placed in an isothermal oven at 85 °C overnight. The crystals were centrifuged again with fresh dry DMF. For yield calculation, TGA and NMR analysis, the solvent was replaced with anhydrous acetone (5 times). After acetone was decanted, the crystals were dried under vacuum. Yield: 15 mg.

MUF-777-cychexyl nanocrystals, [Zn_4O(tat-cychexyl)$_{4/3}$(bpdc)$_{1/2}$(bdc)$_{1/2}$]

To a solution of H_3tat-cychexyl (17.3 mg, 22.59 µmol), H_2bpdc (2.6 mg, 10.73 µmol) and H_2bdc (1.4 mg, 8.43 µmol) in 2 mL of DMF/H_2O (50:1, v/v) was added a solution of $Zn(OAc)_2 \cdot 2H_2O$ (27.5 mg, 0.15 mmol) in 0.5 mL DMF. The mixture was stirred at room temperature for 30 minutes. The resulting suspension was centrifuged thrice with fresh DMF and placed in an isothermal oven at 85 °C overnight. The crystals were centrifuged again with fresh dry DMF. For yield calculation, TGA and NMR analysis, the solvent was replaced with anhydrous acetone (5 times). After acetone was decanted, the crystals were dried under vacuum. Yield: 17 mg.

3. ^{1}H NMR spectra of digested MOFs

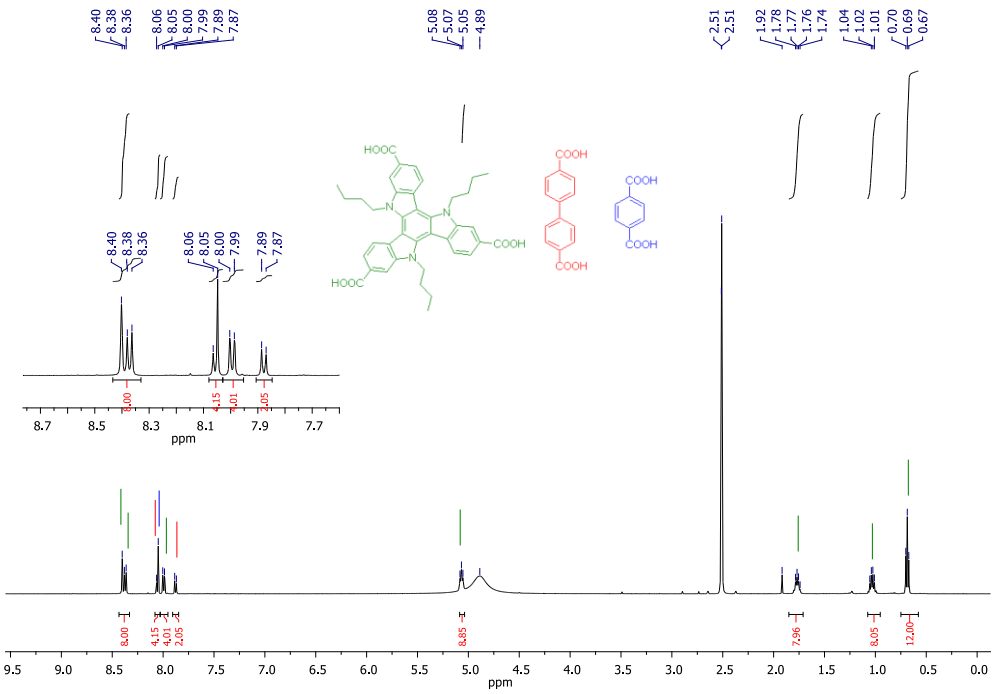

Figure A. 1 ^{1}H NMR spectrum of digested MUF-777-butyl.

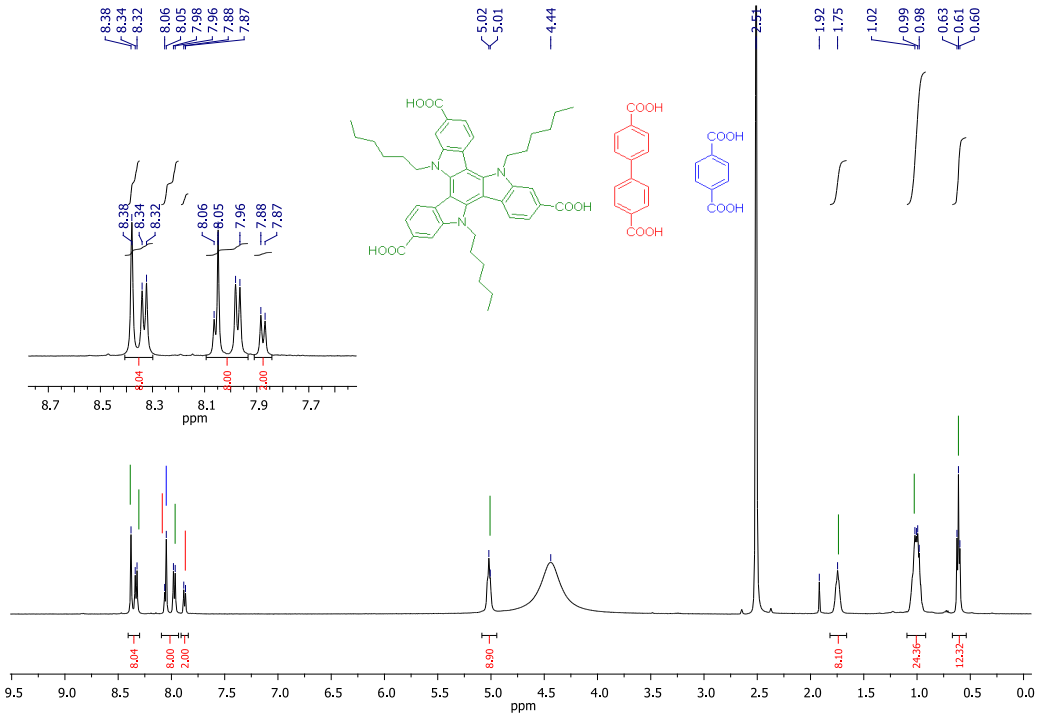

Figure A. 2 ^{1}H NMR spectrum of digested MUF-777-hexyl.

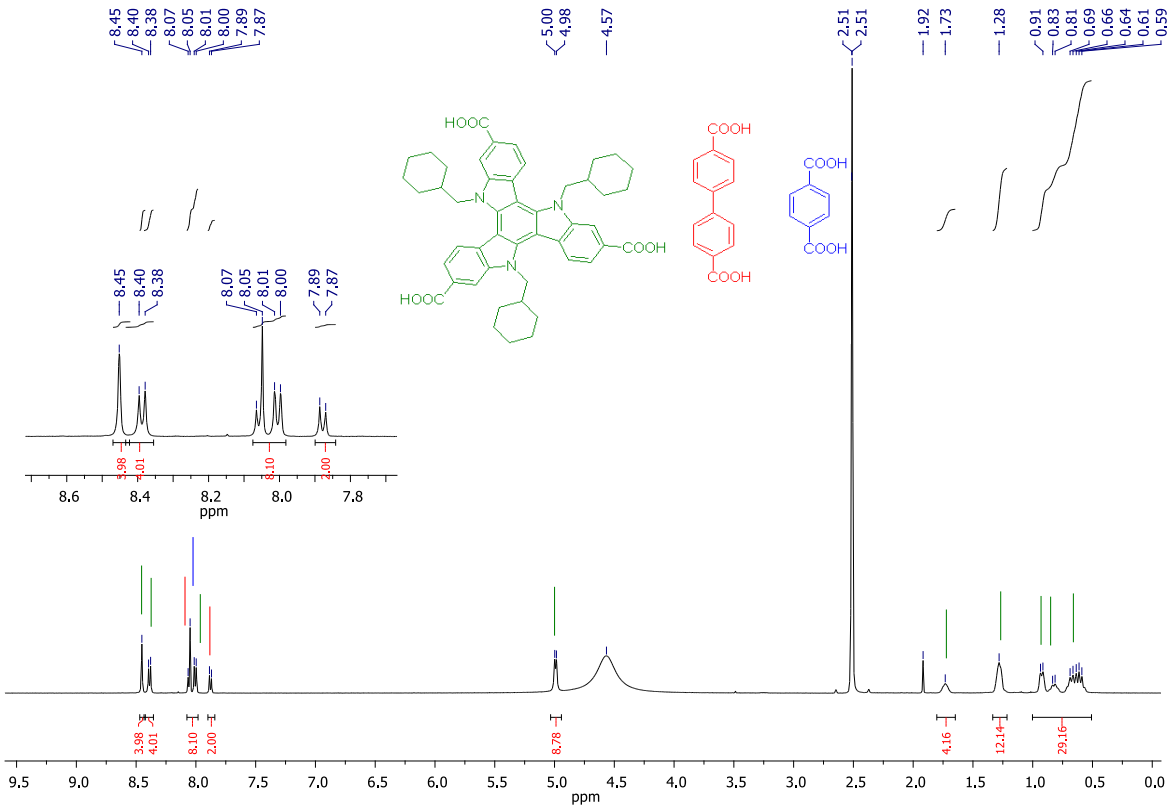

Figure A. 3 ^{1}H NMR spectrum of digested MUF-777-cychexyl.

4. Powder X-ray diffraction patterns

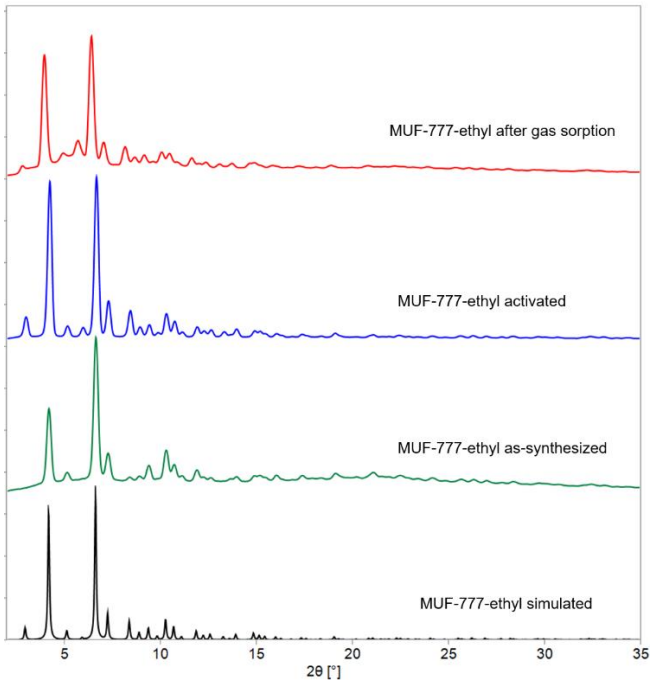

Figure A. 4 PXRD patterns of MUF-777-ethyl; as-synthesized, activated and sample after gas adsorption measurement.

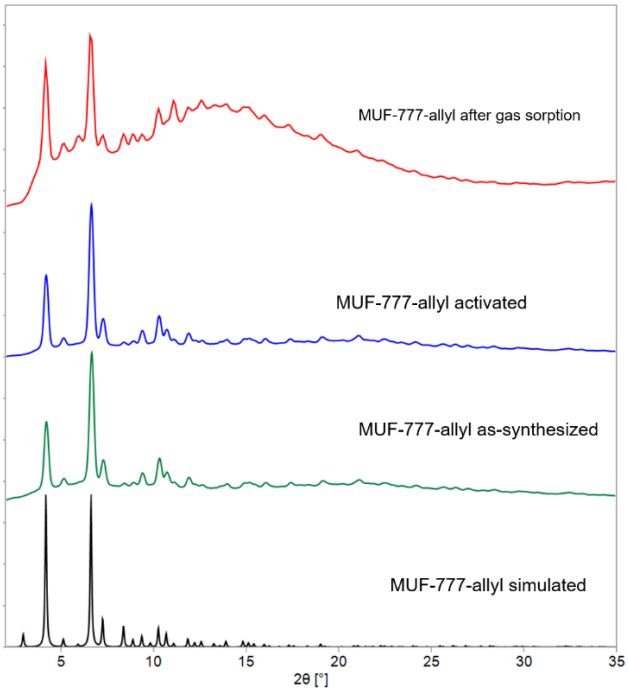

Figure A. 5 PXRD patterns of MUF-777-allyl; as-synthesized, activated and sample after gas adsorption measurement.

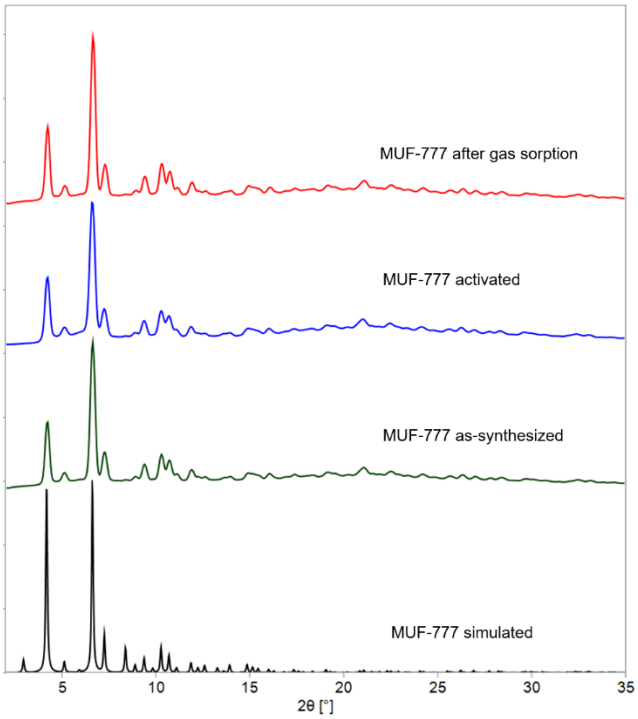

Figure A. 6 PXRD patterns of MUF-777; as-synthesized, activated and sample after gas adsorption measurement.

5. Gas adsorption measurements

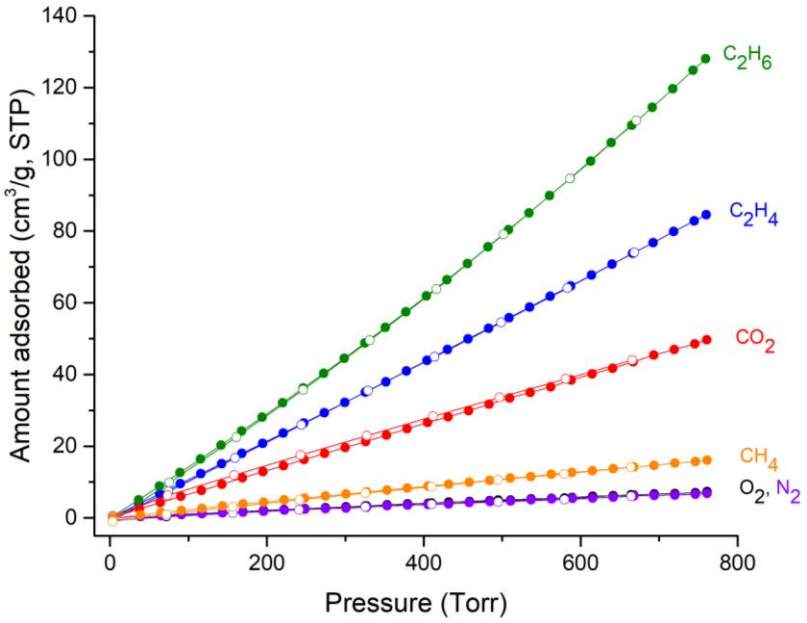

Figure A. 7 Adsorption and desorption isotherms of MUF-777-ethyl at 273 K with various gases.

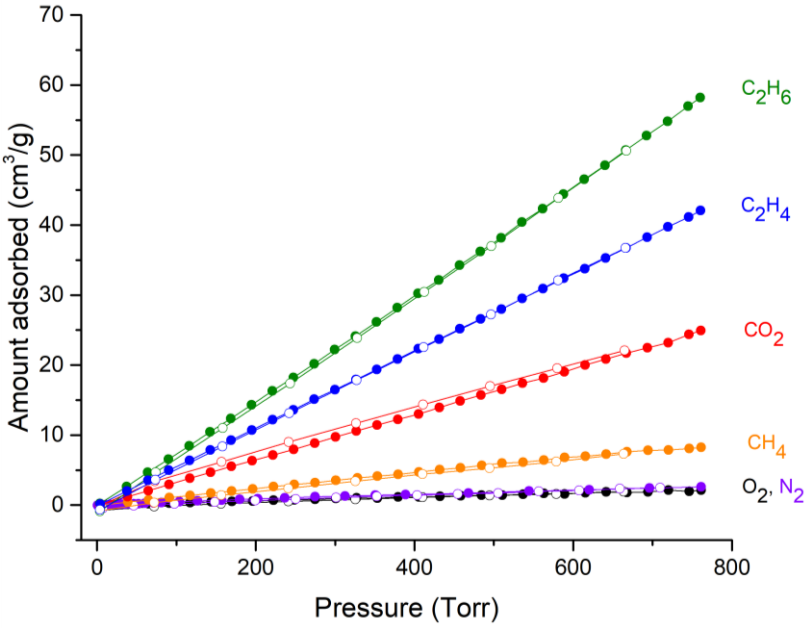

Figure A. 8 Adsorption and desorption isotherms of MUF-777-ethyl at 298 K with various gases.

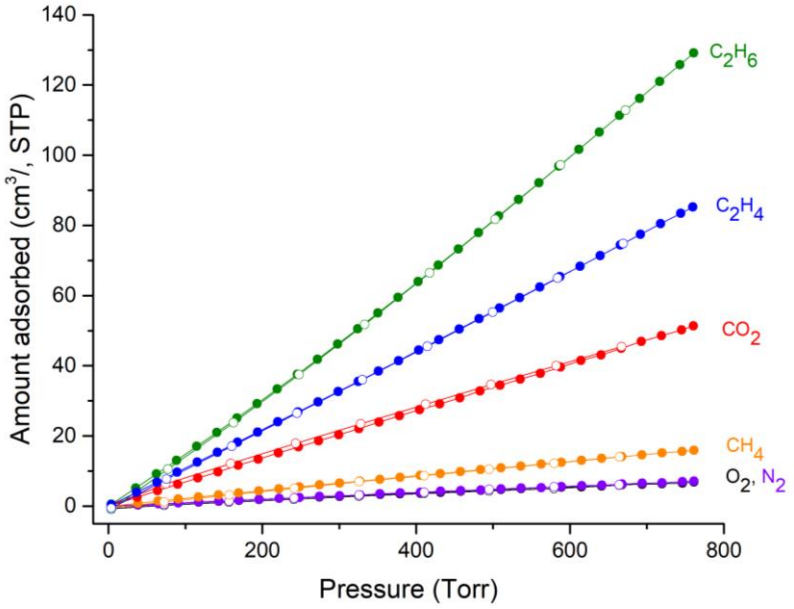

Figure A. 9 Adsorption and desorption isotherms of MUF-777-allyl at 273 K with various gases.

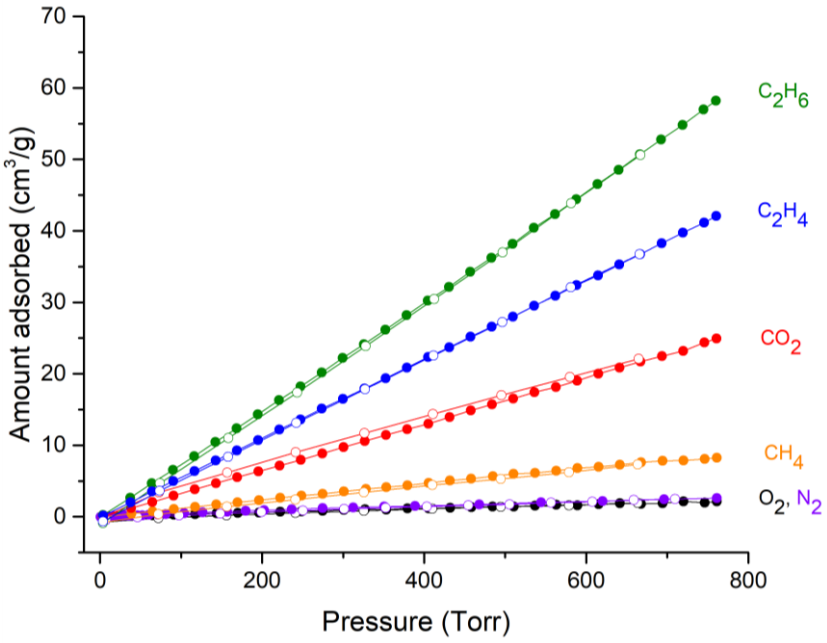

Figure A. 10 Adsorption and desorption isotherms of MUF-777-allyl at 298 K with various gases.

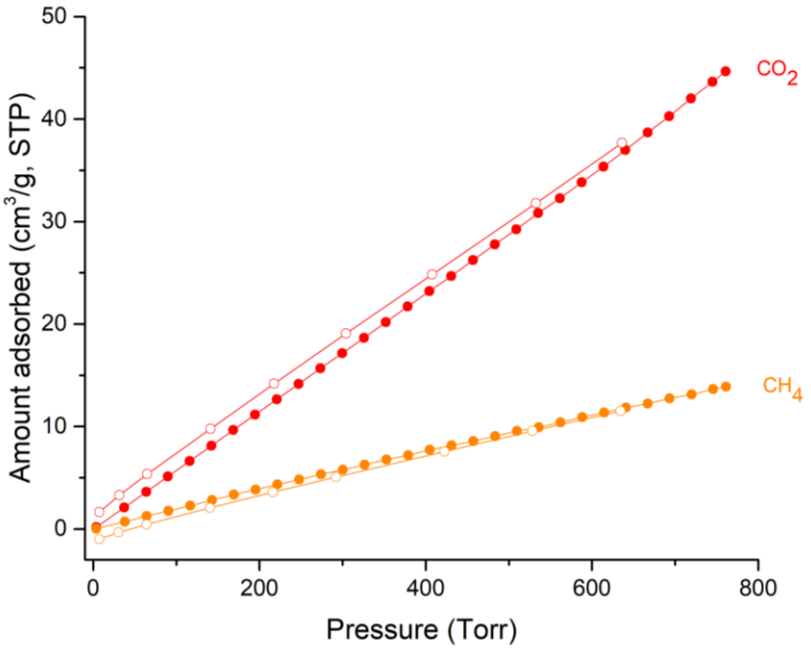

Figure A. 11 Adsorption and desorption isotherms of MUF-777 at 293 K with CO_2 and CH_4.

6. TGA plots

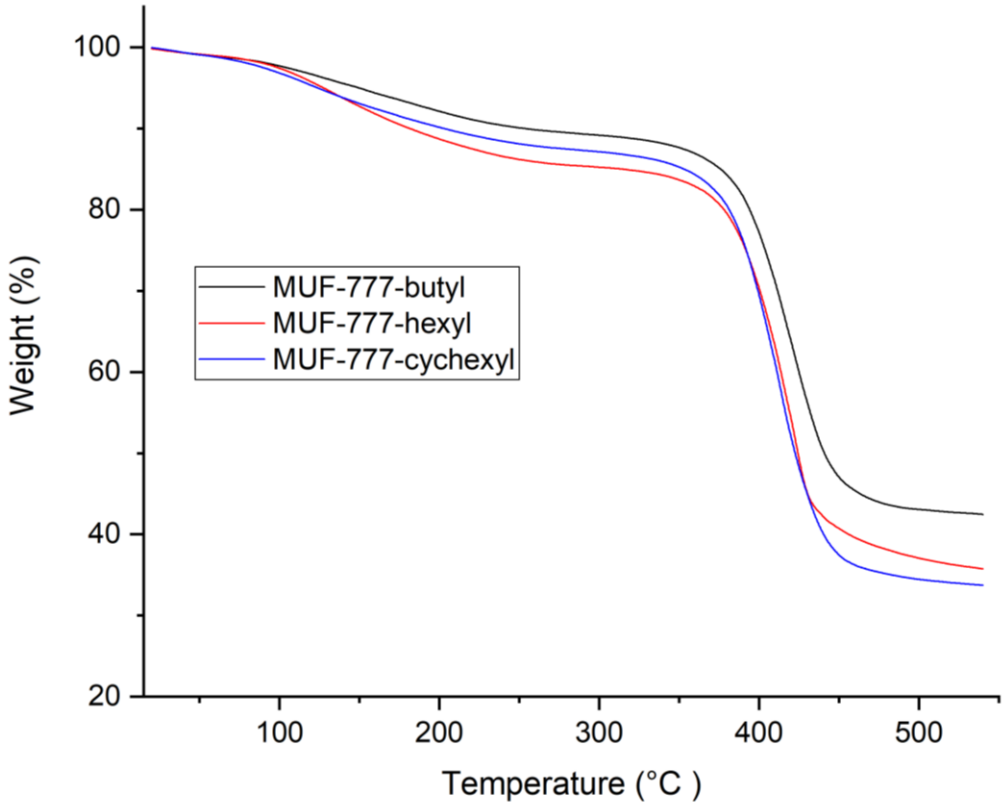

Figure A. 12 TGA plot of MUF-777-butyl, MUF-777-hexyl and MUF-777-cychexyl occluded with DMF

Appendix B for Chapter 3

Experimental Details and Supporting Information for Chapter 3

1. Ligand synthesis and characterization

Me_2cychcdc

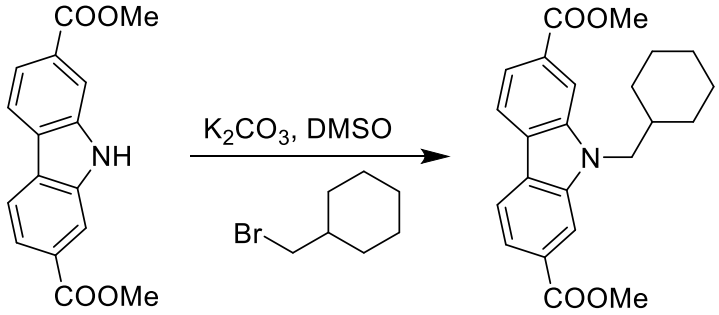

9H-carbazole-2,7-dicarboxylate[2] (142 mg, 0.50 mmol) and K_2CO_3 (500 mg) were combined in DMSO (3 mL) and stirred at RT for 15 minutes. Then, bromomethyl cyclohexane (140 µL, 1 mmol) was added and the reaction mixture stirred at 70 °C overnight. The mixture was poured into cold water and stirred for half an hour. The white solid was filtered, washed with water and dried. Yield: 173 mg, 0.46 mmol, 91%. ^{1}H NMR (500 MHz, $CDCl_3$): δ 8.20-8.18 (m, 4H), 7.97 (d, *J* = 8.3 Hz, 2H), 4.26 (d, j = 7.5 Hz, 2H) 4.03 (s, 6H), 2.02-2.10 (m, 1H) 2.75-2.65 (m, 5H), 2.22-2.11 (m, 5H) ppm. ^{13}C NMR (125 MHz, $CDCl_3$): δ 167.71, 141.56, 128.28, 125.53, 120.73, 120.28, 111.33, 52.30, 49.78, 38.23, 31.59, 31.29, 26.21, 25.71 ppm. ESI (positive mode, CH_3OH): m/z = 380.1846 ($[C_{23}H_{26}NO_4]^+$, calcd. 380.1856).

H_2cychcdc

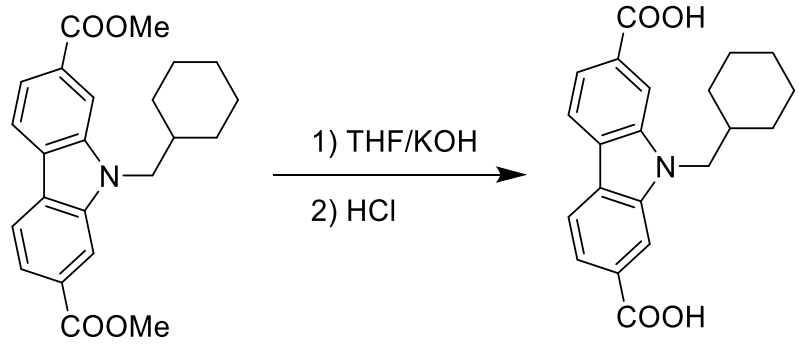

Me_2cychcdc (160 mg, 0.95 mmol) was dissolved in 20 mL 1:1 (V/V) THF/KOH (aq., 1M) and the solution was refluxed overnight. THF was removed under reduced pressure and the reaction mixture then was acidified with 1 M aqueous HCl while it was kept on an ice bath. pH was adjusted to around 1, and the mixture was stirred for 1 hour. A yellow solid was filtered, washed with water and dried under vacuum. Yield: 140 mg, 0.40 mmol, 95%. ^{1}H NMR (500 MHz, DMSO-*d*6): δ 13.04 (br, 2H), 8.34 (d, j = 7.8 Hz, 2H), 8.23 (s, 2H), 7.85 (d, j = 7.7 Hz, 2H), 4.38 (dt, j = 5.9 Hz, 2H), 1.94 (s, 1H), 1.75-1.35 (m, 5H), 1.22- 1.05 (m, 5H) ppm. ^{13}C NMR (125 MHz, DMSO-*d*6): 168.33, 141.58, 129.45, 125.08, 121.44, 120.46, 111.82, 48.97, 38.33, 30.86, 26.26, 25.69 ppm. ESI (negative mode, CH_3OH): m/z = 350.1390 ($[C_{21}H_{20}NO_4]^-$, calcd. 350.1387).

Me_2mcdc

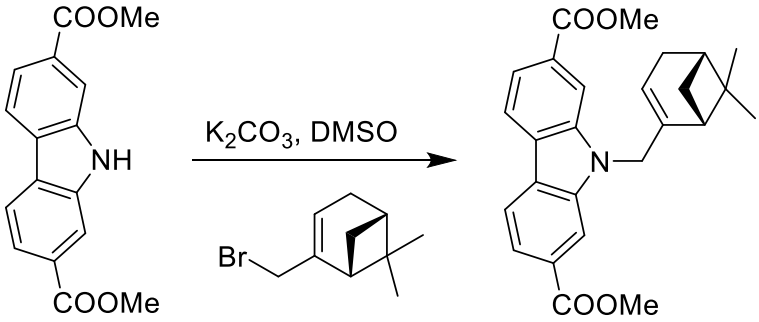

9H-carbazole-2,7-dicarboxylate (100 mg, 0.36 mmol) and K_2CO_3 (500 mg) were combined in DMSO (2 mL) and stirred at RT for 15 minutes. Then, (-)-Myrtenyl bromide (120 mg, 0.56 mmol)

was added and the reaction mixture stirred at 70 °C overnight. The mixture was poured into cold water and stirred for half an hour. After extraction with ethyl acetate, organic layer was separated and dried over anhydrous magnesium sulfate. The crude material was purified by column chromatography on silica gel using EA/hexane (1:6) as eluent. Yield: 127 mg, 0.30 mmol, 86%. ^{1}H NMR (500 MHz, $CDCl_3$): δ 8.23-8.14 (m, 4H), 7.98 (d, *J* = 8.3 Hz, 2H), 5.12 (s, 1H) 4.91 (dd, j = 55.5, 17.3 Hz, 2H), 4.01 (s, 6H) 2.39 (dt, *J* = 8.7, 5.6 Hz, 1H), 2.30-2.05 (m, 4H), 1.27-1.18 (m, 4), 0.82 (s, 3H) ppm. ^{13}C NMR (125 MHz, $CDCl_3$): δ 167.62, 142.51, 141.44, 128.31, 125.56, 120.71, 118.75, 111.40, 52.25, 47.67, 43.71, 38.31, 31.47, 31.00, 26.11, 20.95 ppm. ESI (positive mode, CH_3OH): m/z = 418.2010 ($[C_{26}H_{28}NO_4]^+$, calcd. 418.2013).

H_2mcdc

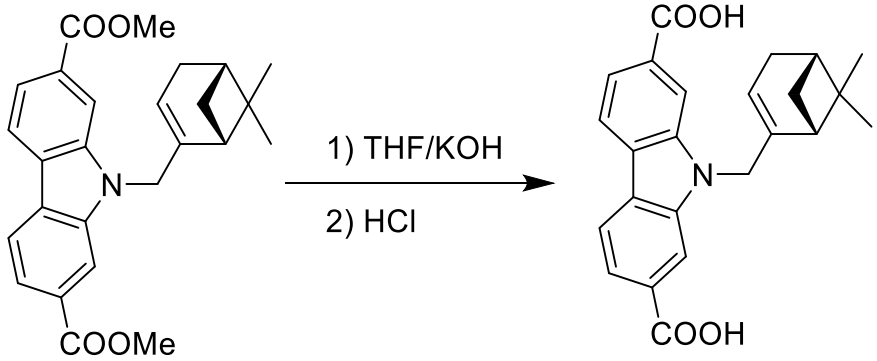

Me_2mcdc (115 mg, 0.28 mmol) was dissolved in 20 mL 1:1 (V/V) THF/KOH (aq., 1M) and the solution was refluxed for 2 days. THF was removed under reduced pressure and the reaction mixture then was acidified with 1 M aqueous HCl while it was kept on an ice bath. pH was adjusted to around 1, and the mixture was stirred for 1 hour. The yellow solid was filtered, washed with water and dried under vacuum. 107 mg, 0.27 mmol, 99%. ^{1}H NMR (500 MHz, DMSO-*d*6): δ 12.98 (br, 2H), 8.34 (d, j = 8.2 Hz, 2H), 8.21 (s, 2H), 7.85 (d, j = 8.2 Hz, 2H), 5.22-4.91 (m, 3H), 2.33 (dt, j = 8.4, 5.6 Hz, 1H), 2.25-1.93 (m, 4H), 1.22-1.02 (m, 4H), 0.66 (s, 3H) ppm. ^{13}C NMR (125 MHz, DMSO-*d*6): 168.25, 143.97, 141.50, 129.42, 125.15, 120.60, 117.87, 111.89, 47.24, 43.62, 38.15, 31.48, 31.02, 26.38, 21.20 ppm. ESI (negative mode, CH_3OH): m/z = 388.1563 ($[C_{24}H_{22}NO_4]^-$, calcd. 388.1543).

2. MOF synthesis and characterization

$[Zn_4O(hmtt)_{4/3}(ecdc)_{1/2}(bdc\text{-}Pro)_{1/2}]$

H_3hmtt (16.0 mg, 28.6 μmol), (S)-H_2bdc-ProBoc (17.4 mg, 44.4 μmol), H_2ecdc (12.2 mg, 43.1 μmol), benzoic acid (55.0 mg, 433.9 μmol) and $Zn(NO_3)_2 \cdot 4H_2O$ (75.0 mg, 287.0 μmol) were dissolved in a mixed solvent of dry DEF (5 mL) and water (0.175 mL). The reaction was carried out in an 85 °C isothermal oven for 20 hours to obtain yellow crystals. The mother liquor was replaced with anhydrous DMF and this process was repeated five times. The DMF was then replaced with fresh anhydrous acetone and the solvent replenished five times within an hour. The acetone-occluded crystals were thermolyzed to produce $[Zn_4O(hmtt)(ecdc)_{1/2}(bdc\text{-}Pro)_{1/2}]$ by heating the crystals at a rate of 20 °C / min and holding the temperature at 200 °C for 20 hours under a dynamic vacuum. Yield: 15 mg.

$[Zn_4O(hmtt)_{4/3}(cychcdc)_{1/2}(bdc\text{-}Pro)_{1/2}]$

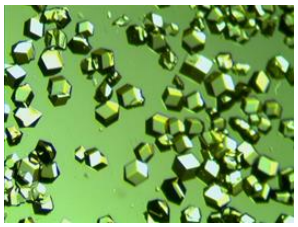

H_3hmtt (15.3 mg, 27.3 μmol), (S)-H_2bdc-ProBoc (13.9 mg, 35.5 μmol), H_2cychcdc (15.2 mg, 43.3 μmol), benzoic acid (56.0 mg, 441.7 μmol) and $Zn(NO_3)_2 \cdot 4H_2O$ (76.0 mg, 290.8 μmol) were dissolved in a mixed solvent of dry DEF (5 mL) and water (0.120 mL). The reaction was carried out in an 85 °C isothermal oven for 20 hours to obtain yellow crystals. The mother liquor was replaced with anhydrous DMF and this process was repeated five times. The DMF was then replaced with fresh anhydrous acetone and the solvent replenished five times within an hour. The acetone-occluded crystals were thermolyzed to produce $[Zn_4O(hmtt)(cychcdc)_{1/2}(bdc\text{-}Pro)_{1/2}]$ by heating the crystals at a rate of 20 °C / min and holding the temperature at 200 °C for 20 hours under a dynamic vacuum. Yield: 14.0 mg.

[$Zn_4O(hmtt)_{4/3}(mcdc)_{1/2}(bdc\text{-}Pro)_{1/2}$]

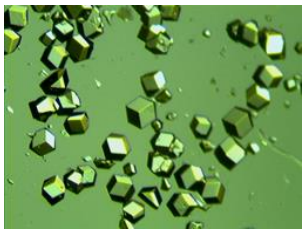

H_3hmtt (15.2 mg, 27.0 μmol), (S)-H_2bdc-ProBoc (14.1 mg, 35.9 μmol), H_2mcdc (16.5 mg, 42.3 μmol), benzoic acid (52.5 mg, 414.0 μmol) and $Zn(NO_3)_2 \cdot 4H_2O$ (75.0 mg, 287.0 μmol) were dissolved in a mixed solvent of dry DEF (5 mL) and water (0.100 mL). The reaction was carried out in an 85 °C isothermal oven for 20 hours to obtain yellow crystals. The mother liquor was replaced with anhydrous DMF and this process was repeated five times. The DMF was then replaced with fresh anhydrous acetone and the solvent replenished five times within an hour. The acetone-occluded crystals were thermolyzed to produce [$Zn_4O(hmtt)(mcdc)_{1/2}(bdc\text{-}Pro)_{1/2}$] by heating the crystals at a rate of 20 °C / min and holding the temperature at 200 °C for 20 hours under a dynamic vacuum. Yield: 14.0 mg.

3. ^{1}H NMR spectra of digested MOFs

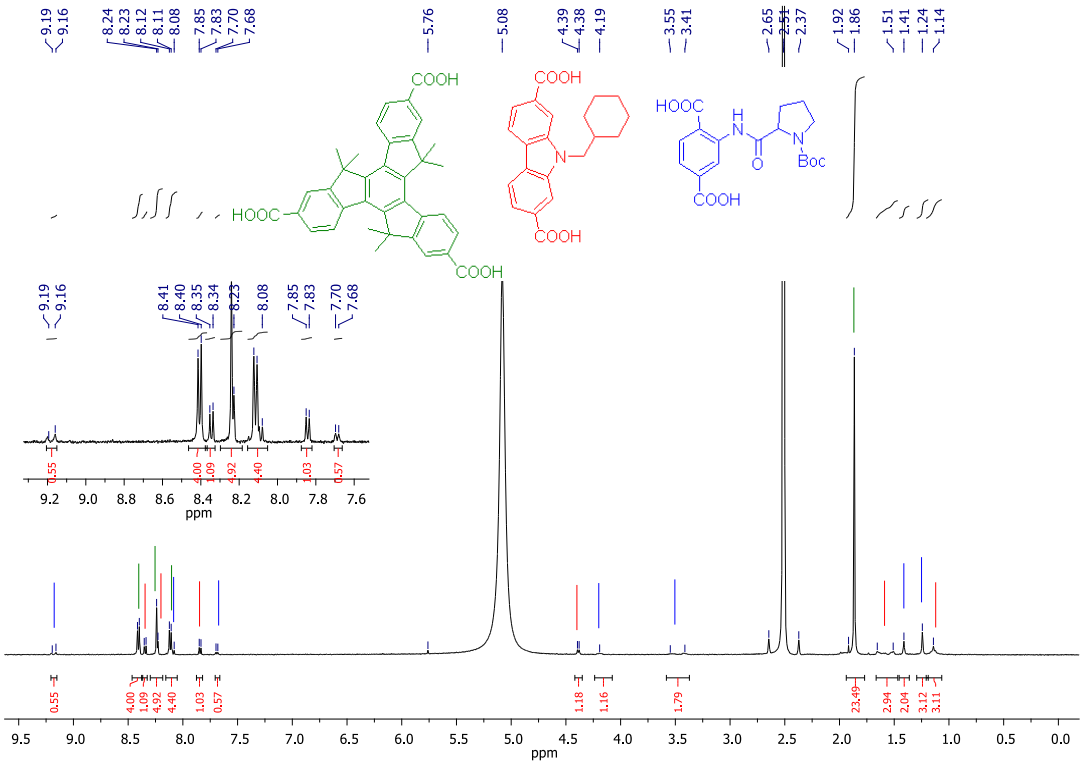

Figure B. 1 ^{1}H NMR spectra of digested [$Zn_4O(hmtt)_{4/3}(cychcdc)_{1/2}(bdc\text{-}ProBoc)_{1/2}$].

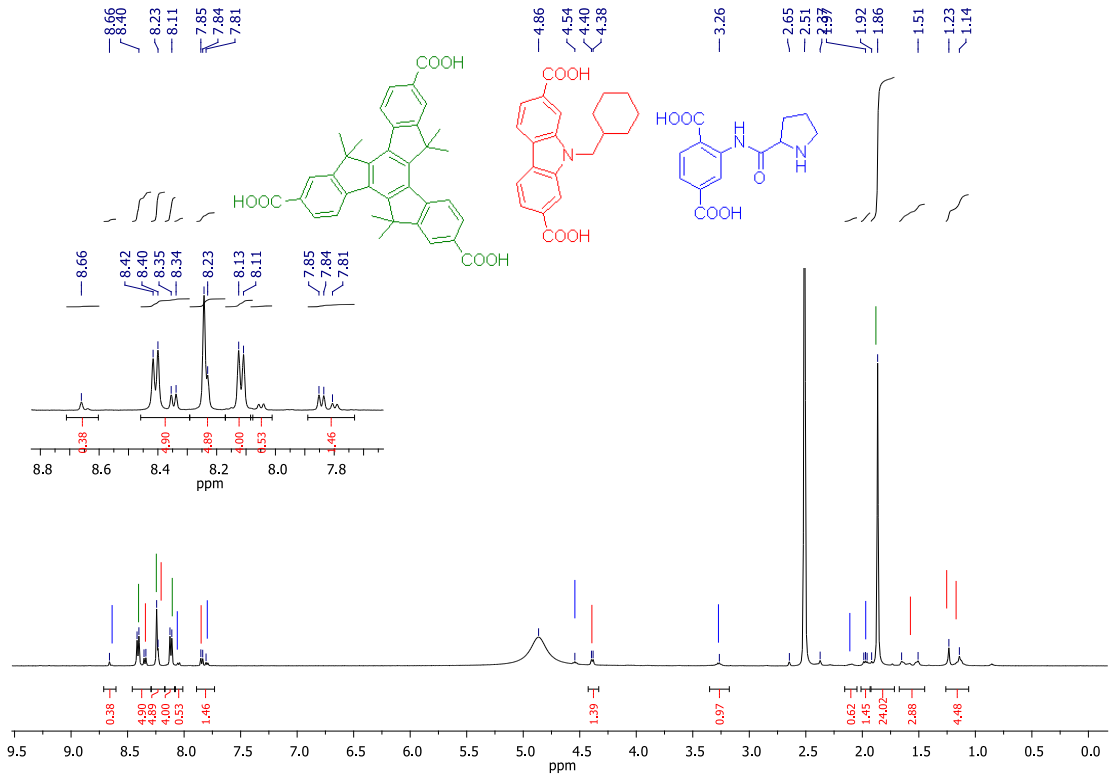

Figure B. 2 ^{1}H NMR spectra of digested $[Zn_4O(hmtt)_{4/3}(cychcdc)_{1/2}(bdc\text{-}Pro)_{1/2}]$.

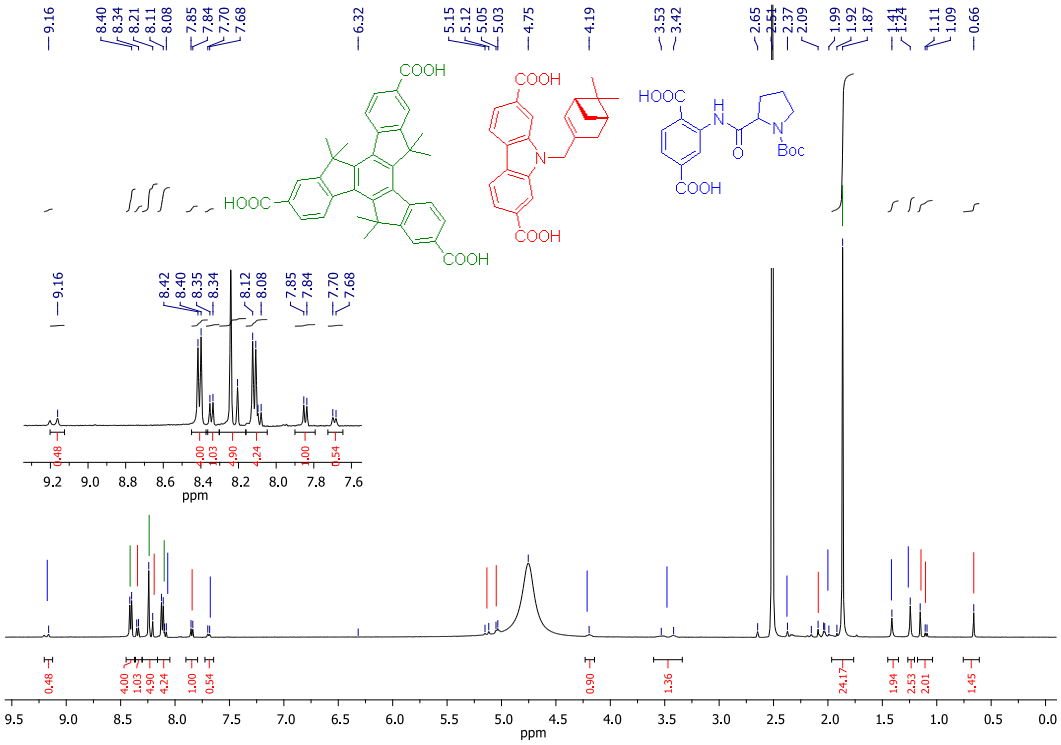

Figure B. 3 ^{1}H NMR spectra of digested $[Zn_4O(hmtt)_{4/3}(mcdc)_{1/2}(bdc\text{-}ProBoc)_{1/2}]$.

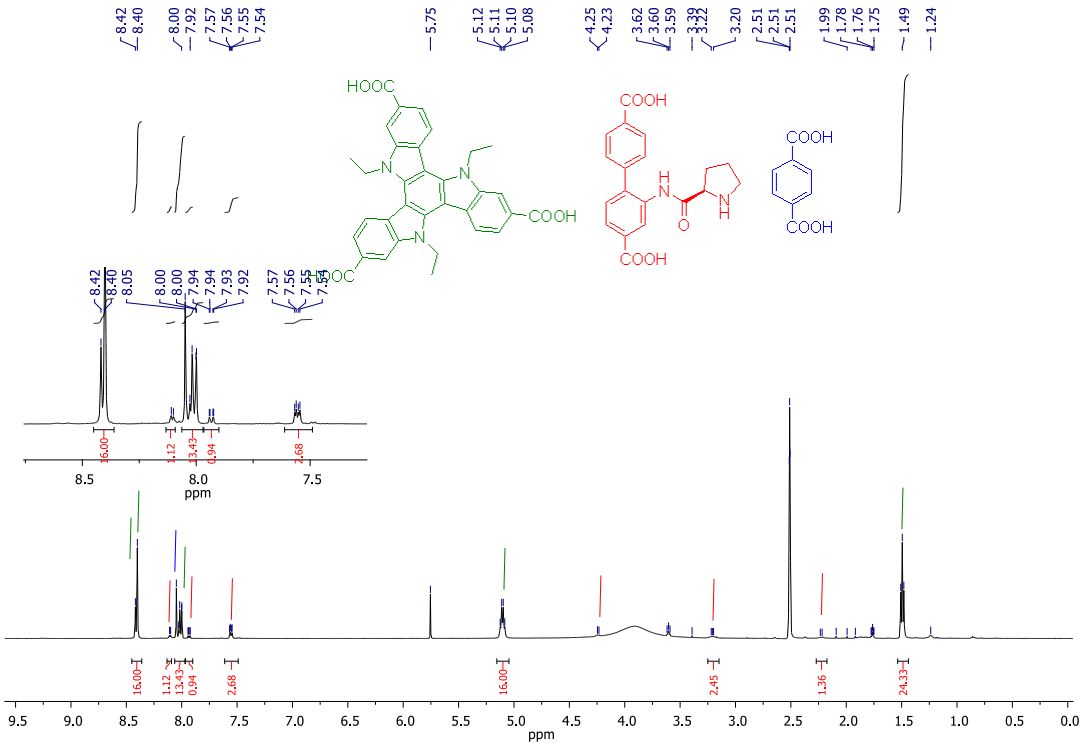

Figure B. 4 The ^{1}H NMR spectrum of digested MUF-777-bpdc-Pro after catalysis.

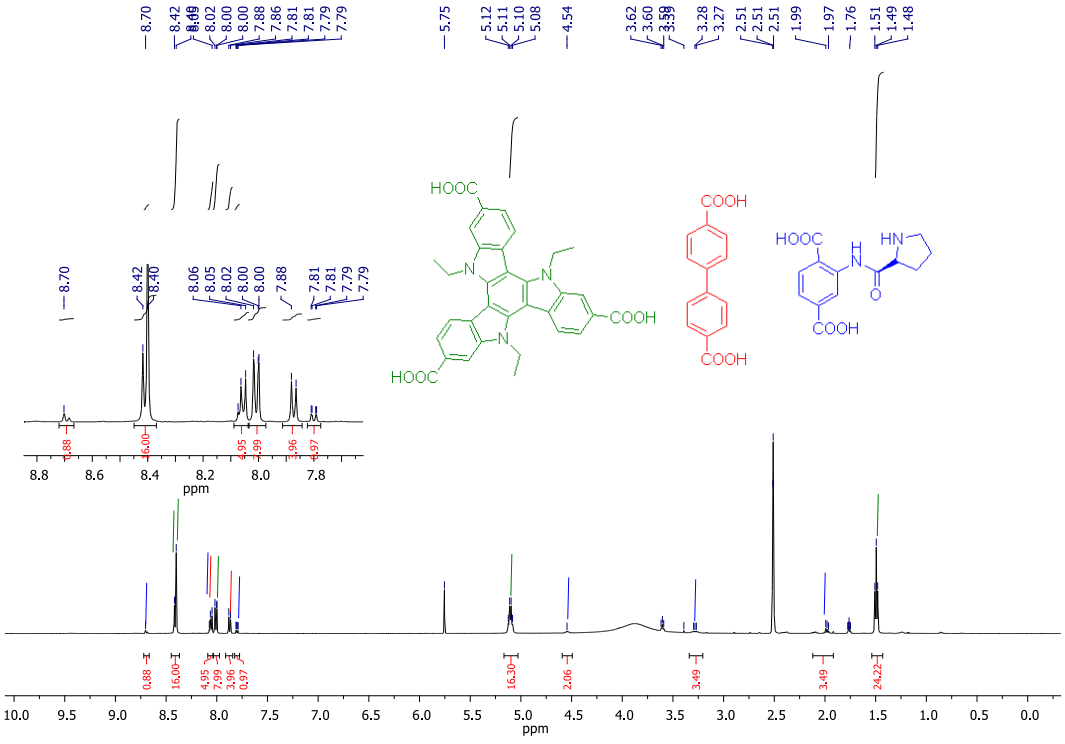

Figure B. 5 The ^{1}H NMR spectrum of digested MUF-777-bdc-Pro after catalysis.

4. Powder X-ray diffraction patterns

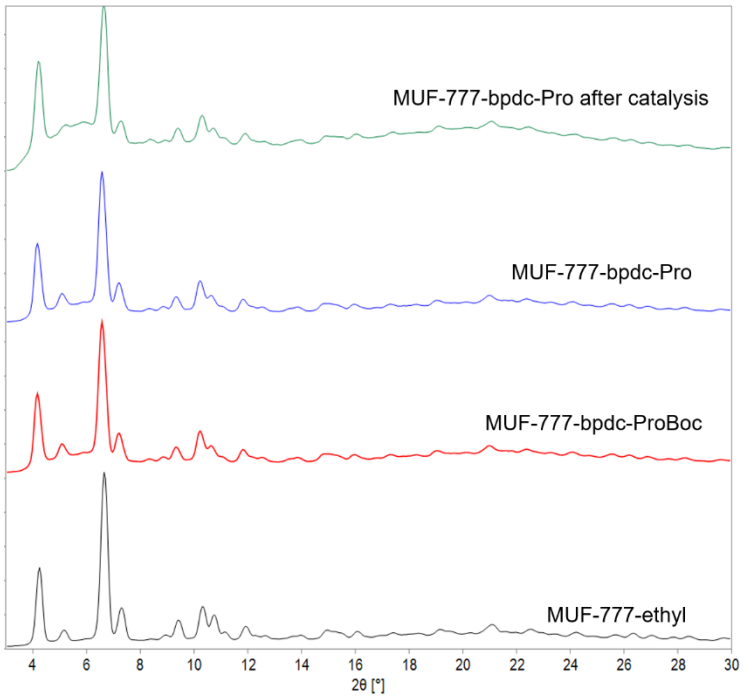

Figure B. 6 PXRD patterns of MUF-777-ethyl, MUF-777-bpdc-ProBoc and MUF-777-bpdc-Pro (before and after catalysis).

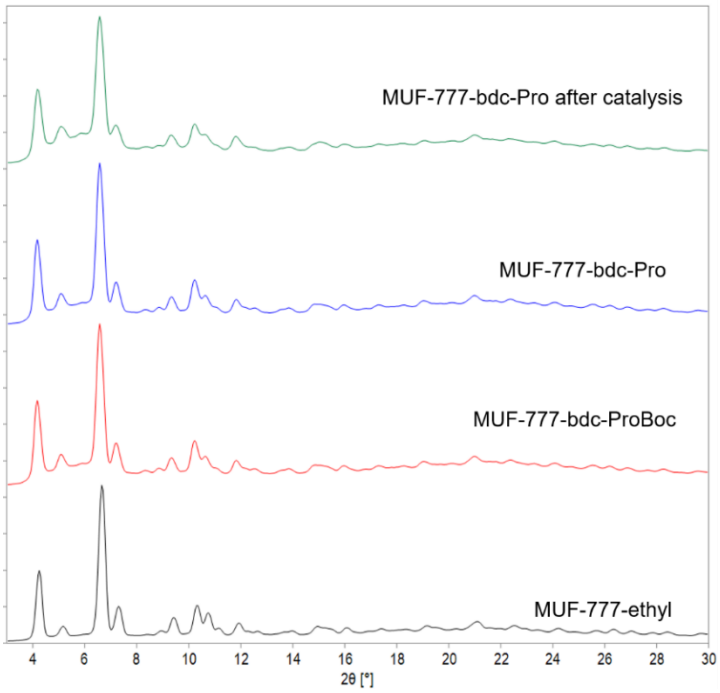

Figure B. 7 PXRD patterns of MUF-777-ethyl, MUF-777-bdc-ProBoc and MUF-777-bdc-Pro (before and after catalysis).

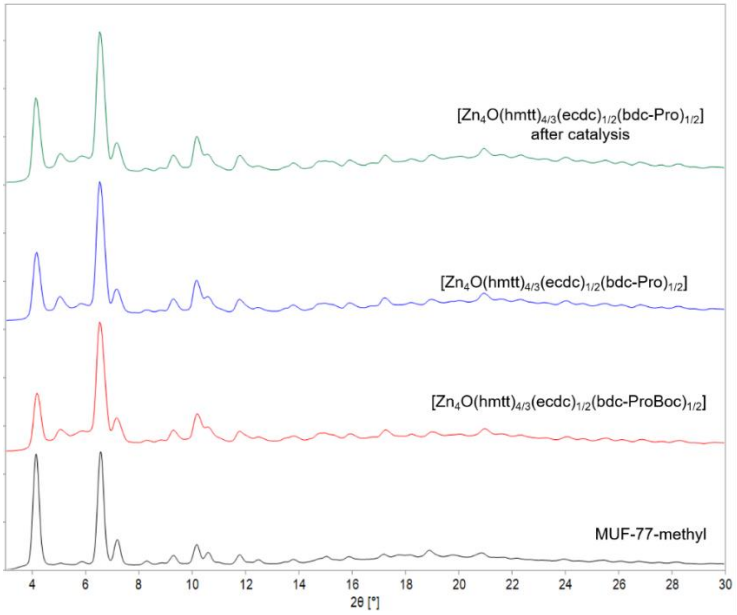

Figure B. 8 PXRD patterns of MUF-77-methyl, $[Zn_4O(hmtt)_{4/3}(ecdc)_{1/2}(bdc\text{-}ProBoc)_{1/2}]$ and MUF-77-cat-1 (before and after catalysis).

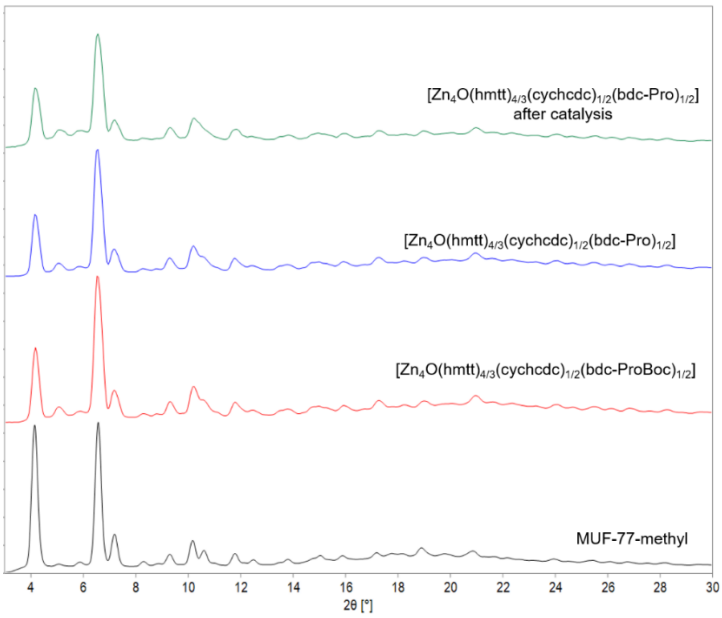

Figure B. 9 PXRD patterns of MUF-77-methyl, $[Zn_4O(hmtt)_{4/3}(cychcdc)_{1/2}(bdc\text{-}ProBoc)_{1/2}]$ and MUF-77-cat-2 (before and after catalysis).

5. Catalysis

Reaction kinetics plots for catalyst.

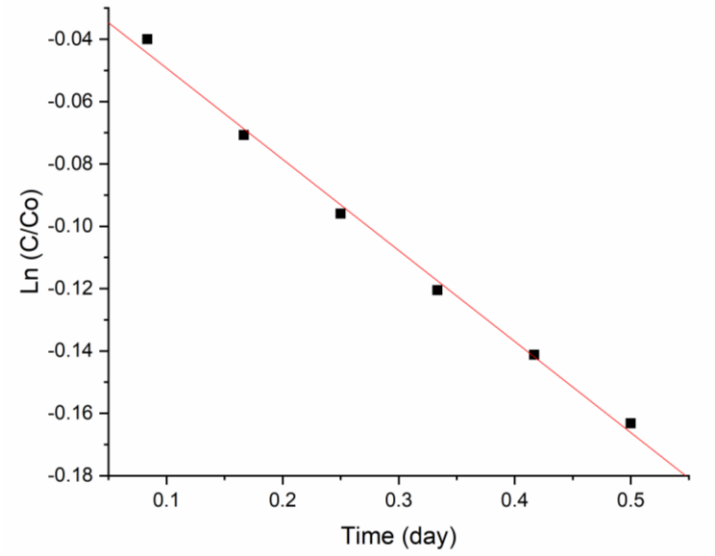

Figure B. 10 Reaction kinetics plot for the aldol reaction catalyzed by $[Zn_4O(hmtt)_{4/3}(ecdc)_{1/2}(bdc\text{-}Pro)_{1/2}]$.

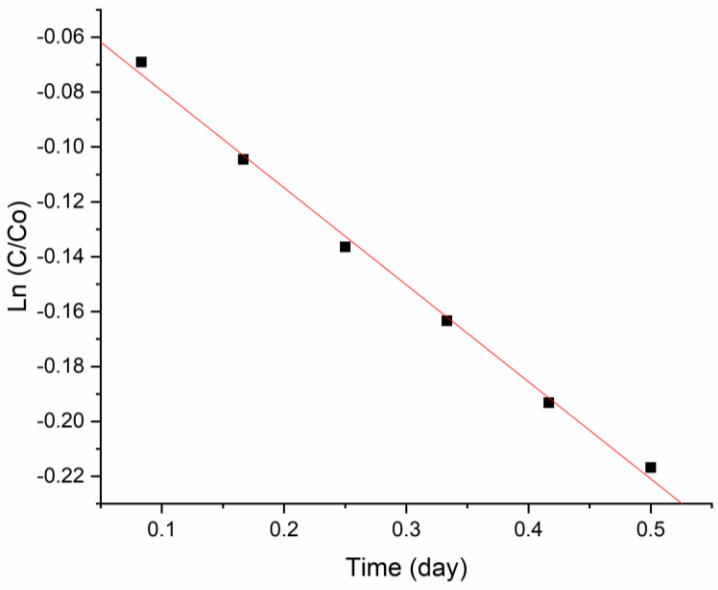

Figure B. 11 Reaction kinetics plot for the aldol reaction catalyzed by $[Zn_4O(hmtt)_{4/3}(cychcdc)_{1/2}(bdc\text{-}Pro)_{1/2}]$**.**

Appendix C for Chapter 4

Experimental Details and Supporting Information for Chapter 4

1. Ligand synthesis and characterization

Me_2azecdc-Boc

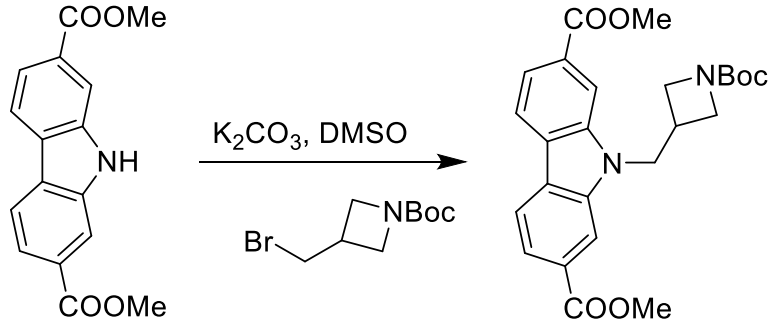

9H-carbazole-2,7-dicarboxylate (142 mg, 0.5 mmol) and K_2CO_3 (500 mg) were combined in DMSO (3 mL) and stirred at RT for 15 minutes. Then, 1-Boc-3-(bromomethyl)-azetidine (250 mg, 1 mmol) was added and the reaction mixture stirred at 70 °C overnight. After cooling to RT, the mixture was poured into cold water and stirred for half an hour. After extraction with DCM; the organic layer was separated and concentrated. The product then, was purified by column chromatography on silica gel using EA/hexane (1:1) as eluent. Yield: 221 mg, 0.49 mmol, 98%. ^{1}H NMR (500 MHz, $CDCl_3$): δ 8.27-8.15 (m, 4H), 8.01 (d, *J* = 8.1 Hz, 2H), 4.67 (d, j = 7.7 Hz, 2H), 4.09-3.95 (m, 8H), 3.88-3.75 (m, 2H) 3.31 (br, 1H), 1.47 (s, 9H) ppm. ^{13}C NMR (125 MHz, $CDCl_3$): δ 167.42, 156.30, 141.04, 128.68, 125.85, 120.99, 120.90, 110.67, 79.82, 52.38, 46.42, 28.59, 28.38 ppm. ESI (positive mode, CH_3OH): m/z = 475.1798 ($[C_{25}H_{28}N_2O_6Na]^+$, calcd. 475.1840).

H_2azecdc-Boc

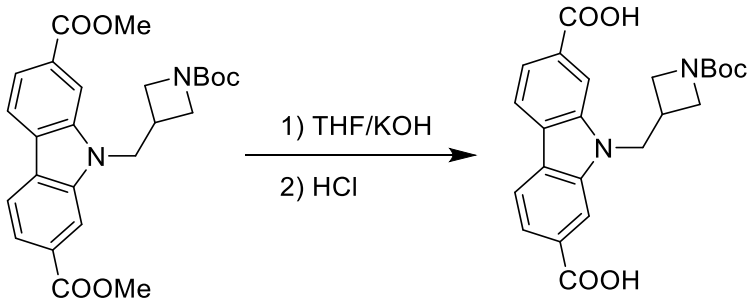

Me_2azecdc (162 mg, 0.37 mmol) was dissolved in 20 mL 1:1 (V/V) THF/KOH (aq., 1M) and the solution was refluxed overnight. THF was removed under reduced pressure and the reaction mixture then was acidified with 1 M aqueous HCl while it was kept on an ice bath. pH was adjusted to around 4-5, and the mixture was stirred for 1 hour. A white solid was filtered, washed with water and dried under vacuum. Yield: 141 mg, 0.33 mmol, 93%. ^{1}H NMR (500 MHz, DMSO-*d*6): δ 13.06 (br, 2H), 8.48-8.27 (m, 4H), 7.86 (d, j = 7.0 Hz, 2H), 4.85 (d, j = 6.1 Hz, 2H), 3.85-3.74 (m, 4H), 3.17 (s, 1H), 1.36 (s, 9H) ppm. ^{13}C NMR (125 MHz, DMSO-*d*6): 168.32, 156.00, 141.28, 129.79, 125.25, 121.49, 120.76, 111.68, 79.00, 49.07, 45.44, 28.96, 28.54 ppm. ESI (negative mode, CH_3OH): m/z = 423.1566 ($[C_{23}H_{23}N_2O_6]^-$, calcd. 423.1551).

Me_2azecdc-NH

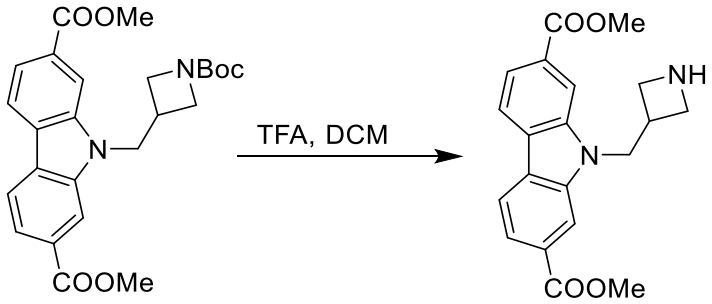

Me_2azecdc (53 mg, 0.12 mmol) was dissolved in DCM (5 mL) and the solution was cooled on an ice-water bath. To this solution, TFA (1 mL) was added slowly. The solution then was stirred overnight. After addition of water (10 mL), solid K_2CO_3 was added to neutralize the acid. Then DCM was removed and the white solid filtered, washed with water and dried under vacuum. Yield: 33 mg, 0.09 mmol, 78%. ^{1}H NMR (500 MHz, DMSO-*d*6): δ 8.45-8.35 (m, 4H), 7.89 (d, j = 8.2,

2H), 4.86 (d, j = 7.2 Hz, 2H), 3.95 (s, 6H) 3.85-3.75 (m, 2H), 3.70-3.60 (m, 2H), 3.43-3.22 (m, 1H), ppm. ESI (positive mode, CH_3OH): m/z = 353.1486 ($[C_{20}H_{21}N_2O_4]^+$, calcd. 353.1496).

Me_2teacdc

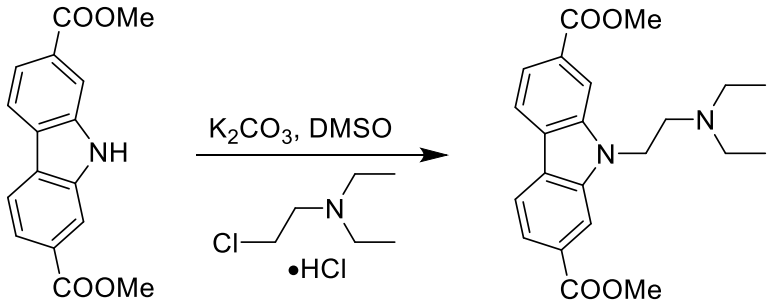

9H-carbazole-2,7-dicarboxylate (283 mg, 1 mmol) and K_2CO_3 (1.3 g) were combined in DMSO (5 mL) and stirred at room temperature for 15 minutes. Then, 2-chlorotriethylamine hydrochloride (344 mg, 2 mmol) was added and the reaction mixture stirred at 70 °C for 4 hours. The mixture was poured into cold water and stirred for half an hour. After extraction with DCM, organic layer was separated, dried over anhydrous magnesium sulfate and concentrated under reduced pressure to obtain product as yellow solid. Yield: 335 mg, 0.86 mmol, 88%. ^{1}H NMR (500 MHz, $CDCl_3$): δ 8.25 (s, 2H), 8.18 (d, *J* = 8.2 Hz, 2H), 8.98 (d, *J* = 8.2 Hz, 2H), 4.54 (s, 2H), 4.02 (s, 6H), 2.91 (s, 2H), 2.65 (d, j = 5.9 Hz, 4H), 1.01 (t, *J* = 6.7 Hz, 6H) ppm. ^{13}C NMR (125 MHz, $CDCl_3$): δ 167.63, 141.16, 128.30, 125.68, 120.80, 120.45, 111.11, 52.28, 51.70, 47.62, 42.42, 11.83 ppm. ESI (positive mode, CH_3OH): m/z = 383.1965 ($[C_{22}H_{27}N_2O_4]^+$, calcd. 383.1965).

H_2teacdc

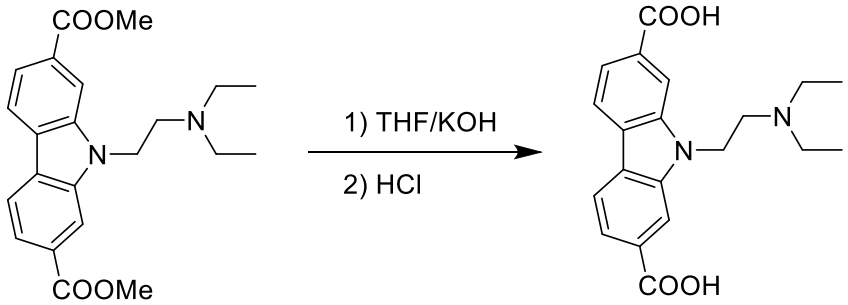

Me_2teacdc (300 mg, 0.8 mmol) was dissolved in 30 mL 1:1 (V/V) THF/KOH (aq., 1M) and the mixture was refluxed overnight. THF was removed under reduced pressure and the reaction mixture then was acidified with 1 M aqueous HCl while it was kept on an ice bath. pH was adjusted

to around 6-7, and the mixture was stirred for 1 hour. After removing about half of water, a yellow solid was filtered and dried under vacuum. Yield: 253 mg, 0.71 mmol, 91%. ^{1}H NMR (500 MHz, DMSO-*d*6): δ 8.2 (d, j = 8.2 Hz, 2H), 8.26 (s, 2H), 7.84 (d, j = 8.1 Hz, 2H), 4.60 (t, *J* = 7.0 Hz, 2H), 2.81 (t, *J* = 7.0 Hz, 2H), 2.49 (m, 4H), 0.76 (t, j = 7.0, 6H) ppm. ^{13}C NMR (125 MHz, DMSO-*d*6): 168.37, 149.39, 129.38, 125.16, 121.34, 120.44, 111.90, 51.81, 47.29, 40.50, 12.15 ppm. ESI (positive mode, CH_3OH): m/z = 355.1645 ($[C_{20}H_{23}N_2O_4]^+$, calcd. 355.1652).

Et$_3$tat-pip-Boc

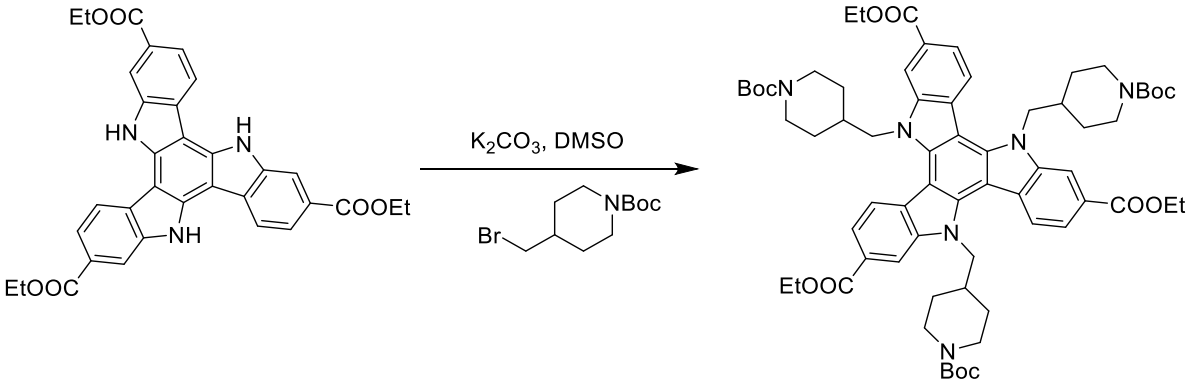

Et$_3$tat (465 mg, 0.83 mmol) and K_2CO_3 (2.07 g, 15 mmol) were combined in DMSO (7 mL) and the mixture was stirred at room temperature for 10 minutes. Then, 1-Boc-4-bromomethylpiperidine (1.23 g, 4.42 mmol) in 3 mL of DMSO was added. The reaction mixture then was heated at 70 °C and stirred overnight. After cooling to RT, 50 mL of water was added, and the mixture was stirred for 30 minutes. A yellow solid was filtered, washed with water and dried under vacuum. The product was obtained as a yellowish solid after purification by column with hexane/EA (from 1:0 to 3:2). Yield: 710 mg, 0.61 mmol, 74%. ^{1}H NMR: (500 MHz, $CDCl_3$): δ 8.41 (s, 3H), 8.28 (d, *J* = 8.5 Hz, 3H), 8.13 (d, *J* = 8.4 Hz, 3H), 5.01 (d, *J* = 7.4 Hz, 6H), 4.54 (q, *J* = 7.1 Hz, 6H), 3.79 (br, 6H), 2.27 (m, 6H), 2.04 (m, 3H), 1.55 (m, 9H), 1.33(s, 27H), 1.01-0.89 (m, 12H), ppm. ^{13}C NMR: (125 MHz, $CDCl_3$): 167.11, 154.36, 145.89, 141.16, 140.49, 126.48, 125.17, 121.62, 121.34, 113.03, 103.58, 79.45, 61.17, 52.05, 43.06, 36.23, 29.21, 28.31, 14.53 ppm. ESI (positive mode, CH_3OH): m/z = 1175.6028 ($[C_{66}H_{84}N_6O_{12}Na]^+$, calcd. 1175.6039).

H_3tat-pip-Boc

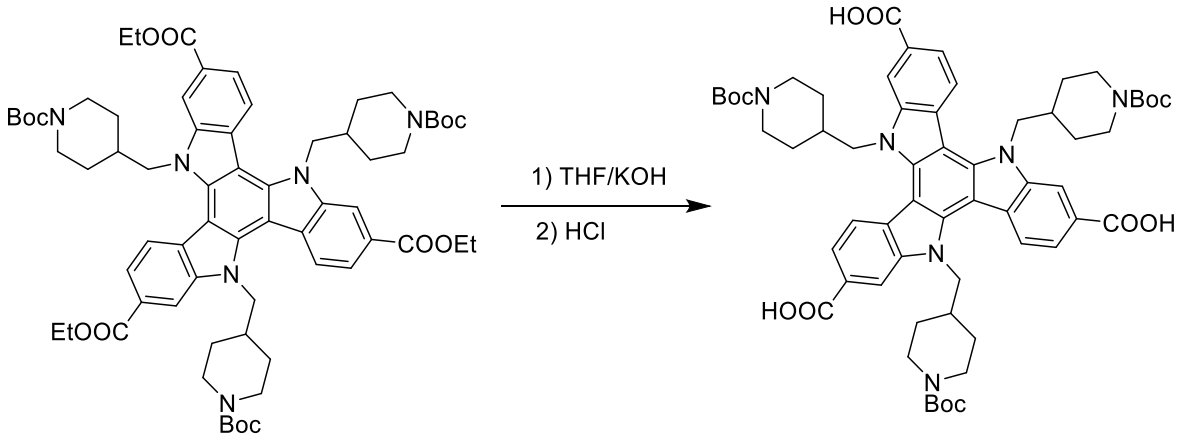

Et_3tat-pip-Boc (540 mg, 0.47 mmol) was dissolved in 50 mL 1:1 (V/V) THF/KOH (aq., 1M) and the solution was refluxed for 3 days. THF was removed under reduced pressure and the reaction mixture then was acidified with 1 M aqueous HCl while it was kept on an ice bath. pH was adjusted to around 4, and the mixture was stirred for 1 hour. A yellowish solid was filtered, washed with water and dried under vacuum. Yield: 493 mg, 0.46 mmol, 98%. ^{1}H NMR: (500 MHz, DMSO-*d*6): δ 12.95 (br, 3H), 8.52 (s, 3H), 8.39 (d, *J* = 8.5 Hz, 3H), 8.03 (d, *J* = 8.5 Hz, 3H), 5.08 (d, *J* = 6.2 Hz, 6H), 4.54, 3.56 (br, 6H), 2.24 (s, 6H), 1.91 (d, j = 4.2 Hz, 3H), 1.10 (s, 27H), 1.09-0.76 (m, 12H) ppm. ^{13}C NMR: (125 MHz, DMSO-*d*6): 168.47, 153.83, 140.82, 140.80, 126.27, 125.94, 122.15, 122.10, 113.63, 103.48, 78.88, 60.65, 51.58, 42.57, 36.08, 29.11, 28.36 ppm. ESI (negative mode, CH_3OH): m/z = 1067.5153 ($[C_{60}H_{71}N_6O_{12}]^-$, calcd. 1067.5124).

Et_3tat-pip-NH

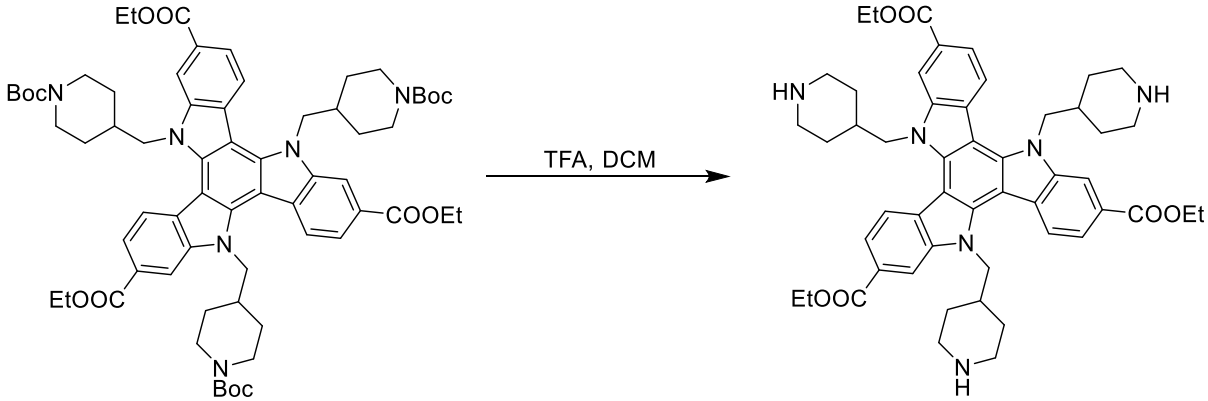

Et_3tat-pip-Boc (93 mg, 0.08 mmol) was dissolved in DCM (5 mL) and the solution was cooled on an ice-water bath. To this solution, TFA (2 mL) was added slowly. The solution then was stirred overnight. After addition of water (10 mL), solid K_2CO_3 was added to neutralize the acid. Then DCM was removed and the yellowish solid filtered, washed with water and dried under vacuum. 61 mg, 0.08 mmol, 100%. ^{1}H NMR: (500 MHz, DMSO-*d6*): δ 8.56 (s, 3H), 8.44 (d, *J* = 8.6 Hz, 3H), 8.09 (d, *J* = 8.7 Hz, 3H), 5.14 (d, *J* = 7.2 Hz, 6H), 4.45 (q, *J* = 7.1 Hz, 6H), 2.92 (d, j = 12.3 6H), 2.47-2.41 (m, 6H), 2.04 (s, 3H), 1.44 (t, j = 7.2 9H), 1.05 (s, 12H) ppm. ESI (positive mode, CH_3OH): m/z = 853.4640 ($[C_{51}H_{61}N_6O_6]^+$, calcd. 853.4647).

2. MOF synthesis and characterization

[Zn_4O(tatpip-Boc)$_{4/3}$(bpdc)$_{1/2}$(bdc)$_{1/2}$]

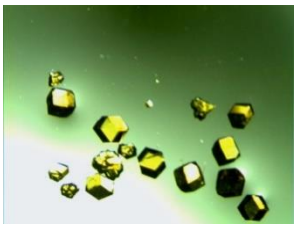

H_3tatpip-Boc (28.8 mg, 26.9 μmol), H_2bpdc (10.0 mg, 41.3 μmol), terephthalic acid (6.9 mg, 41.5 μmol), benzoic acid (46.0 mg, 376.4 μmol) and $Zn(NO_3)_2{\cdot}4H_2O$ (73.0 mg, 279.4 μmol) were dissolved in a mixed solvent of dry DEF (5 mL) and water (0.100 mL). The reaction was carried out in an 85 °C isothermal oven for 40 hours to obtain light orange color crystals. The mother liquor was replaced with anhydrous DMF and this process was repeated five times. The DMF was then replaced with fresh anhydrous acetone and the solvent replenished five times within an hour. The acetone-occluded crystals were thermolyzed to produce [Zn_4O(tatpip-NH)$(bpdc)_{1/2}(bdc)_{1/2}$] by heating the crystals at a rate of 20 °C / min and holding the temperature at 200 °C for 20 hours under a dynamic vacuum. Yield: 23 mg.

[Zn_4O(hmtt)$_{4/3}$(teacdc)$_{1/2}$(bdc)$_{1/2}$]

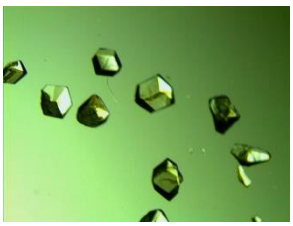

H_3hmtt (17.2 mg, 28.9 μmol), H_2teacdc (14.9 mg, 42.0 μmol), terephthalic acid (7.5 mg, 45.1 μmol), benzoic acid (52.5 mg, 429.5 μmol) and $Zn(NO_3)_2{\cdot}4H_2O$ (72.5 mg, 277.5 μmol) were dissolved in a mixed solvent of dry DEF (5 mL) and water (0.100 mL). The reaction was carried out in an 85 °C isothermal oven for 19 hours to obtain colorless crystals. The mother liquor was replaced with anhydrous DMF and this process was

repeated five times. The DMF was then replaced with fresh anhydrous acetone and the solvent replenished five times within an hour.

3. ^{1}H NMR spectra of digested MOFs

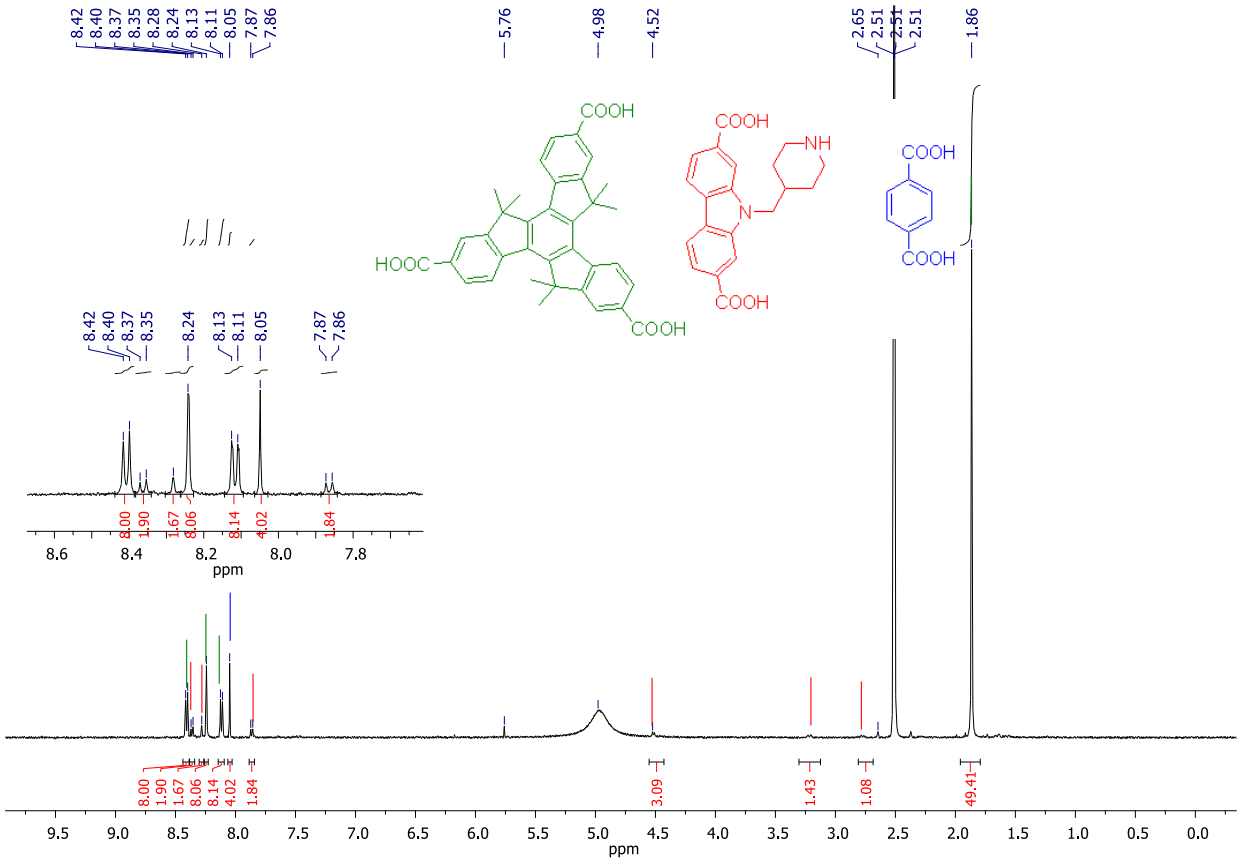

Figure C. 1 The ^{1}H NMR spectrum of digested MUF-777-tatpip-NH after solvothermal deprotection process.

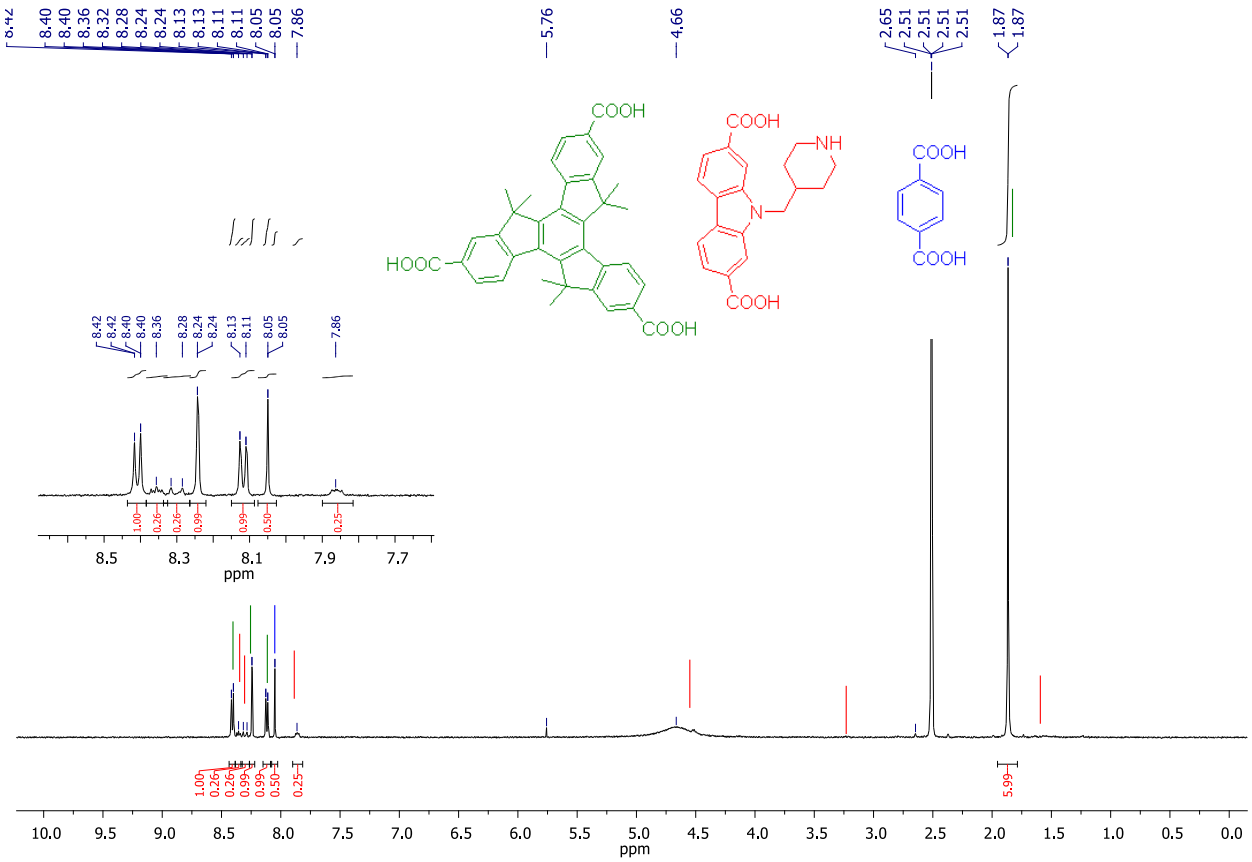

Figure C. 2 The ^{1}H NMR spectrum of digested MUF-77-pipcdc-NH after Michael reaction.

Appendix D

1. Crystallographic Information Files for MOFs

Cif files for MOFs uploaded to https://sites.google.com/site/telferlab/adil

References

1. Luan, S.; Ge, Q.; Chen, Y.; Dai, M.; Yang, J.; Li, K.; Liu, D.; Zhao, L., Discovery and structure-activity relationship studies of N-substituted indole derivatives as novel Mcl-1 inhibitors. *Bioorg. Med. Chem. Lett.* **2017,** *27* (9), 1943-1948.
2. Olkhovik, V. K.; Vasilevskii, D. A.; Pap, A. A.; Kalechyts, G. V.; Matveienko, Y. V.; Baran, A. G.; Halinouski, N. A.; Petushok, V. G., Synthesis of new polyconjugated molecules with biphenyl, dibenzothiophene, carbazole and phenanthrene units. *ARKIVOC* **2008,** *(ix)* 69-93.